A Critical Evaluation of Measuring $K_{0,NC}$ during Triaxial Compression Testing

A thesis submitted by

Padraig Doran

in partial fulfilment of the requirements for the degree of

Master of Science

in

Civil and Environmental Engineering

Tufts University

May 2023

Advisor: Professor J. T. Germaine

I. Abstract

Triaxial constant rate of strain K_0 consolidation can be performed to measure the stress state of fine-grained soil samples during uniaxial compression. Researchers from MIT, then the TAG Laboratory have used computer feedback control to perform triaxial K_0 consolidation tests for some time.

This research sought first to investigate previous test datasets to assess the risk for potential errors in K_0 measurements. From this data, systematic radial contraction was found during tests. This was due to apparatus compressibility not being accounted for when calculating the axial strain of the specimen. An analytical approach based on Wissa Linear Theory was used to quantify excess pore pressure generation in the specimen during consolidation. Resedimented Gulf of Mexico, Eugene Island clay was found to generate high excess pore pressures in the specimen due to its high compressibility and low permeability. This led to measured effective stresses being larger than actual effective stresses, and thereby higher measured K_0 values.

Finite element analyses were conducted to simulate specific test data and verified the results attained from the analytical approach. Simulations of triaxial tests utilizing geotextile side drains were then performed and found to reduce excess pore pressure generation within the specimen to negligible levels.

A correction for apparatus compressibility was included in the triaxial control software. Triaxial K_0 tests were run on Resedimented Boston Blue Clay and the effects were found to be negligible. Tests using geotextile side drains were performed. This resulted in good agreement with CRS and Oedometer uniaxial compression behaviour. The K_0 measured during these tests was lower than that measured in past research and corresponds with what was calculated using the analytical approach based on Wissa Linear Theory.

II. Acknowledgements

I want to give my utmost thanks to my advisor, Dr. John Germaine. It was a pleasure to work under him. Just to be able to absorb some of the knowledge that he possesses alone gave worth to my time spent at Tufts. His advice, sense of humour and encouragement are things that I will not forget over my lifetime.

I would like to thank my committee members for taking the time to review and provide comments to the research presented in this thesis. I would like to particularly thank Dr. Luis Dorfmann for the time he spent with me whilst trying to model soil behaviour using Abaqus FEA.

I would also like to thank Ward and Burke Microtunnelling Ltd. for sponsoring my degree.

My lab mates, George and Emre, deserve a special amount of appreciation for helping me to keep my sanity over the past two years.

Finally, I would like to thank Destiny for putting up with me moving to Boston for two years.

III. Contents

IV. List of Tables

V. List of Figures

Key Words

Clay, At Rest Lateral Stress Ratio, Triaxial Test, Excess Pore Pressure, Apparatus Compressibility, Side Drains

Terminology

A/D	Analog to Digital
CH	High Plasticity Clay
LL	Liquid Limit
CL	Low Plasticity Clay
CRS	Constant Rate of Strain
CSL	Critical State Line
DC	Direct Current
FEA	Finite Element Analysis
GeoFluids	Research Consortium
LVDT	Linear Variable Differential Transformer
MCC	Modified Cam-Clay
MIT	Massachusetts Institute of Technology
OCR	Overconsolidation Ratio
PI	Plasticity Index
PID	Proportional–Integral–Derivative
PVA	Pressure-Volume Actuator
PVC	Polyvinyl Chloride
RBBC	Resedimented Boston Blue Clay
RLC	Resedimented London Clay
RGoM-EI	Resedimented Gulf of Mexico, Eugene Island
RGoM-Ursa	Resedimented Gulf of Mexico, Ursa
RUC	Resedimented Ugnu Clay
RPC	Resedimented Presumpscot Clay
SS	Skibbereen Silt
TAG	Tufts Advanced Geomaterials
UC	Undrained Compression
USB	Universal Serial Bus
VCL	Virgin Compression Line
XRPD	X-ray Powder Diffraction

Symbols

A_0	Initial specimen area
H_0	Initial specimen height
H_d	Specimen drainage height
K	Lateral stress ratio
K_0	Coefficient of lateral earth pressure at rest
$K_{0,NC}$	Coefficient of lateral earth pressure at rest for a NC soil
$K_{0,a}$	Average corrected coefficient of lateral earth pressure at rest
$K_{0,a}$	Average corrected coefficient of lateral earth pressure at rest
C_c	Compression Index
e	Void ratio
e_0	Initial void ratio
σ_c	Cell pressure
φ'_{CS}	Effective critical state friction angle
φ'_0	Mobilized effective friction angle
S_u	Undrained shear strength
σ_v, σ'_v	Vertical total stress, vertical effective stress
σ_h, σ'_h	Horizontal total stress, horizontal effective stress
σ_a, σ'_a	Axial total stress, axial effective stress
σ_r, σ'_r	Radial total stress, radial effective stress
$\sigma'_{a,a}$	Average axial effective stress corrected for excess pore pressure
$\sigma'_{r,a}$	Average radial effective stress corrected for excess pore pressure
σ'_{vc}	Vertical consolidation effective stress
$\sigma'_{a,max}$	Maximum past vertical consolidation effective stress
σ'_p	Preconsolidation pressure
$\sigma_1, \sigma_2, \sigma_3$	Principal stresses
$\sigma'_1, \sigma'_2, \sigma'_3$	Principal effective stresses
p'	Mean effective stress
q	Shear stress
u	Pore pressure
u_b	Backpressure
$u_{e,c}$	Excess pore pressure at the centre of the specimen
m_v	Coefficient of volume compressibility
c_v	Coefficient of consolidation
n	Porosity
ε_a	Axial strain
ε_{vol}	Volumetric strain
μ	Poisson's ratio
$\dot{\varepsilon}$	Strain rate

κ	Slope of swelling line
λ	Slope of virgin compression line
$v_{s,M}$	Specific volume of swelling lines at *lnp' = 1*
M	Slope of critical state line
V_{geo}	Volumetric loss of geotextile
k_p	Hydraulic conductivity of filter paper
k_s	Hydraulic conductivity of soil
k_v	Vertical hydraulic conductivity of soil
k_h	Horizontal hydraulic conductivity of soil

1 Introduction

1.1 Problem Statement

The at rest lateral stress ratio, K_0, is one of our fundamental soil parameters. This parameter describes the in-situ stress-state and mechanical behaviour of soils in the deposited in the field and consolidates under a zero lateral strain condition. K_0 is defined by the following equation:

$$K_0 = \frac{\sigma'_h}{\sigma'_v} = \frac{\sigma'_r}{\sigma'_a} \qquad \textit{(Eq. 1-1)}$$

Where σ'_v is the vertical effective stress (axial effective stress, σ'_a the experimental triaxial testing domain) and σ'_h is the (horizontal effective stress (σ'_r in the experimental triaxial testing domain).

Although there are in-situ methods of measuring in-situ lateral stress in soft clays (Bjerrum and Anderson, 1972) and by use of the dilatometer (Massarsch, and Broms, 1976), experimental triaxial K_0 consolidation through stringent and systematic triaxial testing is needed to fully understand the evolution of K_0 for different materials over differing stress ranges. This is especially important with regard to the petroleum industry, where understanding the relationship between K_0 and stress level allows the interpretation of borehole stability calculations, normal compression behaviour and predictions of the least principal stress. This research sought to improve the triaxial testing protocol of fine-grained soils in the Tufts Advanced Geomaterials Laboratory by first assessing the effects of experimental in measurements of K_0 during triaxial testing, and to thereby develop methods to eliminate these errors in future testing.

1.2 Thesis Objectives

The objectives of this thesis are fourfold: (1) to investigate past triaxial data of fine-grained soils in order to assess the possibility of error in K_0 measurements or protocol, (2) to devise an analytical approach to quantify these errors and provide a correction to rectify these past data sets, (3) to utilize constitutive models and finite element analyses using Abaqus to investigate and confirm the validity of the analytical approach and to probe the efficacy of different methods proposed to eliminate the errors in K_0 measurements in future experimental testing and (4) to implement these methods to eliminate the identified errors in K_0 measurements in testing. These objectives are solely focused on the measurement of the at-rest lateral stress ratio in the normally consolidated range, $K_{0,NC}$, and ultimately to provide a best estimate of $K_{0,NC}$ for both RBBC and RGoM-EI clay.

1.3 Organisation of Thesis

This thesis is organized into ten chapters. Chapter two will provide background information pertaining to the research and material described in the following chapters.

Chapter three will summarize the relevant information regarding the testing materials that were utilized as a part of this research including a description of the source, index properties and engineering properties, those materials being Resedimented Boston Blue Clay (RBBC) and Resedimented Gulf of Mexico, Eugene Island (RGoM-EI).

Chapter four will describe the resedimentation procedure used at the Tufts Advanced Geomaterials Laboratory to produce testing samples to the required stress-state and composition.

The equipment utilized during this research will then be outlined in chapter five. This will include the medium pressure and high pressure triaxial systems, data acquisition system, control software and various correction implemented as a part of this research.

Chapter six will expound on the analytical approaches used to quantify the magnitudes of excess pore pressures generated in triaxial specimens with vertical drainage conditions during K_0 consolidation and will discuss the use of radial drainage conditions and its advantages.

Chapter seven will explain and report on the results of the finite element analyses conducted during this research and compare to the analytical results from chapter six.

Chapter eight will then set out the procedures utilized during experimental testing (setting up and dismantling the tests). This chapter will also provide an explanation on back pressure saturation, K_0 consolidation, and hold pressure subroutines.

Chapter nine will present and discuss the experimental results, from tests using both side drainage and tests without side drainage but corrected using the analytical approach presented in chapter six.

Finally, chapter 10 will provide the conclusions reached by the author over the course of this research and give recommendations for future areas of research that the author suggests should be investigated.

2 Background

2.1 Introduction

This chapter seeks to provide context to the research presented in this thesis. The concept of the at rest lateral earth pressure ratio or coefficient, K_0, was first introduced by (Donath, 1891) as "the stationary concept of unlimited ground." (Terzaghi, 1923) first provided an equation relating K_0 to the effective friction angle, followed subsequently by (Jâky, 1944) who's equation is commonly used to this day. Experimental K_0 ratio measurements have been performed in experimental testing using modified "rigid ring" apparatuses or triaxial K_0 compression testing.

This chapter will first describe some previous studies undertaken on the $K_{0,NC}$ consolidation behaviour of clay, paying particular attention the test materials used in this research (RBBC and RGoM-EI). Then, a synopsis of widely available correlations for $K_{0,NC}$ will be provided, followed by a comparison of resedimented and intact materials, and the utilization of side drains in triaxial testing.

2.2 Previous Studies of Triaxial $K_{0,NC}$ Consolidation Behaviour

(Abdulhadi, 2009) conducted numerous CK_0UC triaxial tests on RBBC on a stress range between 0.1 and 10 MPa using an earlier version feedback-controlled software utilized in this study. The compression curves for these triaxial tests were in good agreement with those obtained for uniaxial CRS testing performed on the same material. In general, there was a reduction in K_0 with increasing axial effective stress, σ'_a. K_0 reached its lowest values at preconsolidation pressure (or maximum past stress experienced during resedimentation), σ'_p. After this initial dip, K_0 in the normally consolidated regime, $K_{0,NC}$, exhibited stress

dependent behaviour, with increasing $K_{0,NC}$ with increasing axial effective stress. The values of $K_{0,NC}$ ranged from 0.52 at 0.15 MPa to 0.56 at 10 MPa (Figure 2-1).

(Hanley, 2017) performed multiple triaxial K_0 consolidation tests on intact BBC. These tests exhibit far larger scatter in the measure K_0 values in comparison to resedimented material, displaying the high variability of intact soil samples (Figure 2-3).

(Casey, 2014) found similar behaviour over the range of resedimented fine-grained cohesive materials tested between 0.1 and 100 MPa (Figure 2-2), with RBBC showing the same range in $K_{0,NC}$ values as found by (Abdulhadi, 2009). There was also dependency shown on the increase in $K_{0,NC}$ with stress and the plasticity of the soil, with high plasticity soil displaying larger increases in $K_{0,NC}$ with increasing stress, medium plasticity soil displaying medium increases in $K_{0,NC}$ with increasing stress and low plasticity soils showing a decrease in $K_{0,NC}$ with increasing stress (Figure 2-4). (Casey, 2014) provided power law regressions relating $K_{0,NC}$ to vertical effective stress for both RBBC and RGoM-EI. (Figure 2-5). With regards to the high plasticity clay RGoM-EI, $K_{0,NC}$ ranged from 0.61 at 0.1 MPa to 0.92 at 60 MPa axial effective stress.

(Hanley, 2017) reported values similar to (Casey, 2014) for $K_{0,NC}$ for RGoM-EI at the low stress range of 0.1 to 1MPa, with $K_{0,NC}$ exhibiting stress dependency (Figure 2-6).

(Tsuchida and Kikuchi, 1991) performed uniaxial K_0 consolidation on intact samples of Japanese marine clays in a fully automated triaxial apparatus utilizing side drains (Figure 2-7). These tests exhibit the same behaviour as found in previously mentioned studies, with the measured K_0 value decreasing to a minimum at σ'_p after which it increased with increasing axial effective stress.

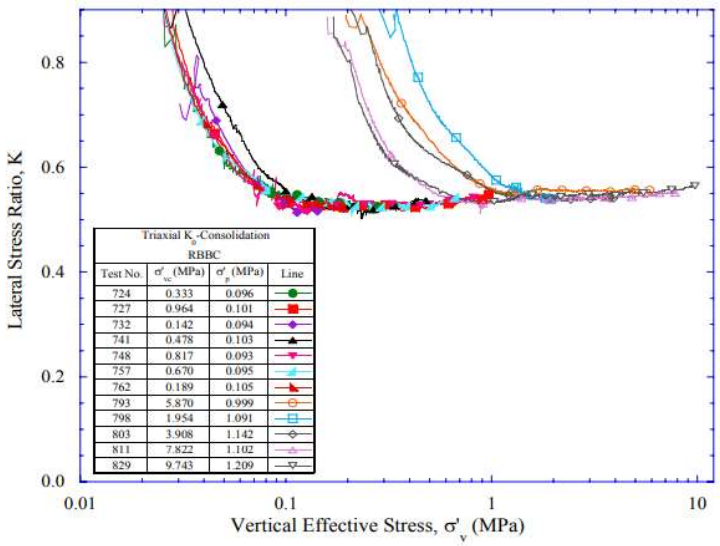

Figure 2-1 K_0 versus axial effective stress for RBBC (Abdulhadhi, 2009).

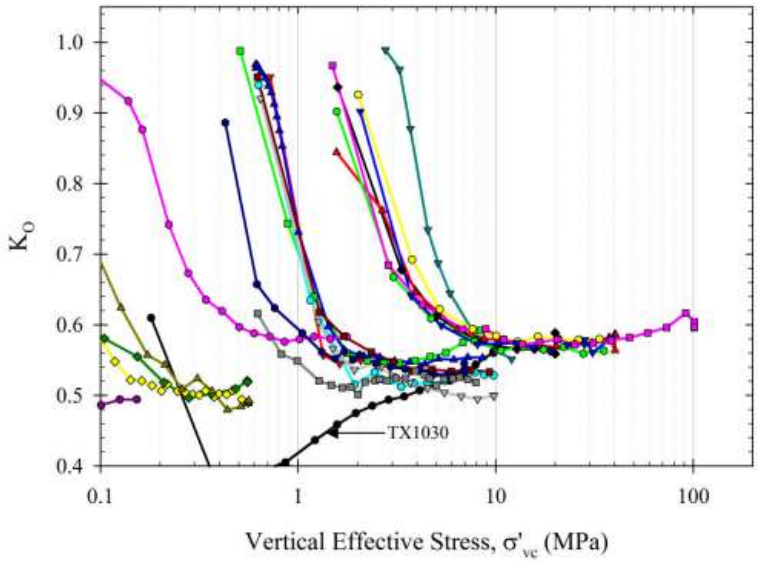

Figure 2-2 K_0 versus axial effective stress for RBBC (Casey, 2014).

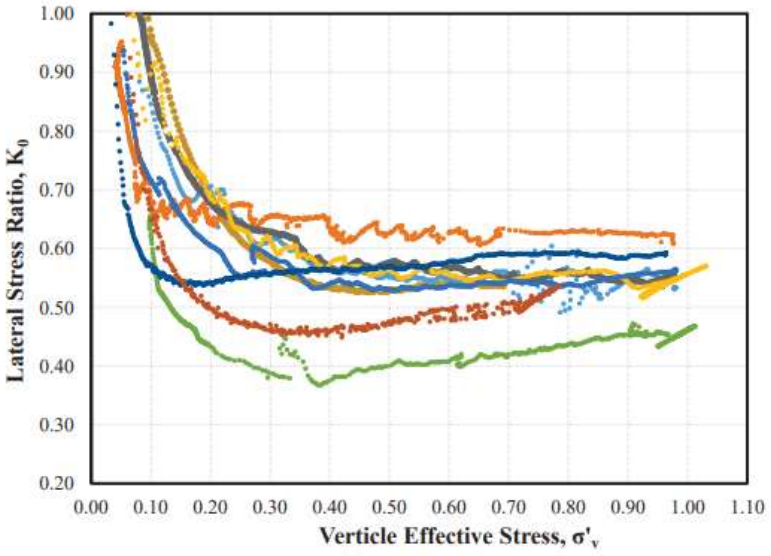

Figure 2-3 Plot of K_0 versus axial effective stress for intact BBC samples (Hanley, 2017).

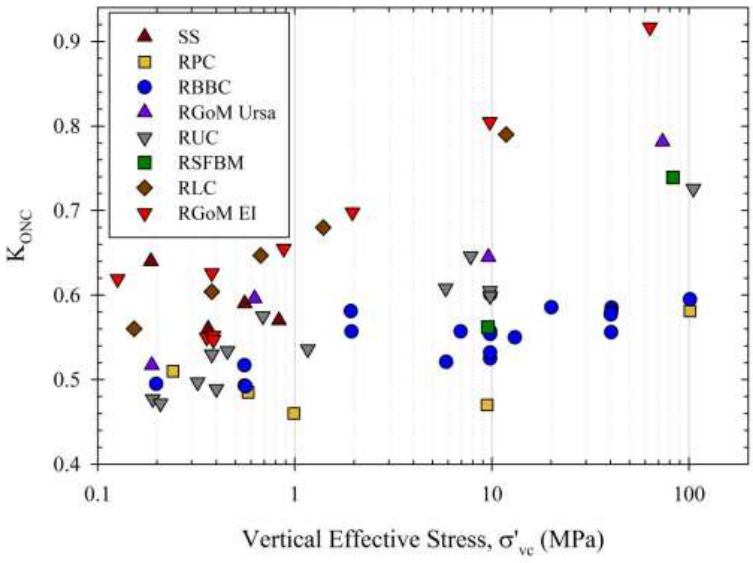

Figure 2-4 $K_{0,NC}$ measured at the end of consolidation versus axial effective stress (Casey, 2014).

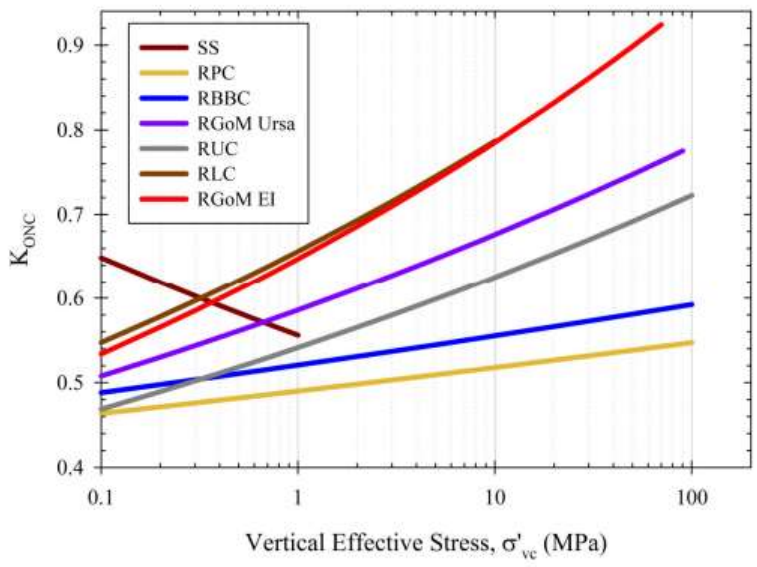

Figure 2-5 Power law regressions for $K_{0,NC}$ as a as a function of axial effective stress for various soils tested by (Casey, 2014).

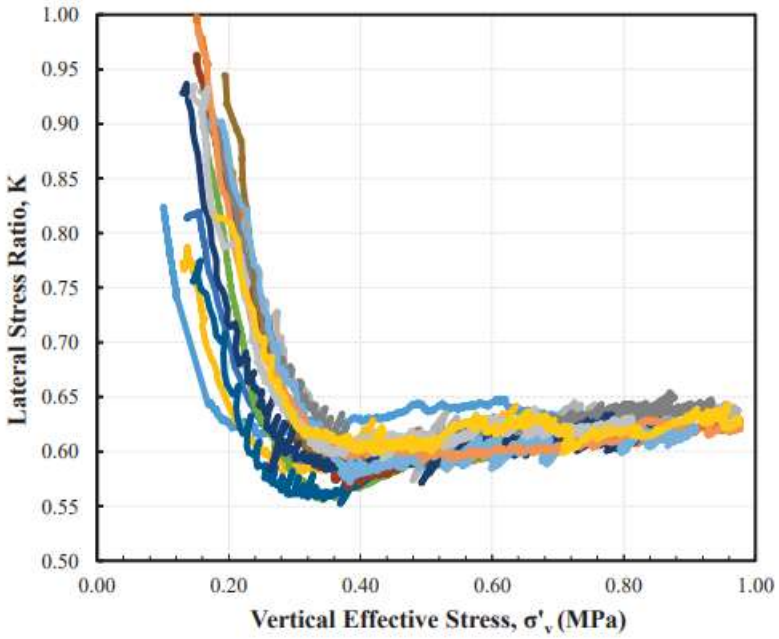

Figure 2-6 A plot of K_0 versus axial effective stress for RGoM-EI at low stress levels (Hanley, 2017).

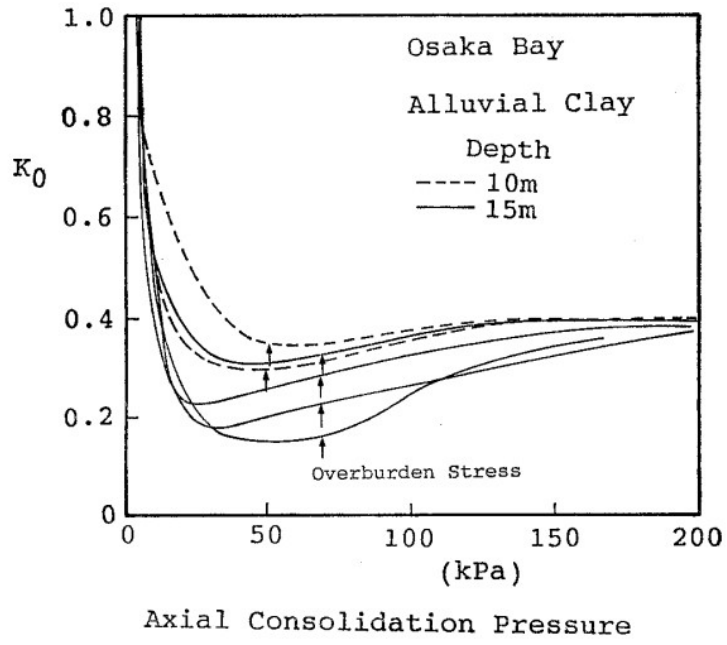

Figure 2-7 K_0 versus axial effective stress for Osaka Bay alluvial clay (Tsuchida and Kikuchi, 1991).

2.3 Empirical Correlations for $K_{0,NC}$

(Jâky, 1944) provided a relationship between K_0 and its maximum friction angle through analysis of granular talus slopes, where the critical state effective friction angle, φ'_{cs}, is equal to the angle of repose:

$$K_0 = 1 - \sin \varphi'_{cs} \qquad \textit{(Eq. 2-1)}$$

Figure 2-8 (Mesri and Hayat, 1993) gives a comparison of values of K_0 given by the Jâky equation and values of the K_0 for clays measured at the end of primary consolidation and the measured φ'_{cs}. Although the Jâky equation was formulated for granular soils, it provides reasonable agreement fine-grained soils (Figure 2-8).

(Booker and Ireland, 1965) modified the Jâky equation, providing the following relationship which predicts lower values of K_0 for a given φ'_{cs} (Figure 2-9):

$$K_0 = 0.95 - \sin \varphi'_{CS} \quad \textit{(Eq. 2-2)}$$

Interestingly, research has shown that normally consolidated soils exhibit a reduction in φ'_{cs} with increasing axial effective stress. Figure 2-11 shows the relationship between φ'_{cs} and the maximum pre-shear maximum axial effective stress (Casey, 2014). This reduction in φ'_{cs} leads to an increase in $K_{0,NC}$ with increasing stress level, concurring with what is seen during experimental testing.

Correlations with index properties of a soil have also been presented in past research. Figure 2-10 shows the relationship of both φ'_{cs} and PI versus K_0 (Ladd et al, 1977), with K_0 increasing with increasing PI.

(Casey, 2014) provided a correlation based on both liquid limit, w_L, and maximum axial consolidation effective stress, σ'_{av}:

$$K_{0,NC} = K_{0,10}\left(0.1\sigma'_{av(MPa)}\right)^J \quad \textit{(Eq. 2-3)}$$

$$K_{0,10} = 0.0056 w_{L(\%)} + 0.33 \quad \textit{(Eq. 2-4)}$$

$$J = 0.257 \log_{10}(w_{L(\%)}) - 0.398 \quad \textit{(Eq. 2-5)}$$

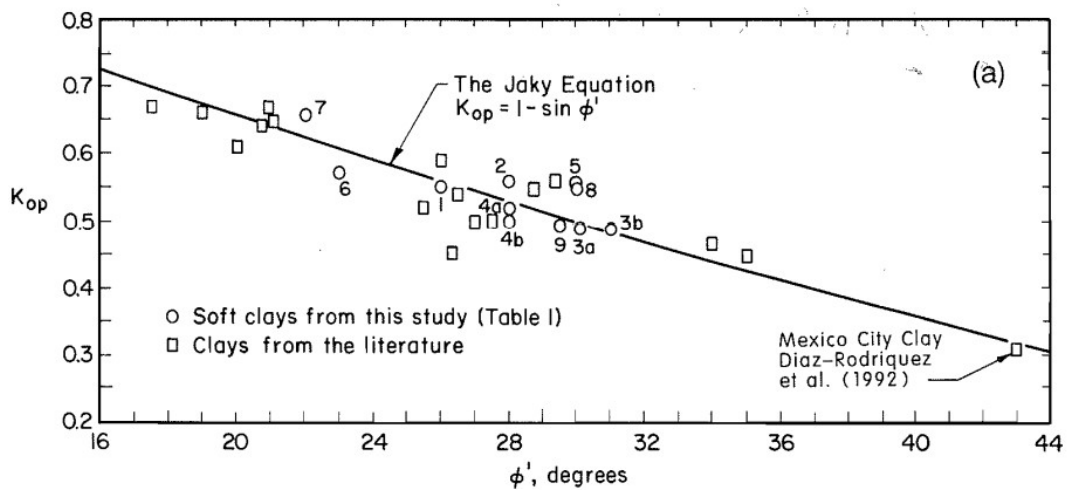

Figure 2-8 Plot of the end of primary consolidation at rest lateral stress ratio versus the effective friction angle comparing the Jaky correlation verses measured test data for clays (Mesri and Hayat, 1993).

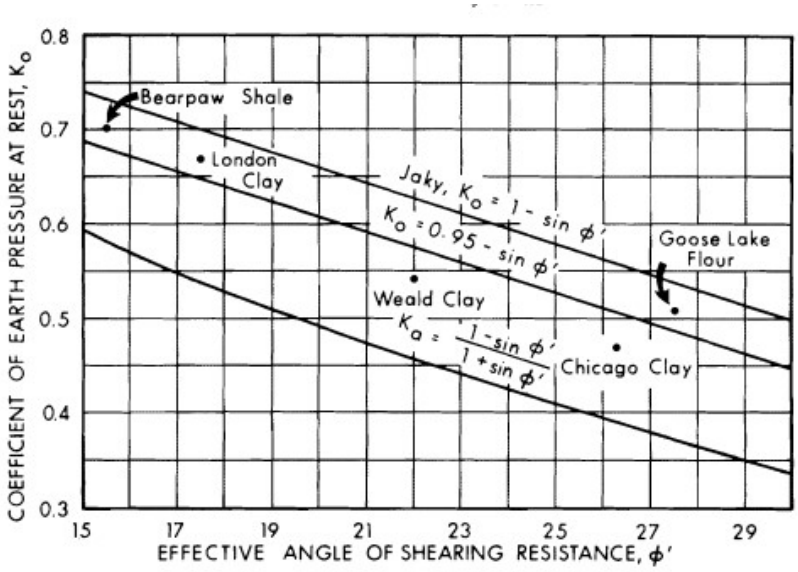

Figure 2-9 Coefficient of lateral at rest stress ratio versus effective friction angle (Booker and Ireland, 1965).

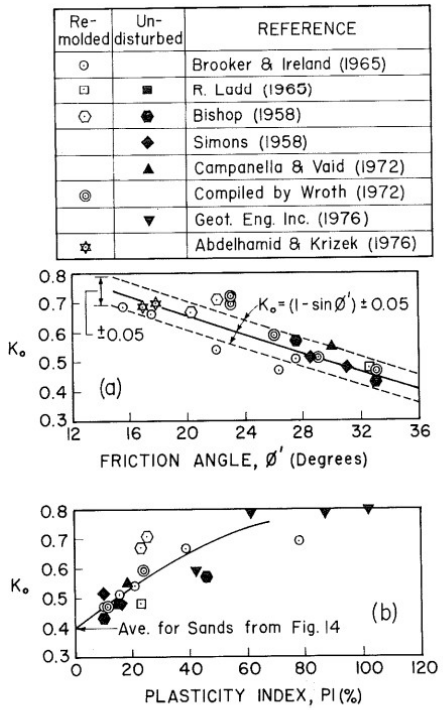

Fig. 30 K_O of normally consolidated clays vs friction angle (a) and plasticity index (b).

Figure 2-10 K_0 versus friction angle and plasticity index for normally consolidated remoulded and "undisturbed" clay (Ladd et al., 1977).

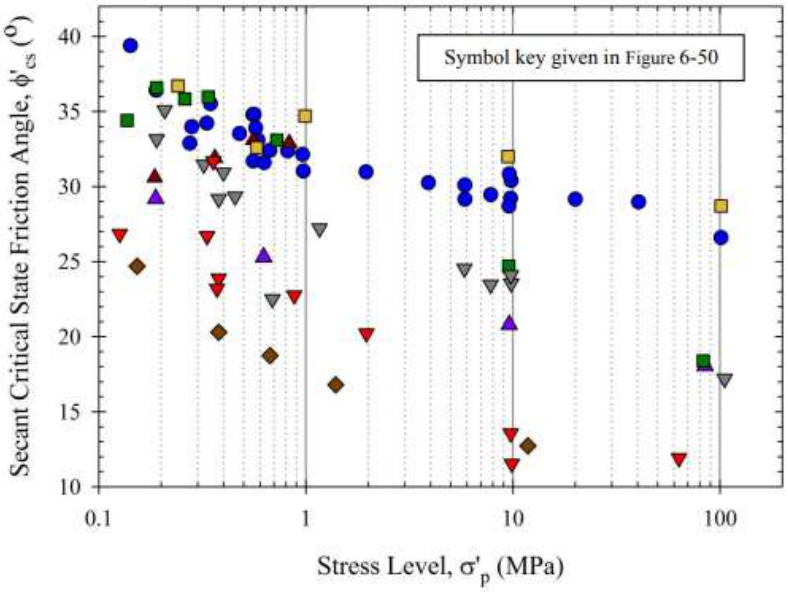

Figure 2-11 Plot of secant critical state friction angle versus pre-consolidation pressure for various soils (Casey, 2014).

2.4 Resedimented Consolidation Behaviour

(Betts, 2014) was the first to process and produce the bulk material GoM-EI powder for use in resedimentation. The behaviour of the resedimented material, RGoM-EI, was found to be in good agreement with in-situ Gulf of Mexico mudrocks. Figure 2-12 shows a plot of permeability versus porosity comparing the behaviour of permeabilities obtained from resedimented CRS testing data, and intact core measurements provided by (Stump and Flemings, 2001). Both intact and resedimented permeabilities concur, although the intact measurements are only at one specific porosity and does not cover the range of measurements taken for the resedimented samples. Figure 2-13 compares the compression behaviour of RGoM-EI with intact samples, and field porosities estimated from both bulk densities and sonic velocity correlated measurements. The intact cores agree well with the resedimented data, in both the slope of the virgin compression line, C_c, and in the porosity for a given axial effective stress.

(Horan, 2012) compared RBBC series IV to intact BBC obtained from the Killian Court location. Concurring with (Betts, 2014), this research found that both compression and permeability behaviour of both intact and resedimented material exhibited similar behaviour (Figure 2-14 and 2-15). For the intact material, at stresses less than the maximum past effective stress, the void ratios are much lower than the resedimented. As expected, this can be explained through considering the age of the intact material and it being subjected to multiple log cycles of secondary compression. Once the material is in the normally consolidated regime, both intact and resedimented agree in both slope and magnitude for both compression behaviour and permeability.

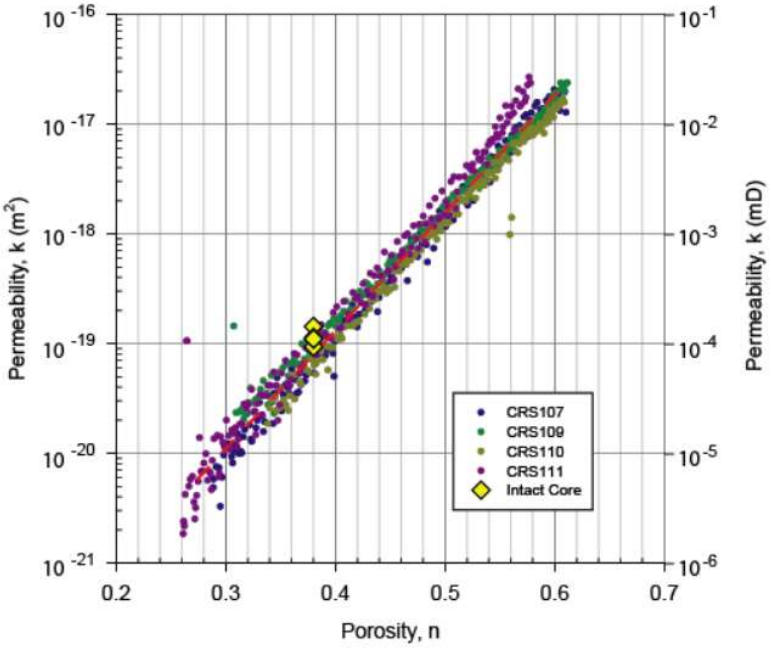

Figure 2-12 Plot of permeability versus porosity comparing intact and resedimented behaviour (Betts, 2014)

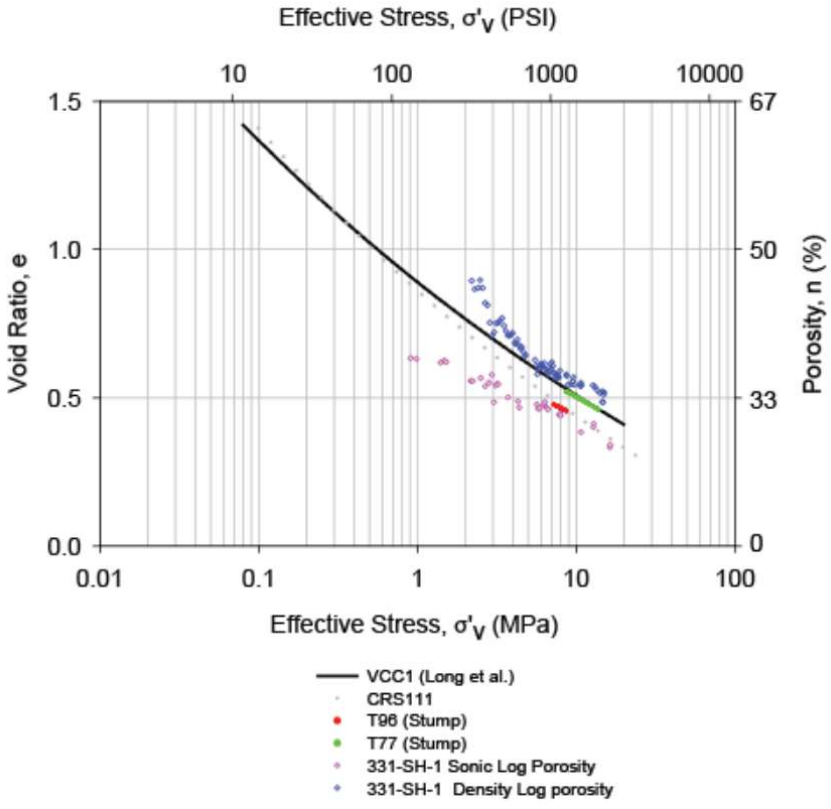

Figure 2-13 Plot void ratio versus axial effective stress comparing resedimented compression behaviour of RGoM-EI with intact samples and geophysical field measurements (Betts, 2014).

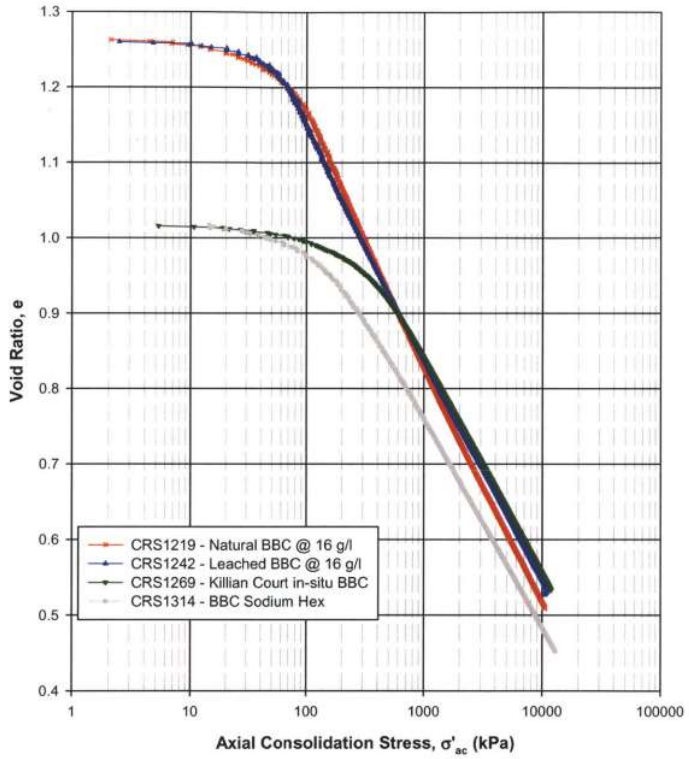

Figure 2-14 Plot of void ratio versus axial effective stress comparing intact BBC to RBBC (Horan, 2012).

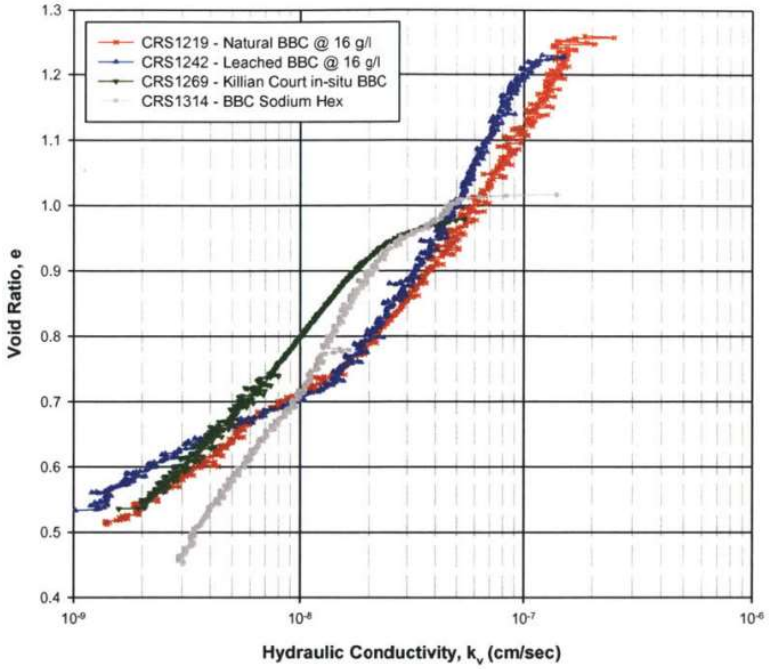

Figure 2-15 Plot of void ratio versus hydraulic conductivity comparing intact and resedimented behaviour for BBC (Horan, 2012).

2.5 Use of Side Drains for Triaxial Testing

(Bishop and Henkel, 1962) recommended the use of side drains for soils with low permeabilities to decrease the consolidation times to practical levels and to manage the equalization of pore pressures during drained and undrained shear. (Bishop and Gibson, 1963) expressed the average degree of consolidation at failure, $\overline{U}_f$:

$$\overline{U}_f = 1 - \frac{h^2}{\eta c_v t_f} \qquad \textit{(Eq. 2-7)}$$

Where h is the height of the specimen, η is a parameter based on the drainage conditions at the boundaries, c_v is the coefficient of consolidation and t_f is the time to failure. This equation can be generalized for use during consolidation and does not necessarily need to be expressed to time of failure.

However, side drain materials have finite permeability, and do not cover the whole surface of the test specimen. The drain effectiveness of the side drain material (its comparison to a perfect, infinite permeability drainage boundary), ξ, is given by the following equation (Bishop and Gibson, 1963):

$$\xi = \frac{\pi^2 k_p}{4 \cdot k_s} \cdot \frac{a \cdot \delta}{h^2} \qquad \textit{(Eq. 2-7)}$$

Where k_p is the hydraulic conductivity of the side drain material, k_s is the hydraulic conductivity of the soil, a is the radius of the specimen, h is the drainage height, H_d and δ is the side drain material thickness.

Figure 2-16 compares the effects of drain effectiveness of the material to the infinite permeability case on the coefficient of consolidation (Bishop and Henkel, 1962). The drain

effectiveness directly effects the measured actual coefficient of consolidation, showing an increase in c_v with decreasing drain effectiveness.

(Leroueil et al., 1988) performed an extensive analysis on the influence of filter paper drains on consolidation. First, the drainage capacities of the filter papers were ascertained through conducting permeability tests using a triaxial set-up and a dummy specimen, over a confining stress range of 50 to 400 kPa. Permeabilities of four Champlain clay soils, samples taken using a Laval sampler, were measured using the falling head tests method. Figure 2-18 compares the drainage capacities of the filter papers to those of the tested clays. It shows that the drainage capacities of both Whatman No. 54 and No. 40 are generally 10 to 60 times higher than the drainage capacity of the tested soils reducing consolidation times by a factor of between 5 and 10. (Leroueil et al., 1988), however, concluded that in the normally consolidated regime, the introduction of side drains reduced the time to consolidate by a factor of 2.5. It was surmised that this reduction in efficiency was possibly due to the filter paper clogging with clay particles.

(Oswell et al., 1991) conducted a testing program to study the performance of side drain materials between 2 and 6 MPa. This studied compared the conventional side drain filter papers (e.g., Whatman No. 54) to a geotextile side drain material (Figure 2-19). The testing concluded that side drain effectiveness decreases with increasing effective confining stresses, with the geotextile showing the highest permeabilities over the given stress range. Testing was also conducted on Winnipeg clay specimens, with and without side drains (Figure 2-20). It showed that the geotextile side drains provide the highest rates volumetric reduction rates with time, with these rates decreasing with the use of Whatman No. 54, Whatman No.1 and lastly the no side drain condition. However, it is not clear whether these tests accounted for the volume compressibility of the side drain material when calculating the volumetric reduction rates.

(Tsuchida and Kikuchi, 1991) analysed the effects of side drain compressibility on K_0 behaviour of clays. This study performed compression testing on the side drain material and found that K_0 measured in the normally consolidated range were lower if the side drain compressibility was not accounted for (Figure 2-21). This, of course, is dependent on how the condition of uniaxial consolidation is maintained during triaxial consolidation. If radial measurements are being performed directly with an internal measurement system, the volumetric compressibility of the material should not affect the measured K_0. However, if the K_0 condition is maintained through measurements in total volumetric strain (through measuring the volume of fluid expelled from the specimen), the compressibility of the material is considerably more important.

(Force, 1998) examined the effects of side drain usage for testing on RBBC. Figure 2-22 shows K_0 versus axial effective stress of RBBC for multiple tests with differing side drain configurations. Volumetric compressibility of the side drain material was ignored during the K_0 uniaxial control protocol. When using filter drains that covered the whole lateral surface area of the specimen, lower K_0 values were measured, although there is still considerable scatter in the measurements. Overall, the $K_{0,NC}$ measurements presented by (Force, 1998) plot generally lower than those measurements made by (Abdulhadi, 2009) and (Casey, 2014), with upper bound values of $K_{0,NC}$ of 0.475 at 1.3 MPa to 0.51 at 10 MPa, showcasing the effects of side drain compressibility on lowering measured values of $K_{0,NC}$.

ν	c_v deduced assuming $k_p = \infty$ / c_v actual I. Drainage to one end* and radial drainage	c_v deduced assuming $k_p = \infty$ / c_v actual II. Drainage to both ends* and radial drainage	t_f by more exact theory / t_f by eqn. 69 and Table 19 For Case II
∞	1	1	1
100	0·834	0·953	0·98
10	0·341	0·674	0·85
5	0·212	0·515	0·81
1	0·064	0·208	0·80

Figure 2-16 Influence of side drain of finite permeability on the coefficient of consolidation (Bishop and Henkel, 1962)

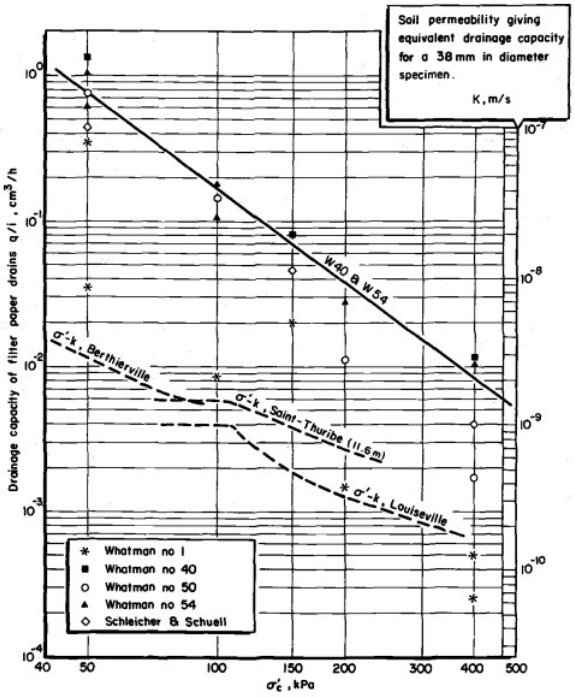

Figure 2-17 Drainage capacities of side drains and various soils tested by (Leroueil et al., 1988)

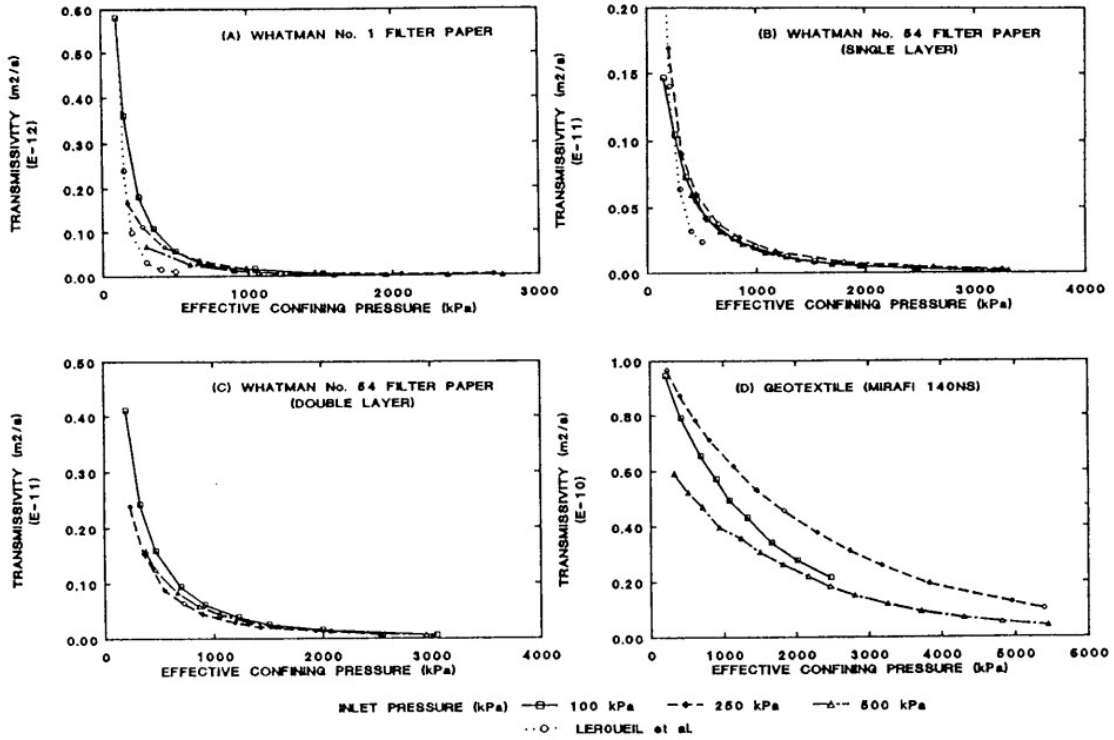

Figure 2-18 Transmissivity versus effective confining pressure for permeability tests on four different side drain materials (Oswell et al., 1991).

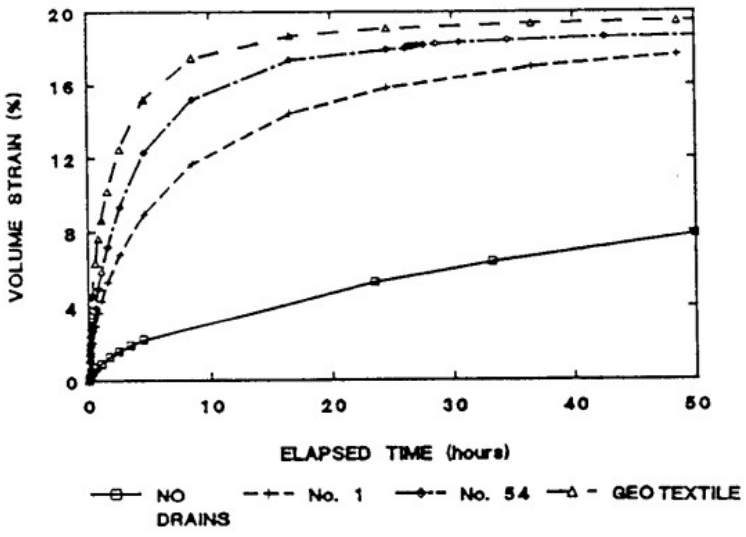

Figure 2-19 Volumetric strain versus time for consolidation portion of tests on Winnipeg clay (with and without side drains) (Oswell et al., 1991).

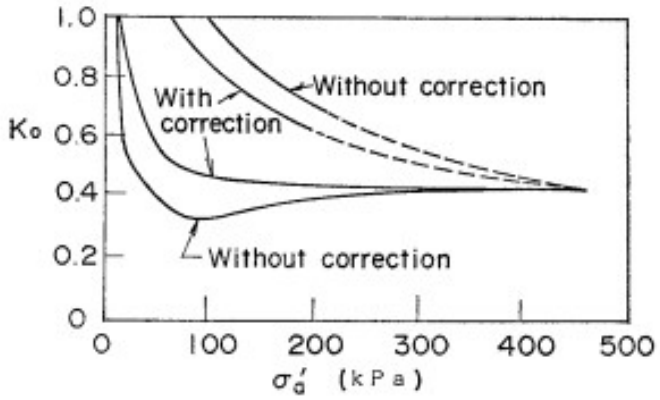

Figure 2-20 K_0 versus axial effective stress showing the effects of drain compressibility on measurements (Tsuchida and Kikuchi, 1991).

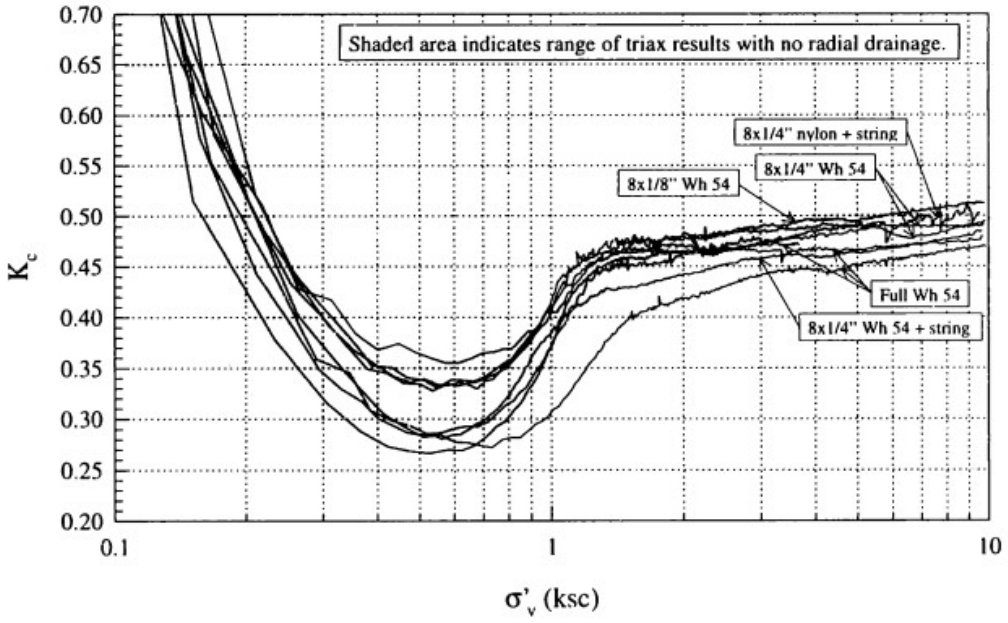

Figure 2-21 At rest lateral stress ratio versus vertical effective stress (Force, 1998).

2.6 Conclusion

Previous research has found a stress dependent behaviour of K_0 for fine-grained soils, with an increase in K_0 with increasing stress. For the materials being tested in this research, those being RBBC and RGoM-EI, RGoM-EI exhibited higher stress dependency with K_0 increasing by 33% over two log cycles of stress. A stress dependency is also inherent when utilizing the Jâky equation to calculate K_0, as φ'_{cs} decreases with increasing stress leading to K_0 increasing with increasing stress. It is also apparent that the use of side drainage during triaxial consolidation is an effective method of increasing the rate of pore pressure drainage, thereby reducing excess pore pressures within the sample during constant rate of strain consolidation. Specifically, geotextile side drain material was shown to be adequate for use at higher stress levels. However, side drain compressibility should be considered and corrected for during K_0 consolidation using volumetric measurements to ensure K_0 conditions are being maintained. If no correction is applied, the measured K_0 will be lower.

3 Test Materials

3.1 Introduction

This chapter will describe the source, index properties and engineering properties of the test materials used during this research. The index properties covered will be Atterberg limits, specific gravity, and pore fluid characteristics. The engineering properties described will be the compressibility and permeability. The test materials used in this research were Boston Blue Clay and Gulf of Mexico, Eugene Island Clay. These two materials are fine grained soils, however, differ in geologic origin, composition, and engineering properties. These materials have been extensively studied prior to this research, and additional information can be found in these previous research dissertations.

3.2 Resedimented Gulf of Mexico, Eugene Island

3.2.1 Introduction

The Gulf of Mexico, Eugene Island (RGoM-EI) clay used for this research is a smectite-rich high plasticity clay originating approximately 270 km off the coast of Louisiana in the Gulf of Mexico. This region is located at a Pilo-Pleistocene minibasin. The clay utilised in this research was obtained from two 10.2 cm drill cores from wells A-12 and A-20ST2 from depths of 2300 m to 2500 m below the mudline (Betts, 2014). This coring was conducted as part of the Integrated Ocean Drilling Program. The core material was then processed as outlined in Chapter 4.

3.2.2 Mineralogy

Mineralogy of processed RGoM-EI powder was analyzed using X-ray powder diffraction (Phillips, 2011). The results of this analysis are presented in Table 3-1 below. As can be seen, RGoM-EI powder is smectite dominant forming 87% of the clay-size fraction.

Table 3-1 Mineralogy of RGoM-EI from XRD analysis (Phillips, 2011)

RGoM-EI Overall Mineralogy (%)		**Clay-size fraction mineralogy (%)**	
Quartz	27.8	Kaolinite	4
Plagioclase	5.3	Illite	8
K-Feldspar	4.0	Illite+Smectite	87
Calcite	1.2	Chlorite	1
Dolomite	0.8		
Siderite	1.0		
Pyrite	0.7		
Anatase	0.2		
Barite	3.2		
Halite	0.2		
Muscovite	1.9		
Illite + I/S	44.4		
Kaolinite	9.1		
Chlorite	0.4		
Total	100.2	Total	100

3.2.3 Grain Size Analysis

Grain size distribution presented in Figure 3-1 was determined using the hydrometer method (ASTM D7928) by (Betts, 2014). As can be seen, 65% of material is passing a #200 sieve, or has a particle diameter of less than 0.002 mm. Thereby, the soil can be classified as fine-grained.

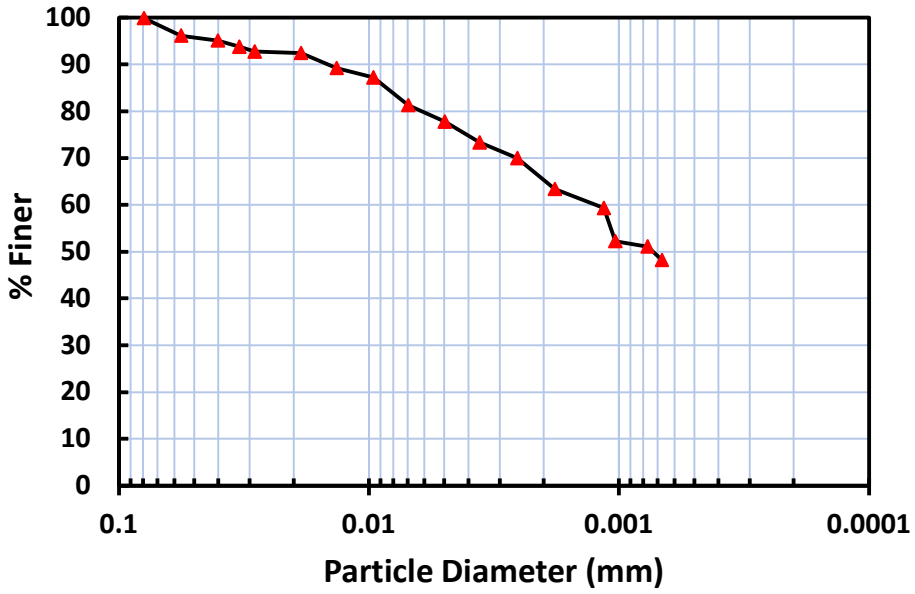

Figure 3-1 Grain size distribution of RGoM-EI Powder (after Betts, 2014)

3.2.4 Atterberg Limits

RGoM-EI can be classified as a high plasticity clay (CH). Liquid limit and plasticity index were determined by (Casey, 2014) as per ASTM D4318. Figure 3-2 shows where RGoM-EI powder lies on the Casagrande Chart.

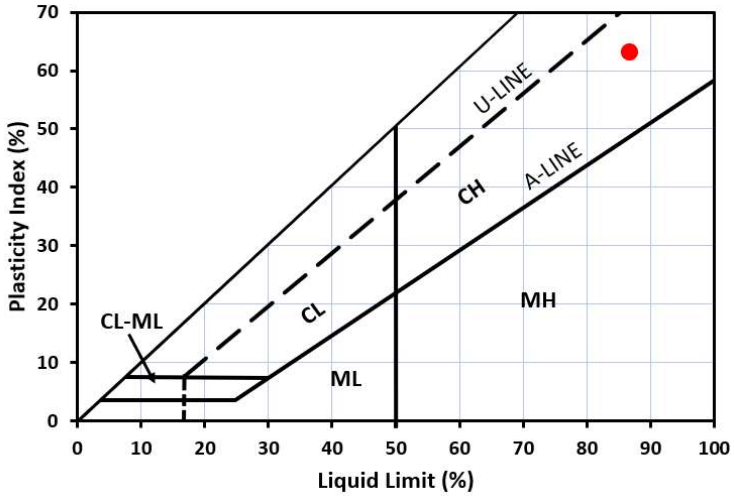

Figure 3-2 Casagrande Charts for RGoM-EI (after Hanley, 2017)

3.2.5 Specific Gravity

A specific gravity, G_s, of 2.775 for RGoM-EI was used for this research. Specific gravity tests were conducted on the RGoM-EI powder using the water submersion method (ASTM D854) by (Fahy, 2014) at MIT. An iodine flask and matched plug was used rather than a pycnometer for this testing method.

3.2.6 Pore Fluid Characteristics

In-situ pore fluid salinities for the Eugene block 330 field ranges between 74 to 80 g/L (Losh and Wood, 1995). For this research, a pore fluid salinity of 80 g/L was used.

The salinity of the RGoM-EI powder was analyzed during this research using the electrical conductivity method described in (Germaine & Germaine, 2009). The soil salinity of RGoM-

EI powder was found to be 12.17 g/kg. The salt present in the powder is accounted for when creating the saltwater solution for sedimentation to produce a specimen with pore fluid salinity of 80 g/L.

3.2.7 Compressibility

Figure 3-3 shows the average uniaxial compression curve in the normally consolidated range for RGoM-EI. This curve is the average of numerous CRS and Oedometer uniaxial tests conducted at both MIT and the TAG Laboratory.

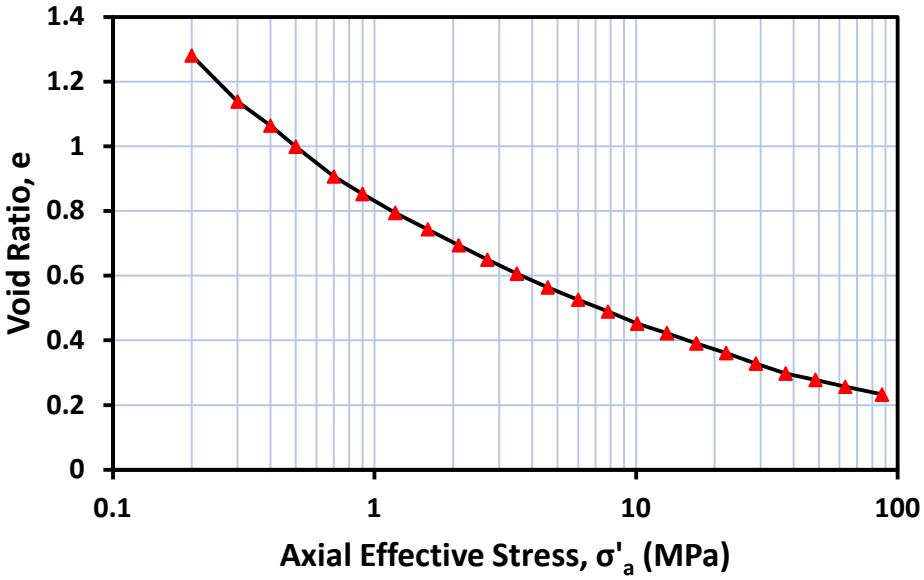

Figure 3-3 Average Uniaxial Compression Curve of RGoM-EI (courtesy of Emre Uyeturk)

3.2.8 Hydraulic Conductivity

Figure 3-4 shows the vertical hydraulic conductivity of RGoM-EI in uniaxial conditions versus void ratio. Hydraulic conductivities were calculated using CRS test data by Emre Uyeturk over a 0.2 to 42 MPa stress range. Figure 3-5 shows the radial hydraulic conductivity of RGoM-EI in uniaxial conditions using a correlation derived by (Nordquist, 2015) using CRS data where only radial drainage conditions were allowed to occur.

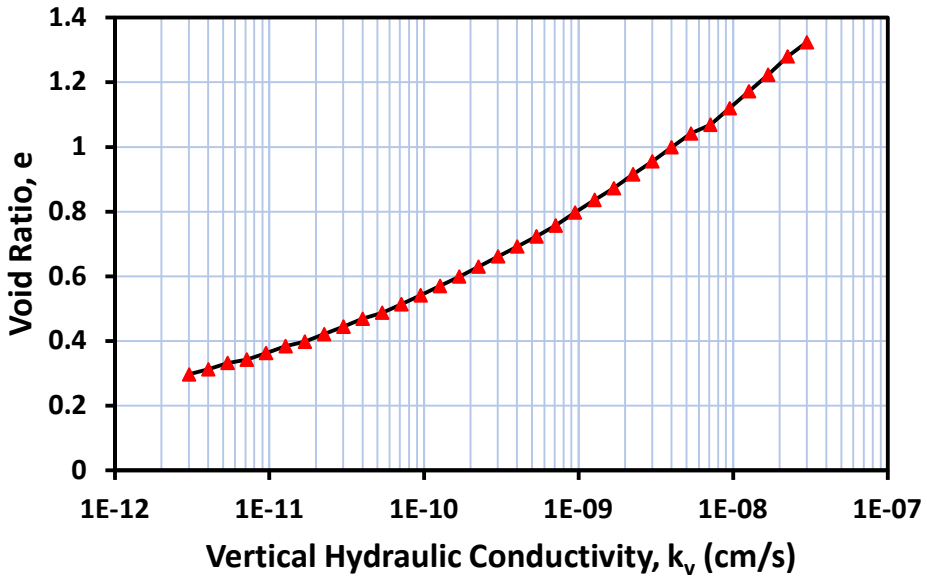

Figure 3-4 Average vertical hydraulic conductivity of RGoM-EI (courtesy of Emre Uyeturk)

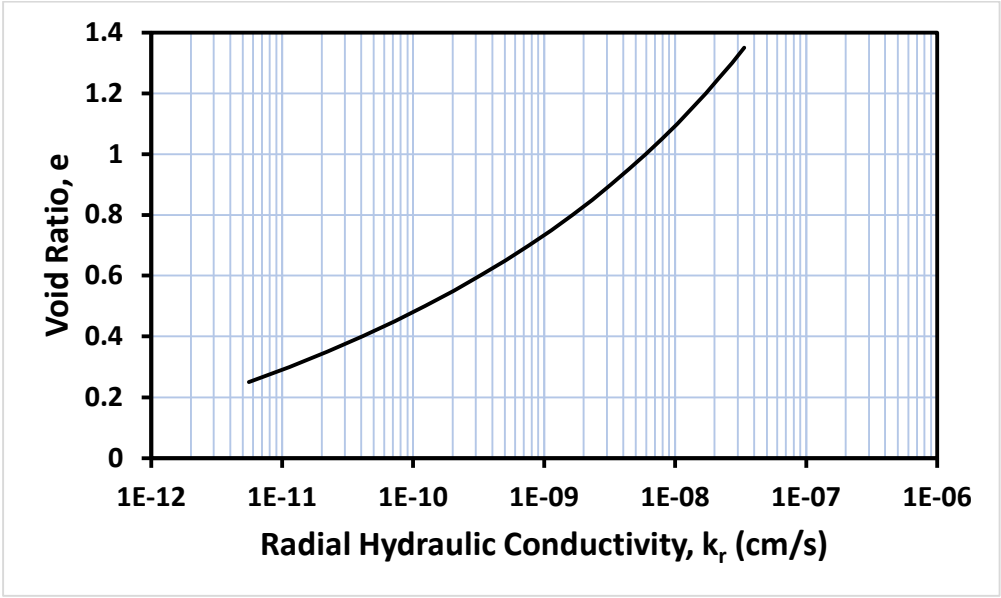

Figure 3-5 Radial hydraulic conductivity of RGoM-EI from (Nordquist, 2015) correlation

3.3 Resedimented Boston Blue Clay

3.3.1 Introduction

Boston Blue Clay (BBC) is low sensitivity, low plasticity glacio-marine clay. It is composed of glacial outwash deposited in a marine environment between 14,000 and 12,000 years ago during a period of sea-level rise associated with a deglaciation event. During this period the sea-level may have been 50 ft higher than today's levels (Kenney, 1964). Boston Blue Clay can be found across the Boston area at depths averaging on 9 m and in layer thickness of 20 to 40 m. As with all soils, variations in composition occur depending on location and depth. Resedimented Boston Blue Clay (RBBC) has been extensively studied by researchers at MIT since 1961 (Bailey, 1961). Several sources of BBC have been used for resedimentation over the years, and each source is given its own individual series. For this research, RBBC Series IV was used. Series IV originated from the base of excavation for the construction of MIT's Biology Building in 1992 (Berman, 1993).

3.3.2 Mineralogy

Mineralogy of processed RBBC powder was analyzed using X-ray powder diffraction (Phillips, 2009). The results of this analysis are presented in Table 3-2 below. As can be seen, RBBC powder is illite dominant forming 65% of the clay-size fraction.

Table 3-2 Mineralogy of RBBC from XRD analysis (Phillips, 2009)

RGoM-EI Overall Mineralogy (%)		**Clay-size fraction mineralogy (%)**	
Quartz	21.3	Kaolinite	2
Plagioclase	20.5	Illite	65
K-Feldspar	8.2	Illite+Smectite	28
Calcite	0.5	Chlorite	5
Dolomite	0.8		
Halite	0.2		
Amphibole	3.8		
Muscovite	13.8		
Illite + I/S	7.3		
Kaolinite	2.9		
Chorite	6.2		
Tri-mica	9.2		
Hydrobiotite	5.4		
Total	100.1	Total	100

3.3.3 Grain Size Analysis

Grain size distribution presented in Figure 3-6 determined using the hydrometer method (ASTM D7928). As can be seen, 55% of material is passing a #200 sieve, or has a particle diameter of less than 0.002 mm. Thereby the soil can be classified as fine-grained.

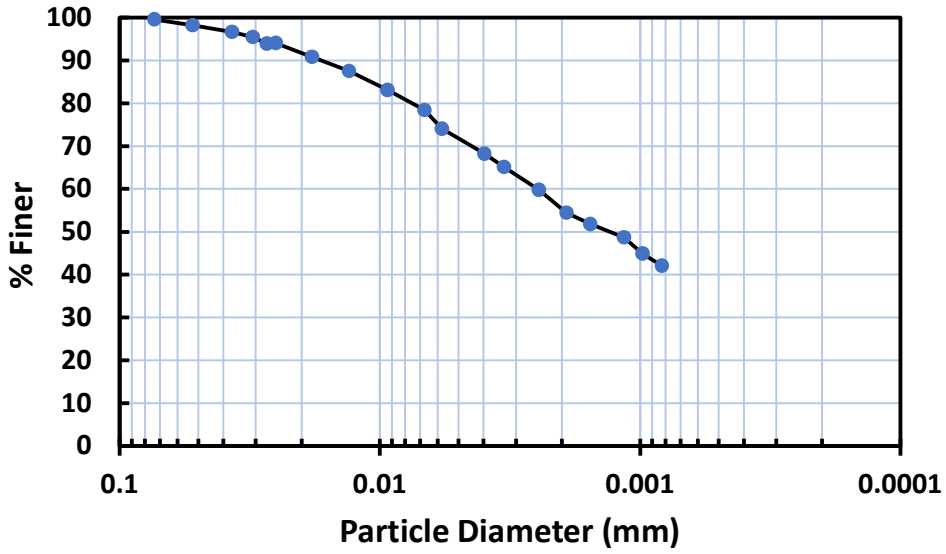

Figure 3-6 Grain size distribution of RBBC (after Hanley, 2017)

3.3.4 Atterberg Limits

RBBC Series IV is classified as a low plasticity clay (CL). The Atterberg Limits have been determined by various previous researchers at both MIT and Tufts University for RBBC Series IV using ASTM D4318 (Santagata,1994), (Abdulhadi, 2009), (Casey, 2012).

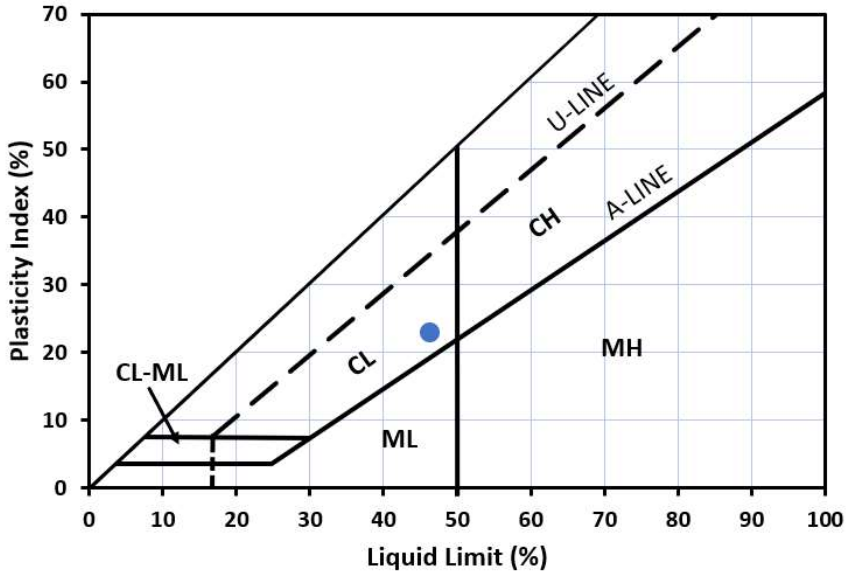

Figure 3-7 Casagrande Chart for RBBC (after Hanley, 2017)

3.3.5 Specific Gravity

A specific gravity, G_s, of 2.779 for RBBC was utilized for this research. Specific gravity tests were performed on the RBBC powder using the water submersion method (ASTM D854) by numerous previous researchers at MIT (Santagata, 1994), (Abdulhadi, 2009), (Horan, 2012), (Casey, 2014).

3.3.6 Pore Fluid Characteristics

The pore fluid characteristics of Boston Blue Clay vary as a function of depth and location. For this research, a pore fluid salinity of 16 g/L was used.

3.3.7 Compressibility

The uniaxial normally consolidated compression behaviour of RBBC is presented in Figure 3-8. This curve is the average of both CRS and Oedometer test data from both MIT and the TAG Laboratory.

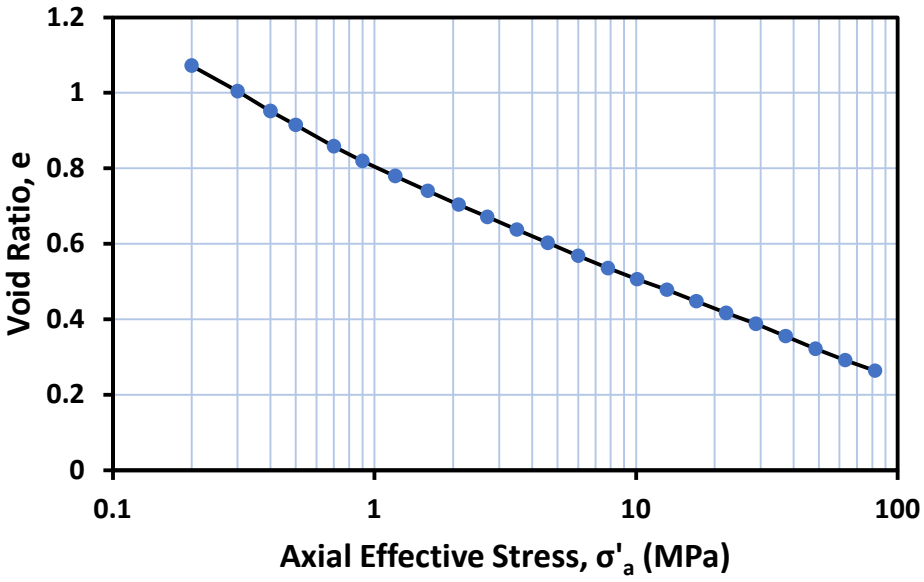

Figure 3-8 Average uniaxial compression curve of RBBC (courtesy of Emre Uyeturk)

3.3.8 Hydraulic Conductivity

The average vertical hydraulic conductivity plotted against void ratio in uniaxial conditions is shown in Figure 3-9. This hydraulic conductivity was calculated from CRS test data by Emre Uyeturk over a 0.8 to 82 MPa stress range.

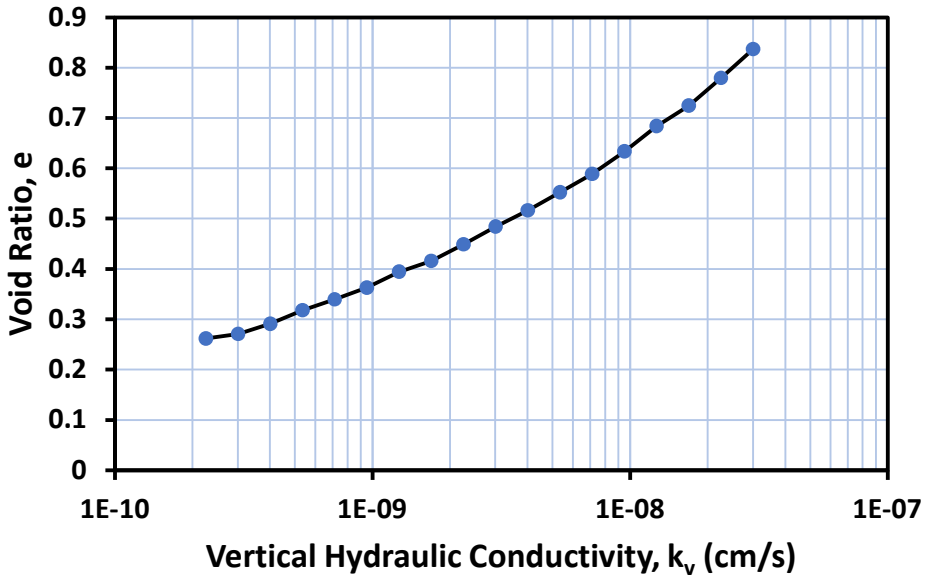

Figure 3-9 Average vertical hydraulic conductivity of RBBC Series IV (courtesy of Emre Uyeturk)

4 Resedimentation Procedure and Sample Preparation

4.1 Introduction

This chapter will explain the process of resedimentation as it relates to this research. All test specimens used in this research were produced through this process. Resedimentation is the process of one-dimensionally consolidating a dilute slurry of fine-grained soil in a rigid wall container. This method was originally conceived in 1965 (Ladd and Varallyay, 1965) to produce large diameter soil blocks which could thereafter be subdivided into individual samples for testing. This earlier technique only produced partially saturated samples that needed 200 kPa to backpressure saturate. The method has been improved upon in subsequent years and now produces fully saturated samples that need minimal trimming. Resedimentation enables the production of samples with identical composition for a given source material. Samples can be produced with any desired stress history, porosity, and pore fluid concentration. This allows the effects of these variables to be isolated and investigated thoroughly through systematic laboratory testing. The resedimentation procedure overcomes problems of sampling disturbance and costs associated with intact sampling. Large numbers of identical test specimens also allow the laboratory to develop, test and proof new experimental equipment. One disadvantage of using resedimentation is that it cannot replicate the processes of chemical diagenesis that a soil experiences over time in its geologic depositional context.

4.2 Processing

For RGoM-EI, the material was removed from the core tubes by hand and any sand lenses were discarded. The material was then air-dried for 18 days. After this period, the material was roller-ground such that 99% passed through a #100 sieve. The material was then hand mixed yet again and stored in 5-gallon sealed containers for future use (Betts, 2014). In the case of RBBC, the process is much the same. Excavated material was cleared of sand lenses, shells, or wood. Again, the material was ground until 99% of material pass a #100 sieve and stored in sealed containers (Santagata, 1998).

4.3 Batching

When batching a powdered soil for resedimentation, the quantity of clay powder, distilled water and salted needed for a specific batch is calculated using a standardized laboratory Excel spreadsheet. For RGoM-EI, the slurry was batched to a slurry water content of 110% as were recommended by (Hanley, 2017). The RGoM-EI powder has a natural salt content of 12.17 g/kg. The necessary salt mass was calculated to produce a slurry of pore fluid concentration of 80 g/L. For RBBC, a slurry water content of 105% was used, the RBBC powder has a natural salt content of 2.7 g/kg, and the final pore fluid salinity was designed at 16 g/L. The mixture was mixed and allowed to temper (allowing the clay particles to fully hydrate) for 24 hours. The mixture was remixed and placed in a sealed vessel. The slurry was exposed to a vacuum and de-aired until all air bubbles ceased to appear in the slurry. This was usually left for a minimum of 30 minutes. The vessel was allowed to re-pressurize slowly as to avoid explosive decompression. The de-aired material was transferred to a 0.6 L suction gun and tremied into a PVC resedimentation tube. Multiple diameter resedimentation tubes are used in the laboratory for different applications and to achieve various stress levels. The standard sample cross-sectional area used in this research was 10 cm^2. Silicon oil is used to

lubricate the inside of resedimentation tube to reduce sidewall friction. For the high stress testing, the author began using stainless steel resedimentation tubes to consolidate specimens to 30 MPa. The resedimentation tube sat in a bath of water with the same salinity as the pore fluid, with the nylon filter fabric and bottom filter paper porous stone sitting on a PVC spacer. Another layer of nylon filter fabric accompanied by porous stone was placed on the top of the specimen along with another spacer. The use of two spacers allows the specimen to strain from both ends, further halving sidewall friction. The consolidometer set-up is shown in Figure 4-1.

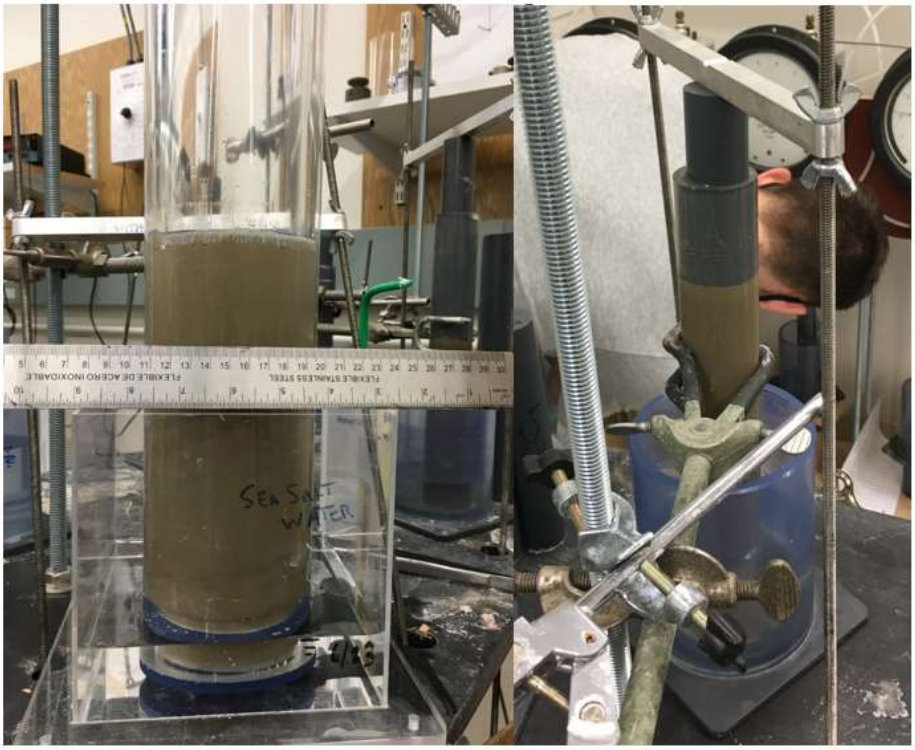

Figure 4-1 Resedimentation tube set up during initial stages of consolidation using a 4 inch and 1.5-inch-diameter PVC tubes.

4.4 Consolidation

The specimens were consolidated in the resedimentation tubes by incremental loading. The pore pressures are allowed to fully drain between each step in load. A load increment ratio of 1 was used for the specimens i.e., the load was doubled for each step. This load increment ratio was used to provide a balance between production and extrusion minimization. The time between load increments was chosen through analysing strain versus time curves for several increments by previous researchers (Eagle, 2021). 2.5 days was used for RGoM-EI. Although for RBBC a shorter time step could have been used for increments, it was kept to 2.5 days.

Four apparatus were used for consolidation of the resedimentation samples. Firstly, physical steel or lead weights were placed on top of the slurry using the hanger system (Figure 4-2). After about 40 kg, or 0.4 MPa, the resedimentation tube was then transferred to the pneumatic consolidometer (Figure 4-3). This allowed the specimen to be consolidated to 400 kg, or 4 MPa. The specimen can then be transferred to the 100:1 mechanical gravity load frame to stresses of 8 MPa and to reach stresses of above 8 MPa the specimens were consolidated in the high stress pneumatic load frame (Figure 4-4). If using the high stress load frame, the author began consolidation in the stainless steel resedimentation tube. For this study, specimens used in the medium stress triaxial system were consolidated to 0.8 MPa, and specimens used in the high stress triaxial system were consolidated to 10 MPa. Once the specimens reached the target stress value, they were unloaded to an OCR = 4 as to implement an isotropic state of stress within the specimen. This is believed to help minimize sampling disturbance during extrusion and trimming. (Santagata & Germaine, 2002). The samples are then left for a minimum of 2 days prior to extrusion.

Figure 4-2 Hanger system utilized for early stages of consolidation with maximum load of 40 kg.

Figure 4-3 Pneumatic piston system used for maximum loads of 400 kg.

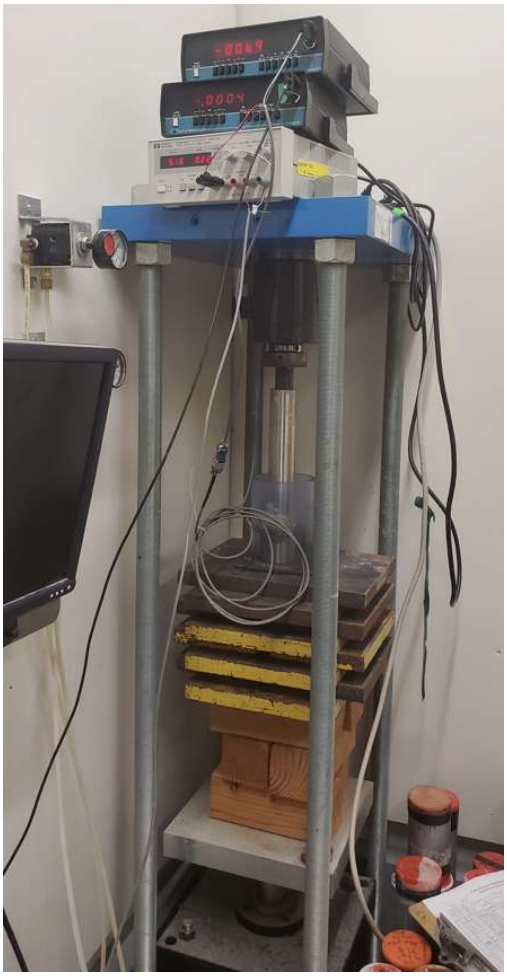

Figure 4-4 Pneumatic load frame used for consolidation stresses of over 8 MPa.

4.5 Extrusion and Trimming

The samples are extruded from the PVC or stainless steel resedimentation tube using a manual hydraulic extruder. The sample is then trimmed to the required dimensions using a trimming jig, piano wire, and draper's razor. The standard dimension used for medium stress testing was a height of 4.05 cm and a diameter of 3.55 cm. For the high stress testing, a height of 8.1 cm and diameter of 3.5 cm was used. The wet mass, average height and average diameter was then measured. The specimen was then ready to transfer to the triaxial apparatus. The sample could be stored in a sealed sandwich bag along with another semi-sealed sandwich bag containing a damp paper towel for generally less than 1 hour. The damp paper towel ensured that the sample would not dehydrate due to the low relative humidity in the laboratory. Figure 4-5 shows a trimmed RBBC sample prior to testing.

Figure 4-5 Trimmed RBBC sample ready for triaxial testing.

5 Equipment

5.1 Introduction

This chapter provides a description of the equipment utilized in the triaxial testing program involving both RGoM-EI and RBBC over an effective stress range of 1 MPa to 40 MPa. Two different automated triaxial systems were used during this research. A "medium pressure" triaxial system with a limiting cell pressure of 14 MPa and a "high pressure" triaxial system with a limiting cell pressure of over 100 MPa. These systems were originally designed and built at MIT. Modifications have been made to the systems in the Tufts Advanced Geomaterials Lab.

5.2 Overview of Triaxial Systems

The triaxial systems used during this research consist of 5 main parts: triaxial cell, load frame, pressure volume actuators (PVA, flow pumps), computer and motor control box. Figure 5-1 shows the medium pressure triaxial system used for this research.

The triaxial cells are designed to house a 3.5 cm diameter 8.1 cm tall specimen and acts as a pressure vessel to provide confining stress to the specimen. The load frame allows for the application of axial load, the pressure volume actuators provide cell, axial load and pore pressure. Transducers powered by a 5.5 V DC supply are connected to the both the triaxial cell and the pore pressure PVA. These transducers measure pore pressure, cell pressure, axial load, axial displacement, and volumetric displacement. The transducer output voltages are recorded by the laboratory's central data acquisition unit and are also read by the triaxial system's independent computer which contains the control software program. The control software uses a PID (Proportional-Integral-Derivative) control algorithm to produce control signal voltages. These control signal voltages are relayed to the motor control box, containing

three motor controllers. The three motor controllers then provide the appropriate voltages to drive the three DC motors for the cell, load, and pore pressure PVAs.

Both the medium and high pressure triaxial systems share all these basic constituents, however the high pressure triaxial system is designed with consideration for the higher pressures it experiences during testing.

Figure 5-1 Medium pressure triaxial system enclosed in temperature control box at Station 6.

5.3 Automated Stress Path Triaxial Cell

Both medium (Figure 5-2) and high pressure (Figure 5-3) triaxial cells are built to accommodate a standard size triaxial test specimen of 8.1 cm high and 3.5 cm diameter, however for this research the medium pressure cell was modified to test 4.1 cm tall specimens. This was done by adding a piston extension piece. The medium pressure cell consists of a zinc-plated carbon steel with a wall thickness of 10 mm. The high pressure cell has a wall thickness of 38 mm and is composed of 17-4 PH high strength stainless steel.

Within both cells are internal load cells connected to the axial piston. Connected to the bottom of the load cell is an alignment cap. In the case of the high pressure cell this alignment cap doubles as an O-ring sealed suction cap, which provides a vacuum seal to the top cap located on the specimen. When a vacuum is applied to the suction cap through the piston, the suction cap allows triaxial extension tests to be performed. The medium pressure triaxial cell also has the capability of being modified to run extension tests.

The top cap located on top of the specimen contains a drilled bore, which is connected to the base and the pore manifold via a top drainage line. The pedestal, situated at the base of the specimen, also has a bored drainage path that connects to the pore manifold. This allows the specimen to drain from both top and bottom.

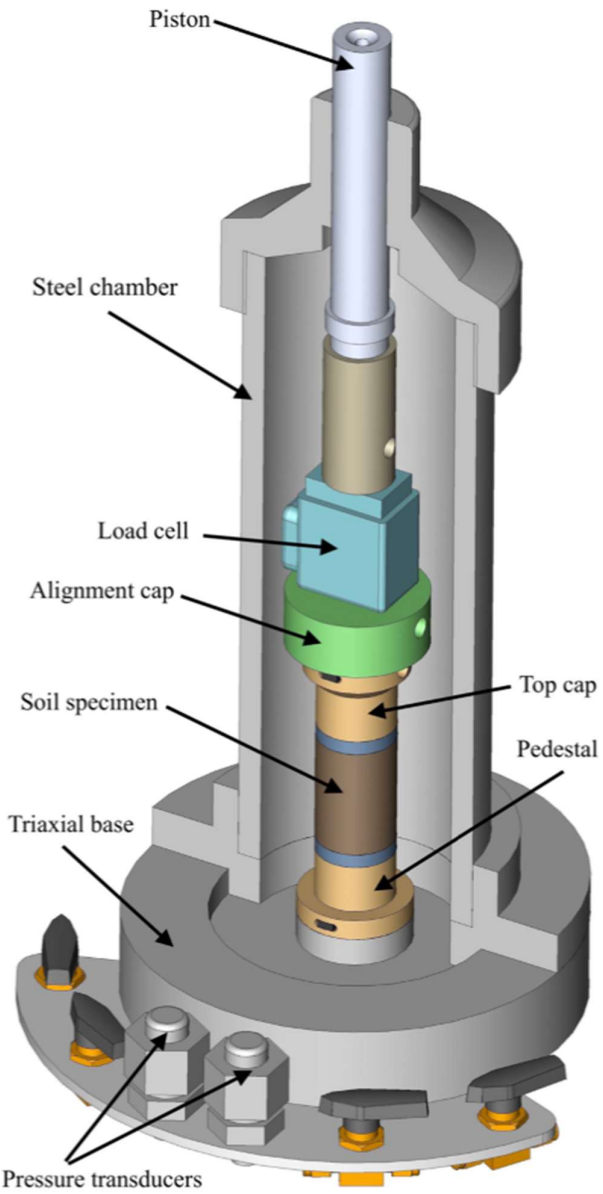

Figure 5-2 Cad section drawing of a medium pressure triaxial cell.

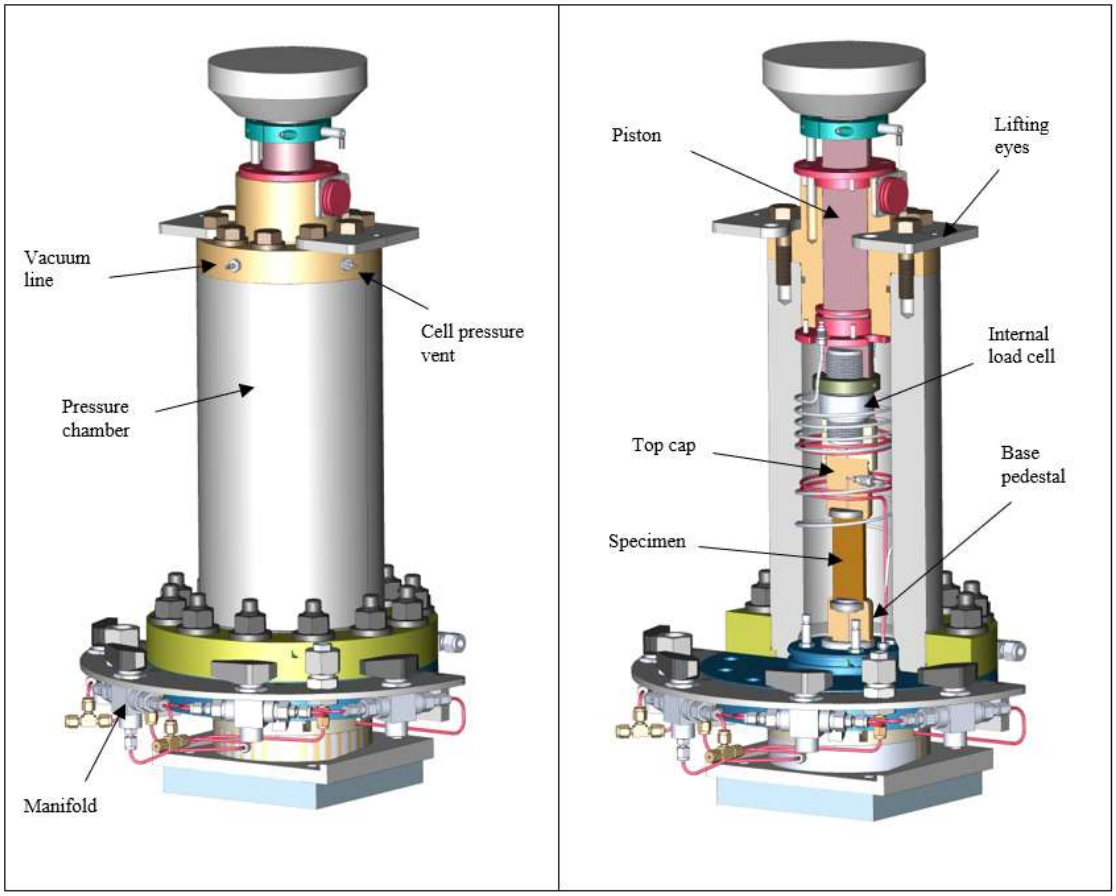

Figure 5-3 Cad drawing of the high pressure triaxial cell with section on the right showing internals (Adapted from Eagle, 2021)

5.3.1 Silicone Oil

Dow Corning® PMX-200, 20 centistoke low viscosity silicone oil is used to apply cell pressure to the specimen. Silicone oil is used as it does not permeate the specimen latex membranes, it has dielectric properties allowing electronic instrumentation within the cell, it is chemically inert, does not degrade the latex membranes and is non-toxic.

5.3.2 Load Frame

The medium pressure triaxial cell is contained within a 10-ton load frame. The high pressure triaxial cell is contained within a 24-ton load frame. Both load frames are hydraulic with the pressure supplied by appropriately sized Pressure Volume Actuators.

5.4 Transducers

There were four types of transducers used during triaxial testing over the course of this research. These are linear variable displacement transformers (LVDTs), string potentiometers (string pots), pressure transducers and shear beam load cells. All transducers were calibrated in-house to ensure the conversion into engineering units is reliable.

5.4.1 Displacement Transducers

Two different types of displacement transducers were used on the medium and high pressure systems.

In the medium pressure system, two Hewlett Packard® LVDTs were used to measure axial displacement of the piston on the exterior of the triaxial cell and thereby axial deformation of the specimen within the cell can be calculated (Figure 5-4). These LVDTs have a 4 V DC linear output range (-2 to + 2 V), however voltages were maintained to within a 2 V (-1 to +1 V) range for this research to ensure linearity. A TE Connectivity® SP2-12 string pot is used on the pore fluid PVA to measure the relative displacement of the PVA piston as it moves inside the pressure chamber. This displacement is used to calculate the volumetric displacement of the pore fluid in the specimen. String pots provide the advantage of having a linear output voltage over their full operational range, allowing the measurement of larger displacements.

In the high pressure system, string pots are used to measure both the axial displacement of the triaxial cell piston and the pore fluid PVA piston.

Figure 5-4 Two LVDTs used to measure specimen axial displacements on the medium pressure triaxial system Station 6

5.4.2 Pressure Transducers

The medium pressure triaxial system utilized two Omega® PX-102, 1000 psi capacity flush diaphragm pressure transducers to measure the cell pressure and pore pressure. A valve on the manifold allows the user to isolate either the measurement of pore pressure in specimen or the backpressure in the pore PVA chamber.

The high pressure triaxial system used two Omega® PX309 stainless steel pressure transducers to measure both cell and pore pressure.

5.4.3 Load Cells

The medium pressure triaxial cell contains an internal Data Instruments® JP-1000 load cell with a capacity of 8.9 kN. Internal load cells are required as they remove the need to account for frictional forces created at the piston's O-ring seal.

The high pressure triaxial cell contains an internal Futek® LCM550 load cell with a capacity of 222 kN. For this research, it was necessary to maintain power supply to the load cell to eliminate "warm up" effects at the beginning of a test. This reduced fluctuations in the initial zero load reading.

5.4.4 Resolution

Transducer resolutions are provided in the following sections 5.4.4 and 5.4.5 for both triaxial systems utilized during this research. These resolutions are based on the voltage resolution of the central data acquisition system and the AD1170 analog to digital converter used in the control computer

5.4.5 Medium Pressure Triaxial

Table 5-1 Table of transducer specifications, adapted from (Casey 2014)

Transducer	**Transducer Range**	**Precision**		**Resolution**	
		ADC	**Central acq.**	**ADC**	**Central acq.**
Axial displacement	3 cm	0.00001 mm (0.0024 mV)	0.00060 mm (0.1 mV)	0.00002%	0.00074%
Specimen volume	47 cm^3	0.01 mm3 (0.0024 mV)	0.40 mm^3 (0.1 mV)	0.00001%	0.00054%
Cell pressure	7 MPa	0.015 kPa (0.00024 mV)	0.063 kPa (0.001 mV)	0.0002%	0.0009%
Pore pressure	7 MPa	0.015 kPa (0.00024 mV)	0.063 kPa (0.001 mV)	0.0002%	0.0009%
Load cell	8.9 kN	0.012 N (0.00024 mV)	0.05 N (0.001 mV)	0.0002%	0.0009%

5.4.6 High Pressure Triaxial

Table 5-2 Table of transducer specifications, adapted from (Casey 2014)

Transducer	Transducer Range	Precision		Resolution	
		ADC	Central acq.	ADC	Central acq.
Axial displacement	7.6 cm	0.00003 mm (0.0024 mV)	0.0014 mm (0.1 mV)	0.00002%	0.00074%
Specimen volume	47 cm^3	0.04 mm3 (0.0024 mV)	1.75 mm^3 (0.1 mV)	0.00001%	0.00054%
Cell pressure	69 MPa	1.45 kPa (0.00024 mV)	6.03 kPa (0.001 mV)	0.0002%	0.0009%
Pore pressure	34 MPa	0.08 kPa (0.00024 mV)	0.031 kPa (0.001 mV)	0.0002%	0.0009%
Load cell	222 kN	0.040 N (0.0000024 mV)	18.6 N (0.001 mV)	0.0002%	0.0009%

5.5 Pressure Volume Actuators

In the medium pressure triaxial system, cell pressure, pore/back pressure and axial load are controlled by three distinct PVAs. The PVAs have a pressure capacity of 14 MPa and a volumetric capacity of 47 cm^3. Each PVA consists of a pressure chamber, a 2.85 cm diameter piston which is driven by a 0.5-ton Duff-Norton® inverted screw jack, which is in turn driven by a Maxon M111344 DC servomotor (Figure 5-5). The movement of the piston displaces fluid within the chamber, thereby increasing or decreasing the pressure. Each piston uses an O-ring seal at the opening to the pressure chamber.

The pore/back pressure PVA is connected directly to the specimen within the triaxial cell and contains salt water. The salinity of this salt water is changed depending on the material being tested. The cell pressure PVA is connected directly to the triaxial cell and contains silicone oil.

The axial load PVA contains hydraulic oil and is connected to a hydraulic jack situated below the triaxial cell. This hydraulic jack pushes the triaxial cell's piston against the load frame, providing the reaction force that is applied to the specimen within the triaxial cell.

The high stress triaxial system uses an identical pore pressure PVA as the medium pressure. Due to the increased pressures necessary for the high stress triaxial system, the cell pressure and axial load PVAs are each designed differently to increase their capacities (Figure 5-6). The cell pressure PVA has a piston diameter of 3.18 cm and a volume capacity of 200 cm^3, producing a maximum of 110 MPa. The axial load PVA has a piston diameter of 6.35 MPa and a volume capacity of 800 cm^3, producing a maximum pressure of 28 MPa. A 10-ton Duff-Norton® inverted screw jack is used to drive the piston in both PVAs, which are in turn driven by Maxon® M166235 DC servomotors.

PVAs in both the medium and high pressure triaxial systems have limit switches to prevent the PVAs exceeding their operational ranges. The high pressure system's cell and axial load PVAs also contain pressure relief valves to ensure that pressures do not go beyond the capacity of the PVAs. These fail-safe mechanisms prevent damage to the PVAs and increase the user-safety of the system.

Figure 5-5 14 MPa capacity PVAs utilised at Station 6.

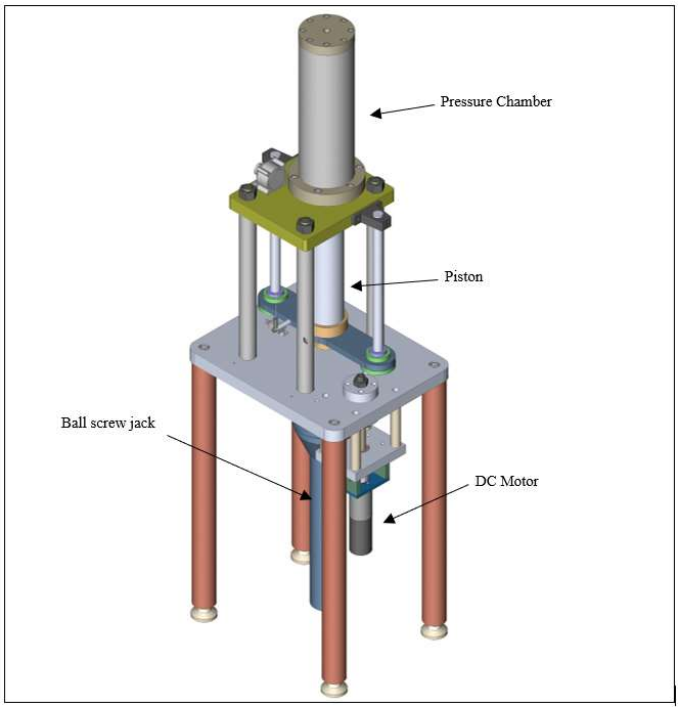

Figure 5-6 28 MPa PVA used to actuate the load frame at the high pressure triaxial system Station 3.

5.6 DC Motors

The 14 MPa capacity PVAs are driven by Maxon® DC servomotors providing 80 mNm of torque. The 110 MPa and 28 MPa capacity PVAs in the high stress triaxial system are driven by Maxon® DC servomotors proving 184 mNm of torque.

5.7 DC Motor Controllers

The motor control box houses three Maxon® ESCON 50/5 DC motor controllers used to control the three DC servomotors. The motor controllers have a programmable software that allows, via a USB interface, the signal voltage gain, speed constant (rpm/V), maximum permissible speeds, and the voltage range to be adjusted. Tachometers in the DC motors measure the rotational speed of the motor. This allows the user to fine tune the motors. The motor control box also contains a control card, cooling fan, AC to DC power supply, electronics to control the limit switches and manual switches to allow manual adjustment of the motors. Table XX shows the control settings used in each motor controller.

Table 5-3 DC Motor Controller Settings

Motor Controller	Speed Constant	Maximum Permissable Speed
Axial Load	1 rpm/V	50 rpm
Cell Pressure	5 rpm/V	80 rpm
Pore Pressure	50 rpm/V	1000 rpm

5.8 Triaxial Control System

The medium and high pressure triaxial systems are automated by employing a software that was originally developed in MIT by (Sheahan, 1991) in the 1980s. Operating independently from the central data acquisition system, the triaxial control system controls the three DC motors on the PVAs using a PID closed loop feedback. Output signal voltages from the transducers are transferred to an Analog Devices® AD1170 multichannel analogue to digital converter. This in turn passes into the triaxial systems computer containing the control software. The control programme software calculates the engineering values and based on the target values inputted by the user, the programme sends a digital signal to a multichannel digital to analog converter, which converts the digital signal to an analog signal which is then be sent to the motor control box.

5.8.1 Analog to Digital Converter

An Analog Devices® AD1170 multichannel A/D converter used within both the systems. This A/D converter has a 22-bit resolution. On a ±5V scale, a 22-bit resolution provides a sensitivity (i.e., smallest digital increment) of 0.0000024 V. Gains of 10, 100, or 1000 are used on each channel depending on the transducer signal output. The AD1170 card is connected to the system computer using an ISA port within the computer.

5.8.2 Digital to Analog Control Card

A Strawberry Tree Inc. Analog Connection AO (I/O) 112-1A digital to analog ISA board is utilized to convert the digital DC motor control signals calculated in the triaxial control software to analog signals. The analog control signals are subsequently sent to the DC motor controllers housed in the motor control box.

5.8.3 Triaxial Control Software

The triaxial control software is a QBASIC programme originally developed and written at MIT in the 1980s and runs on MS-DOS. The software allows for a variety of testing protocols, including fixed stress path and K_0 consolidation, to be implemented. Figure 5-7 shows the control software display screen for the K_0 consolidation subroutine. The software receives digital signal voltages from the AD1170 A/D converter and converts these voltages to various engineering values. Based on the target engineering values and parameters entered by the user, the software calculates digital output signal voltages. These output signal voltages are sent to the D/A converter and then used to control the PVA DC motors.

As part of this research, axial and volumetric strain corrections were added to the control software. The axial strain correction accounts for apparatus compressibility of the triaxial system due to increases in cell pressure or axial load. If apparatus compressibility is not accounted for and the correction is not applied, the axial strain calculated from axial displacement measurements is larger than the actual axial strain experienced by the test specimen. As side drainage was used during this research, and additional volumetric strain correction was implemented to correct for the compressibility of the side drain material. As confining pressure is increase, the side drain material compresses and expels pore fluid. If this correction is not implemented the volumetric strain calculated from the volumetric displacement measurements would be larger than the actual volumetric strain of the specimen.

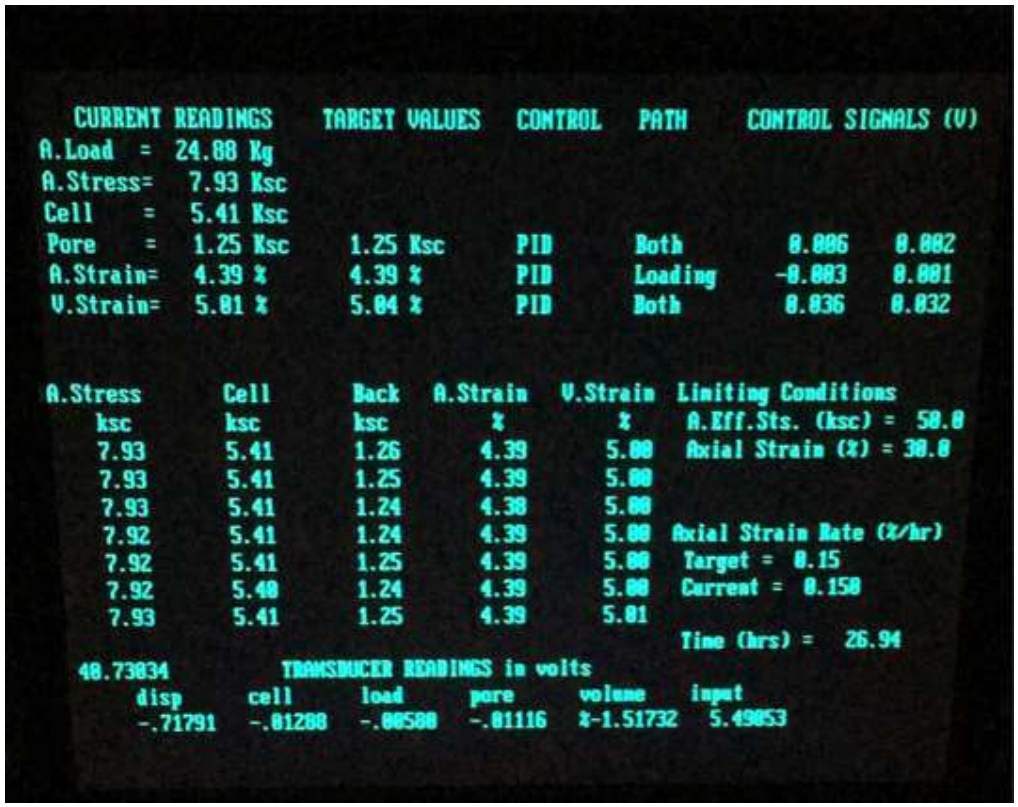

Figure 5-7 Control software display during triaxial K_0 consolidation protocol.

5.9 Central Data Acquisition System

The TAG laboratory utilizes a Hewlett Packard® 3497A Central Data Acquisition System to collect and record voltages simultaneously from transducers across 200 data channels in the laboratory. This data acquisition system uses a dual slope integrating A/D converter. Dual slope A/D converters have a slow rate operation, rely on precision analog electronics, and are no longer manufactured, however for the purpose of triaxial testing they are extremely effective at eliminating signal noise. Auto-ranging voltage signal amplification is used by the system to four voltage scales: 0.1, 1, 10 and 100 V. A computer connected to the HP 3497A machine allows interface, channel selection, data reading rate and data transfer for further processing. Transducers calibrated using the central data acquisition system can be utilized

across all channels in the laboratory using the same calibration factor. This is a key advantage increasing productivity in the laboratory.

5.10 Data Analysis

A DAT file with raw voltages was transferred from the central data acquisition interface computer and converted to engineering values using a QBASIC data reduction programme developed at MIT. Calibration factors, normalized zero voltages and apparatus compressibility information, along with the raw signal voltages are inputted into the programme. As part of this research, an additional apparatus compressibility correction equation accounting for cell pressure and axial load was added to the data reduction programme to correct the axial strain engineering values. Another correction to account for side drain compressibility when calculating the volumetric strain was also added near the end of the research.

5.11 Membrane

For testing in the medium stress triaxial, a combination of one unlubricated latex prophylactic and one Humboldt MFG. Co. 1.4-inch diameter 0.025-inch-thick latex membrane was used. These membranes were secured to the bottom and top caps respectively by using 3 O-rings.

For the high stress tests, 2-inch PVC heat-shrink tubing was used as the specimen membrane. (Eagle, 2021) investigated and found the impact of the stiffness of these membranes are negligible on the stresses throughout the specimen using an analytical membrane equation. These membranes were secured to the bottom and top caps using three loops of steel tying wire twisted into tension.

5.12 Temperature Control

Both the medium and high pressure triaxial cells are housed in temperature control housings to prevent fluctuations in ambient temperatures which can influence transducer measurements. Within the temperature control housing, infrared heat lamps, accompanied by fans, attached to a temperature-controlled relay circuit maintain the temperature to 25°C within a range of ± 0.1°C. This temperature control was used throughout this research in the high pressure triaxial system. In the medium pressure triaxial system temperature control was only utilised near the end of the research period.

5.13 Geotextile Side Drains

Terrafix® 360R light weight nonwoven geotextile was the material used for the specimen side drains. Compressibility of the geotextile material was measured up to 100 MPa using a CRS apparatus. Hydraulic conductivity tests were performed on this material up to a maximum confining pressure of 11 MPa. The geotextile material was cut into 50 mm x 6.35 mm strips. Eight of these strips were placed around the specimen, prior to the placement of the latex membranes.

Figure 5-8 shows the compressibility, in centimetres, of Terrafix® 360R with increasing vertical effective stress. The compressibility of the geotextile material is highly non-linear. Figure 5-9 shows the equivalent specimen volumetric strain due to compressibility of the geotextile side drains. This was calculated using an assumed specimen size of 4.05 cm high and 3.5 cm diameter and the test set-up volume of eight 6.35 mm x 50 mm geotextile strips. As the side drains are fully saturated, compression in them leads to pore fluid being pushed out of the system and into the PVA. As can be seen, the volume loss of the side drains is a significant proportion of the volume of the specimen. This leads to the necessity of implementing a volume correction for pore fluid expelled from both the specimen and the

filter drains during testing, to account for the side drain compressibility. The following equation form was used to fit the side drain compressibility data (Figure 5-12) and was implemented into the triaxial control programme for medium pressure testing:

$$V_{geo}\ (cm^3) = 0.22885ln(\sigma'_r) + 0.17214 \qquad \textit{(Eq. 5-1)}$$

Figure 5-10 shows the hydraulic conductivity of Terrafix® 360R material compared to the vertical hydraulic conductivity of RGoM-EI over a 0.2 to 11 MPa stress range. The geotextile material has hydraulic conductivities of seven orders of magnitudes larger than RGoM-EI over this stress range. Figure 5-11 shows the drain effectiveness, ξ, of both Terrafix 360R and Whatman 54 filter paper for RGoM-EI. Drain effectiveness, ξ, is a measure of how a drainage material compares to a perfect drainage boundary for a particular soil type, a perfect drainage boundary being infinite drain effectiveness. The equation for calculating drain effectiveness is shown in Equation 5-2. The higher the value of drain effectiveness the closer it is to a perfect drainage boundary. As can be seen in Figure 5-11, the drain effectiveness is far greater than Whatman 54, and at an effective stress of 11 MPa has a value of 1,000,000. This confirms that Terrafix® 360R is a suitable material for use as side drains for RGoM-EI.

$$\xi = \frac{3k_p rt}{k_s h^2} \qquad \textit{(Eq. 5-2)}$$

k_p = hydraulic conductivity of drainage material

r = radius of specimen

t = thickness of geotextile

k_s = hydraulic conductivity of soil

h = height of specimen

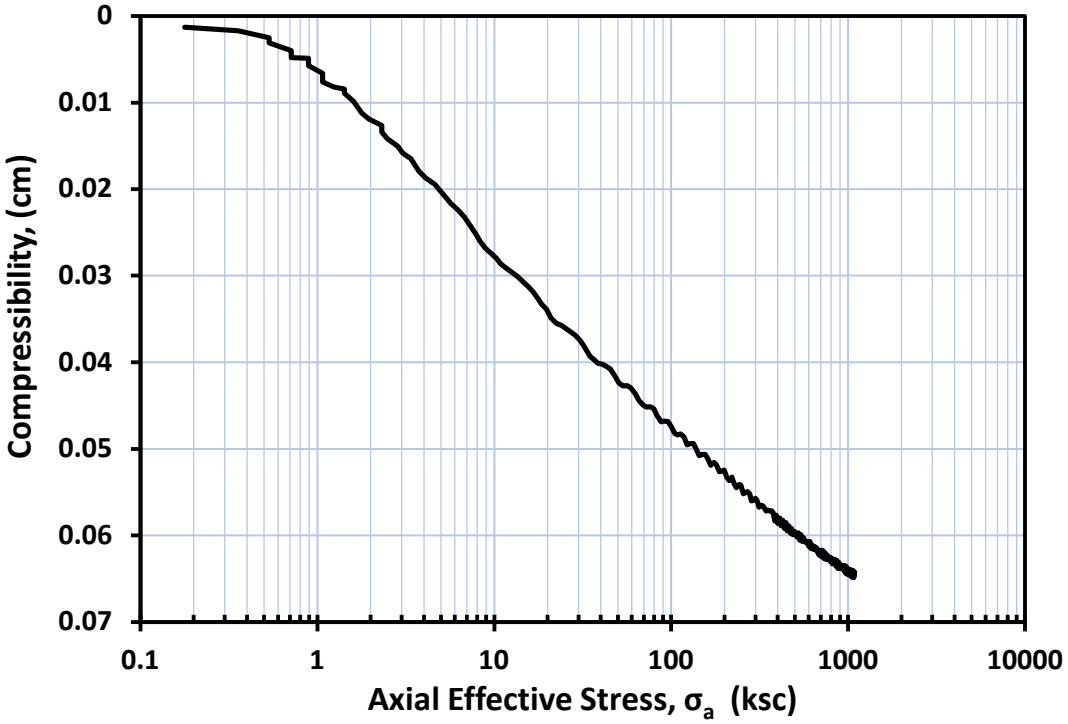

Figure 5-8 Compressibility of Terrafix® 360R geotextile fabric measured using a CRS apparatus.

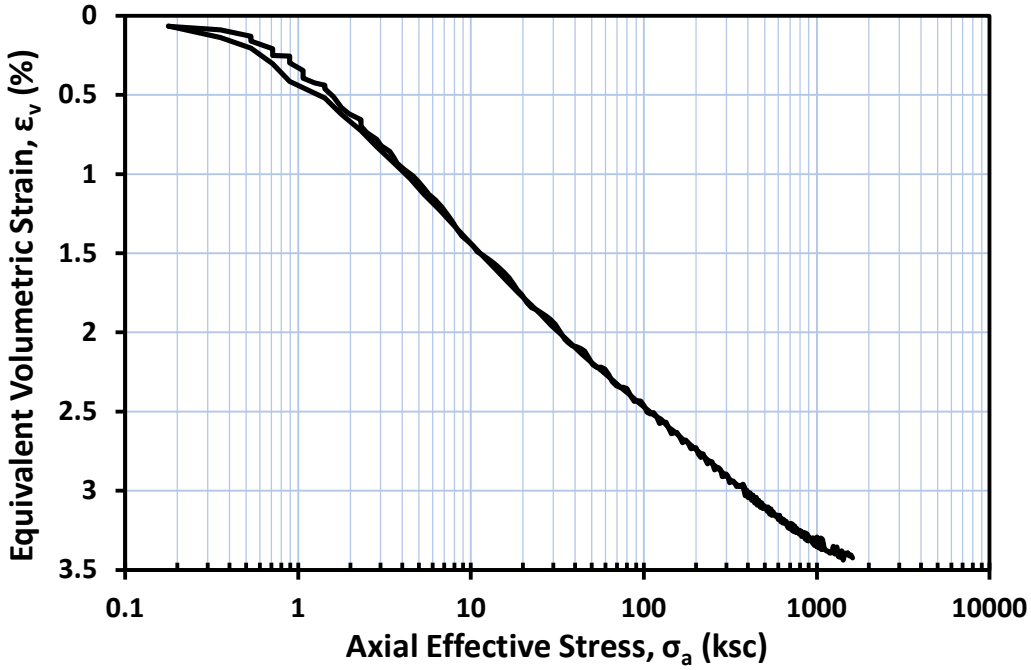

Figure 5-9 Equivalent specimen volumetric strain of eight 6.35 x 50 mm strips of Terrafix® 360R geotextile.

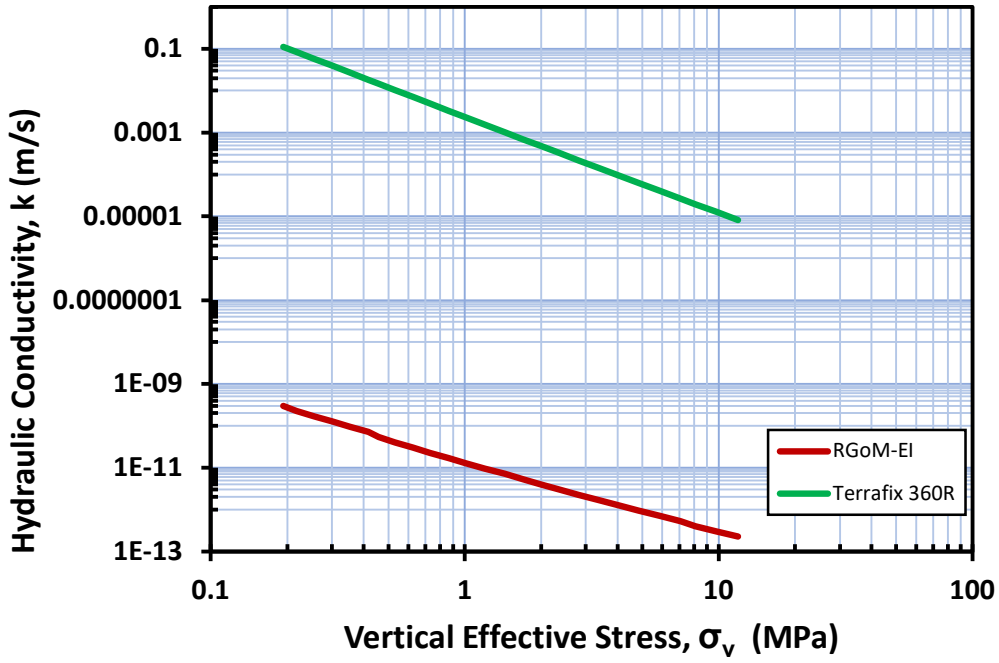

Figure 5-10 A comparison of the hydraulic conductivities of Terrafix® 360R geotextile and RGoM-EI.

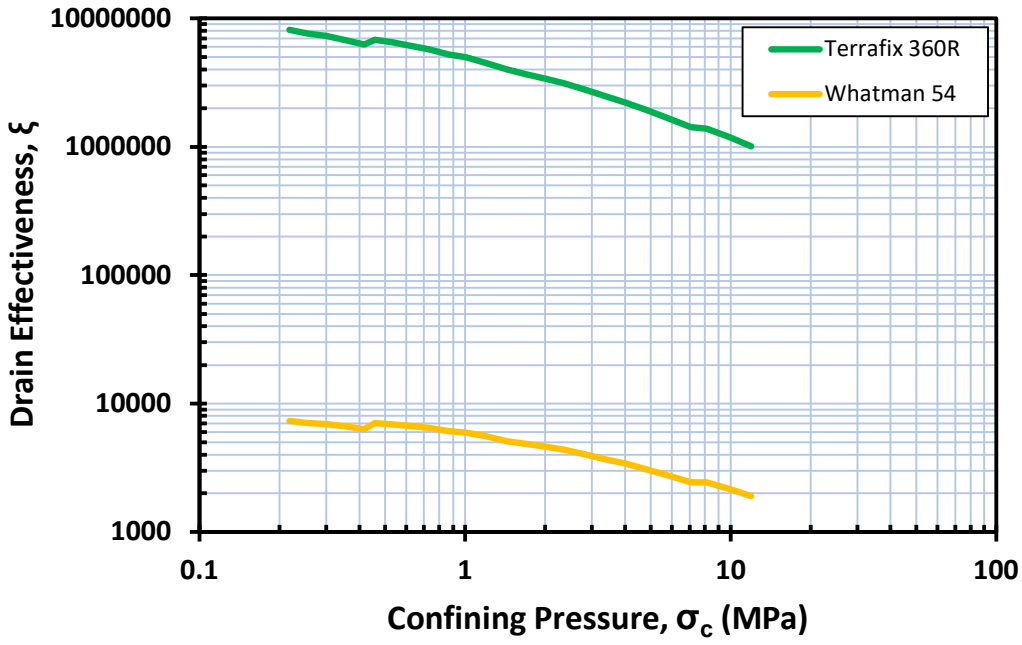

Figure 5-11 Comparison of the drain effectiveness of Terrafix 360R® and Whatman 54 filter paper for RGoM-EI.

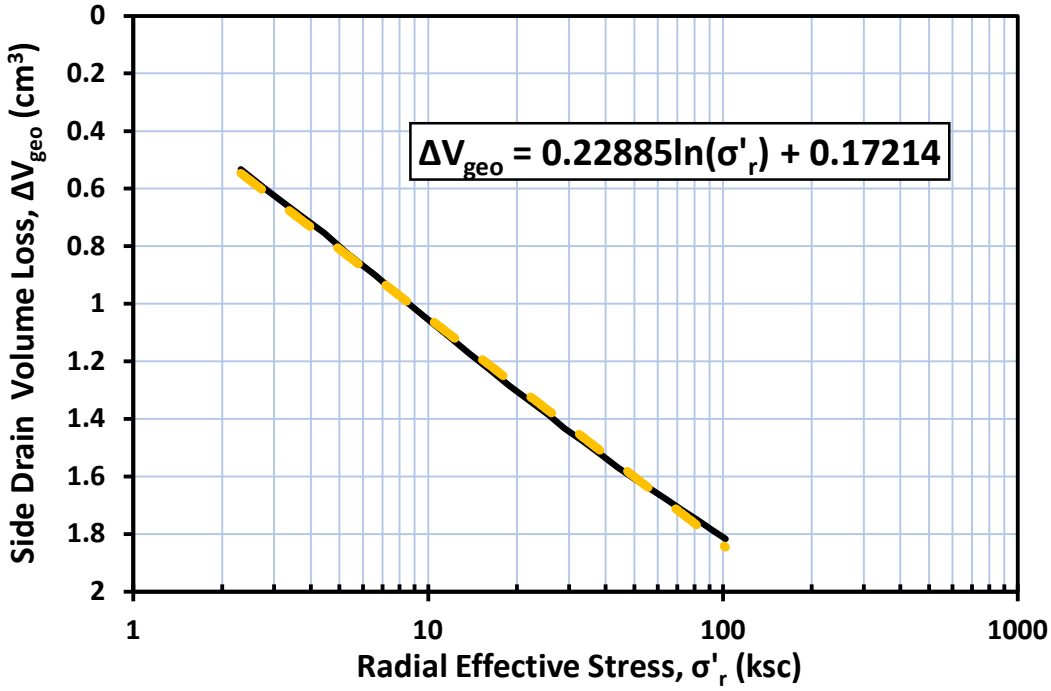

Figure 5-12 Logarithmic fit used for side drain volumetric correction in medium pressure triaxial testing.

5.14 Apparatus Compressibility

The triaxial control software K_0 consolidation protocol adheres to the condition of uniaxial strain by attempting to maintain the change in axial strain of the specimen equal to the change in volumetric strain. During this research, the author noticed that, although previous researchers corrected their test data for apparatus compressibility after a test, the triaxial control program did not account for apparatus compressibility during the testing protocol. Therefore, two apparatus compressibility corrections were implemented into the triaxial control software to correct axial strain for apparatus compressibility. One correction was for apparatus compressibility due to axial load, the other was for apparatus compressibility due to cell pressure.

Figures 5-13 through to 5-16 show the apparatus compressibility curves used for both axial load and cell pressure compressibility for both the medium and high pressure triaxial cells. To calculate the apparatus compressibility, the triaxial cell was set up as to run a test. A steel

dummy specimen, with a known Young's Modulus, was used to replace the soil specimen. The triaxial cell flange bolts were torqued to 22.4 Nm in the case of Station 6 and 130 Nm in the case of Station 3. For axial load apparatus compressibility, the cell pressure was maintained at a constant value while the axial load was increased. For cell pressure apparatus compressibility, the axial load is maintained constant at a seating load of 100 kg, whilst the cell pressure is increased. As can be seen when comparing Station 3, high pressure triaxial cell, and Station 6, medium pressure triaxial cell, apparatus compressibility's, Station 3 is a much stiffer system overall. The equations in the graphs are then used in both the control and the analysis software.

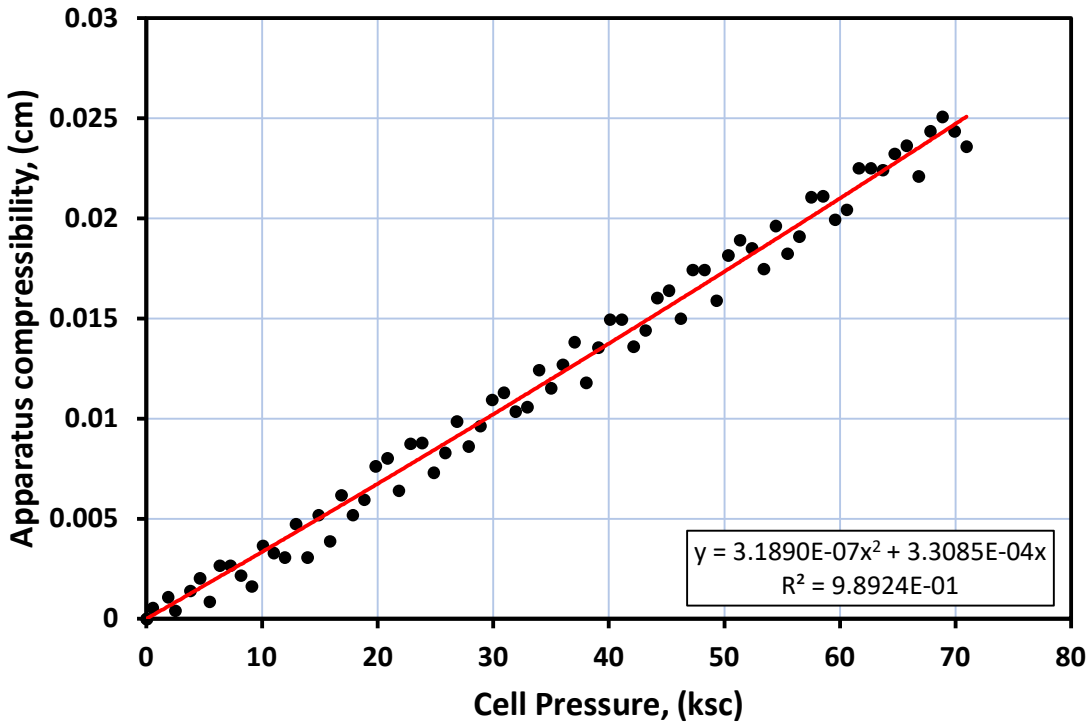

Figure 5-13 Apparatus compressibility curve due to cell pressure increase for Station 6.

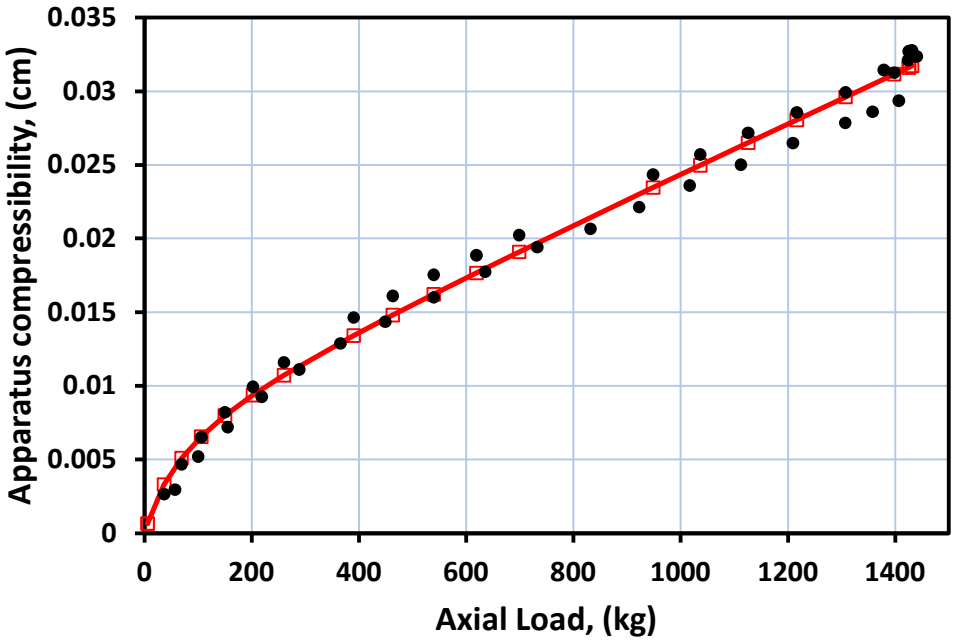

Figure 5-14 Apparatus compressibility curve due to increase in axial load for Station 6.

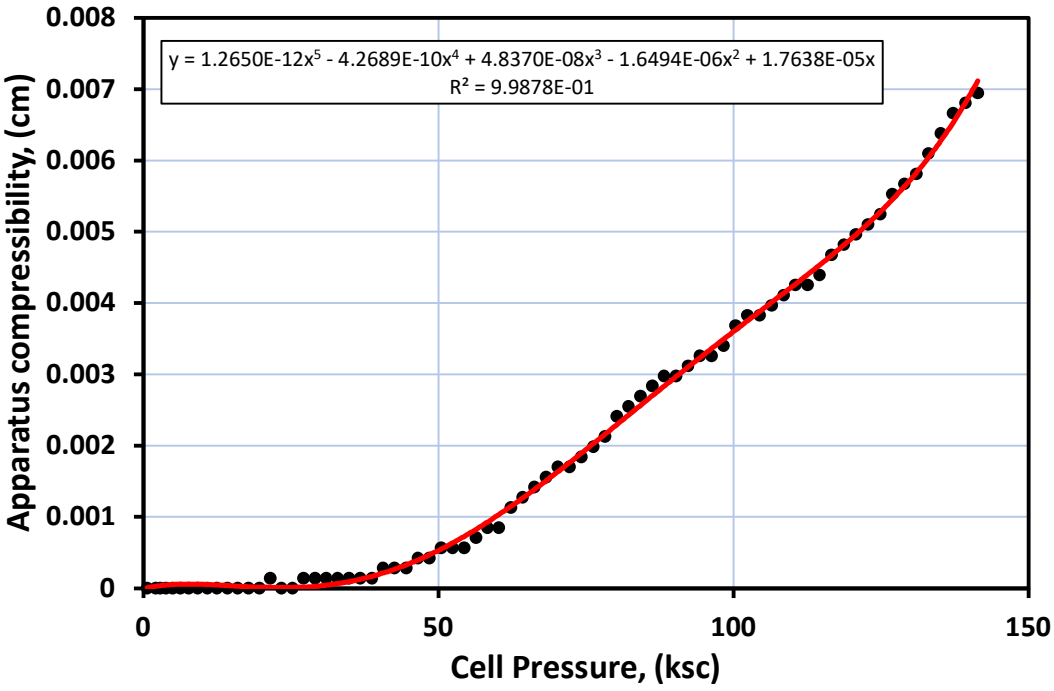

Figure 5-15Apparatus compressibility curve for increase in cell pressure for Station 3.

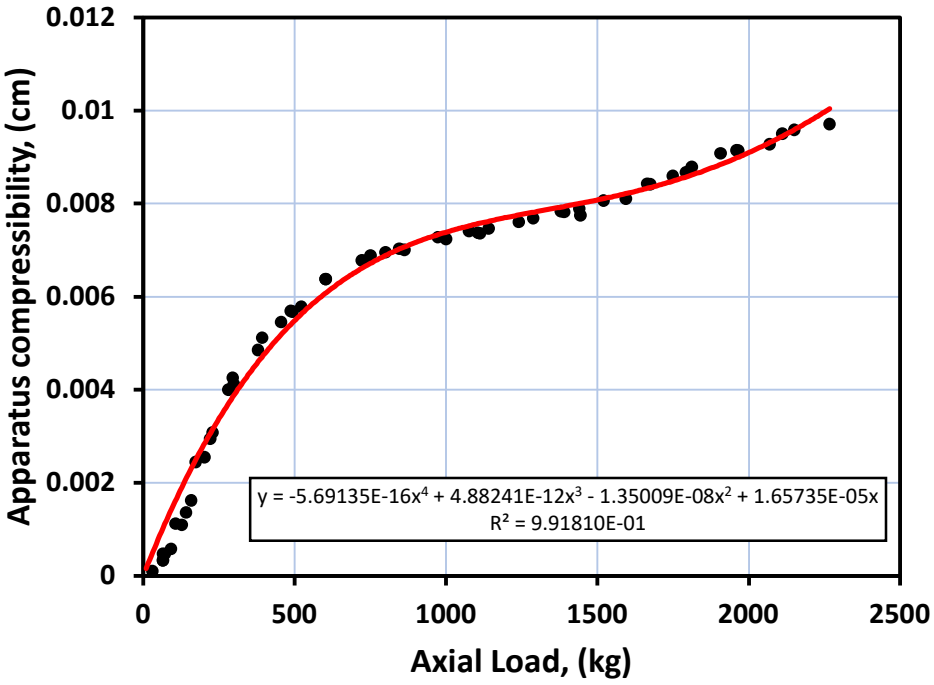

Figure 5-16 Apparatus compressibility curve for increase in axial load for Station 3.

6 Analysis of Past K_0 Consolidation Test Data

6.1 Introduction

This chapter will focus on the analysis undertaken as a part of this research to ascertain the possibility of the generation of excess pore pressure within a sample during consolidation. These excess pore pressures could not be measured in the triaxial system, and therefore could not be accounted for during testing. The generation of excess pore pressures during constant rate of strain consolidation in triaxial testing could lead to a reduction in effective stresses, therefore leading to uncertainty in the K_0 measured for those tests. The excess pore pressures generated are a function of the consolidation strain rate, the dimensions of the specimen, and the permeability and compressibility of the test material. Triaxial tests generally have vertical drainage conditions at the top and bottom of the specimen. The ASTM D4186 method, derived from constant rate of strain consolidation theories developed by (Wissa et al., 1971) for CRS consolidation testing, was used for the analysis of past triaxial consolidation tests. As this solution was based on a small strain assumption, the equation was modified to account for the reduction in specimen height due to the large strains present during consolidation (Gonzalez, 2000). Previous researchers have been aware of the issue of excess pore pressure generation, especially when testing RGoM-EI, and have lowered strain rates accordingly in an attempt to reduce pore pressure generation during consolidation (Eagle, 2021). However, lowering strain rates does have a practical limit, as this results in lower test output for the laboratory, due to the increase in length of time needed for the specimen to consolidate. This chapter will summarize the theoretical background for this analysis, first looking at vertical drainage conditions and then radial drainage conditions. It will then present the analysis of past triaxial K_0 consolidation and compare results for RBBC and RGoM-EI testing materials.

6.2 Theoretical Background for Analysis

6.2.1 Vertical Drainage Conditions

As forementioned, previous K_0 consolidation data from past researchers was analysed using the ASTM D4186 method to estimate the excess pore pressure in the specimen, derived from constant rate of strain consolidation theories developed by (Wissa et al., 1971) for use in CRS apparatus testing, specifically using the linear theory. This theory was developed for use with CRS devices and can be used to calculate base pore pressures. For triaxial specimens, this base pore pressure in CRS testing can be equated to the excess pore pressure at the centre of the specimen. This is due to triaxial specimens having drainage at the top and the bottom. The drainage height, H_d, is half the specimen's total height at a given time. The linear theory by (Wissa et al., 1971) has the following assumptions:

1. Small strain.
2. Deformation and flow occur in one dimensionally.
3. Incompressibility of fluid and soil solids.
4. The soil specimen is completely saturated.
5. The flow through the porous media obeys Darcy's Law (laminar flow).
6. There is a constant coefficient of volume compressibility (m_v).
7. The variation in stress is one dimensional.

Figure 6-1 shows the evolution of the state of strain at early times. There is a transient phase at the beginning of a test, which comes to steady state after a period of time, when the dimensionless time factor, T_v, is approximately 0.5:

$$T_V = \frac{c_v t}{{H_d}^2} \qquad \textit{(Eq. 6-1)}$$

This parabolic deviation in strain must exist to provide the gradient needed for constant flow of pore fluid (Wissa et al., 1971). This parabolic distribution of strains is at a maximum at X = 0 (drainage boundary), and a minimum at X =1 (impervious boundary). In terms of a CRS test, this would mean maximum strain at the top of a specimen and minimum at the base. Given the assumption that the soil has linear compressibility, the parabolic distribution in strain translates to a parabolic distribution of pore pressures. In the case of CRS consolidation testing, the maximum excess pore pressures are experienced at the base of the specimen, with the minimum at the drainage boundary. In triaxial testing, the maximum excess pore pressures are at the centre of the specimen with the minimum at the two drainage boundaries.

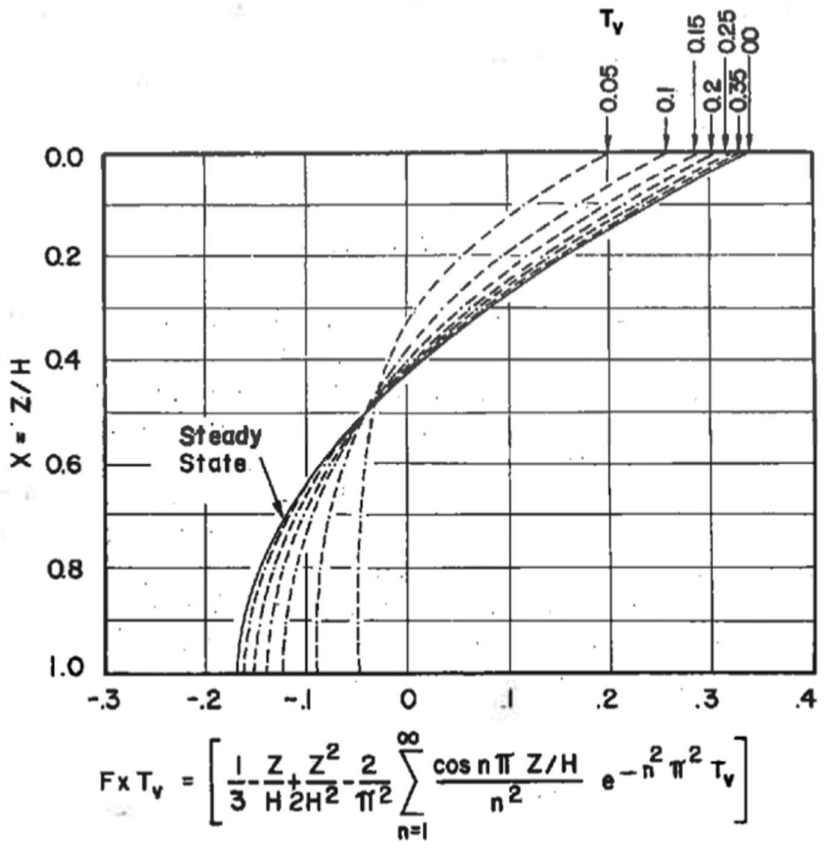

Figure 6-1 Deviation of strain from its average times $c_v t/rH^2$ as a funtion of depth for different time factors (Wissa et al., 1971)

Using this theory with minor adjustments, excess pore pressures at the centre of the specimen, $u_{e,c}$, can be calculated with the following equation:

$$u_{e,c} = \frac{\dot{\varepsilon} H_0 H \gamma_w}{2k_v} \qquad \textit{(Eq. 6-2)}$$

H = Current specimen height

H_0 = Initial specimen height

k_v = Vertical hydraulic conductivity of soil

γ_w = Unit weight of pore fluid at 20ºC

$\dot{\varepsilon}$ = Strain rate

Equation 6-2 shows the dependence of excess pore pressures on strain rate, specimen height, specific weight of water and the vertical hydraulic conductivity of the material. The changes in specific weight in water do not have a substantial practical effect on excess pore pressures, as this value does not fluctuate considerably in reality. However, increasing strain rates, specimen height (drainage distance), and reducing the material's hydraulic conductivity can have significant effects on increasing excess pore pressures.

Given the parabolic distribution of pore pressures in the specimen, the integrated excess pore pressure across the specimen would be $^2/_3\, u_{e,c}$. Therefore, the average effective stresses can be calculated using the following equations:

$$\sigma'_{a,a} = \sigma_a - {}^2/_3\, u_{e,c} \;\; \textbf{\textit{or}} \;\; \sigma'_{r,a} = \sigma_r - {}^2/_3\, u_{e,c} \qquad \textit{(Eq. 6-3)}$$

Where the initial subscript defines the direction of loading ("a" is axial, "r" is radial), and the second subscript denotes "average". With this knowledge, a correction can be also made for the at rest lateral stress ratio, K_0:

$$K_{0,a} = \frac{\sigma'_{r,a}}{\sigma'_{a,a}} \qquad \textit{(Eq. 6-4)}$$

Figure 6-5 showing the excess pore pressure, effective stress and K_0 versus specimen depth for an instance in time during K_0 consolidation of a triaxial test, illustrates how the correction for the generation of excess pore pressure is made on the measured K_0. There is a parabolic distribution in excess pore pressures. The measured radial effective stress, σ'_r, and measured σ'_a are constant along the depth of the specimen. When these measured stresses are corrected for excess pore pressure generation, there is a parabolic distribution in both the effective stresses, σ'_{cor}, along the depth of the specimen. The greatest error in effective stresses is at the centre of the specimen where the excess pore pressure is at a maximum. Using the effective stresses corrected for excess pore pressure, we can then calculate a K_0 corrected for excess pore pressure along the depth of the specimen. We can then average these $K_{0,corrected}$ values in order to calculate $K_{0,a}$.

Figure 6-2 shows the average error in axial effective stress versus the applied axial total stress for RGoM-EI for a stress range of 0 to 50 MPa and strain rates of 0.02 to 0.06 %/hr using the average uniaxial compression and average hydraulic conductivity models given in Chapter 4. The error in effective stress is defined with the following equation:

$$Error\ (\%) = \frac{\sigma'_a - \sigma'_{a,a}}{\sigma'_a} \qquad \textit{(Eq. 6-5)}$$

An initial standard height of 8.1 cm was used, giving a drainage height of 4.05 cm. There is a significant effect of strain rate on the error in effective stresses. Using the standard laboratory consolidation strain rate of 0.06 %/hr for medium pressure testing, at a stress of 10 MPa there would be a 28% error in effective stresses.

The effects of material properties are shown through comparing Figure 6-2 with Figure 6-3, which shows a plot of average error in effective stress vs axial total stress for RBBC. RBBC appears to generate far less excess pore pressure than RGoM-EI, and after an initial peak at 15 MPa begin to reduce with increasing stress. Using the standard laboratory consolidation strain rate for RBBC of 0.15 %/hr for medium pressure testing, there would be a 1.15% error in effective stresses. The compressibility behaviour of RGoM-EI and RBBC is relatively similar. However, the hydraulic conductivity of RGoM-EI if far lower than RBBC. This difference is illustrated in Figure 6-4 with a comparison of coefficient of compressibility, vertical hydraulic conductivity, and coefficient of consolidation of RBBC and RGoM-EI.

Although valuable to perform a general analysis on RGoM-EI and RBBC using uniaxial compression and permeability material properties from oedometer and CRS testing, further individual analysis was needed on individual past triaxial test data. This was done initially to assess the risk for errors in past data, and furthermore to investigate whether a correction could simply be applied to test data after the fact. Section 6.3 will cover this analysis in detail.

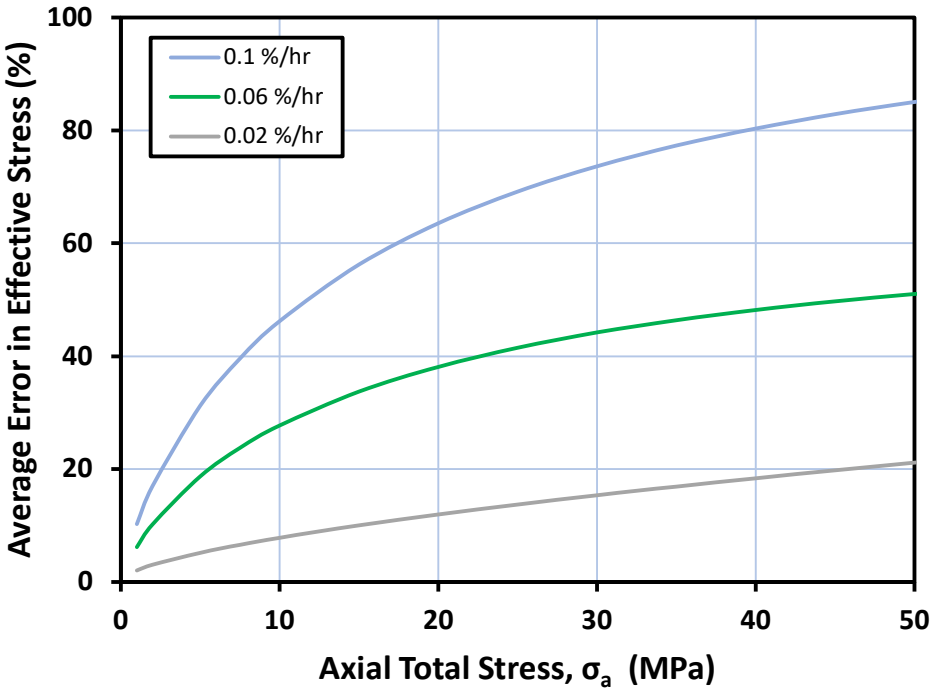

Figure 6-2 Average error in axial effective stress versus axial total stress for various strain rates using average compressibility and hydraulic conductivity data for an 8.1 cm tall and 3.5 cm diameter RGoM-EI specimen.

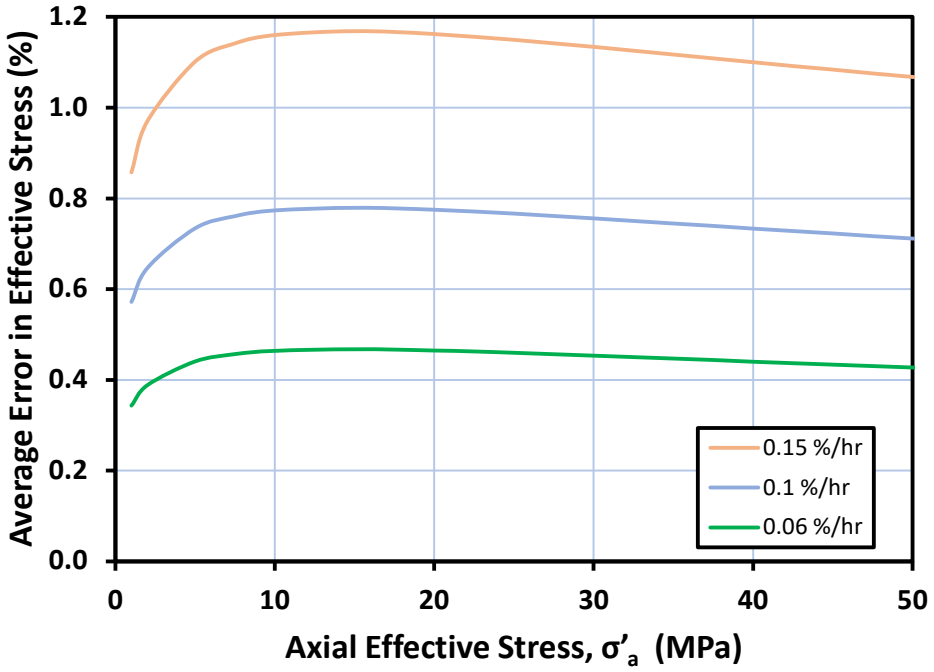

Figure 6-3 Average error in axial effective stress versus axial total stress for various strain rates using average uniaxial compressibility and hydraulic conductivity data for 8.1 cm tall and 3.5 cm diameter RBBC specimen.

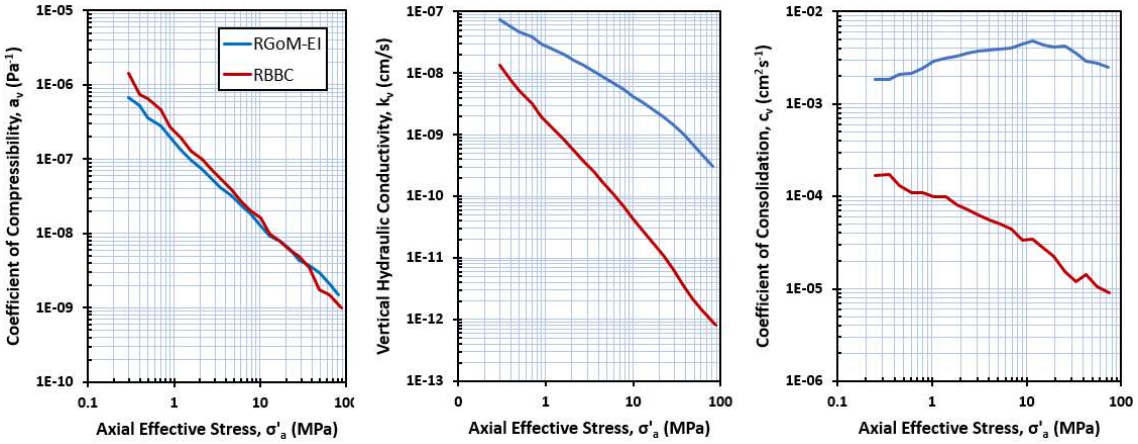

Figure 6-4 Comparison of coefficient of compressibility, vertical hydraulic conductivity, and coefficient of consolidation of RBBC and RGoM-EI

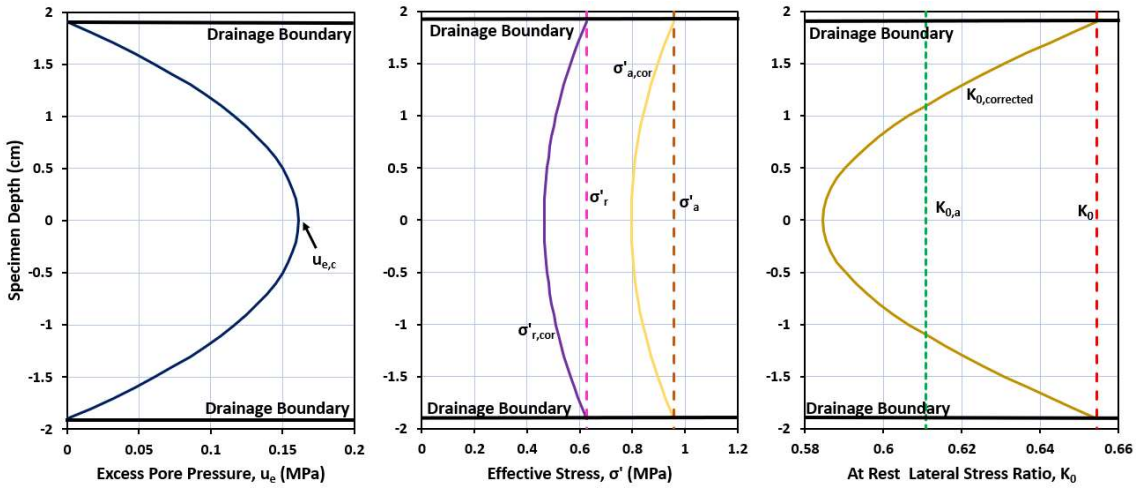

Figure 6-5 Excess pore pressure, effective stress and the at rest lateral stress ratio versus specimen depth for an instance in time during the K_0 consolidation of TX1548

6.2.2 Radial Drainage Conditions

The radial drainage conditions were analysed to ascertain the potential feasibility of utilizing side drains in the testing program and to assess what strain rates would be reasonable to use. This analysis assumes that the drainage boundary is the full radial surficial area of the specimen cylinder. When using side drains only a portion of the perimeter area is covered by the drains. Also, this analysis only considers radial drainage whereas a triaxial compression test using side drains will have both vertical and radial drainage. The analysis was done similarly to that of vertical drainage. The average uniaxial compression behaviour for RGoM-EI and the (Nordquist, 2015) model for radial hydraulic conductivity. Excess pore pressures at the centre of the specimen were calculated using the theory developed by (Yune & Chung, 2005):

$$u_{e,c} = \frac{\gamma_w \, C \, r^2}{4(1+e)k_r} \qquad \textit{(Eq. 6-6)}$$

$$where, \qquad C = \frac{\dot{\varepsilon} H_O A}{V_s} = -\frac{de}{dt} \qquad \textit{(Eq. 6-7)}$$

C = Volumetric strain rate

k_r = Radial permeability of the soil

r = Specimen radius

V_s = Volume of soil grains

A = Cross-sectional area of specimen

There is a triangular distribution of excess pore pressures when a specimen is compressed axially with only radial drainage. This has a maximum pore pressure at the centre of the

specimen and a zero at the perimeter radius. The integrated average excess pore pressure across the sample is $^1/_2\, u_{e,c}$, so the average effective stresses in the sample can be calculated as:

$$\sigma'_{a,a} = \sigma_a - {}^1/_2\, u_{e,c} \quad \textbf{or} \quad \sigma'_{r,a} = \sigma_r - {}^1/_2\, u_{e,c} \qquad \textit{(Eq. 6-8)}$$

Figure 6-5 highlights the benefits of radial drainage. It shows a plot of average percentage error in effective stress versus vertical total stress over a stress range of 0 to 50 MPa for GoM-EI. Using the laboratory standard consolidation strain rate of 0.06 %/hr for medium pressure triaxial testing, we can see that the error stays below 3 % up to axial total stresses of 50 MPa. It should be said that the radial hydraulic conductivity of RGoM-EI is almost an order of magnitude higher than the vertical conductivity over this stress range. This, coupled with the shortened drainage distance of 1.75 cm, which remains constant in uniaxial conditions, reduces the excess pore pressures generated. The effects of both radial drainage and the introduction of side drains was further analysed using finite element analysis modelling, which will be covered in Chapter 7.

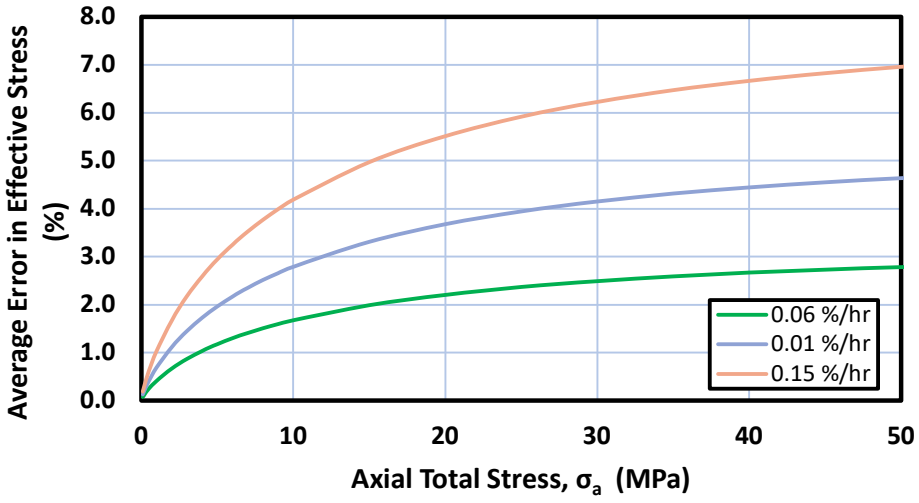

Figure 6-6 Average error in axial effective stress versus axial total stress for various strain rates using average uniaxial compressibility and radial hydraulic conductivity correlation from (Nordquist, 2015) for 8.1 cm tall, 3.5 cm diameter RGoM-EI specimen.

6.3 Data Analysis

6.3.1 Procedure

This section will provide a description of the analysis conducted on past triaxial K_0 consolidation data. An excel spreadsheet was created to calculate the excess pore pressures at the centre of the specimen and provide a correction to the axial and radial stresses measured during consolidation. From there a corrected at rest lateral stress ratio, $K_{0,a}$, could be calculated. Time, measured vertical effective stress (MPa), measured radial effective stress (MPa), axial strain (%), volumetric strain (%), and void ratio from past triaxial test data was inputted into the spreadsheet along with the initial values of A_0 (m^2) and H_0 (m)

Time and axial strain were used to calculate the consolidation strain rate in %/hr, which was then converted to s^{-1}. Hydraulic conductivity of the specimen was calculated for a given void ratio using the average uniaxial vertical hydraulic conductivity models presented in Chapter 4. The current height, H, was calculated using the volumetric strain and the initial volume calculated using A_0 and H_0. Using these values, the excess pore pressure generated at the centre of the specimen can be calculated using Equation 6-2, and the average effective stresses can then be calculated using Equation 6-3. Table 6-1 and 6-2 show an example of the excel spreadsheet used to perform the analysis. In this example spreadsheet, the strains are negative due the specimen swelling during the pressure-up and back pressure saturation stages of the experimental test.

Section 6.3.2 provides results and discussion for this analysis with a comparison of excess pore pressures, normal compression curve behaviour and at rest lateral stress ratio, K_0, measurements for four samples with various geometries, using different consolidation strain rates and over a range of stress levels across low pressure, medium pressure, and high pressure triaxial systems.

Table 6-1 Example of excel spreadsheet used to analyse excess pore pressures at the centre of the specimen during consolidation (Part 1).

Time	MeasuredVetical Effective Stress	Back Pressure	Measured Radial Effective	Axial Strain	Stress Ratio	Void Ratio	Volumetric Strain	Total Volume	Volume Reduction	New Height
(s)	*(MPa)*	*(MPa)*	*(Mpa)*	*(%)*	*K*	*e*	*%*	*V*	V_{red}	*m*
0	2.86332549	0.97278961	2.565479412	-1.697	0.896	0.577	-3.713067	7.94E-05	-2.84E-06	8.40E-02
1	2.861304902	0.97402716	2.56355	-1.697	0.896	0.577	-3.713377	7.94E-05	-2.84E-06	8.40E-02
3	2.863972549	0.97339382	2.566073529	-1.697	0.896	0.577	-3.713608	7.94E-05	-2.84E-06	8.40E-02
6	2.864048039	0.97342284	2.566105882	-1.697	0.896	0.577	-3.713067	7.94E-05	-2.84E-06	8.40E-02
12	2.86732549	0.97215637	2.569261765	-1.696	0.896	0.577	-3.713067	7.94E-05	-2.84E-06	8.40E-02
30	2.870716667	0.97215637	2.572411765	-1.696	0.896	0.577	-3.712605	7.94E-05	-2.84E-06	8.40E-02
40	2.87267451	0.97212745	2.574268627	-1.695	0.896	0.577	-3.712915	7.94E-05	-2.84E-06	8.40E-02
89	2.881535294	0.97276069	2.582454902	-1.695	0.896	0.577	-3.712683	7.94E-05	-2.84E-06	8.40E-02
389	2.913706863	0.97278961	2.630363725	-1.696	0.903	0.576	-3.708672	7.94E-05	-2.84E-06	8.40E-02
689	2.96982451	0.97278961	2.682647059	-1.685	0.903	0.576	-3.705665	7.94E-05	-2.84E-06	8.40E-02
989	3.027866667	0.97215637	2.736822549	-1.671	0.904	0.576	-3.702657	7.94E-05	-2.84E-06	8.40E-02
1289	3.093027451	0.97405608	2.797289216	-1.671	0.904	0.576	-3.698956	7.94E-05	-2.83E-06	8.40E-02
1589	3.170105882	0.97342284	2.869105882	-1.666	0.905	0.576	-3.693867	7.94E-05	-2.83E-06	8.40E-02
1889	3.268261765	0.98102157	2.923869608	-1.657	0.895	0.576	-3.687853	7.94E-05	-2.82E-06	8.40E-02
2189	3.308773529	0.97342284	3.016508824	-1.647	0.912	0.576	-3.682764	7.94E-05	-2.82E-06	8.40E-02
2489	3.391889216	0.97405608	3.093987255	-1.638	0.912	0.576	-3.675593	7.94E-05	-2.82E-06	8.40E-02
2789	3.47629902	0.97468931	3.17272549	-1.627	0.913	0.576	-3.669115	7.94E-05	-2.81E-06	8.40E-02
3089	3.565405882	0.97532255	3.255872549	-1.617	0.913	0.576	-3.661018	7.94E-05	-2.80E-06	8.40E-02
3389	3.653589216	0.97342284	3.338401961	-1.603	0.914	0.576	-3.647833	7.94E-05	-2.79E-06	8.40E-02
3689	3.717301961	0.97532255	3.41587451	-1.599	0.919	0.575	-3.638118	7.94E-05	-2.79E-06	8.39E-02
3989	3.798126471	0.97468931	3.491468627	-1.588	0.919	0.575	-3.627014	7.94E-05	-2.78E-06	8.39E-02
4289	3.879648039	0.97405608	3.567694118	-1.581	0.92	0.575	-3.614985	7.94E-05	-2.77E-06	8.39E-02
4589	3.936369608	0.97532255	3.638867647	-1.569	0.924	0.575	-3.604575	7.94E-05	-2.76E-06	8.39E-02
4889	4.015662745	0.97342284	3.713207843	-1.557	0.925	0.575	-3.592547	7.94E-05	-2.75E-06	8.39E-02
5189	4.088418627	0.97468931	3.781233333	-1.546	0.925	0.575	-3.5826	7.93E-05	-2.74E-06	8.39E-02
5489	4.182938235	0.98292157	3.832842157	-1.536	0.916	0.574	-3.571265	7.93E-05	-2.74E-06	8.39E-02
5789	4.217718627	0.97468931	3.920447059	-1.53	0.93	0.574	-3.559466	7.93E-05	-2.73E-06	8.39E-02
6089	4.290308824	0.97468931	3.988477451	-1.518	0.93	0.574	-3.5479	7.93E-05	-2.72E-06	8.39E-02
6389	4.360956863	0.97468931	4.054620588	-1.513	0.93	0.574	-3.534947	7.93E-05	-2.71E-06	8.39E-02
6689	4.430936275	0.97468931	4.120134314	-1.509	0.93	0.574	-3.52523	7.93E-05	-2.70E-06	8.39E-02
6989	4.494701961	0.97468931	4.17997549	-1.495	0.93	0.573	-3.510426	7.93E-05	-2.69E-06	8.38E-02
7289	4.535551961	0.97342284	4.236671569	-1.479	0.934	0.573	-3.498165	7.93E-05	-2.68E-06	8.38E-02
7589	4.610662745	0.97405608	4.28894902	-1.464	0.93	0.573	-3.485441	7.93E-05	-2.67E-06	8.38E-02
7889	4.646933333	0.97405608	4.341231373	-1.453	0.934	0.573	-3.472025	7.93E-05	-2.66E-06	8.38E-02
8189	4.70475	0.97468931	4.395401961	-1.448	0.934	0.573	-3.462077	7.93E-05	-2.65E-06	8.38E-02
8489	4.757859804	0.97468931	4.445166667	-1.446	0.934	0.573	-3.450512	7.92E-05	-2.64E-06	8.38E-02
8789	4.810708824	0.97405608	4.494930392	-1.429	0.934	0.572	-3.436631	7.92E-05	-2.63E-06	8.38E-02
9089	4.85874902	0.98228824	4.521342157	-1.418	0.931	0.572	-3.425297	7.92E-05	-2.62E-06	8.38E-02

Table 6-2 Example of excel spreadsheet used to analyse excess pore pressures at the centre of the specimen during consolidation (Part 2).

Hydraulic Conductivity	Strain Rate	Strain Rate	Pore Pressure Centre	Average Vertical Effective Stress	Average Radial Effective Stress	Error	Corrected K
m/s	*ε' (%/hr)*	*ε'*	*(MPa)*	*(MPa)*	*(MPa)*	*(%)*	
1.485E-12		0	0.00000				
1.485E-12		0	0.00000				
1.485E-12		0	0.00000				
1.485E-12	0.23	6E-07	3.62531	0.45	0.15	84.387	0.33
1.485E-12	0.07	2E-07	1.11936	2.12	1.82	26.026	0.86
1.485E-12	0.01	2E-08	0.13471	2.78	2.48	3.1283	0.89
1.485E-12	0.06	2E-07	1.00851	2.20	1.90	23.405	0.86
1.485E-12	0.09	3E-07	1.41010	1.94	1.64	32.624	0.85
1.484E-12	0.09	3E-07	1.41221	1.97	1.69	32.312	0.86
1.483E-12	0.09	3E-07	1.45233	2.00	1.71	32.602	0.86
1.482E-12	0.10	3E-07	1.55799	1.99	1.70	34.303	0.85
1.481E-12	0.10	3E-07	1.49929	2.09	1.80	32.316	0.86
1.480E-12	0.10	3E-07	1.51360	2.16	1.86	31.831	0.86
1.479E-12	0.10	3E-07	1.50744	2.26	1.92	30.749	0.85
1.478E-12	0.10	3E-07	1.55427	2.27	1.98	31.316	0.87
1.476E-12	0.10	3E-07	1.61890	2.31	2.01	31.819	0.87
1.474E-12	0.11	3E-07	1.75402	2.31	2.00	33.638	0.87
1.472E-12	0.11	3E-07	1.75622	2.39	2.09	32.838	0.87
1.469E-12	0.11	3E-07	1.65617	2.55	2.23	30.22	0.88
1.467E-12	0.11	3E-07	1.80374	2.51	2.21	32.348	0.88
1.464E-12	0.11	3E-07	1.80683	2.59	2.29	31.714	0.88
1.462E-12	0.11	3E-07	1.74768	2.71	2.40	30.032	0.89
1.459E-12	0.11	3E-07	1.79211	2.74	2.44	30.351	0.89
1.456E-12	0.12	3E-07	1.87891	2.76	2.46	31.193	0.89
1.454E-12	0.12	3E-07	1.94446	2.79	2.48	31.707	0.89
1.451E-12	0.12	3E-07	1.94780	2.88	2.53	31.044	0.88
1.449E-12	0.12	3E-07	1.84634	2.99	2.69	29.184	0.90
1.446E-12	0.11	3E-07	1.82864	3.07	2.77	28.415	0.90
1.443E-12	0.12	3E-07	1.91644	3.08	2.78	29.297	0.90
1.441E-12	0.12	3E-07	1.96146	3.12	2.81	29.512	0.90
1.437E-12	0.12	3E-07	1.90248	3.23	2.91	28.218	0.90
1.434E-12	0.12	3E-07	1.96954	3.22	2.92	28.95	0.91
1.431E-12	0.12	3E-07	1.93097	3.32	3.00	27.92	0.90
1.428E-12	0.11	3E-07	1.84980	3.41	3.11	26.538	0.91
1.426E-12	0.12	3E-07	1.87392	3.46	3.15	26.554	0.91
1.423E-12	0.11	3E-07	1.74927	3.59	3.28	24.511	0.91
1.420E-12	0.11	3E-07	1.85978	3.57	3.26	25.773	0.91
1.417E-12	0.12	3E-07	1.92728	3.57	3.24	26.444	0.91

6.3.2 Results and Discussion of Analysis

Presented in this section are the analysis results from the consolidation phase of five different triaxial tests, across the three triaxial systems utilized in the TAG Laboratory, with differing consolidation strain rates and different specimen geometries. Four of these tests were performed on RGoM-EI, and one test performed on RBBC is shown for comparison.

Figure 6-7 through to Figure 6-11 shows the predicted excess pore pressure generated at the centre of the specimen, $u_{e,c}$, versus the measured axial effective stress, σ'_a, for the five different tests. Figure 6-7 shows TX1548, a test with an initial height of 4.064 cm and a strain rate of 0.6 %/hr. There is a steady increase in $u_{e,c}$ with increasing σ'_a. The magnitude of excess $u_{e,c}$ is considerable at 1.52 MPa, which leads to a 20 % error in effective stress at the end of consolidation (Figure 6-12). Again, the error in effective stress is calculated using the average predicted excess pore pressure at the centre of the specimen, $^2/_3\, u_{e,c}$, and is defined by Equation 6-5. The magnitude of predicted excess pore pressure is generated due to the high strain rate of 0.6 %/hr. This is 10 times the standard laboratory strain rate for RGoM-EI and was performed to highlight the effect of strain rates on excess pore pressure. Figure 6-9 shows TX1566, a test with an initial height of 4.866 cm and a strain rate of 0.05 %/hr. This test is consolidated close to the same measured effective stress as TX1548 and has a larger initial height, but the strain rate is 12 times slower. The predicted excess pore pressure generated is 0.2 MPa at the centre of the sample, which amounts to a 3.3 % error in average effective stress (Figure 6-13).

Figure 6-7 shows the predicted excess pore pressure for TX1550, a high pressure test conducted on RGoM-EI at 0.02 %/hr with an initial height of 8.109 cm. Although the low strain rate, there is still considerable generation of predicted excess pore pressures at the centre of the specimen. This is due to the larger drainage height and the low permeabilities of

RGoM-EI. At 17 MPa, there is a 7.5% error in average effective stress in this specimen (Figure 6-14).

Figure 6-10 shows the predicted excess pore pressure generated at the centre of the specimen for TX1381, a low-pressure test performed on RGoM-EI at a strain rate of 0.15 %/hr and an initial height of 8.007 cm. There is significant pore pressure generation, causing a 13 % error in the average effective stress measured due to the high strain rate (Figure 6-15).

Figure 6-11 shows TX1031. This test was performed on RBBC, at a strain rate of 0.15 % per hour. The pore excess pressures generated at the centre of the specimen are minimal, with 0.07 MPa generated at a measured axial effective stress of 5.9 MPa causing a 0.8% error in effective stresses (Figure 6-16).

From Figure 6-7 to Figure 6-16, dependence of excess pore pressure generation on strain rate, drainage height and material properties can be deciphered. RBBC is shown to have minimal pore pressure generation, whereas RGoM-EI develops considerable excess pore pressures unless mitigated through a combination of the use of drainage hight reduction and low strain rates. The initial spike in average error at the early stages of the test is due to transient conditions, which come to steady state equilibrium.

Figures 6-17 to 6-21 show plots of void ratio, e, versus axial effective stress σ'_a. The compression curves for the measured data and the corrected data are plotted and compared to the average uniaxial compression behaviour models. For RGoM-EI, with the exception of Figure 6-19 showing data for TX1566, correcting the axial effective stress for excess pore pressure generation causes a significant shift in the compression curve to the left, resulting in the compression curve to be in better agreement with the average uniaxial compression model for RGoM-EI. TX1566 has minimal excess pore pressure generation due to its low consolidation strain rate and its reduced drainage height and is, therefore, in good agreement

with the average uniaxial compression curve to begin with. For RBBC, in Figure 6-21 we see no significant shift in the compression curve with the correction applied as there was minimal pore excess pore pressure generation.

Figures 6-22 to 6-26 show plots of at rest lateral stress ratio versus axial effective stress. These figures compare the measured K_0 with the corrected $K_{0,a}$. For RGoM-EI, there is a significant reduction in the corrected K_0 compared with the measured data. This reduction in K_0 is dependent on the strain rate and drainage height used, which is highlighted by TX1566 in Figure 6-24. This test has the lowest error in K_0 due to the reduced drainage height and low strain rate utilized over a lower stress range of 0 to 4 MPa. Figure 6-26 shows there is an insignificant impact of excess pore pressures on K_0 measured on RBBC with both measured and corrected data being almost indistinguishable.

The data presented shows that excess pore pressure generation has a considerable impact on RGoM-EI triaxial consolidation measurements whereas excess pore pressure generation in RBBC has negligible effects due to its larger hydraulic conductivity over the given stress range. Correcting for average excess pore pressures shift the compression curve to the left by lowering the axial effective stress for a given void ratio, providing better agreement with the average uniaxial compression curve for RGoM-EI, and showing that RGoM-EI should have a more ductile response to increasing stress in triaxial consolidation testing i.e. there should be more strain for a given axial effective stress. The generation of excess pore pressures in a specimen during consolidation could also lead to an overestimation of K_0 for RGoM-EI in past triaxial measurements. Figure 6-27 shows a plot of at rest lateral stress ratio versus the log of axial effective stress for a number of tests that have been corrected for the generation of excess pore pressure in the centre of the specimen. Figure 6-28 compares this corrected data to the power law fit provided by (Casey, 2014). The corrected data points plot markedly lower than Casey's fit.

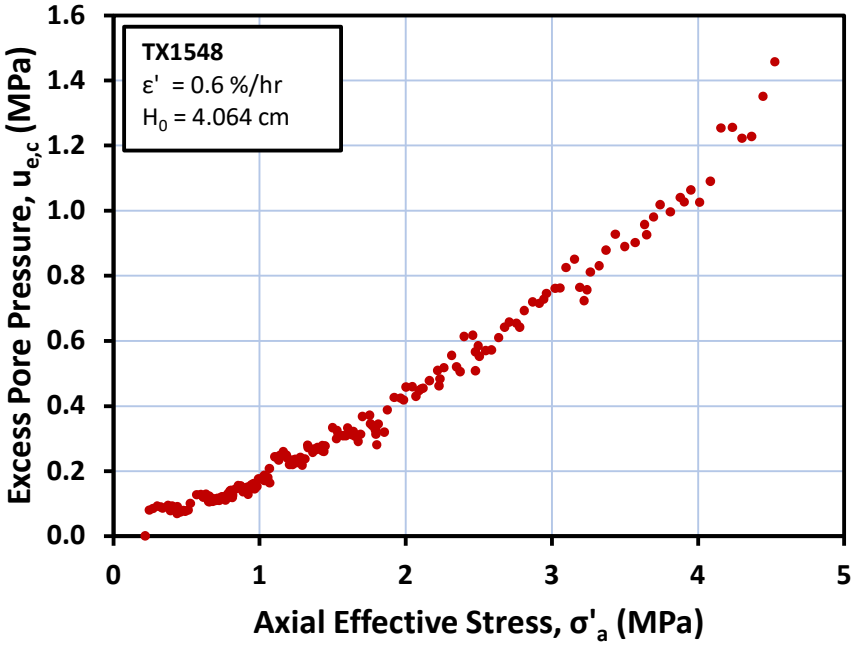

Figure 6-7 Predicted excess pore pressure at the centre of TX1548 specimen versus measured axial effective stress during the consolidation portion of a medium pressure test on RGoM-EI with specimen height of 4.064 cm and consolidation strain rate of 0.6 %/hr.

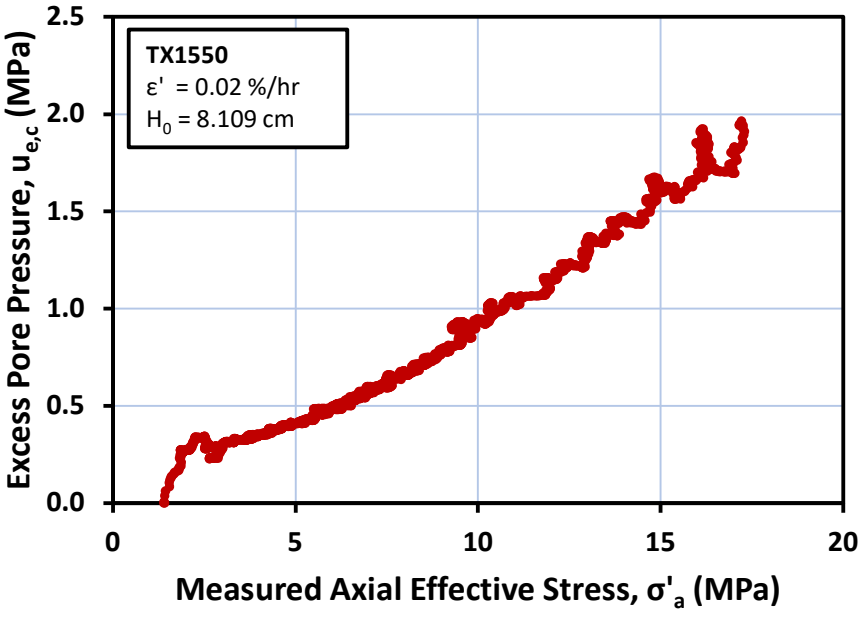

Figure 6-8 Predicted excess pore pressure at the centre of specimen TX1550 versus measured axial effective stress during the consolidation portion of a high pressure test on RGoM-EI with specimen height of 8.109 cm and consolidation strain rate of 0.02 %/hr.

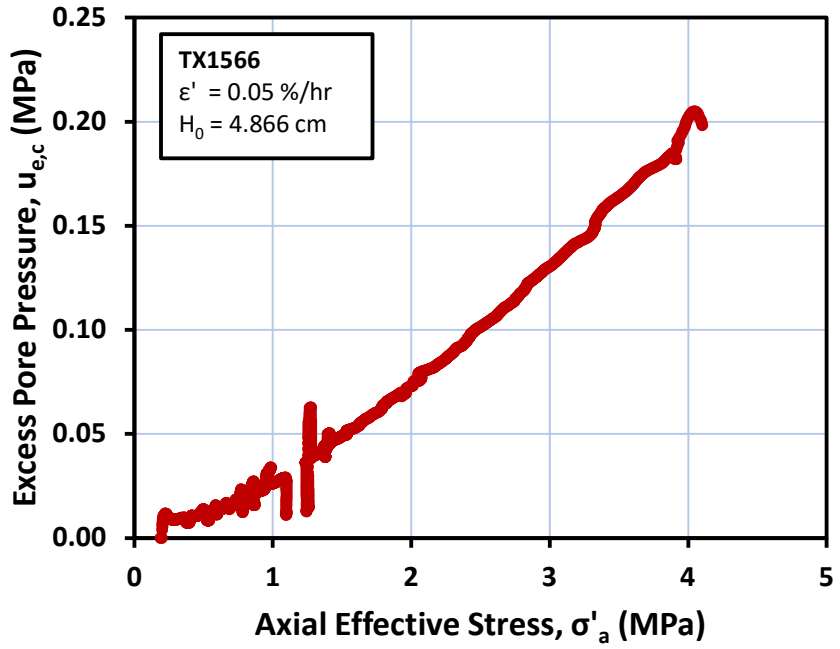

Figure 6-9 Predicted excess pore pressure at the centre of specimen TX1566 versus measured axial effective stress during the consolidation portion of a medium pressure test on RGoM-EI cubic specimen with height of 4.866 cm and consolidation strain rate of 0.05 %/hr.

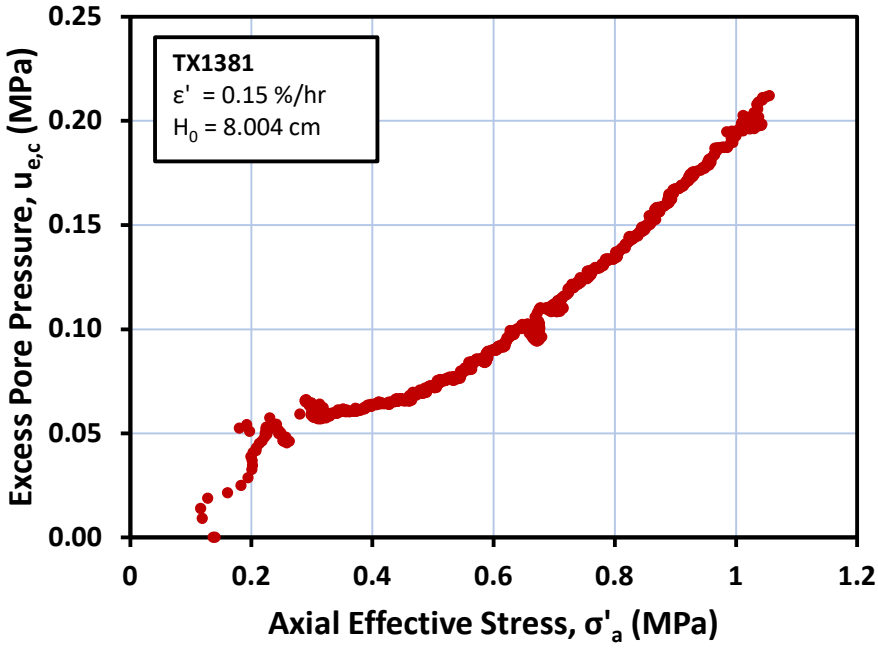

Figure 6-10 Predicted excess pore pressure at the centre of specimen TX1381 versus measured axial effective stress during the consolidation portion of a low pressure test on RGoM-EI with specimen height of 8.004 cm and consolidation strain rate of 0.15 %/hr.

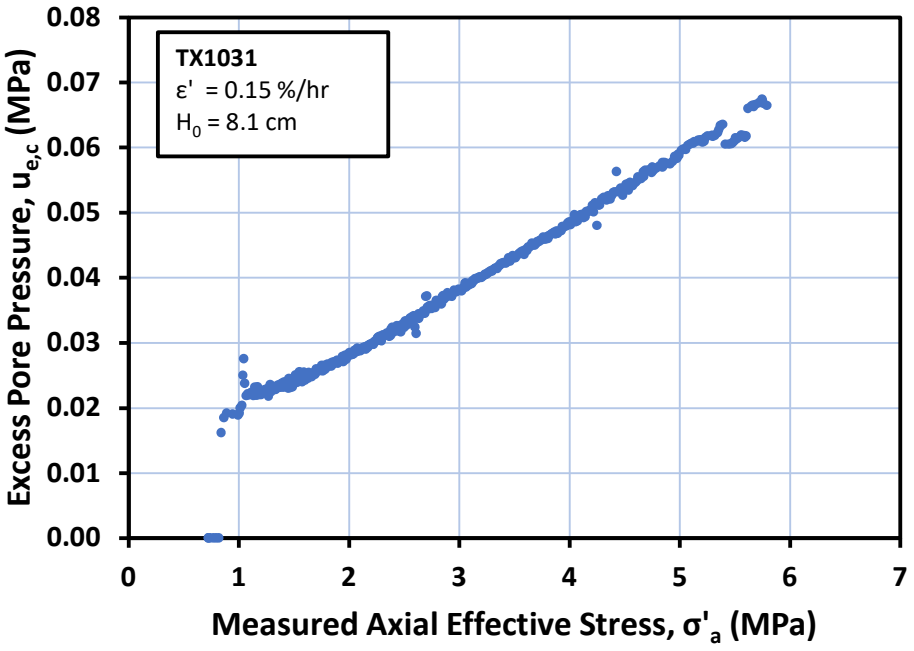

Figure 6-11 Predicted excess pore pressure at the centre of specimen TX1031 versus measured axial effective stress during the consolidation portion of a medium pressure test on RBBC with specimen height of 8.1 cm and consolidation strain rate of 0.15 %/hr.

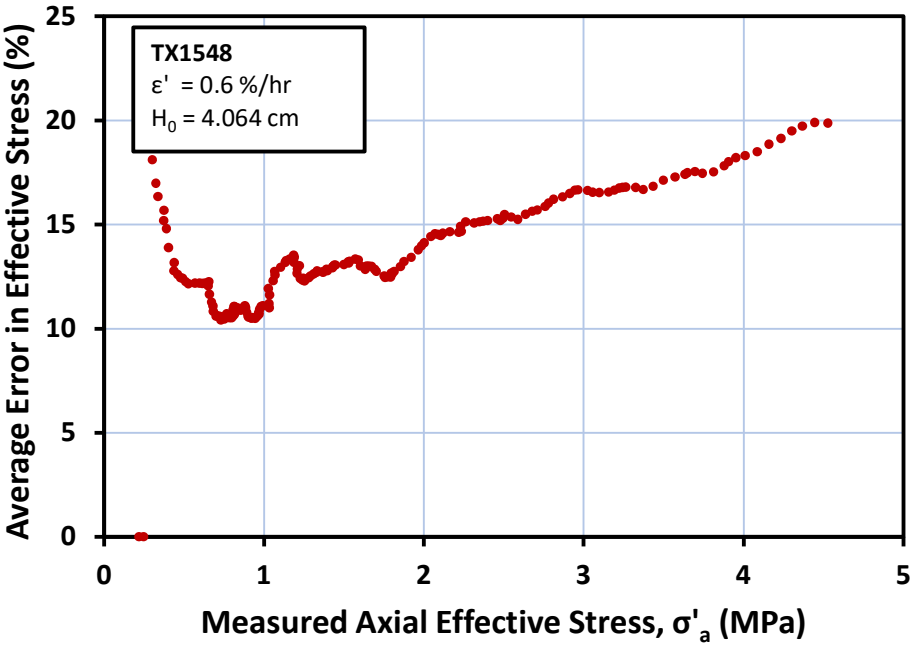

Figure 6-12 Average error in effective stress versus measured axial effective stress during the consolidation portion of RGoM-EI TX1548 with specimen height of 4.064 cm and consolidation strain rate of 0.6 %/hr.

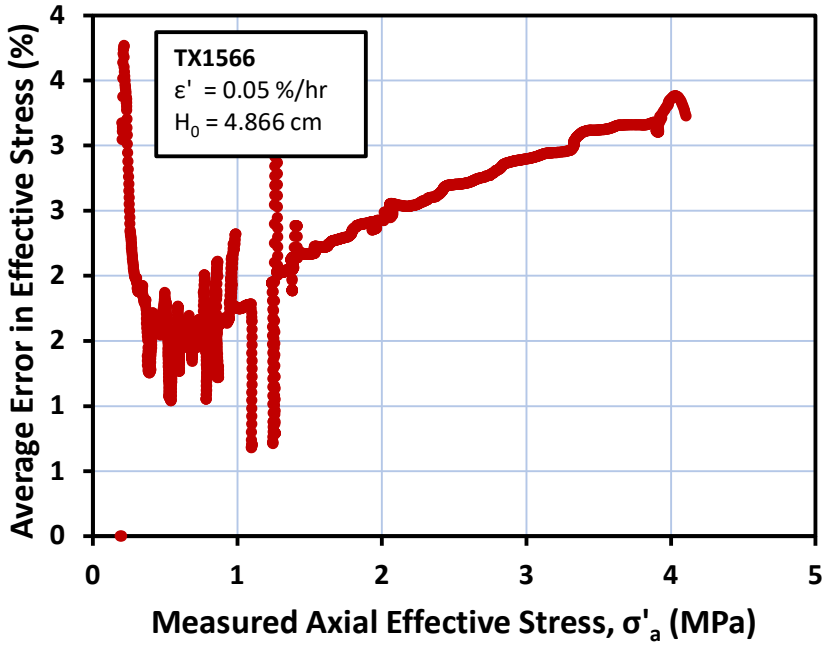

Figure 6-13 Average error in effective stress versus measured axial effective stress during the consolidation portion of on RGoM-EI TX1556 with specimen height of 4.866 cm and consolidation strain rate of 0.05 %/hr.

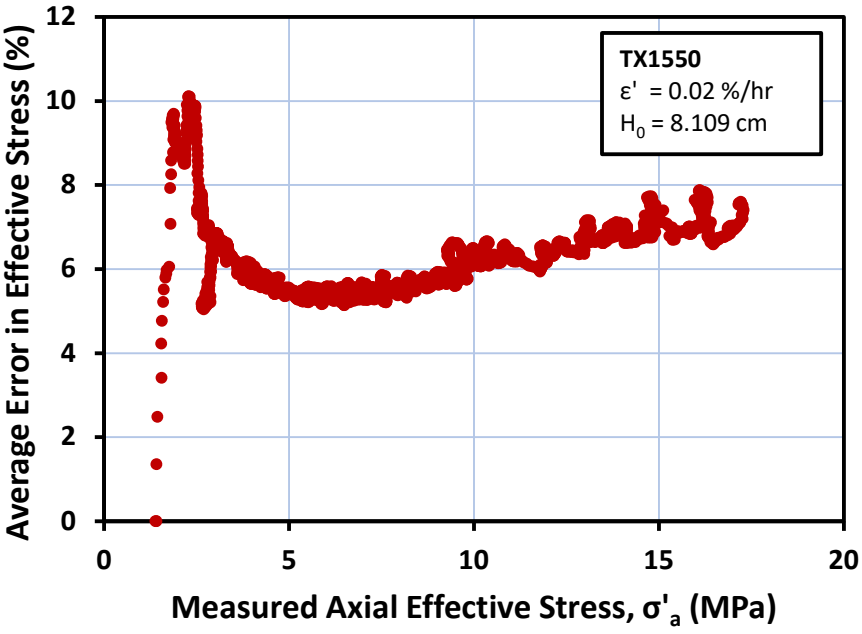

Figure 6-14 Average error in effective stress versus measured axial effective stress during the consolidation portion of RGoM-EI TX1550 with specimen height of 8.109 cm and consolidation strain rate of 0.02 %/hr.

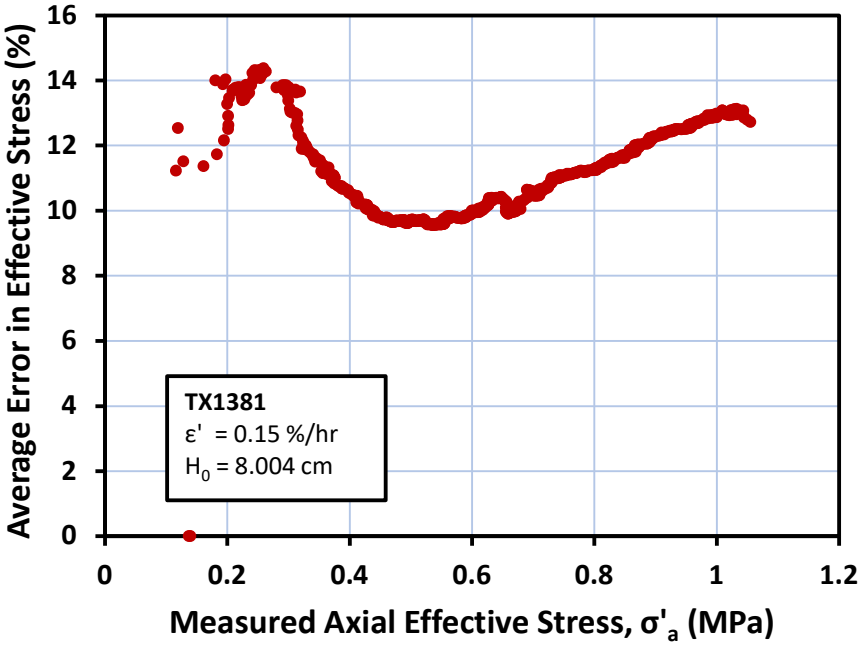

Figure 6-15 Average error in effective stress versus measured axial effective stress during the consolidation portion of RGoM-EI TX1381 with specimen height of 8.004 cm and consolidation strain rate of 0.15 %/hr.

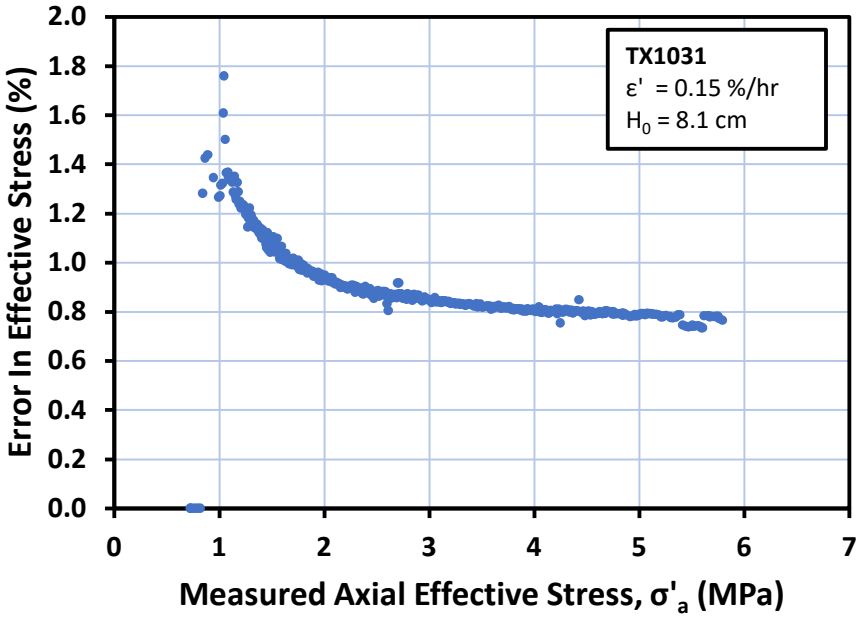

Figure 6-16 Average error in effective stress versus measured axial effective stress during the consolidation of RBBC TX1031 with specimen height of 8.1 cm and consolidation strain rate of 0.15 %/hr.

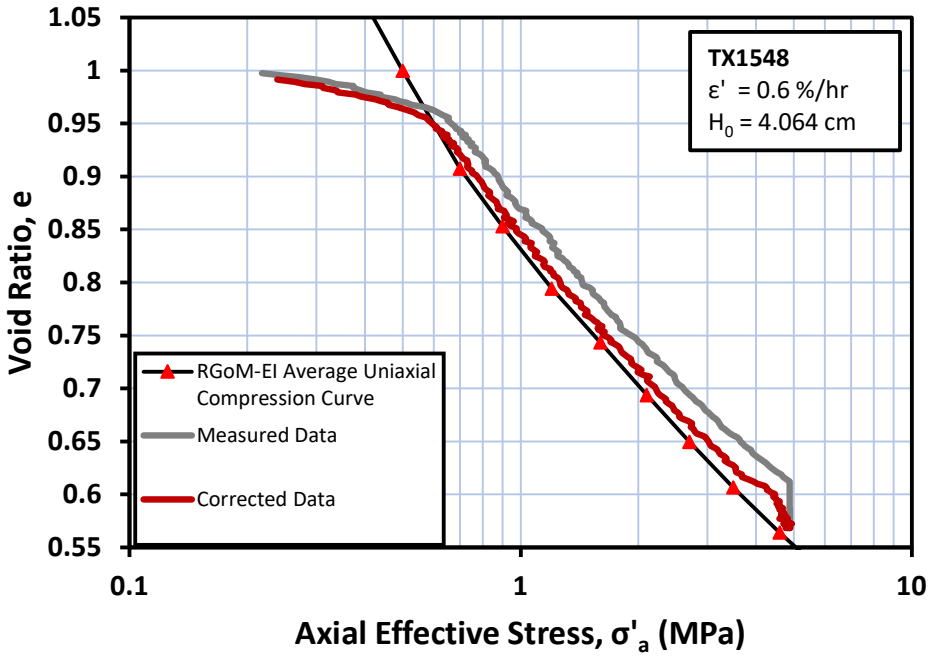

Figure 6-17 Plot of void ratio versus axial effective stress for measured data and corrected data from the K_0 consolidation portion of TX1548 with a strain rate of 0.6 %/hr compared to the RGoM-EI average uniaxial compression curve.

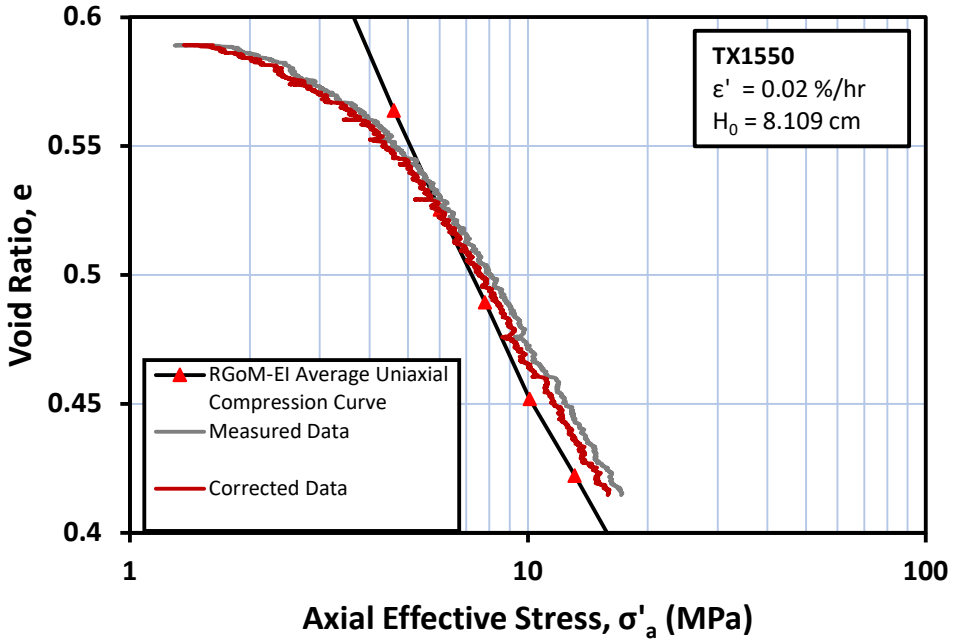

Figure 6-18 Plot of void ratio versus axial effective stress for measured data and corrected data from the K0 consolidation portion of TX1550 using a strain rate of 0.02 %/hr compared to the RGoM-EI average uniaxial compression curve.

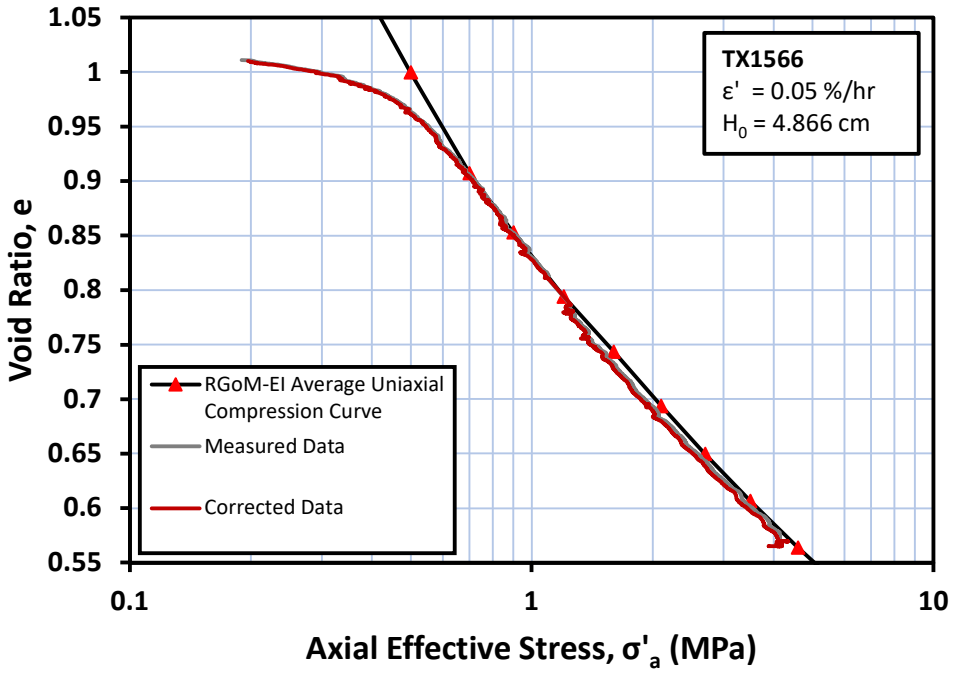

Figure 6-19 Plot of void ratio versus axial effective stress for measured data and corrected data from the K0 consolidation portion of a cubic TX1566 using a strain rate of 0.05%/hr compared to the RGoM-EI average uniaxial compression curve.

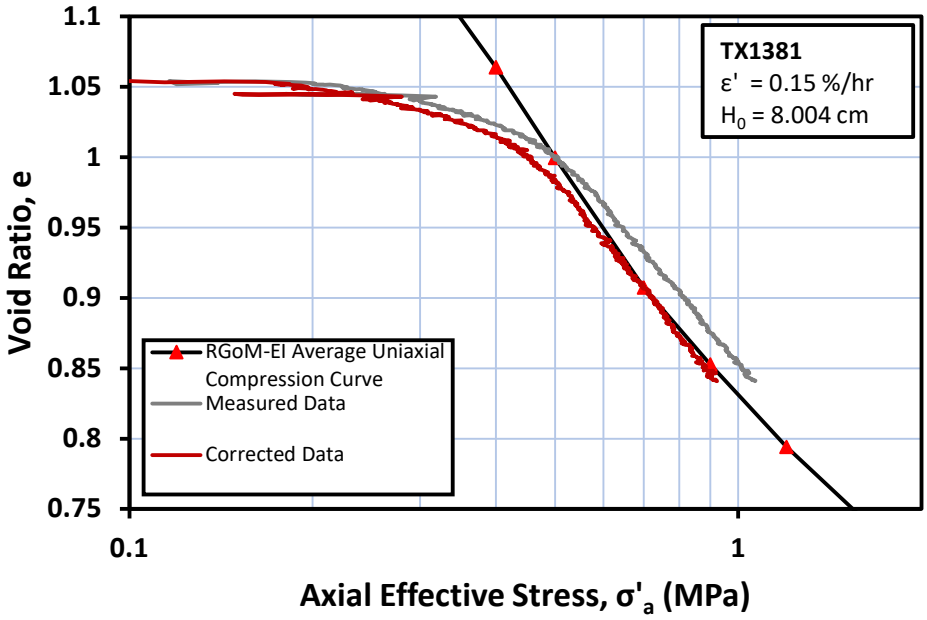

Figure 6-20 Plot of void ratio versus axial effective stress for measured data and corrected data from the K0 consolidation portion of TX1381 with a strain rate of 0.15 %/hr compared to the RGoM-EI average uniaxial compression curve.

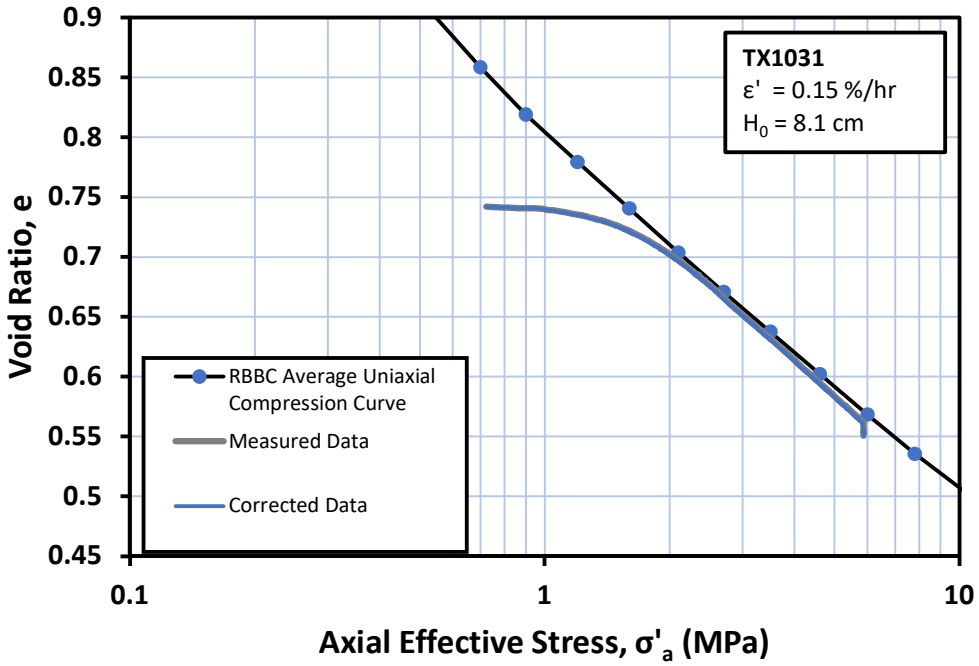

Figure 6-21 Plot of void ratio versus axial effective stress for measured data and corrected data from the K0 consolidation portion of TX1031 with a strain rate of 0.15 %/hr compared to the RBBC average uniaxial compression curve.

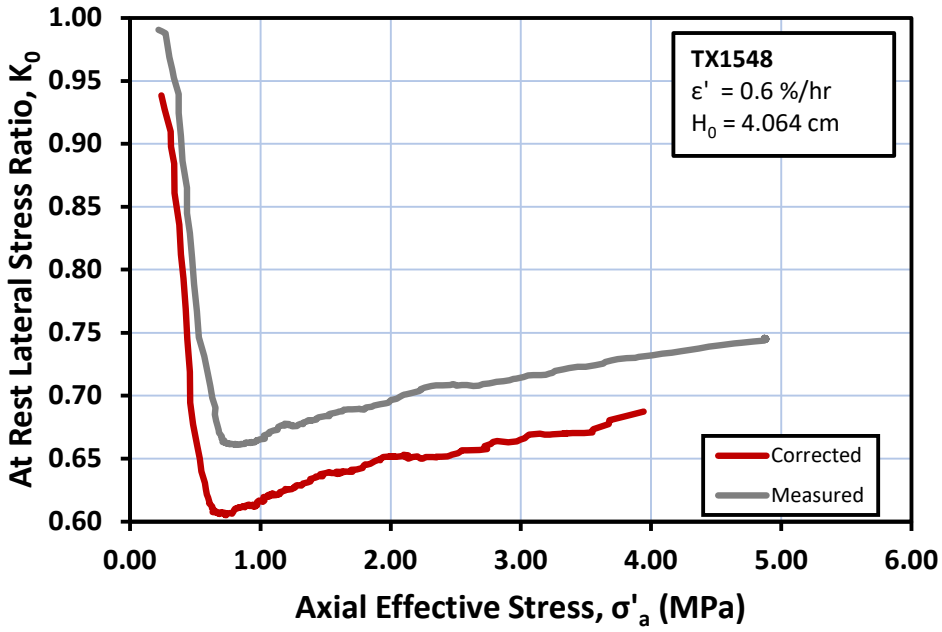

Figure 6-22 At rest lateral stress ratio, K_0, versus axial effective stress comparing the measured K_0 and the corrected $K_{0,a}$ for the consolidation stage of a RGoM-EI TX1548 using a strain rate of 0.6 %/hr.

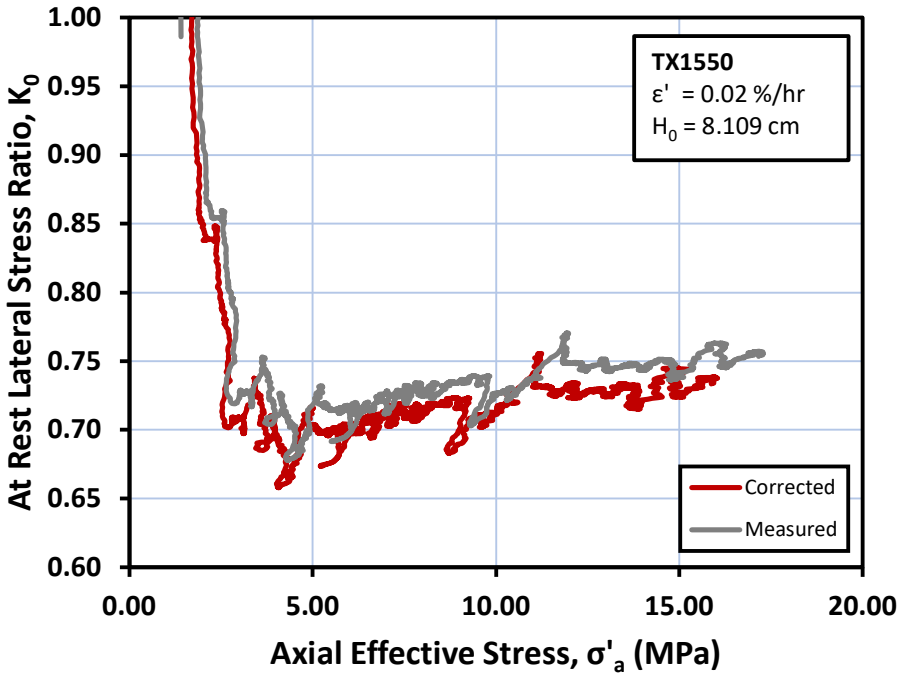

Figure 6-23At rest lateral stress ratio, K0, versus axial effective stress comparing the measured K0 and the corrected $K_{0,a}$ for the consolidation stage of a RGoM-EI TX1550 using a strain rate of 0.02 %/hr.

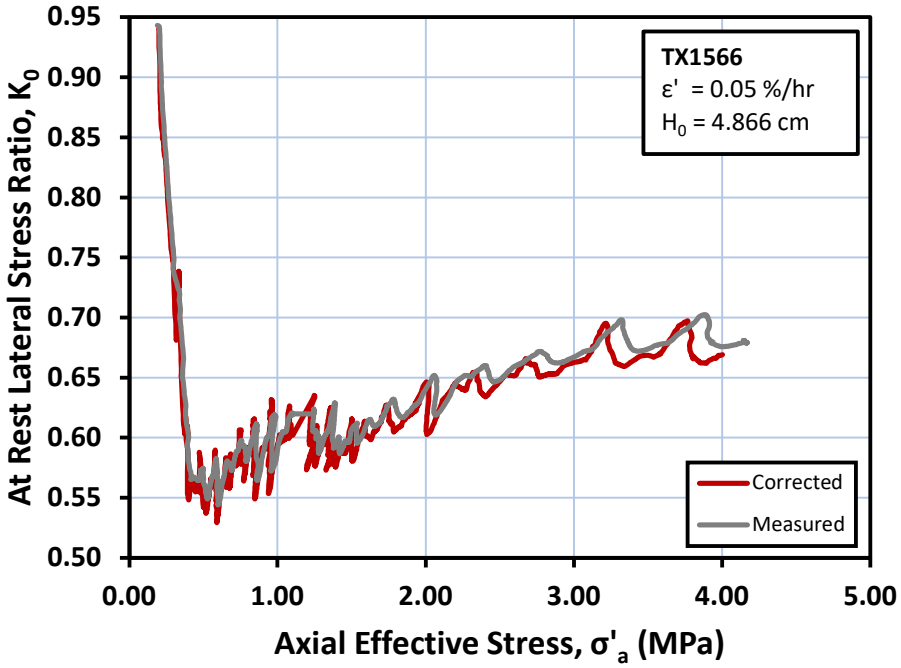

Figure 6-24 At rest lateral stress ratio, K0, versus axial effective stress comparing the measured K0 and the corrected $K_{0,a}$ for the consolidation stage of a RGoM-EI cubic TX1566 with a strain rate of 0.05 %/hr.

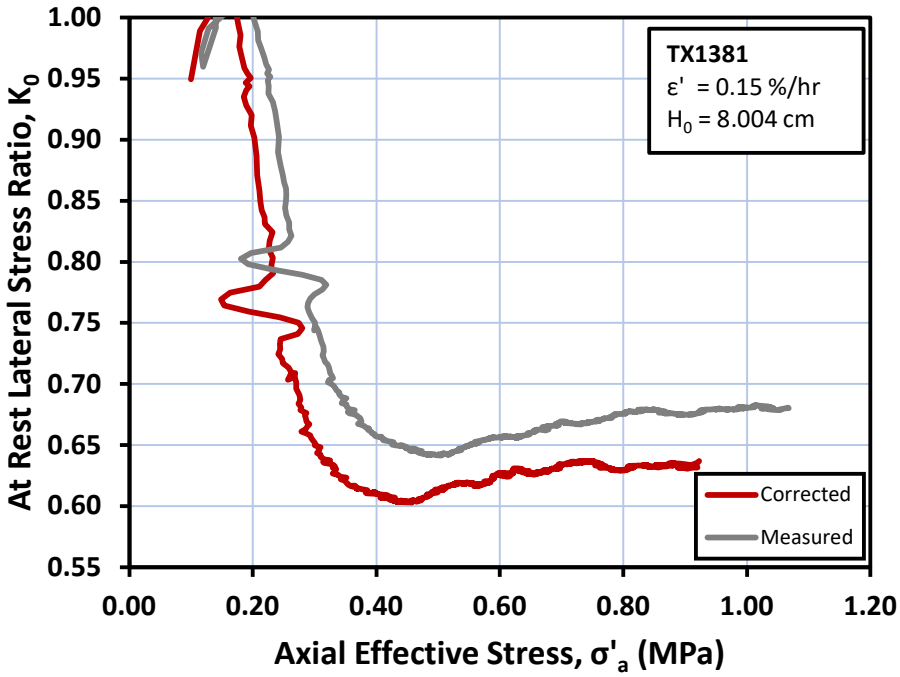

Figure 6-25 At rest lateral stress ratio, K0, versus axial effective stress comparing the measured K0 and the corrected $K_{0,a}$ for the consolidation stage of a RGoM-EI TX1381 with a strain rate of 0.15 %/hr.

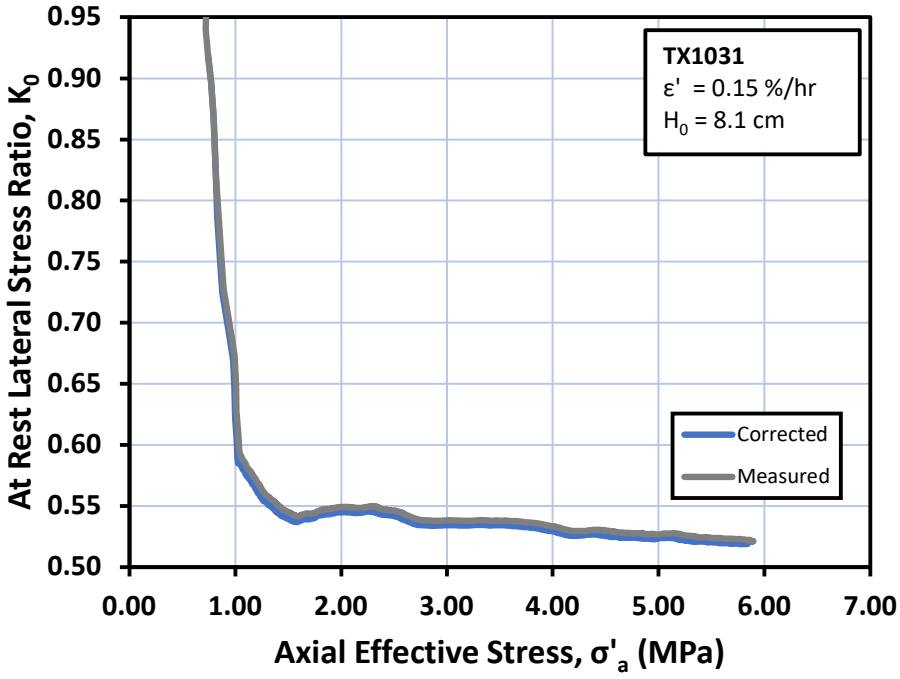

Figure 6-26 At rest lateral stress ratio, K0, versus axial effective stress comparing the measured K0 and the corrected $K_{0,a}$ for the consolidation stage of a RBBC TX1031 with a strain rate of 0.15 %/hr.

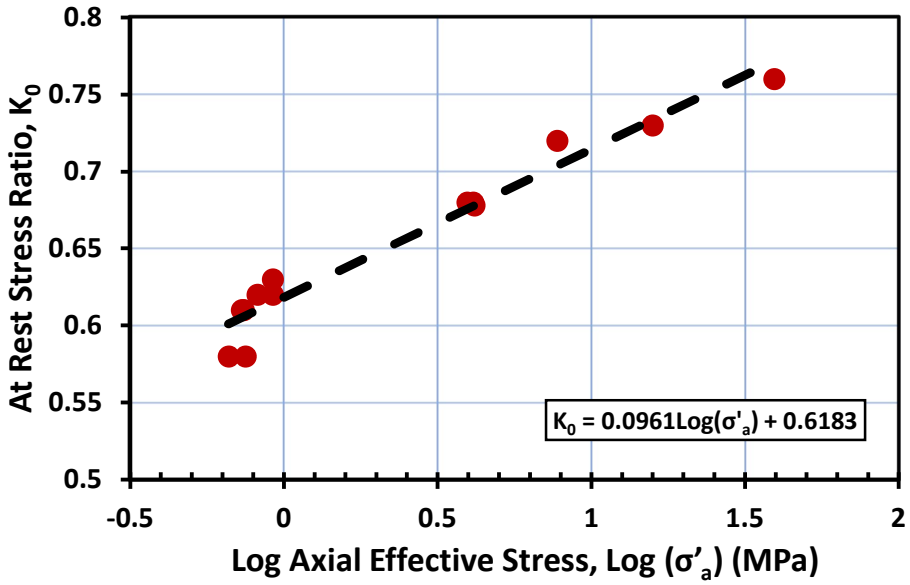

Figure 6-27 The corrected at rest vertical stress ratio versus log of the axial effective stress for various RGoM-EI tests corrected for excess pore pressure generated at the centre of the specimen.

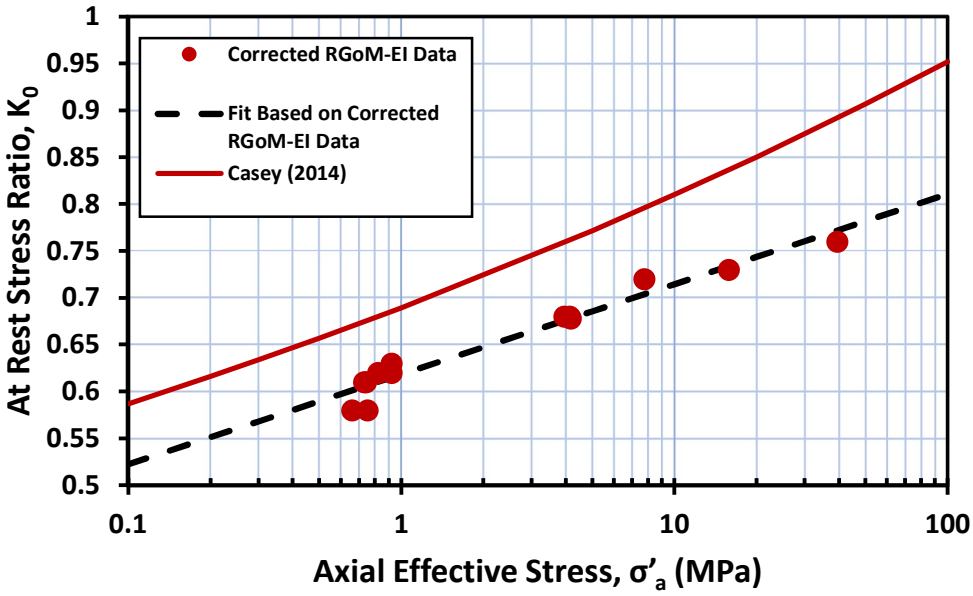

Figure 6-28 At rest stress ratio versus axial effective stress comparing data corrected for the generation of excess pore pressures and the previous fit for RGoM-EI provided by (Casey, 2014).

7 Numerical Modelling

7.1 Introduction

To further assess the effects of excess pore pressure generation in constant rate of strain triaxial K_0 consolidation and the efficacy of radial drainage and side drains, Finite Element Analysis (FEA) simulations were conducted for some individual tests. Abaqus FEA was the software utilized to perform the simulations. Abaqus FEA has the Modified Cam-Clay (MCC) constitutive model built into the software under its Clay Plasticity material sub-option. MCC is an elastoplastic critical state model developed by (Rosco and Burland, 1968). This chapter will first provide an overview of the MCC constitutive model, it will then cover the methodology using Abaqus to run the triaxial test simulation, and finally the simulation results will be discussed for a plane strain simulation using vertical drainage, axisymmetric models with vertical and radial drainage conditions and then a 3-dimensional simulation modelling a triaxial test using both vertical drainage and introducing radial drainage using geotextile side drains.

7.2 Modified Cam-Clay (MCC)

Modified Cam-Clay is an elastoplastic strain hardening model based on Critical State theory developed by (Schofield & Wroth, 1968). The model describes three aspects of soil behaviour: strength, volume change and the critical state at which soil elements experience unlimited distortion with no changes in stress or volume.

MCC was originally developed for triaxial loading conditions and the model is based on the following characteristics (Potts & Zdravkovic, 1999):

- In *v-ln p'* space (where *v* = specific volume = *1 + e* and *p'* = mean effective stress = $(\sigma'_1 + \sigma'_2 + \sigma'_3)/3$), a clay element under slow drained isotropic compression moves

along the virgin compression line (normal compression line) on first loading (plastic deformation). If unloaded, the element will travel along the swelling lines (unload-reload lines) (elastic deformation). When reloaded, the element will travel along the swelling line until the point of intersection with the virgin compression line where the element will travel again along the virgin compression line (Figure 7-1). These lines are assumed linear in *v-ln p'* space. The equation for the virgin compression line is described in Eq. 7-1 and the equation for the swelling line is described in Eq. 7-2:

$$v = N - \lambda(ln\, p') \qquad \textit{(Eq. 7-1)}$$

$$v = v_{s,m} - \kappa(ln\, p') \qquad \textit{(Eq. 7-2)}$$

N = Specific volume of virgin compression line at unit pressure (ln p' = 1)

$v_{s,m}$ = Specific volume of swelling lines at unit pressure (ln p' = 1), where the specific volume is dependent on the maximum past pressure

λ = Slope of the virgin compression line

κ = slope of the swelling lines

- The critical state line (CSL) is a state a soil reaches after sustained shearing where further shearing can occur with no changes in stress or volume. In *v – ln p'* space, the CSL is parallel to the virgin compression line (VCL) and lies below it (Figure 7-2). Both CSL and VCL are related through the following equation:

$$\Gamma = N - (\lambda - \kappa)\, ln\, 2 \qquad \textit{(Eq. 7-3)}$$

Γ = Specific volume of critical state line at unit pressure (*ln p'* = 1)

In *p' – q* space (where $q = \sigma_1 - \sigma_3$), the critical state line has a slope of *M*, where *M* is defined as:

$$M = \frac{6sin\varphi'_{cs}}{3 - sin\varphi'_{cs}} \quad \textit{(Eq. 7-4)}$$

φ'_{cs} = Effective critical state friction angle

Figure 7-3 shows the relationship between the CSL and MCC elliptical yield surface in $p' - q$ space. The CSL line intersects the yield surface at co-vertex of the yield surface ellipse i.e., the point of maximum shear stress, q.

- The yield surface is the intersection point between the virgin consolidation line (plastic deformation) and the swelling line. The value of mean stress at this intersection is the mean maximum past pressure or mean preconsolidation stress, p'_0. This parameter, p'_0, essentially controls the size of the yield surface. The yield surface in MCC is represented using the following equation:

$$F = \frac{q^2}{M^2} + p'\left(p' - p'_0\right) = 0 \quad \textit{(Eq. 7-5)}$$

- Plastic strain hardening/softening is isotropic and is controlled by p'_0.
- The plastic strain increment vector is normal to the yield surface and therefore MCC is an associated model.
- Behaviour along the swelling line is elastic and the elastic bulk modulus can be described, K, can be described as:

$$K = \frac{vp'}{\kappa} \quad \textit{(Eq. 7-6)}$$

There are limitations to the MCC model, namely the fact that the model assumes that the effective friction angle and the slope of the virgin compression line are constant, therefore

predicting constant values of lateral stress ratio. Modifications have been made to the MCC model to account for the changes in VCL and φ'_{cs} over large stress ranges (Heidari et al., 2020). For the purpose of this study, namely examining the effects of excess pore pressure generation in a specimen during constant rate of strain K_0 consolidation, and that the stress ranges of tests that were modelled are not significantly large, the unmodified version of MCC that is available in the Abaqus FEA software was deemed suitable by the author.

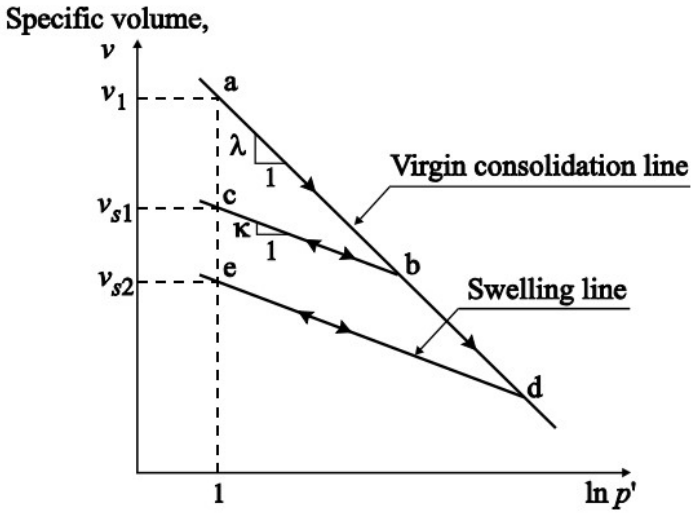

Figure 7-1 Behaviour of soils under isotropic compression using the MCC framework (Potts & Zdravkovic, 1999).

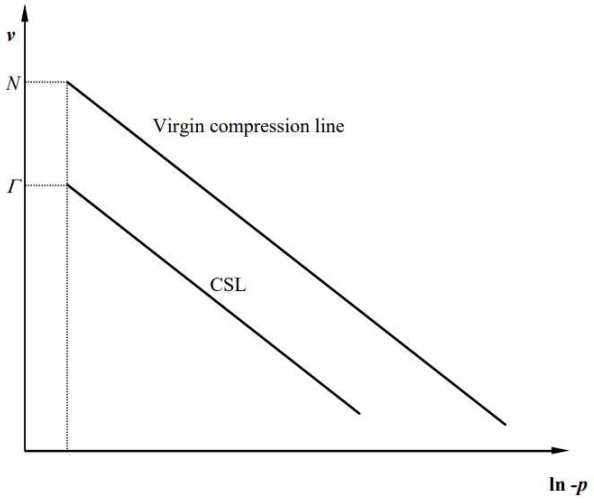

Figure 7-2 Position of the critical state line in relation to the virgin compression line in v - ln p' space

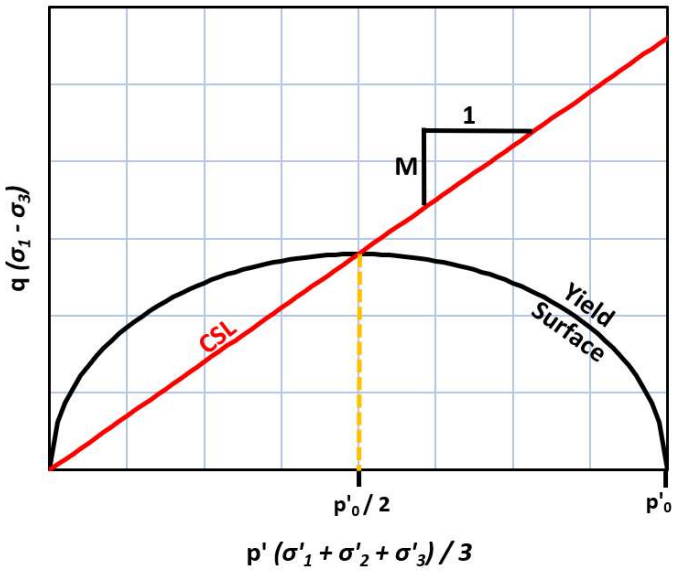

Figure 7-3 Modified Cam-Clay yield surface and critical state line shown in p' - q space.

7.3 Methodology

Abaqus FEA's clay plasticity model was utilized to generate simulations used in this analysis. This model is an extension of the MCC model developed by (Roscoe & Burland, 1968). The MCC model was explained in the previous section. Each simulation was run as a coupled pore fluid diffusion and stress transient analysis. This analysis allows a fully saturated medium to be modelled. The simulations ran were in terms of excess pore pressure. This means that all stresses are the effective stresses seen in the experimental test, and that the "back pressure" in the model is zero. Abaqus uses the effective stress principle for porous media, that considers the medium as a multiphase material. This section will cover how the MCC model was implemented in the Abaqus FEA software.

TX1566 performed on RGoM-EI was used to validate the model. For this validation, the material had been defined for porous elastic, clay plasticity, and permeability. This test was chosen due to the minimal generation of excess pore pressures that was found during the analysis described in Chapter 6. From this test, the mean effective stress was plotted against

void ratio for both the recompression and normally consolidated portions of the test (Figures 7-5 & 7-6). A trendline was fitted to each portion of data and the slope of these were used as the λ and κ parameters for all models. The slope of the critical state line, M, was calculated using Eq. 7-4. The effective critical state friction angle, φ'_{cs}, was calculated using the relationship developed by (Casey, 2014) for RGoM-EI (Figure 7-7):

$$\varphi'_{cs} = 21.98{\sigma'_p}^{-0.1387} \qquad \textit{(Eq. 7-7)}$$

Hydraulic conductivity versus void ratio relationships were inputted into the permeability material section based on the TAG Laboratory average vertical hydraulic conductivity calculated from CRS testing, and the radial hydraulic conductivity calculated from CRS testing by (Nordquist, 2015). Abaqus uses Forchheimer's Law, a form of Darcy's Law that accounts for viscous and inertial effects, to relate change in flow volume to pore pressure. Table 7-1 shows some of the parameters used in all simulations presented. The Poisson ratio value was calculated based on the following equation (Lambe and Whitman, 1969) using an assumed average $K_0 = 0.65$:

$$K_0 = \frac{\mu}{1-\mu} \qquad \textit{(Eq. 7-8)}$$

Table 7-1 Summary of parameters used across all simulations.

MCC Input Parameters for RGoM-EI	
Parameter Description	**Value**
Poisson's Ratio (**μ**)	0.35
Slope of Virgin Compression Line (**λ**)	0.176
Slope of Recompression Line (**κ**)	0.055

The plane strain simulation of TX1566 was used to validate the model. It was run at the same strain rate as the experimental test, 0.05 %/hr. Once the simulation of TX1566 was performed and results compared to the test data to confirm that the results were satisfactory, the MCC input parameters used in the simulation of TX1566 were used to simulate TX1548 using an axisymmetric model. This test was run at 0.6 %/hr and developed significant excess pore pressures based on the analysis presented in Chapter 6. A simulation was then conducted to see what changes would be seen if TX1548 was only allowed to drain radially. Finally, a 3-dimensional flow model was used to simulate the use of both side drains and end drainage on a test specimen with a strain rate of 0.6 %/hr. In this simulation, the Terrafix® 360R geotextile was modelled as perfectly plastic, using material compression and permeability data presented in Chapter 5. The simulation can be used to quantify the amount of fluid squeezed from the side drain material; however, these volumes were neglected from the calculations and reduction of simulation data. The model was allowed to drain both vertically, through the top and bottom drainage boundaries, and radially through the side drains. Figure 7-4 gives a general description of the boundary conditions applied to the models. In order to simulate K_0 conditions, the sides of each model were fixed in the x-direction and allowed to move freely in the y-direction. The bottom of the model was fixed in both x-direction and y-direction. A displacement was then applied in a linear ramp over a fixed time frame to the top surface of the model to simulate compression at a specified rate of strain. Depending on the simulation, either the top and bottom or radial perimeter surfaces of the model could be permitted to drain pore pressure.

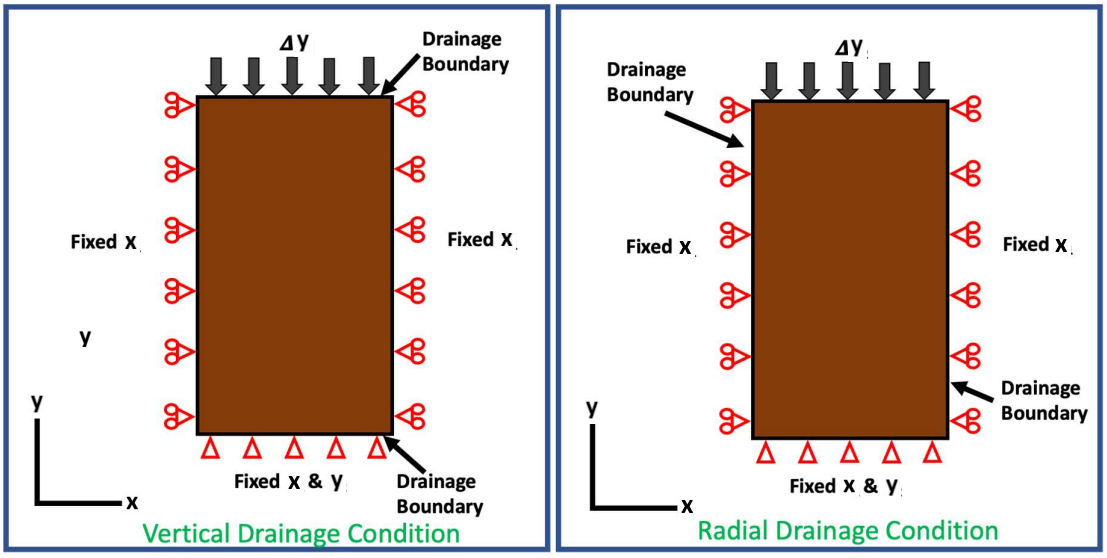

Figure 7-4 Diagrams of Abaqus FEA boundary conditions used in the simulations.

After the simulation, stresses and strains were taken from nodal points on the model and exported to a .csv file. From there, the data were processed and averaged in a MATLAB script. A step-by-step description of how the boundary conditions, loads and material definitions are presented in Appendix A, please refer to this for further information on the modelling details used within this thesis.

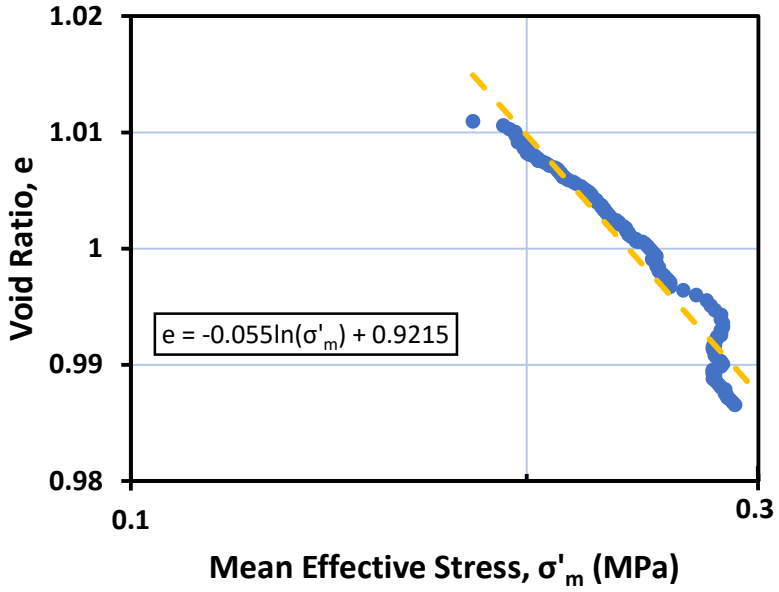

Figure 7-5 Void ratio versus mean effective stress showing the reloading portion of TX1566. The slope of the trendline used to fit the data was used as the κ parameter in Abaqus.

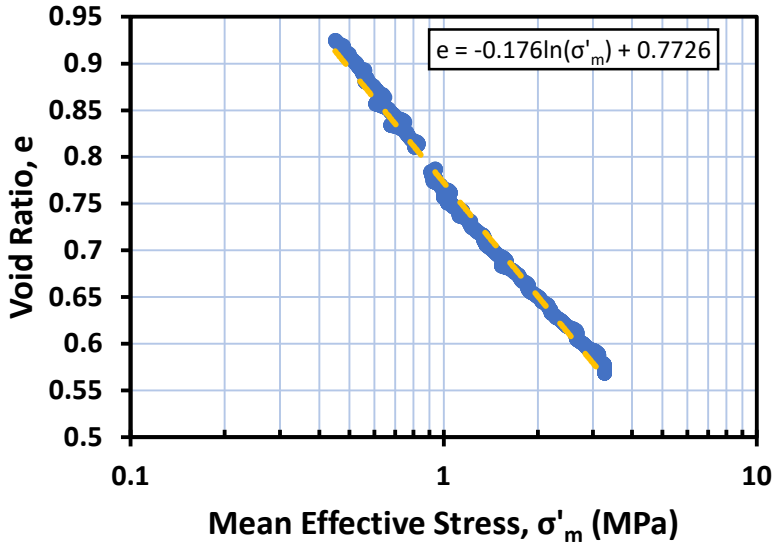

Figure 7-6 Void ratio versus mean effective stress showing the normally consolidated portion of TX1566. The slope of the trendline used to fit the data was used as the λ parameter in Abaqus.

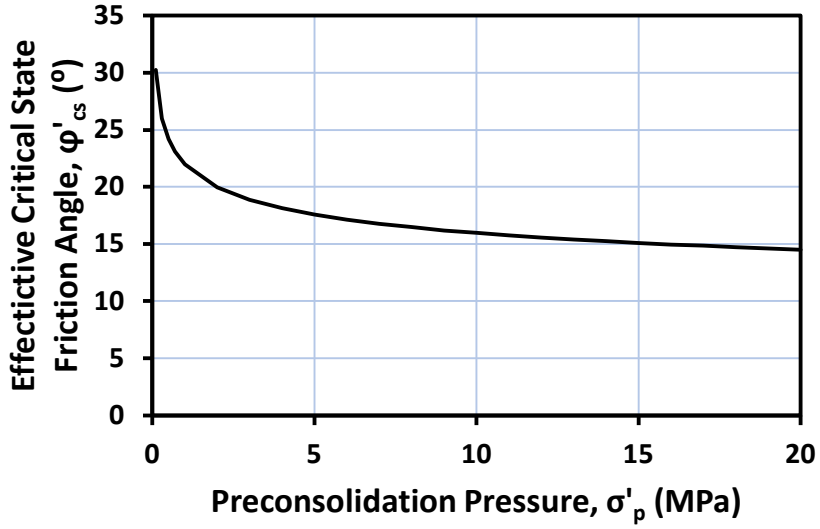

Figure 7-7 Effective critical state friction angle versus preconsolidation stress for RGoM-EI (adapted from Casey, 2014).

7.4 Simulation Results and Discussion

7.4.1 Plane Strain Model Vertical Drainage Conditions (TX1566)

A plane strain model was used to simulate TX1566 as this test was on a cubic specimen. This simulation was used to validate all other models. Vertical effective stress and pore pressure distributions are shown in Figures 7-8 and 7-9. Figure 7-9 shows that the model has a minimum excess pore pressure at the drainage boundaries, and a maximum at the centre of the model, this agrees with the assumption of a parabolic distribution of pore pressures within the sample (Figure 7-10). Figure 7-11 shows a comparison of the excess pore pressures generated at the centre of the specimen calculated using the (Wissa et al., 1971) linear equation and generated in the simulation. Both the simulation and the calculated values agree extremely well. A comparison of TX1566 measured data, corrected data, simulation results for both total stress and effective stress analysis and the average uniaxial compression curve for RGoM-EI is shown in Figure 7-12. Both the total stress (not accounting for excess pore pressure generation) and effective stress simulation results agree well with the measured,

corrected, and uniaxial curve. This confirms at the very least that the model is well calibrated to the test data. There is minimal shift in compression curve between the total and effective stress values, showing the small errors in effective stresses present due to low generation of excess pore pressure in the model.

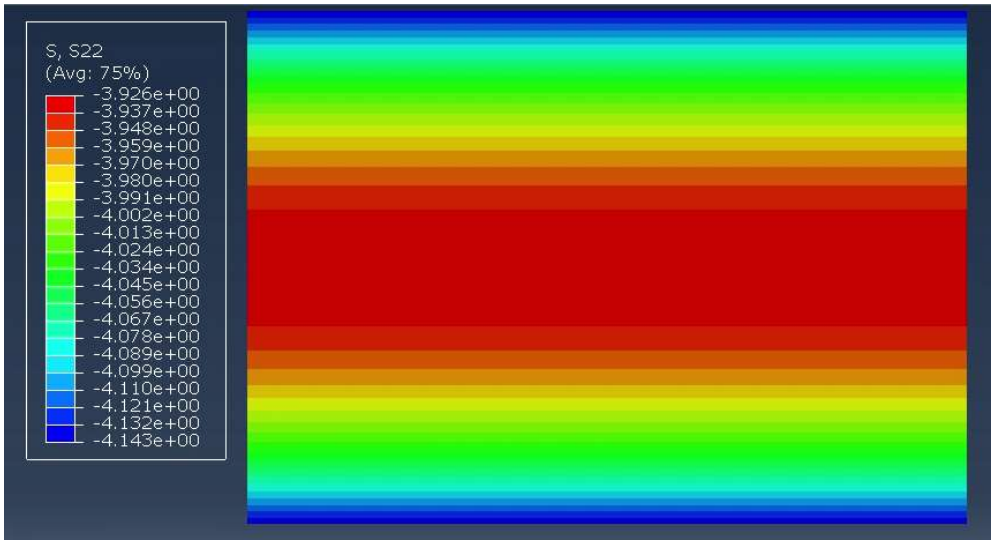

Figure 7-8 Vertical effective stress distribution at the end of simulated consolidation of TX1566. (Values of stress in the key are in MPa)

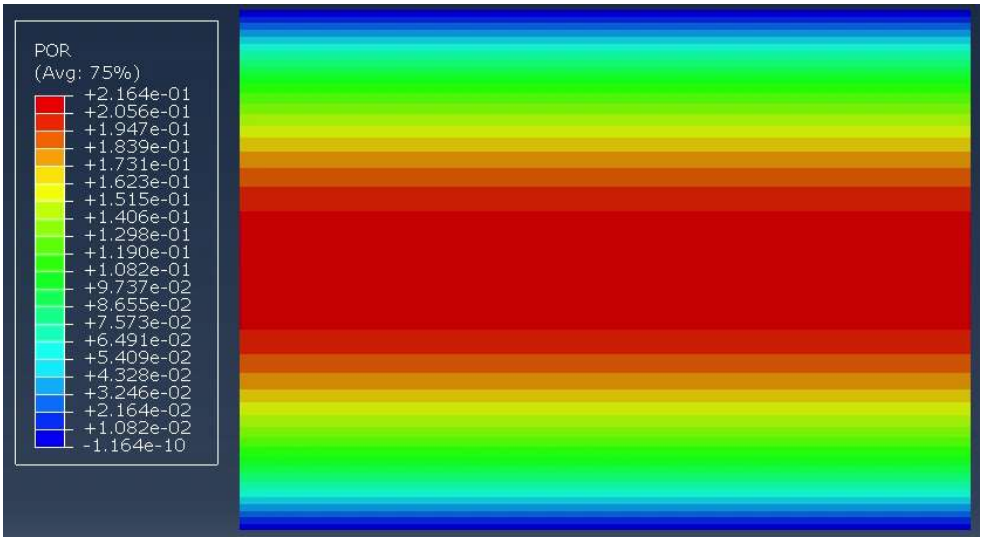

Figure 7-9 Excess pore pressure distribution at the end of simulated consolidation of TX1566. Values of stress in the key are in MPa)

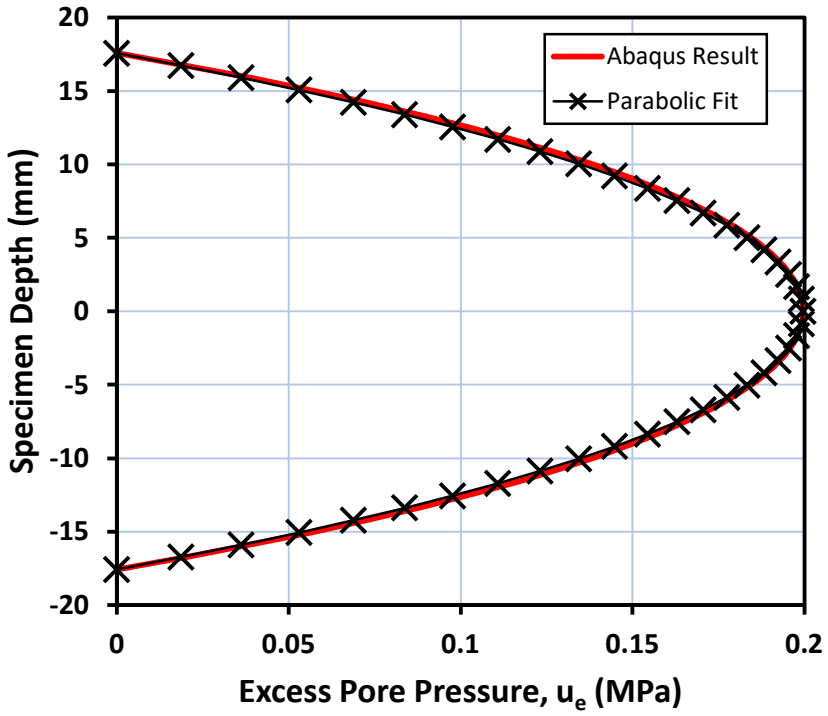

Figure 7-10 Plot of excess pore pressure versus specimen depth, comparing Abaqus results to a parabolic curve fit. Data taken from an individual simulation time-step.

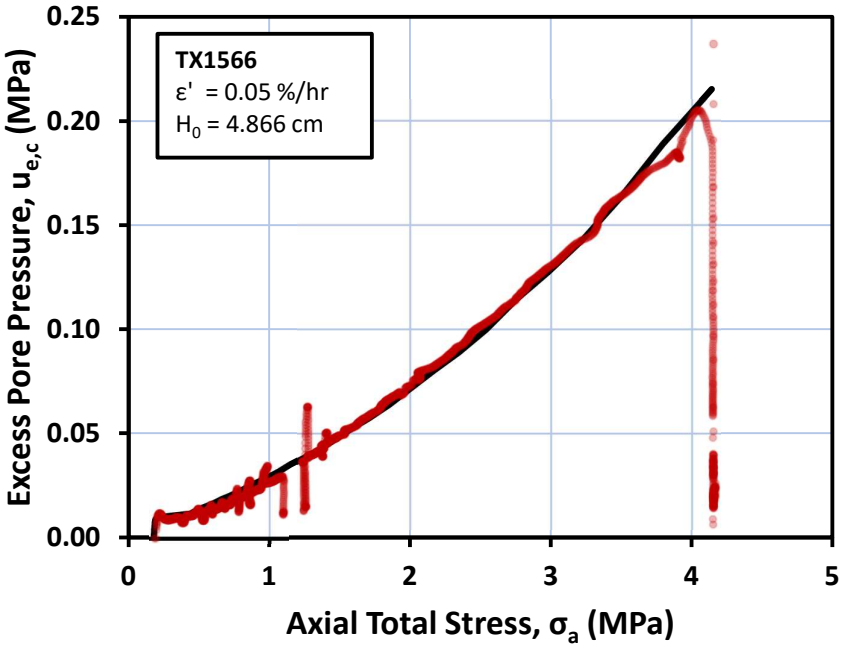

Figure 7-11 Plot of excess pore pressure versus measured axial effective stress comparing the excess pore pressures generation analysed using (Wissa et al., 1971) linear theory and the Abaqus simulation for TX1566.

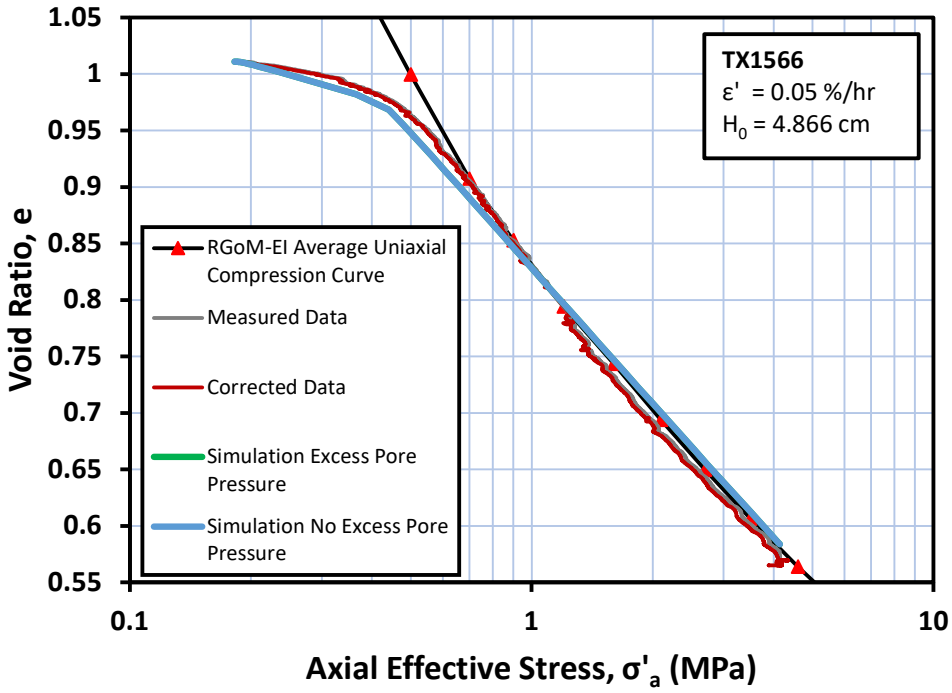

Figure 7-12 Void ratio versus axial effective stress, comparing measured data, corrected data, and simulation results of TX1566 against the average uniaxial compression curve for RGoM-EI.

7.4.2 Axisymmetric Model Vertical Drainage Conditions (TX1548)

The axisymmetric simulation of TX1548, run with a strain rate of 0.6 %/hr shows far greater generation of excess pore pressures in the model. Figures 7-13 and 7-14 show the vertical effective stress and pore pressure distributions respectively. Figure 7-15 shows that the simulation perfectly captures the generation in excess pore pressure calculated using the (Wissa et al., 1971) linear theory. When comparing the total and effective stress simulation result compression curves (Figure 7-16), the total stress analysis results (not accounting for excess pore pressure generation) agrees well with the TX1548 measured compression data. There is some curvature in the compression curve that the simulation does not capture using the trendline fit slope of the virgin compression line, λ. The effective stress analysis (accounting for excess pore pressure generation) corresponds well to the compression curve corrected for excess pore pressure generation.

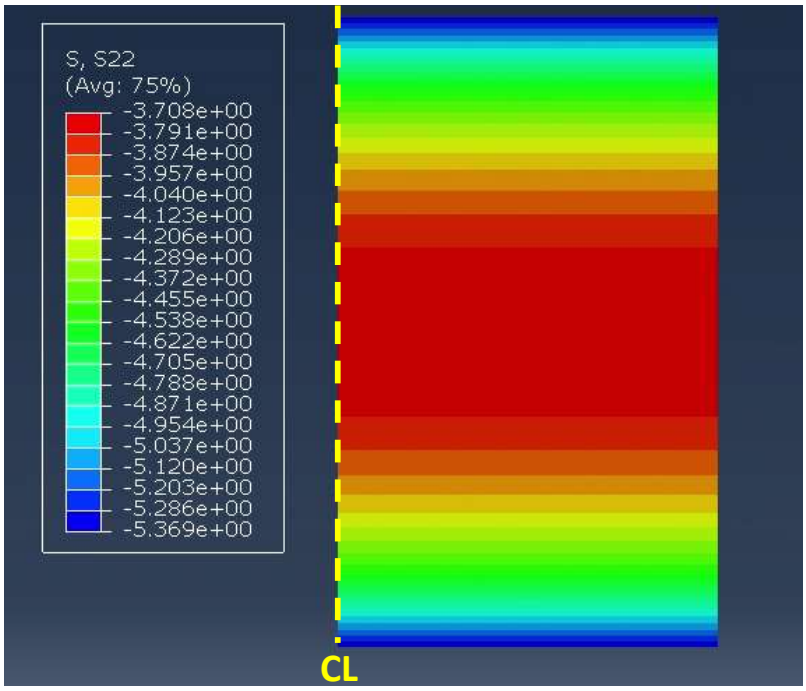

Figure 7-13 Vertical effective stress distribution at the end of simulated consolidation of TX1548. (Values of stress in the key are in MPa)

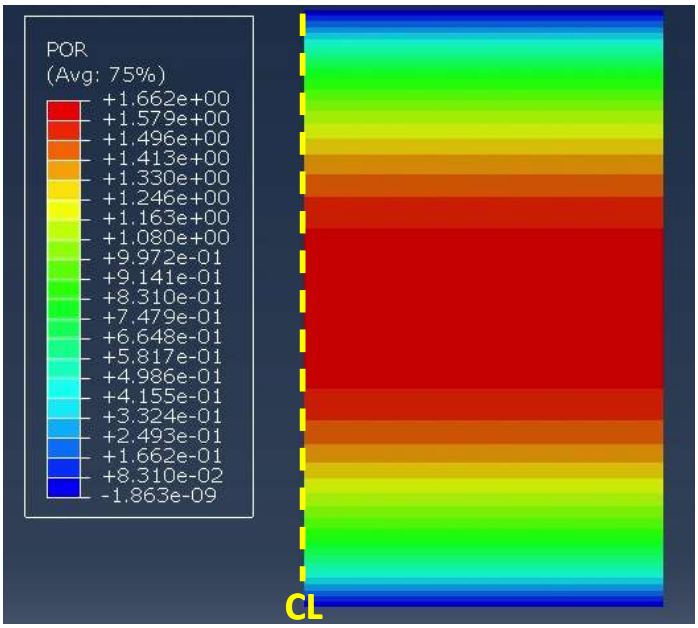

Figure 7-14 Excess pore pressure distribution at the end of simulated consolidation of TX1548. (Values of stress in the key are in MPa)

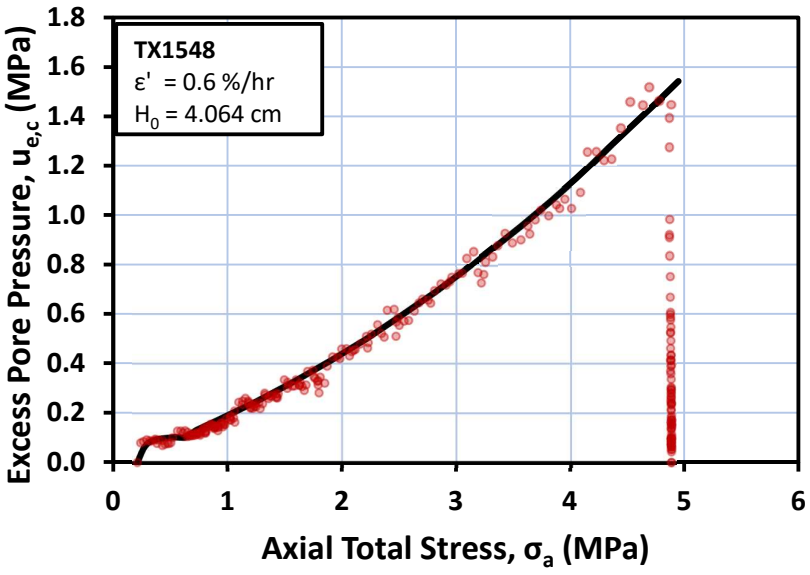

Figure 7-15 Plot of excess pore pressure versus measured axial effective stress comparing the excess pore pressures generation analysed using (Wissa et al., 1971) linear theory and the Abaqus simulation for TX1548.

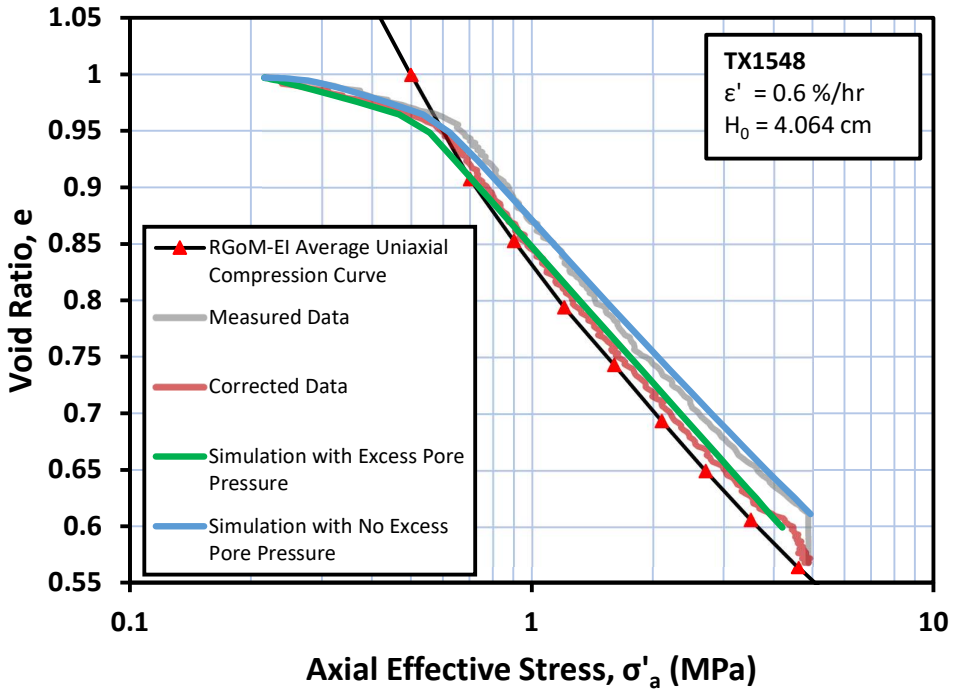

Figure 7-16 Void ratio versus axial effective stress, comparing measured data, corrected data, and simulation results of TX1548 against the average uniaxial compression curve for RGoM-EI.

7.4.3 Axisymmetric Model Radial Drainage Conditions

By allowing the simulation of TX1548, run at 0.6 %/hr, to drain only radially as opposed to only vertically, the vertical effective stress and pore pressures distributions change substantially (Figure 7-17 and 7-18). There is a maximum excess pore pressure along the vertical centreline of the model, decreasing to a minimum along the drainage boundary. Figure 7-19 gives a comparison of the excess pore pressures experienced during the simulation with radial drainage versus vertical drainage. Radial drainage shows a reduction in excess pore pressure at the centre of the specimen, with the magnitude almost four times less than in the vertical drainage scenario. This reduction in excess pore pressures is due to the reduction in drainage height (the specimen is draining radially, H_d is 1.75 cm) and the fact that the radial hydraulic conductivity is higher than the vertical hydraulic conductivity. Figure 7-20 shows a comparison of the total and effective stress analysis compression curves compared to the average uniaxial compression curve for RGoM-EI. There is a slight shift in the effective stress analysis compression curve due to the generation of excess pore pressure, it is significantly less that the shift in compression curves for the vertical drainage cause. This further shows that radial drainage is effective at reducing excess pore pressure generation.

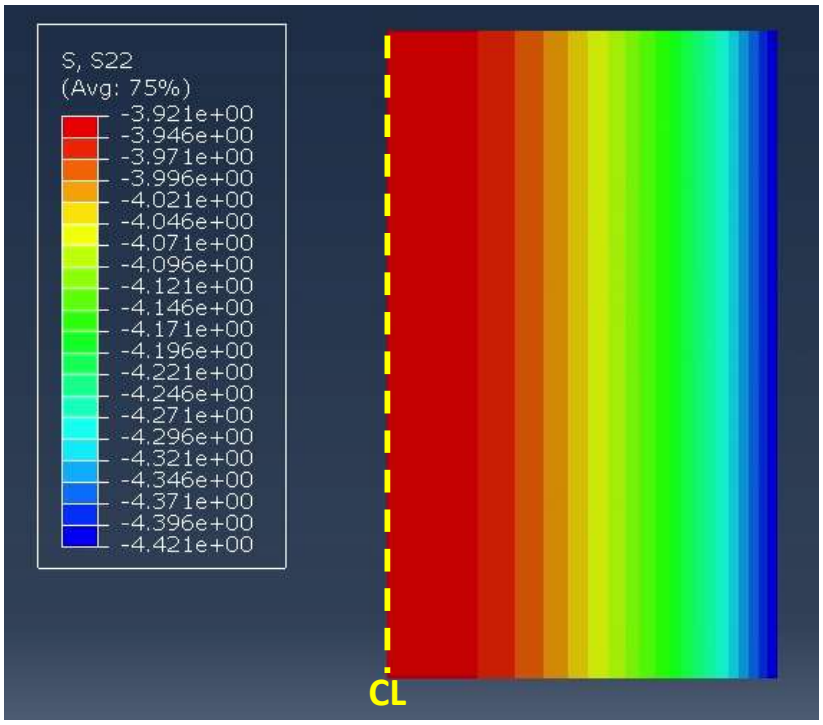

Figure 7-17 Vertical effective stress distribution at the end of simulated consolidation of TX1548 using radial drainage only. (Values of stress in the key are in MPa)

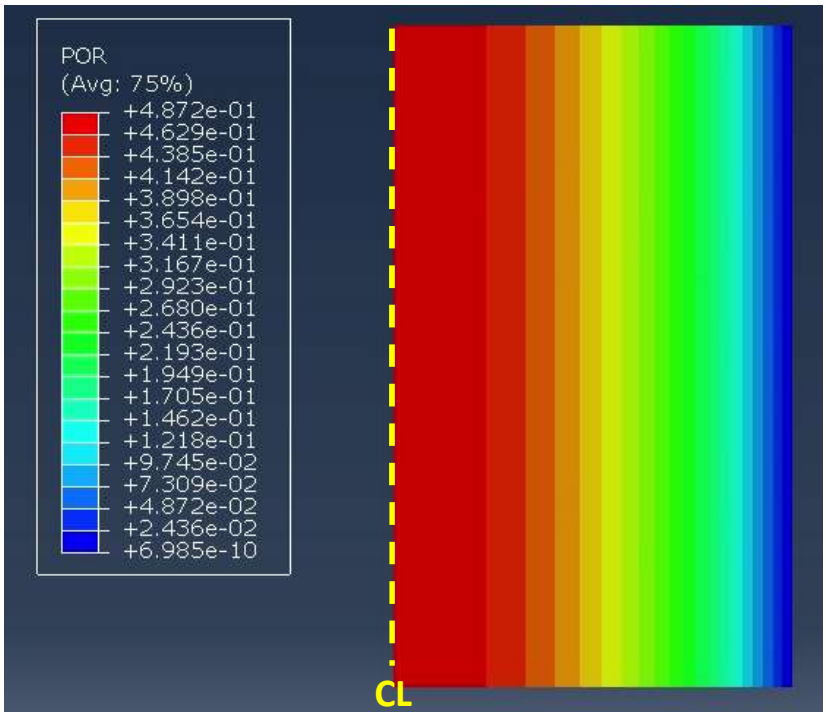

Figure 7-18 Excess pore pressure distribution at the end of simulated consolidation of TX1548 using radial drainage only. (Values of stress in the key are in MPa)

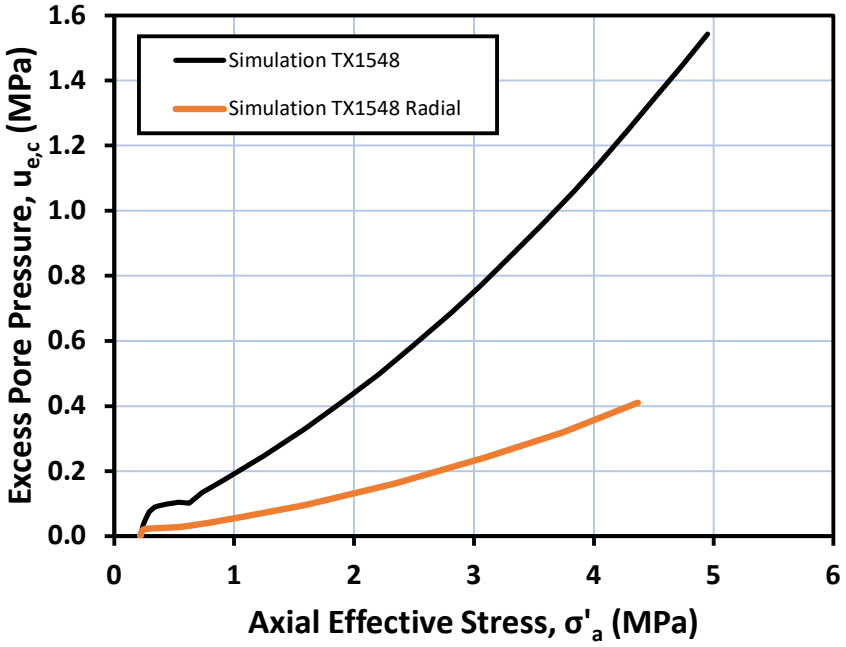

Figure 7-19 Excess pore pressure versus axial effective stress comparing the excess pore pressures generated in the simulation of TX1548 during vertical drainage conditions and radial drainage conditions.

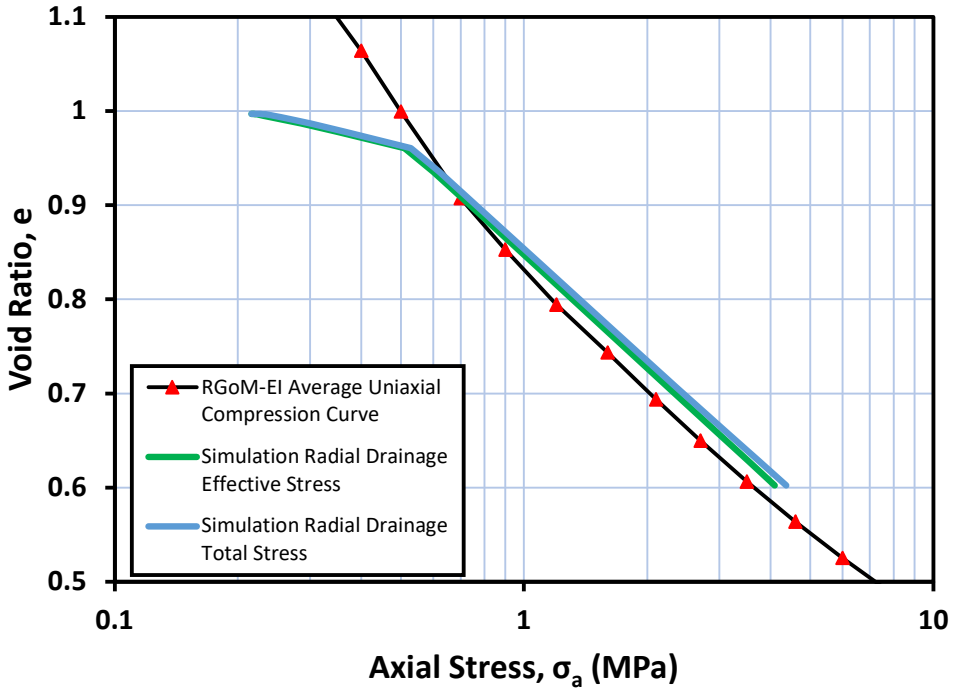

Figure 7-20 Plot of void ratio versus axial stress comparing total stress and effective stress compression curves of the simulation of TX1548 using only radial drainage to the average uniaxial compression curve of RGoM-EI.

7.4.4 3-D Axisymmetric Model of Side Drains

The final simulation performed as a part of this research was to assess the effectiveness of side drains during a test simulation for a standard size specimen (H_0 = 8.1 cm, r = 1.75 cm). The same material parameters were used as the simulations of TX1548, however as the model height was doubled, the applied displacement needed to be doubled to achieve the same strain rate and final stresses. As there are 8 side drains used on a specimen, one eighth of a full specimen was modelled to improve efficiency (Figure 7-21). The model was constructed as one part and partitioned in order to enable different material properties for the side drains and the soil specimen, while allowing a free drainage boundary between them. Figure 7-22 shows the excess pore pressure distribution in the simulation where there was drainage allowed both vertically and radially through the side drains. There is an elliptical concentration of excess pore pressures at the centre of the specimen. When comparing the excess pore pressures generated at the centre of the specimen to the case where there is only vertical drainage (Figure 7-23), there is 4 times less pore pressure generated than the vertical condition. This is a very similar result to the simulation only allowing radial drainage, showing that radial drainage when used dominates the excess pore pressure generation behaviour. When comparing compression curves of the total stress analysis (not accounting for excess pore pressures) and the effective stress analysis, similar to the only radial drainage case, there is a slight shift in the curve to the left when accounting for excess pore pressures. This shows that side drains are effective at reducing excess pore pressures in the specimen during constant rate of strain consolidation. Figure 7-25 shows a cross-sectional cut of the pore pressure distribution. The distribution is relatively uniform, with large decreases in excess pore pressure in close proximity of the side drain material.

Overall, the finite element analyses performed in this research further confirms the probability of excess pore pressure generation in a specimen during triaxial constant rate of

strain K_0 consolidation. Results from the simulations of TX1566 and TX1548 were in close agreement with calculations made using (Wissa et al., 1971) linear theory, giving validity to both analyses. The FEA model of a situation with side drains shows that the Terrafix® 360R material is effective for use as side drains, producing results close to that of a perfect radial drainage boundary. This is very encouraging in prelude to the implementation of side drains in the experimental testing programme.

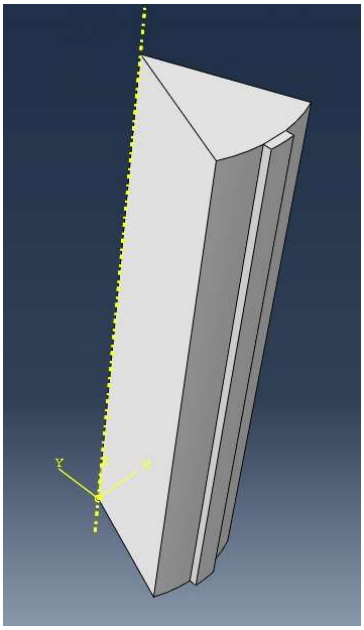

Figure 7-21 Screengrab of 3-D model used to simulate side drain utilization.

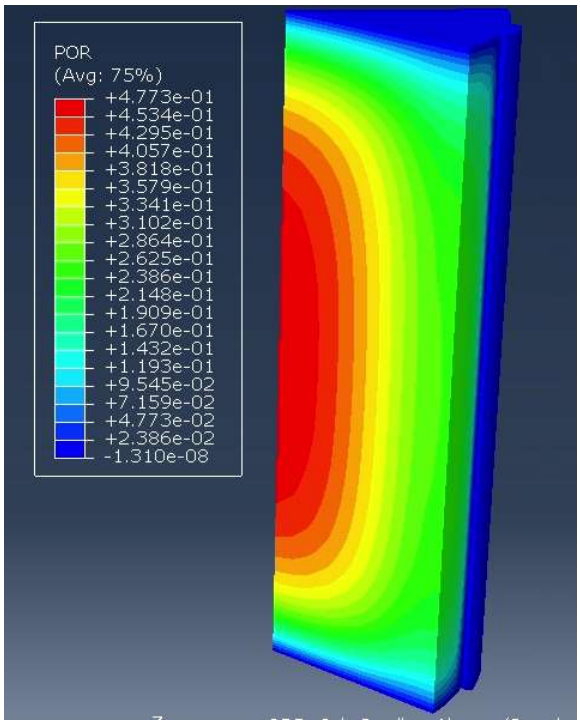

Figure 7-22 Pore pressure distribution of simulation allowing vertical drainage and radial drainage through the side drain (Values of stress in the key are in MPa).

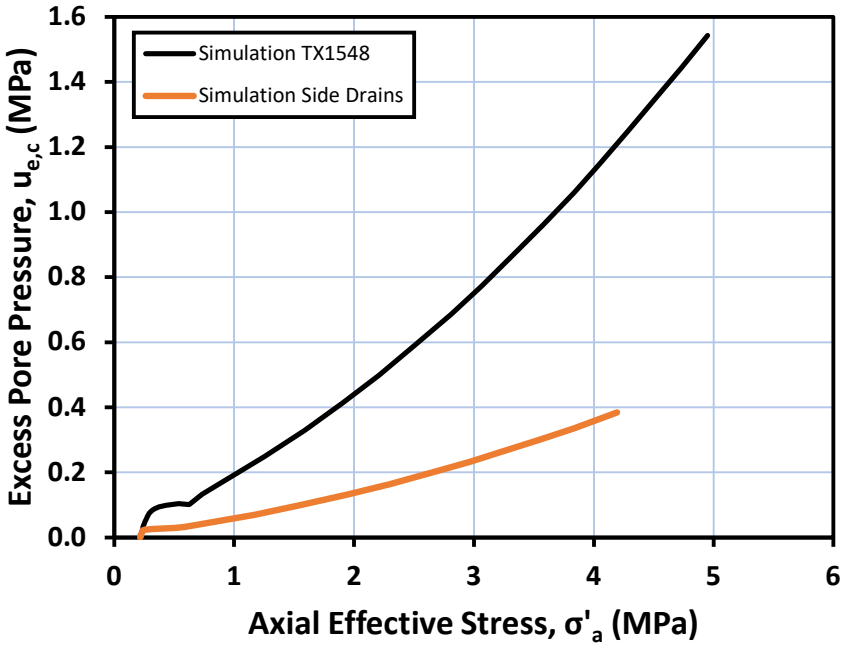

Figure 7-23 Plot of excess pore pressure versus axial effective stress comparing vertical drainage simulation to simulation utilization side drains.

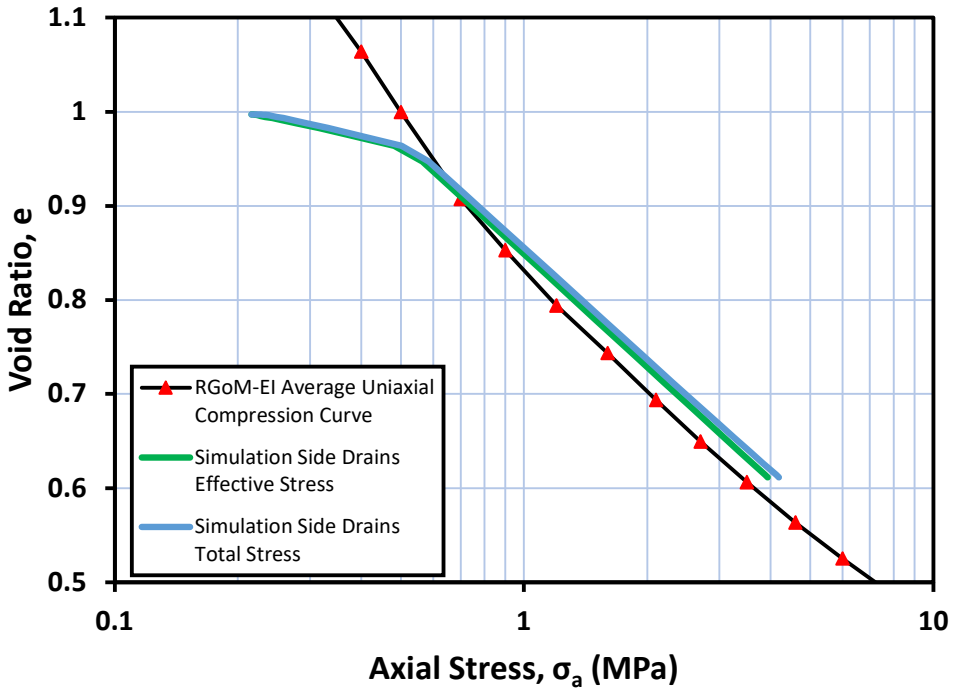

Figure 7-24 Plot of void ratio versus axial stress comparing total stress and effective stress compression curves of the simulation using side drainage to the average uniaxial compression curve of RGoM-EI.

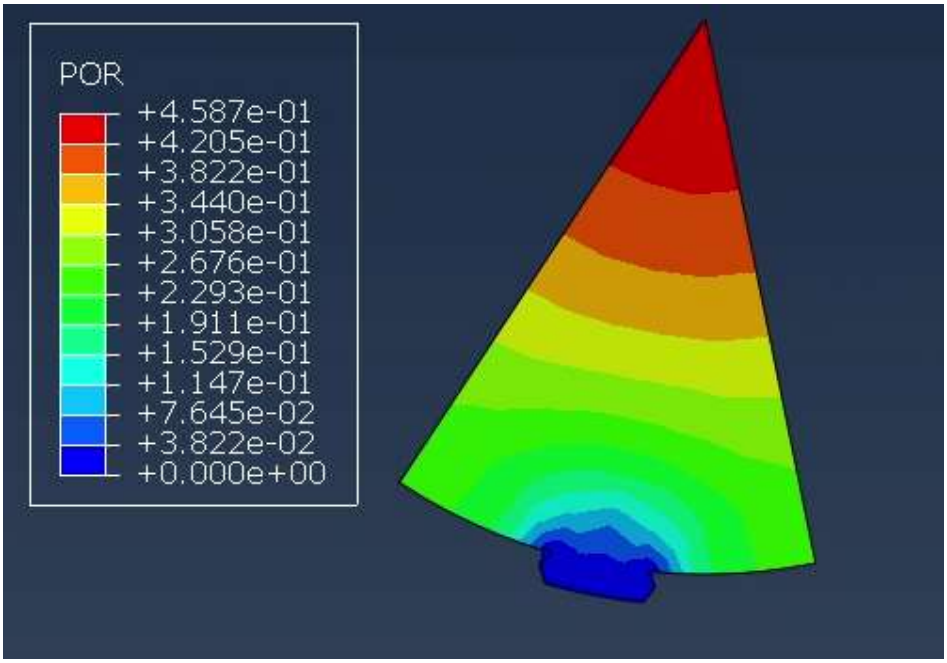

Figure 7-25 Cross-sectional view of the excess pore pressure distribution of 3-dimensional axisymmetric model (Values in key are in MPa).

7.4.5 Summary of Simulation Results

To summarize the results, the plane strain simulation of TX1566 run at 0.05 %/hr was used for model input parameters of λ and κ and to validify the model. This test agreed with the results from the Wissa Linear Theory analysis performed in chapter 6. Figure 7-26 shows the pore pressure distribution results for the simulation of TX1566. The axisymmetric simulation of TX1548 run at 0.6 %/hr also agreed well with the results from the Wissa Linear Theory analysis. Changing the drainage conditions to radial dramatically decreased the generation of excess pore pressure (Figure 7-27). Allowing full perimeter drainage further decreases the excess pore pressures generated. The simulation using both side drains and vertical drainage has results similar to the full perimeter drainage case, with similarly shaped pore pressure distributions. This increases confidence on the effectiveness of side drains during experimental consolidation.

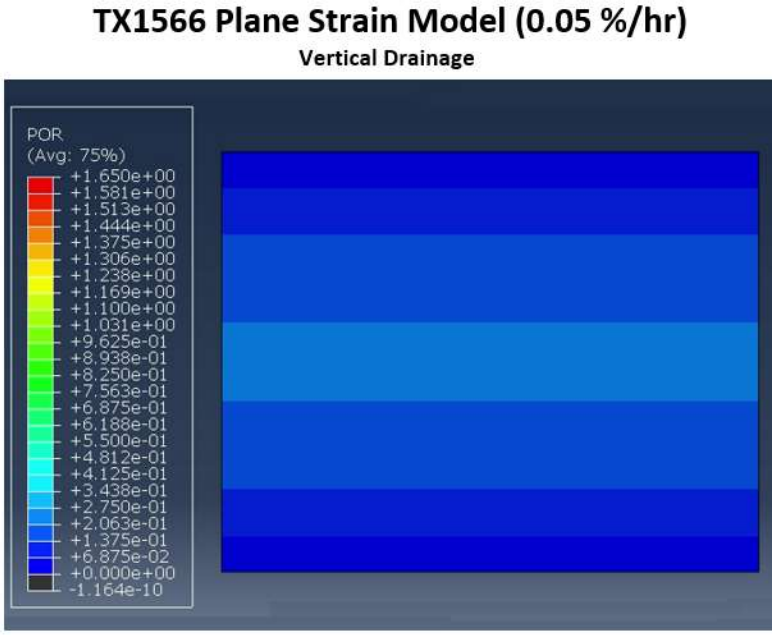

Figure 7-26 Excess pore pressure distribution of the simulation of TX1566 at the end of consolidation. (Values in key in MPa).

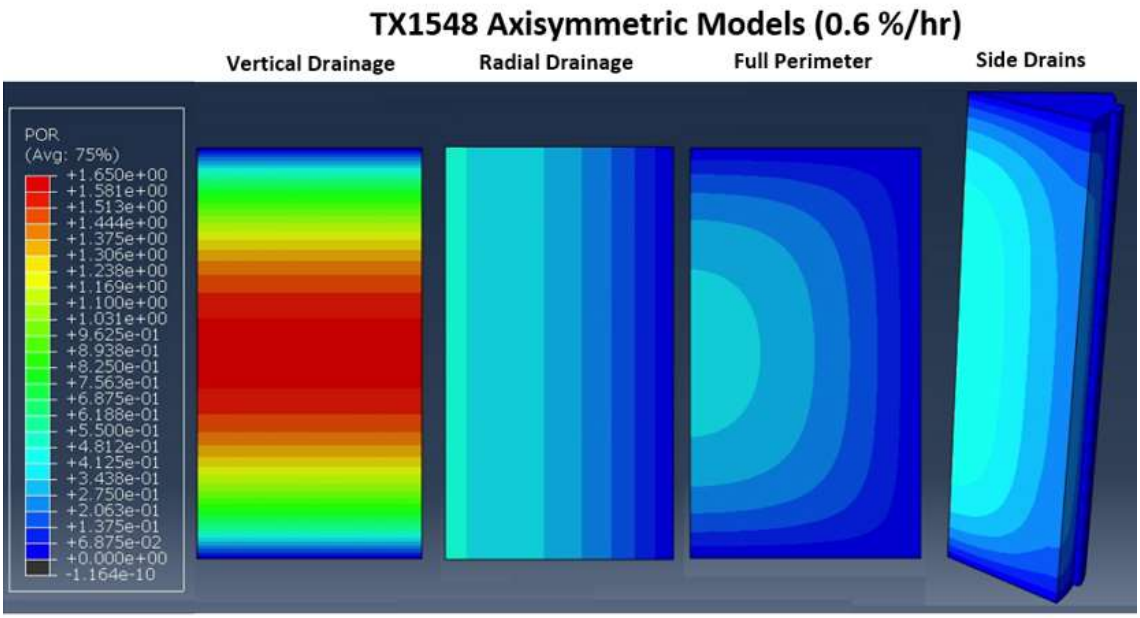

Figure 7-27 Excess pore pressure distributions of simulations of TX1548 using different drainage conditions. (Values in key are in MPa).

8 Testing Procedures

8.1 Introduction

This chapter will describe in detail the procedures used to perform the laboratory triaxial testing using the medium pressure triaxial system. The procedures used to set-up the high pressure triaxial system for testing was identical to that used by (Eagle, 2021), and therefore will not be repeated here. Once the tests were set up in the apparatus, the following procedures were identical, only differing in the stress that they were consolidated to. This chapter will first cover the test set-up for the medium pressure triaxial system. It will then describe the two main phases of testing, back pressure saturation and K_0 consolidation. Finally, a brief overview of the hold stress phase and disassembly of the system will be provided.

8.2 Test Set-Up and Initial Pressure Up

This section will provide a step-by-step description of setting up a triaxial specimen for testing in the medium triaxial cell. The specimens were previously resedimented, extruded and trimmed as outlined in Chapter 3. Each step in the set-up procedure will be numbered for clarity and to provide guidance for future research.

8.2.1 Medium Pressure Triaxial

1. Fill out laboratory testing logbook with triaxial testing number, material, name, project, comments. Fill in the same details in the TAG Lab triaxial test datasheet, including six specimen diameter measurements, three specimen height measurements and the wet mass of the specimen.
2. Prepare 250 mL of sea salt solution in a 1 L vacuum flask. For RGoM-EI, the salt concentration of the salt solution was 80 g/L. For RBBC, salt concentration was 16

g/L unless otherwise noted. San Francisco Salt Co. Pacific Ocean sea salt was used for all salt solutions.

3. Place two porous stones and two nylon filter papers in a Pyrex® measuring beaker with distilled water. Place this jar in an ultrasonic cleaner for 10 minutes to remove any air bubbles from the stones and ensure saturation.
4. Gather the following materials and tools and place on the vacuum pump cart:
    a. Specimen in sealed sandwich bag
    b. Two adjustable wrenches, a 3/8" crowfoot wrench, a 15/16" crowfoot wrench, and a torque wrench
    c. A Pair of tweezers
    d. Rubber mallet
    e. Six 1.4" diameter Buna-N O-rings
    f. Two 1.4" diameter x 0.025" thick latex membranes
    g. One unlubricated prophylactic
    h. A 1 cm strip loop of 1.4" diameter x 0.018" thick latex membrane
    i. Tube of silicon vacuum grease
    j. Vacuum membrane stretcher
    k. Specimen Alignment Jig
    l. Eight 6.35 mm x 50 mm Terrafix 360R geotextile side drain strips
    m. Scissors
    n. Two porous stones and nylon filter screens
    o. Vacuum flask with saltwater solution
    p. O-ring stretcher.
5. Transport the vacuum pump cart with the necessary materials and tools to the triaxial station.

6. Clean the brass top cap and bottom pedestal with a paper towel. Place a thin layer of silicon vacuum grease to both the caps. Ensure that hands are cleaned.
7. Cut 1” from the tip of the prophylactic. Stretch over the greased bottom pedestal, in a position that allows it to be rolled up over the specimen.
8. Stretch the 1 cm strip of 0.018” thick latex membrane over the top 5mm of bottom cap. Ensure that 5 mm of the strip is not in contact with the bottom cap. This will be used to hold the geotextile side drains in place.
9. Place one porous stone on the bottom cap, inside the 5mm of exposed 0.018” thick latex membrane.
10. Use the tweezers to place the eight strips of geotextile side drains evenly spaced between the latex membrane and the porous stone (Figure 8-1).
11. Position the nylon filter screen on the porous stone, then place the specimen on the filter paper.
12. Place filter paper, porous stone, and then top cap on the specimen. Ensure the threaded hole for the top drain line is close to its final orientation.
13. Roll the prophylactic up over the specimen and side drains. Ensure there are no wrinkles as these may provide a path for cell fluid entry.
14. Apply a thin layer vacuum grease to the prophylactic where it covers the top and bottom cap.
15. Cut 7.5 cm from the two 1.4” diameter x 0.025” thick latex membranes.
16. Using the vacuum membrane stretcher, place the first latex membrane over the specimen. Re-grease the ends of the membrane.
17. Clean and grease four Buna-N 1.4” diameter O-rings. Always inspect these O-rings for cracking or cuts as these can allow leaking. Using the O-ring stretcher, place two O-rings on both the top and bottom caps.

18. Place another 0.025” latex membrane on the specimen using the membrane stretcher. Clean and grease two O-rings and carefully use the O-ring stretcher to place these O-rings between the two O-rings previously placed on the top and bottom caps. This provides a tight seal during testing.
19. Grease the O-rings at the face of the geo-measurement connections on the top drain line. Position the top drain line on the specimen. It is important to inspect these geo-measurement connections prior to use, to ensure O-rings are in good condition and well-greased as this is a high-probability leakage location.
20. Holding the specimen in position with the alignment, screw the top drain line into the top cap and base using the 3/8” crowfoot wrench.
21. Use the vacuum pump connected to the vacuum flask with saltwater to apply a vacuum to the specimen via the pore pressure transducer port. These are connected via plastic tubing and rubber stoppers. This is done to draw excess air from the system, maintain the position of the specimen during the following steps, and to check for leaks. Initially the water in the vacuum flask will bubble as it degasses. This will stop after a short period of time. Once the bubbling subsides, lower the end of the plastic tubing into the saltwater solution. If no bubbles are present exiting the plastic tube, the specimen is sealed.
22. Close the pore valve so that the specimen is isolated preventing any air re-entry. Remove stopper from the pore transducer port and turn of the vacuum port. It is extremely important to release the vacuum prior to turning off the pump.
23. After checking that the specimen has maintained alignment during vacuuming, remove the alignment jig. Ensure that the base O-ring is in position.
24. Fully retract the piston in the triaxial cell. Using the electric winch, lift the triaxial cell into position over the specimen. Once a couple of inches from the base, plug the load

cell into the 9-pin Amphenol connector located in the triaxial base. Lower the triaxial cell into position so that the flange of the cell lines up with the bolts on the base. Ensure that the valve located at the top of the triaxial is left open.

25. Place washers and nuts onto the six flange bolts. Tighten these bolts first with the 15/16” crowfoot wrench, then using the torque wrench torque the bolts to 35 Nm. When tightening the flange, do so incrementally and in opposing pairs moving clockwise/anticlockwise around the flange to ensure that the flange is tightened evenly.
26. Start recording the task central data acquisition. Set the reading interval to 1 hour. The central data acquisition should be recording all transducer and power channels. This first recording is the load cell zero voltage reading for the data reduction after the test is complete.
27. Record the load cell “zero” voltage and input voltage, shown on the triaxial control computer program, in the triaxial datasheet. This will be the zero used for triaxial control program.
28. Holding the piston in one hand, lightly tap the top of the piston with the rubber mallet to lower the piston. The piston friction will reduce at a certain point. After that point, the piston can be gently lowered by hand onto the top cap. Once in contact, take three readings on the central data acquisition and record the voltages shown on the triaxial programme for the LVDTs. These will be your zero voltages for both your data reduction and the triaxial control programme respectively.
29. Place the stainless-steel ball on top of the piston. This acts as a moment break. Using the manual controls on the control box, adjust the load PVA, slowly raising the triaxial cell until the steel ball just contacts the shear break on the load frame. The steel ball should still spin; however, no space should allow the ball to move vertically.

30. Fill the triaxial cell with silicone oil by pressurizing the silicone oil reservoir to 20 psi and opening the valve located at the base of the triaxial cell. Attach the overflow container to the valve located at the top of the triaxial cell. Once the overflow container begins to fill, the cell is full and the valve at the base of the triaxial is closed first, then the top valve can be closed.
31. Open the valve on the cell PVA and take the zero-voltage reading for the cell transducer, identical to what was done for both the load cell and the LVDT. Close the valve after taking the readings.
32. Input the normalized zero voltages (signal voltage divided by the input voltage) for the load cell, pressure transducer and LVDT and the specimen measurements (area and height) into the triaxial control programme. Transducer calibration factors are also inputted into the control programme at this stage; these do not need to be inputted for each test unless a transducer is changed or recalibrated. Input the normalized zero used for the apparatus compressibility correction at this stage also.
33. Select the "pressure up" subroutine in the triaxial control programme. Type in the appropriate values to be used for pressure up. This subroutine increases cell pressure while maintaining a seating load to record the sampling effective stress. For this research, a seating axial load of 0.5 kg and a cell pressure of 3 ksc was used. It is important that the cell pressure used is larger than the estimated sampling effective stress.
34. At this point, the vacuum is reapplied to the specimen through the pore transducer port. The end of the tube is placed into the saltwater solution and the vacuum is maintained until there are no further air bubbles exiting the end of the plastic tubing i.e., there is no more air in the system.

35. At the control box, turn on the computer control for both axial load and cell pressure. Allow the system to pressure up.
36. Once at the target stresses, and provided that air bubbles are no longer present exiting the plastic tubing in the vacuum flask, slowly remove the tubing that attached the vacuum pump from the vacuum flask. This will draw water from the flask into the system allowing saturation. Close off all pore pressure valves to the specimen, turning the transducer valve to the backpressure position. Open the valve located at the top of the pore pressure PVA and re-attach the pore pressure transducer. Take the zero voltage readings at the central data acquisition system and the triaxial programme. Input the pore transducer normalized voltage into the control programme. This can be done by pressing CTRL + Break, then F6, and typing “zpore = (normalized zero value)”.
37. Turn the transducer valve back to the “specimen” position and wait for 24 hours. The pore pressure in the specimen should increase, giving the sampling effective stress. If at the end of the 24 hours the cell pressure is equal to the pore pressure there is an internal leak, and the cell fluid is entering the specimen. If this happens, the system needs to be disassembled, the membranes and connections within the cell must be inspected and the process from step 20 onwards repeated.

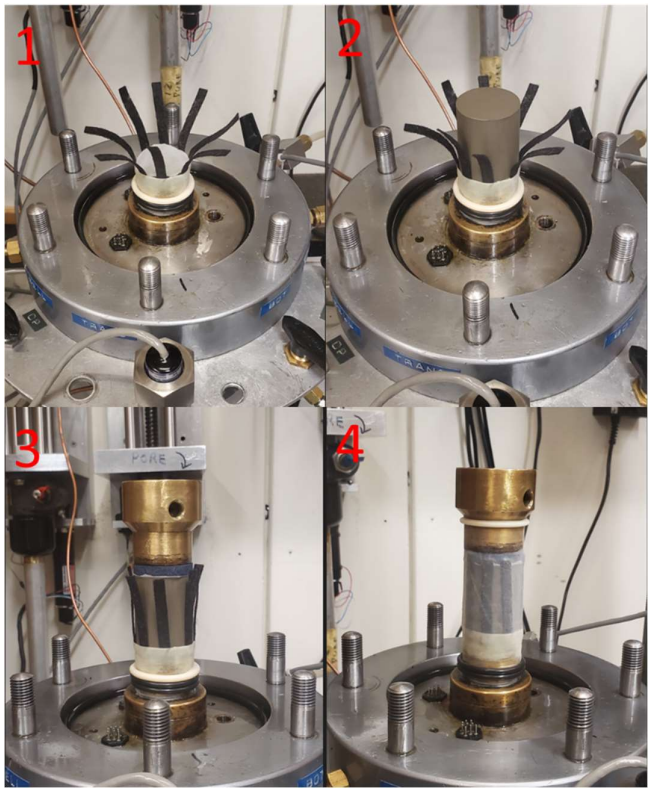

Figure 8-1 Method for placing geotextile side drains.

8.3 Back Pressure Saturation

After the initial set-up and pressure-up stages, the specimen was back pressure saturated. By applying a vacuum to the system at the pressure-up stage, the initial absolute pressure of the system is reduced, reducing the pressure needed for the gas to dissolve in the liquid, thus saturating the specimen. Back-pressure is done to further ensure that the triaxial specimen and pore fluid drainage lines are fully saturated, with no air present in its gaseous phase. Back pressure saturation is the process of increasing the pore pressure in the system and the cell pressure, whilst maintaining the effective stress of the specimen at a constant. This is done by making the change in pore pressure equal to the change in total stress i.e., $\Delta u = \Delta \sigma$. Full saturation is a fundamental assumption in Terzaghi's consolidation theory. It is also important for the K_0 consolidation protocol, as the computer control programme is trying to maintain initial cross-sectional area by keeping the change in axial strain equal to the change

in volumetric strain, meaning that all volumetric changes in a specimen are due to pore fluid being expelled.

According to Henry's Law, increasing the partial pressure of a gas increases the gases solubility in a liquid. Therefore, by increasing the backpressure to above atmospheric pressure, the air trapped in the system can be dissolved in the pore fluid. During back-pressure saturation control programme subroutine, the radial, axial stress, and back pressure were increased in steps of 0.5 ksc. Each step had a duration of 20 minutes. This was done until the back pressure was at a final stress of 4.5 to 5 ksc (450-500 kPa). To saturate the specimen to above 95% in one day, the back pressure should be increased to 4- or 5-times the pressure required to saturate the specimen in infinite time (Black and Lee, 1973) (Figure 8.2). Due to the resedimented specimens having over 98% saturation after the resedimentation procedure and the application for a vacuum, the saturation pressure is very low. During these steps, it is expected that pore fluid will enter the sample to replace the volume of the dissolving gas, which results in a negative volumetric strain. After a period, this reduction in volumetric strain should come to a stop as the system reaches saturation. If the volumetric strain continues to decrease, an external leak may be present. If no leaks are present, the specimen is allowed to equilibrate for 24 hours, after which a B-value check is performed to measure the saturation of the system.

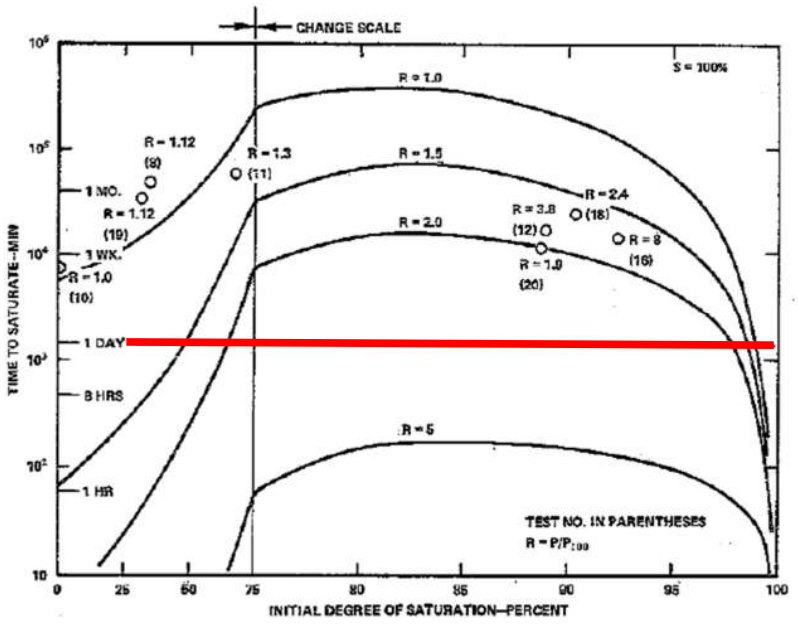

Figure 8-2 Time to saturate versus initial saturation (Black and Lee, 1973)

8.3.1 B-Value and Apparatus Compressibility

The B-value is used as a measure of a system's saturation. The term B-value was first defined by (Skempton, 1954). The change in pore pressure under changes in principle stresses is given as:

$$\Delta u = B(\Delta\sigma_3 + A(\Delta\sigma_1 - \Delta\sigma_3)) \qquad \textit{(Eq. 8-1)}$$

By setting $\Delta\sigma_1$ equal to $\Delta\sigma_3$, the A parameter can be eliminated. This gives:

$$B = \frac{\Delta u}{\Delta\sigma_3} \qquad \textit{(Eq. 8-2)}$$

A B-value of 1 means 100 % saturation of the system. According to ASTM D4767, the specimen is considered sufficiently saturated if the B-value is 0.95 or greater, or if the B-value remains unchanged after additional increases in applied back pressure. However, this does not account for the compressibility of the soil grains or pore fluid. (Bishop, 1973)

derived a relationship for the change in pore pressure for a given change in effective stress that accounts for the compressibility of the soil skeleton and pore fluid:

$$\frac{\Delta u}{\Delta \sigma_3} = \frac{1}{1 + \frac{n(C_w - C_S)}{(C - C_S)}} \qquad \textit{(Eq. 8-3)}$$

C_w and C_s are the compressibility of the pore fluid and soil grains respectively, and C is the bulk compressibility of the soil skeleton. This is particularly important for low compressibility soils, i.e., soils that have been subjected to larger past effective stresses. As the compressibility of the specimen reduces, so does the maximum B-value that can be attained. For medium pressure triaxial testing, with specimens being resedimented to 0.8 MPa, a B-value of 0.9 or above was easily attainable. For high pressure triaxial testing, the author found it difficult to attain B-values above 0.2. This is extremely low, and possibly due to dead space within the pore pressure transducer. These specimens were generally resedimented to a maximum stress of 10 MPa. Further development to consider the system compressibility of the on the B-value was provided by (Bishop, 1976):

$$\frac{\Delta u}{\Delta \sigma_3} = \frac{1}{1 + \frac{n(C_w - C_S)}{(C - C_S)} + \frac{V_L}{V}\frac{C_w}{C - C_S} + \frac{C_L + C_M}{V(C - C_s)}} \qquad \textit{(Eq. 8-4)}$$

C_L and C_M are the compressibility of the pore lines and pore pressure measuring device respectively, V_L is the volume of the pore lines and connections, and V is the volume of the sample.

(Casey and Germaine, 2014) shows the importance of apparatus compressibility on the measurement of B-values, and that measured B-values will always be lower than the true B-

value calculated using Eq. 8-4 above (Figure 8-3) and this reduction in B-value is due to a decrease in the bulk compressibility of the soil skeleton.

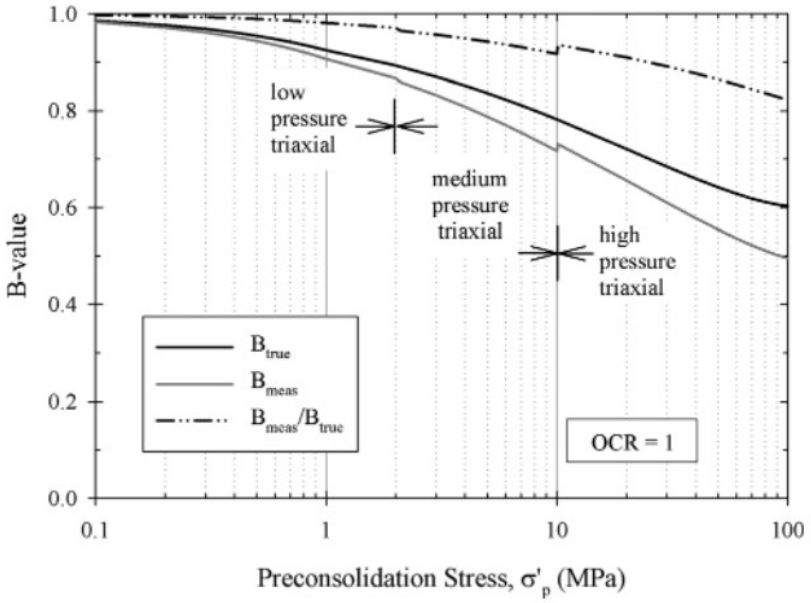

Figure 8-3 B-value versus presconsolidation stress for three different triaxial apparatuses (Casey and Germaine, 2014).

8.4 Triaxial K_0 Consolidation

For the laboratory testing, triaxial specimens are consolidated to a specific effective stress. This is generally done prior to shearing the specimen, either drained or undrained. For past testing, specimens were consolidated to at least twice the maximum past pressure that was reached during consolidation and to about 10 % axial strain (Schmertmann, 1955). This is done to erase any sampling disturbance to due extrusion, trimming and placement in the triaxial apparatus. This research sought to improve the K_0 consolidation protocol undertaken at the TAG Lab.

The K_0 consolidation subroutine utilised in the control programme attempts to keep a constant cross-sectional area during the consolidation stage. This means that the specimen is not allowed to strain radially. Essentially, the specimen is axially loaded at a constant rate of

strain, whilst a PID algorithm continuously adjusts the cell pressure to maintain the change in volumetric strain equal to the change in the axial strain. This keeps the target of constant cross-sectional area (Figure 8-4). A strain rate of 0.06%/hr was generally used for medium pressure testing, whilst a strain rate of 0.02%/hr was used for high pressure testing.

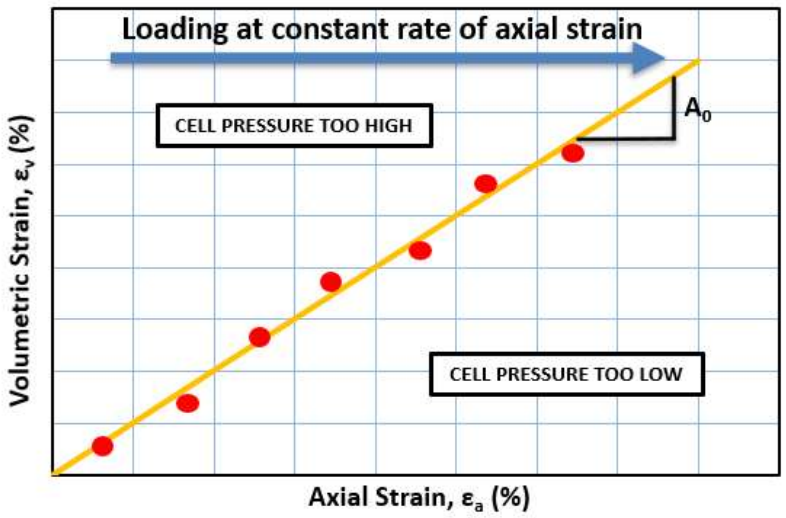

Figure 8-4 Volumetric strain versus axial strain showing how the K_0 consolidation control protocol operates.

During this research, and as mentioned in Chapter 5, the author noticed that neither apparatus compressibility due to axial loading nor applied cell pressure was not being corrected for in the control programme. The area correction inputted for the K_0 consolidation is a right cylinder, and the area of the cylinder, $A_{right\ cyl.}$ is calculated as follows:

$$A_{right\ cyl.} = \frac{A_0(1-\varepsilon_v)}{(1-\varepsilon_a)} \qquad \textit{(Eq. 8-2)}$$

As there was no correction for apparatus compressibility, the calculated axial strain of the specimen was larger than the actual amount the specimen had strained. This led to systematic radial contraction of the specimen during K_0 consolidation, with increasing radial strain with increasing stress. Figure 8-5 shows a plot of radial strain versus axial effective stress

comparing the consolidation portion of two tests performed on RBBC, TX1030 using no apparatus compressibility correction for axial strain, and TX1565 using an axial strain correction for apparatus compressibility. For TX1031, there is an increase in radial strain with increasing axial effective stress, amounting to 0.2 % at the end of the test. For TX1565, there is a decreased radial strain, amounting to -0.03 % at the end of the test. The slight radial expansion in the corrected test, TX1565, is due to a lag in the control software as the "current" volumetric strain is trailing behind its target. This has been improved upon in subsequent tests by refining the PID control constants. The effects that the apparatus compressibility correction would have on K_0 measurements was unknown to the author, and this will be discussed in Chapter 9.

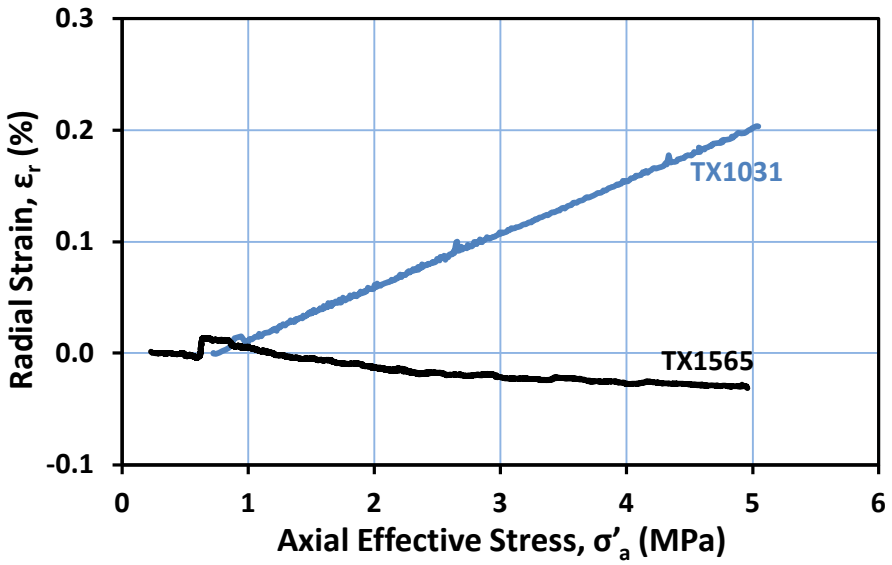

Figure 8-5 Plot of radial versus axial effective stress for the consolidation portion of a test with no apparatus compressibility correction and one with an apparatus compressibility correction.

As examined in Chapters 7 and 8, the effects of excess pore pressures within the specimen led to errors in the measurement of effective stresses during the K_0 consolidation of a specimen for RGoM-EI. During a triaxial tests, the effective stress is the applied total stress minus the back pressure. This holds true if the strain rate applied to the specimen allows for

the drainage of excess pore pressure. If not, a parabolic distribution of pore pressures develops within the specimen, and thereby a parabolic distribution of effective stresses. This leads to an error in the measured effective stresses, with measured being higher than what is being experienced by the specimen. This can also mean that although, on average, the volumetric strain is equal to the axial strain, in reality there would be radial deformations in the specimen leading to an hourglass distribution of strains. This would violate the K_0 condition. At the end of consolidation when the target axial effective stress was reached, the specimen would be put into a hold stress protocol. During this hold stress protocol, both the radial and axial total stresses are kept constant. The excess pore pressures in the specimen would now be allowed to drain, and the measured effective stresses would be the effective stresses experienced by the specimen. However, these stresses are not the K_0 ratio of stresses for uniaxial compression and would lead to an increase in both axial and radial strains.

To reduce excess pore pressure generation, the author adopted the use of radial side drains, as mentioned in the Chapter 5. To utilise the side drains, a correction needed to be inputted to account for the volume loss of the geotextile side drains during testing. Although side drains have been used for previous triaxial testing (Casey, 2011) (Force, 1998), this volumetric loss from the side drain material has, up until this research, been ignored for K_0 testing at both MIT and Tufts University.

8.5 Hold Stress

After the specimen reached its target axial effective stress, the control program entered the Hold Stress subroutine. This subroutine held the total radial and axial stress constant. The specimen was left in hold stress for 24 hours. After 24 hours, the specimen was either subjected to an undrained shear test or dismantled. Generally, for this research, the test was dismantled at the end of hold stress in order to measure the dimensions of the specimen to

ensure K_0 conditions during consolidation. This is just to compare the uniformity of radial deformations.

It should be noted that in the case of previous testing on RGoM-EI, a large amount of excess pore pressure was drained from the specimen during this stage. Therefore, a large amount of primary consolidation had taken place during the Hold Stress subroutine, along with secondary compression. As the specimen drained excess pore pressure, the specimen would deform both radially and axially. As this would lead to a K value higher than K_0, in subsequent undrained shear testing the specimen would exhibit higher undrained shear strength in compression loading (Figure 8-6), and lower undrained shear strengths in extension. In the case of extension, this is just speculation and further shear testing would be required to examine these effects.

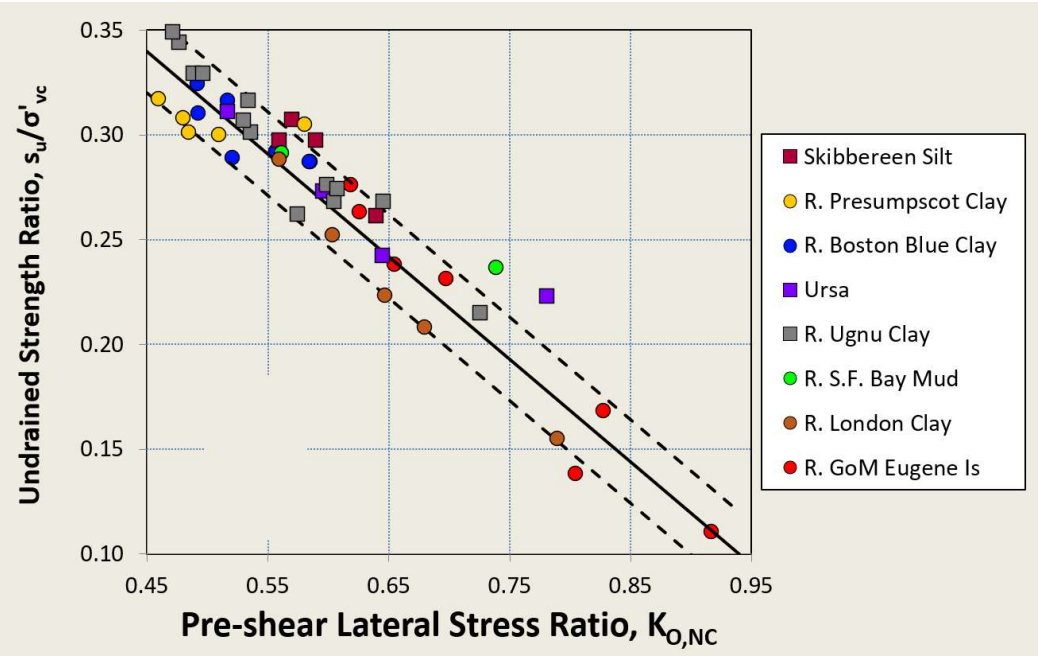

Figure 8-6 Undrained strength ratio versus pre-shear $K_{0,NC}$ for various clays (Ladd Memorial Lecture, 2015).

8.6 Disassembly

After Hold Stress, the specimen was removed from the triaxial cell. In the case of the high pressure triaxial cell, the process for dismantling is identical to that used by (Eagle, 2021). For the medium pressure triaxial cell, the process of disassembly was as follows:

1. Close off pore pressure valves to isolate the specimen.
2. Manually reduce the cell pressure and axial load in tandem.
3. Once the cell pressure and axial load are back to atmospheric pressure, pressurized the cell by connecting the 20-psi air supply to the top valve on the triaxial cell, open the base valve to the silicone oil reservoir, allow the cell to drain. The reservoir will begin to bubble once the cell is empty.
4. Loosen the bolts on the triaxial cell's flange. Loosen evenly to ensure that there is not concentrated stresses on the flange or bolts.
5. Using the electrical winch, lift the triaxial cell off the specimen, unplugging the load cell as the cell is lifted.
6. Dry all surfaces from cell fluid within the cell with paper towel. This includes the base, membrane, top and bottom caps, and top drain line.
7. Disconnect the top drain line, first by unscrewing from the top cap, then the base.
8. Remove the top cap. Dry the membrane again. Remove the top O-rings.
9. Carefully roll each membrane down the specimen. This will allow you to lift the specimen off the bottom cap. The geotextile side drains will still be attached to the specimen.
10. Obtain the tare weight an aluminium drying container and a porcelain evaporating dish.

11. Remove each side drain and place into a porcelain evaporating dish with distilled water to rinse. Once rinsed to satisfaction, remove side drains. Place the evaporating dish in the over at 105ºC.
12. Measure the specimen height and diameter three times each.
13. Place the specimen in the aluminium drying container, weigh the wet mass of the specimen.
14. Place the specimen in the oven at 105ºC for two weeks. Measure the weight at week two and return to the oven. Measure each week for a further two weeks to ensure there is no change in weight and that the specimen is fully dried.
15. Place the porous stones and filter papers in a Pyrex® beaker, fill with distilled water, place in the ultrasonic cleaner for 10 minutes. If there is silicon oil present in the beaker after ultrasonic cleaner, that is a good indication that there was a slow leak in the system that allowed oil travel to the specimen.

9 Experimental Results and Discussion

9.1 Testing Summary

13 tests were successfully completed as a part of this research. The author was attempting to improve the testing protocol. The process of improvement was incremental as individual errors were identified and corrected for. This continuous development also led to many failed tests over the course of the research. The author estimates that over 40 tests were attempted as a part of this research. Of course, this is the reality of experimental testing. Table 9-1 summarizes the successful tests that are presented in this thesis. All tests without side drainage were run at the standard laboratory strain rates, 0.15 %/hr for all RBBC tests, 0.02 %/hr and 0.06 %/hr for high pressure and medium pressure RGoM-EI respectively. Tests using side drains were run at 0.1 %/hr.

Table 9-1 Summary of triaxial consolidation results.

Test No.	Triaxial Station	Soil	Strain Rate (%/hr)	Initial		Final		
				w_c	e_0	$\sigma'_{a,max}$ (MPa)	$K_{0,NC}$	e
TX1531	Station 03	RBBC	0.15	23.61%	0.657	13.81	0.534	0.442
TX1540	Station 06	RGoM-EI	0.06	35.29%	1.038	7.96	0.675	0.501
TX1541	Station 03	RGoM-EI	0.02	17.80%	0.535	39.04	0.773	0.377
TX1548	Station 06	RGoM-EI	0.6	34.49%	1.025	3.68	0.668	0.616
TX1550	Station 03	RGoM-EI	0.02	20.01%	0.584	13.69	0.730	0.414
TX1551	Station 06	RGoM-EI	0.05	21.03%	0.614	10.66	0.759	0.532
TX1555†	Station 06	RGoM-EI	0.1	34.05%	1.015	8.66	0.682	0.522
TX1556*	Station 06	RBBC	0.15	33.45%	0.993	9.89	0.520	0.546
TX1559†	Station 06	RGoM-EI	0.1	36.32%	1.075	1.28	0.628	0.791
TX1564	Station 06	RBBC	0.15	32.01%	0.949	4.91	0.546	0.619
TX1565	Station 06	RBBC	0.15	34.91%	1.024	4.87	0.544	0.538
TX1567†	Station 06	RGoM-EI	0.1	34.12%	0.981	7.87	0.662	0.462
TX1578†	Station 06	RGoM-EI	0.1	33.34%	0.983	5.88	0.69	0.530

*stress path test; †test performed with side drains

9.2 K_0 Consolidation Results and Discussion

The K_0 consolidation results for RBBC and RGoM-EI are presented in the following sections. RBBC was specifically tested to quantify the effects of correcting the axial strain for apparatus compressibility within the control program during K_0 consolidation. RGoM-EI tests using side drainage were performed to evaluate the effects of excess pore pressure generation during K_0 consolidation, and to compare with the analytical correction and FEA simulations presented in chapters 6 and 7. All uncorrected results for tests without side drainage are presented in Appendix B.

9.2.1 Resedimented Boston Blue Clay: Apparatus Compressibility Correction

Three K_0 consolidation tests were conducted on RBBC accounting for apparatus compressibility within the triaxial control program. Two tests, TX1564 and TX1565, were consolidated to 5 MPa in the medium pressure triaxial system and one test, TX1531, was consolidated to 13.7 MPa in the high stress triaxial system.

Figure 9-1 compares the compression behaviour of these three triaxial tests to the average uniaxial compression curve for RBBC. The three tests are in relatively good agreement with the uniaxial compression curve. Both TX1564 and TX1565 curves are shifted slightly to the right of the uniaxial curve. The compression behaviour of TX1531 is initially in good agreement, however, near the end of consolidation the compressibility of the specimen increases slightly leading to the compression curve to fall below uniaxial. This concave down behaviour is not consistent with what we normally observe when consolidating RBBC, as the material usually has concave upwards behaviour.

Figure 9-2 shows a plot of K_0 versus σ'_a showing the evolution of the at rest lateral stress ratio over the course of each test. The at rest stress ratio experiences an initial decrease, as the specimen loads from hydrostatic stress conditions. Unlike previous testing, there is no

distinctive dip in K_0 values at the maximum stress reached during resedimentation (i.e., σ'_p). This is possibly due to issues with transducer signal noise which was encountered during the course of these tests. The maximum batching stress for TX1564 AND TX1565 were both 0.8 MPa. K_0 values for both TX1564 and TX1565 continue to decrease slightly with increasing stress. TX1531, which had a maximum batching stress of 5 MPa, reaches a minimum after which the K_0 values begin to increase gradually, with a sharp reduction in K_0 at σ'_a = 12.12 MPa. This sharp reduction is due to an issue with the control program and not reflective of material properties.

Figure 9-3 compares the K_0 value measured during the hold stress stage at the end of consolidation to individual test data points from previous research that did not account for apparatus compressibility in the triaxial control program. The three tests performed as part of this research all plot within experimental scatter from previous testing. TX1564 and TX1565 are in excellent agreement with past data. TX1531 plots on the low end of the scatter. This is most likely due to the issues with the control software.

Figure 9-4 shows a plot of normalized shear stress versus normalized average stress in MIT stress space. The normalized stress paths for the 3 K_0 consolidated tests show some scatter, however the slopes of each stress path are similar. TX1556, a 0.52 stress path test, was plotted for comparison.

Figure 9-5 shows a plot of strain versus axial effective stress for the consolidation portion of TX1565, comparing the measured axial strain to the calculated radial strain. Although radial strain controls K_0 behaviour, the axial strain is substantially larger than the radial strain. Therefore, in the case of triaxial K_0 consolidation, the plastic axial deformations dominate the K_0 behaviour of the specimen. This leads to the effects of the apparatus compressibility correction for axial strain leading to negligible changes in K_0 values. Therefore, the K_0 versus

axial stress relationships developed by previous researchers (Casey, 2014) for RBBC can be used to reliably predict the K_0 stress ratio at differing effective stresses.

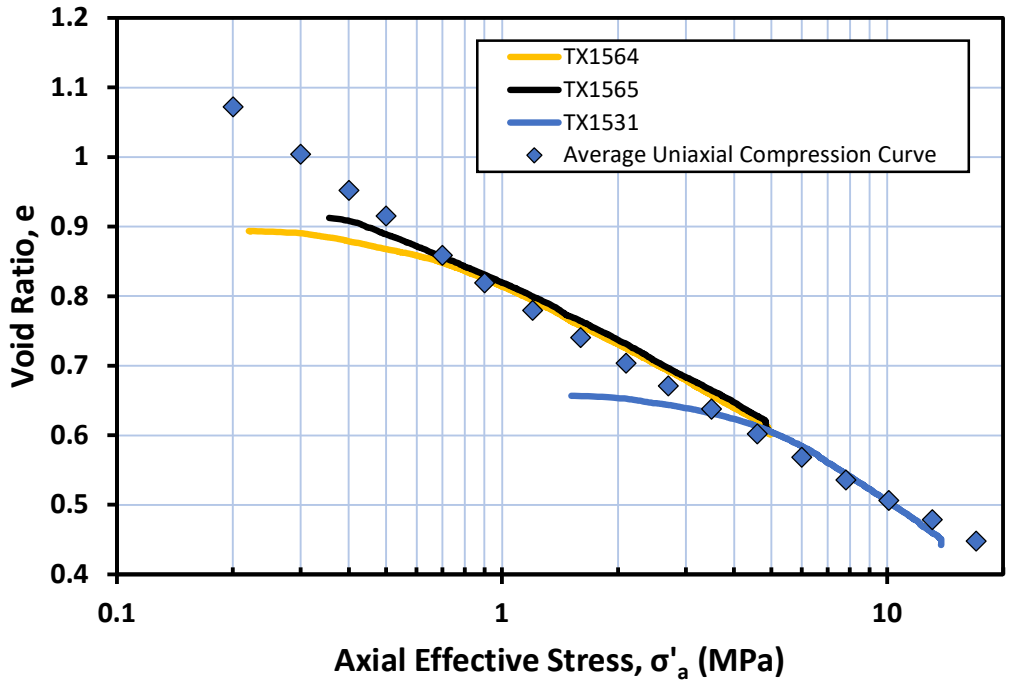

Figure 9-1 Void ratio versus axial effective stress for all K_0 consolidation tests performed on RBBC.

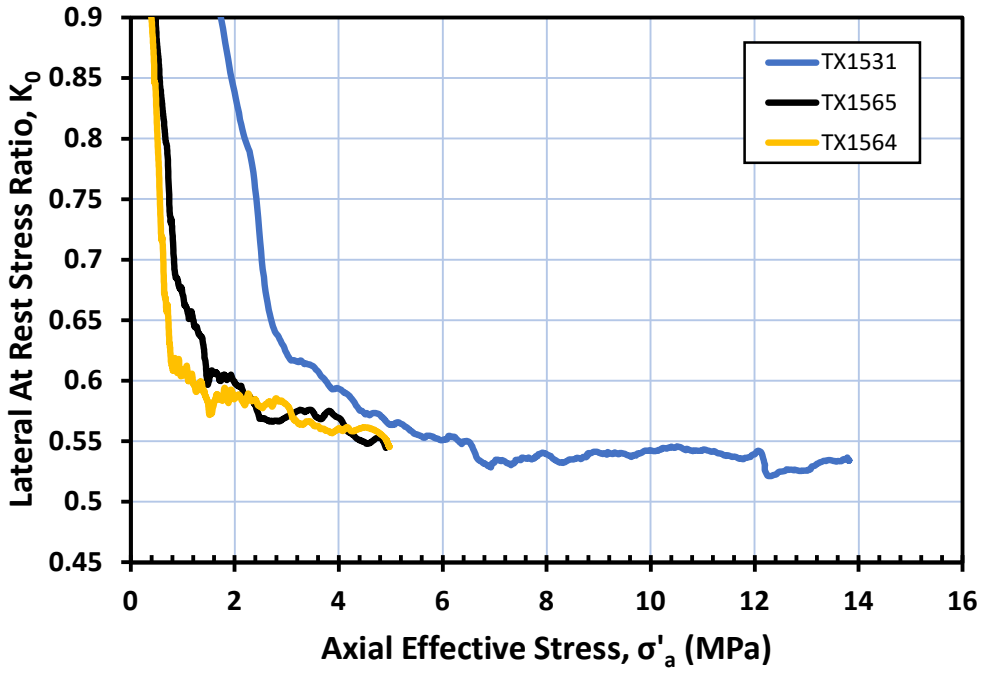

Figure 9-2 Lateral at rest stress ratio versus axial effective stress for RBBC.

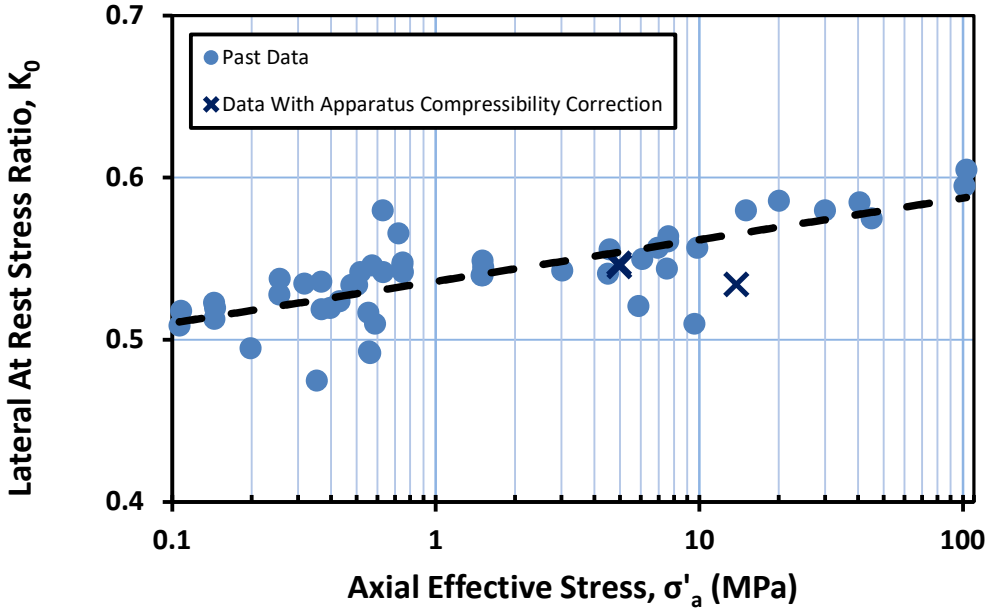

Figure 9-3 Lateral at rest stress ratio versus axial effective stress for RBBC comparing current testing with apparatus compressibility correction to previous data with no correction.

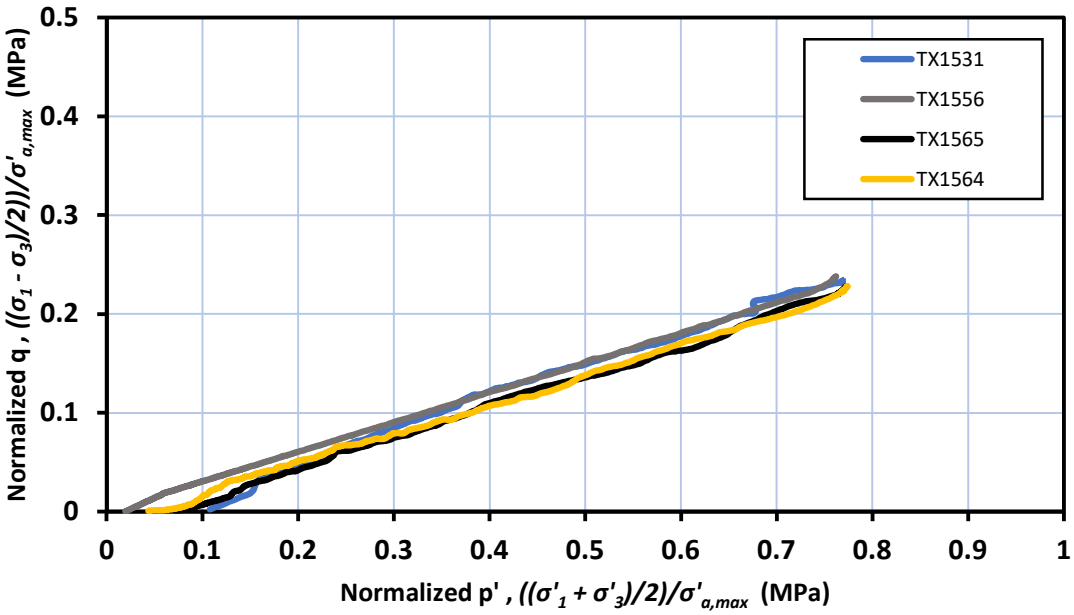

Figure 9-4 Normalized shear stress versus mean effective stress in MIT space showing consolidation stress paths for RBBC.

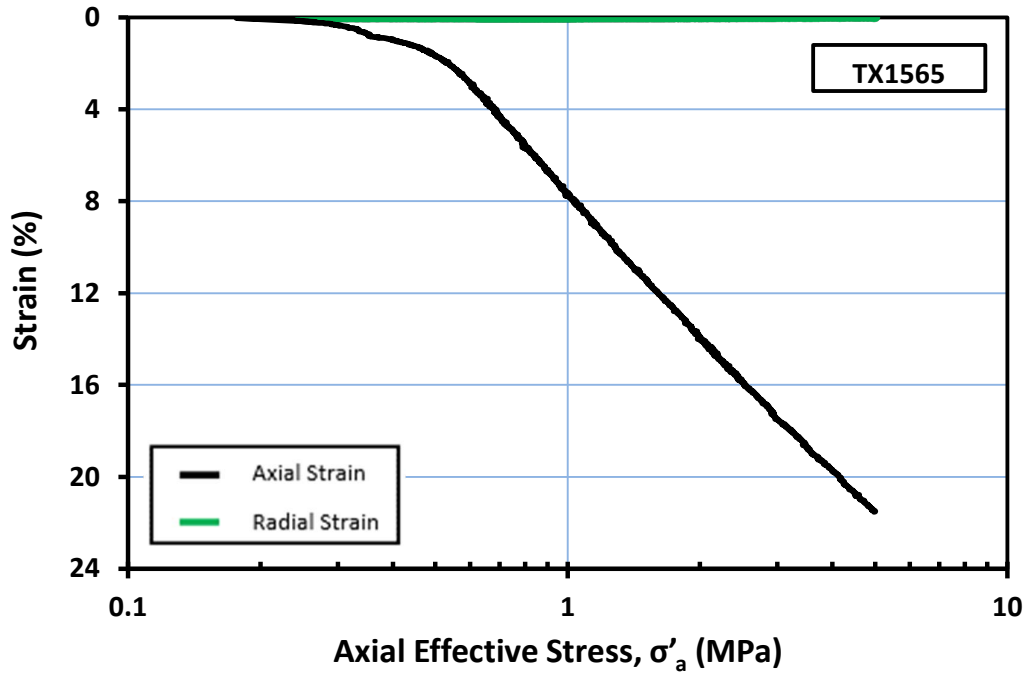

Figure 9-5 Comparison of radial strain and axial strain during the consolidation stage of TX1565.

9.2.2 Resedimented Gulf of Mexico, Eugene Island: Side Drain Implementation

Nine tests in total were successfully performed on RGoM-EI. This consisted of five tests conducted with the axial strain correction for apparatus compressibility: two in the high stress triaxial system (TX1541 and TX1550) and three in the medium stress triaxial system (TX1540, TX1548 and TX1551). These tests have all been corrected for excess pore pressure generation using the analytical method presented in Chapter 6. The uncorrected data are presented in Appendix B. Four tests were conducted utilizing geotextile side drains (TX1555, TX1559, TX1567, and TX1578). Due to control software issues and iterative improvements with each test, TX1559 and TX1578 will be used mainly for comparative purposes as these contain the most reliable data.

Figures 9-6 is a plot of the at rest lateral stress ratio versus axial effective stress showing the evolution in K_0 during the consolidation portions of TX1578 and TX1559. Both tests, as mentioned previously, utilized side drainage. The normally consolidated regime unaffected by sampling disturbance caused by extrusion from the resedimentation tubes and transfer to the triaxial system, is considered to be twice the maximum past pressure during reconsolidation ($2\sigma'_p$). The maximum batching stress for TX1559 and TX1578 were 0.4 MPa and 0.8 MPa respectively. The σ'_p coincides with the dip in K_0. For both of these tests, the $K_{0,NC}$ ranged from 0.60 at σ'_a = 0.90 MPa to 0.69 at σ'_a = 5.89 MPa. These ranges in $K_{0,NC}$ are markedly lower than those measured by (Hanley, 2017) and (Casey, 2014) of $K_{0,NC}$ = 0.61 at σ'_a = 0.1 MPa to 0.79 at σ'_a = 6 MPa.

Figure 9-7 compares the compression behaviour of both TX1578 and TX1559 to the average uniaxial compression curve from CRS and oedometer data for RGoM-EI. As can be seen, both tests are in excellent agreement with the uniaxial curve. This provides good evidence that uniaxial conditions were met during these two tests, and that there was negligible excess

pore pressure generation, leading to the conclusion that K_0 values measured during these tests are reasonable.

Figure 9-8 presents the compression behaviour of all tests without side drains and uncorrected for excess pore pressure generation. The uncorrected data lies to the left of the uniaxial compression curve indicating that measured axial effective stress, σ'_a, is larger than the actual effective stress within the specimen. Once these data are corrected for excess pore pressure generation (Figure 9-9) the compression curves decrease in σ'_a, providing much better agreement with the average uniaxial compression curve and the tests conducted with side drainage.

When comparing normalized stress paths (Figure 9-10), there are two distinct groups of stress paths for tests utilizing side drainage and uncorrected tests without side drainage respectively. The uncorrected tests are grouped below the side drainage tests, meaning that these tests developed less shear stress during consolidation and, hence, higher values of measured K_0. When these tests are corrected for excess pore pressure generation (Figure 9-11) the stress paths come within much better agreement with the tests utilizing side drainage. Figure 9-12 compares the normalized stress path of TX1578 (utilizing side drainage) to TX1566 (a cubic triaxial test conducted by George McAneny at the TAG Laboratory). TX1566 was shown to have negligible excess pore pressure generation in Chapter 6. These two normalized stress paths have excellent agreement with each other, providing further evidence in the reliability of TX1578 test data.

Figure 9-13 compares the K_0 values for TX1578 to K_0 values for TX1548 corrected for excess pore pressure generation. TX1548 (presented in Chapter 6) was run at an axial consolidation strain rate of 0.6%/hr and with calculated excess pore pressures at the centre of the specimen

of 1.52 MPa at the end of consolidation. The corrected TX1548 values of K_0 are in exceptional agreement with those values measured during TX1578.

Comparing TX1578 and TX1559 K_0 data to corrected K_0 data points from individual tests conducted from both this research and past research (Figure 9-15), both side drain tests are in excellent agreement with the corrected data with both tests K_0 measurements lying along the proposed log-fit curve for the corrected $K_{0,NC}$ data:

$$K_{0,NC} = 0.0961\, log_{10}\, \sigma'_{a\ (MPa)} + 0.6183 \qquad \textit{(Eq. 9-1)}$$

Similarly, when comparing all side drain data to the corrected K_0 data (Figure 9-15), both TX1559 and TX1578 data points (highlighted in yellow) are in exceptional agreement with the proposed log-fit curve (Equation 9-1). TX1555 and TX1567 both provide reasonable agreement, lying on the low side of the experimental scatter. This provides strong verification that the utilization of side drains is an effective method of reducing excess pore pressure generation in triaxial K_0 consolidation of RGoM-EI and provides further validation to the analytical method utilized in Chapter 6 for correcting triaxial test measurements for excess pore pressure generation. We can see that the fit provided in this research is 10.1% lower at σ'_a = 1 MPa and 15.7% lower at σ'_a = 100 MPa than the fit provided by (Casey, 2014).

Figure 9-16 compares the normally consolidation portions (i.e., data after $2\sigma'_p$) of TX1578 (with side drainage), corrected TX1541, and corrected TX1550 against the proposed $K_{0,NC}$ log-fit. As can be seen, the fit provides reasonable agreement for each of these normally consolidated portions, with fluctuations in the measured data due to control variations which are to be expected.

When utilizing side drains during triaxial K_0 consolidation, it is important to consider the volumetric compressibility of the side drain material in the triaxial control software if the condition of uniaxial strain is being maintained through keeping the changes in axial and volumetric strain constant to keep the cross-sectional area constant. If using an internal radial strain measurement device, accounting for volumetric compressibility of the side drain material becomes less important within the triaxial control software. However, it should be accounted for when reducing data after the test is performed, although ASTM D4767 does not mention the need for a correction to be performed.

TX1555 was a consolidation test utilizing side drainage but did not correct for the volumetric compressibility of the side drains within the control software. Figure 9-17 shows the compression behaviour of the corrected and uncorrected for volumetric compressibility of the side drains. The uncorrected data agrees well with the uniaxial average compression curve. However, once the data is corrected for side drain compressibility, the compression curve shifts up, as the void ratio is less than what was measured. Side drain compressibility also leads to an error in the measured K_0 (Figure 9-19) and similar to what was found by (Tsuchida and Kikuchi, 1991) could cause lower values of K_0 to be measured.

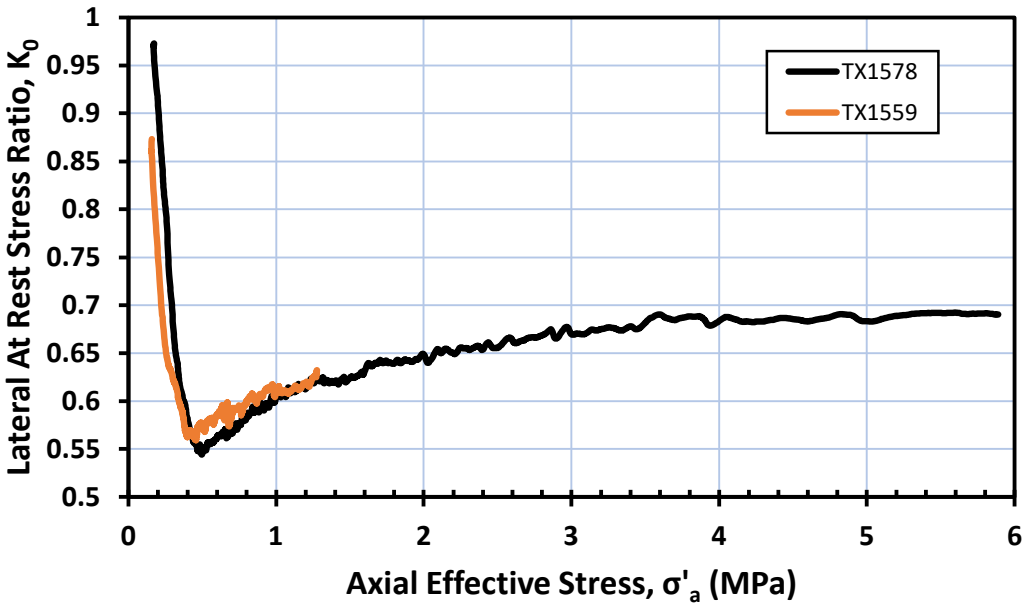

Figure 9-6 Lateral at rest stress ratio versus axial effective stress for TX1578 and TX1559.

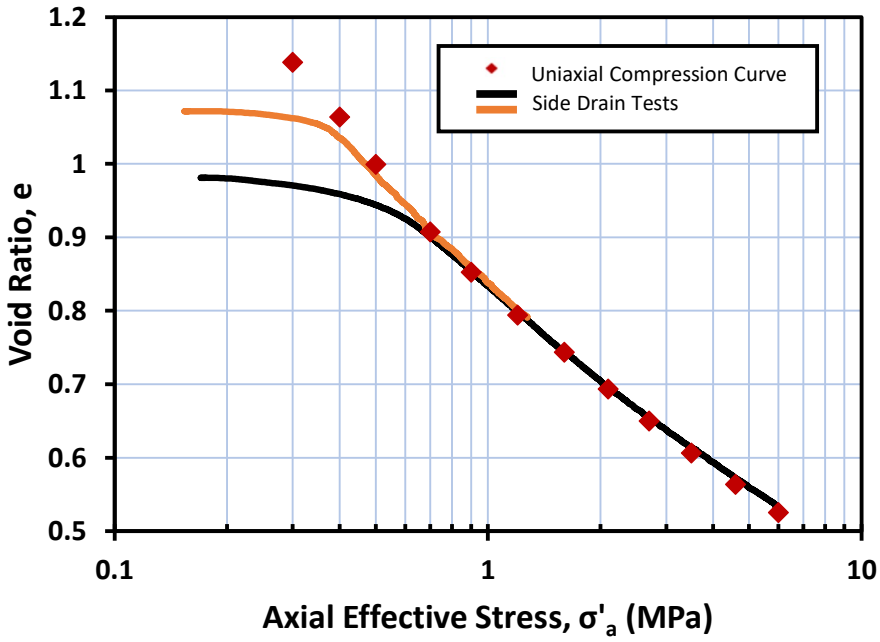

Figure 9-7 Void ratio versus axial effective stress comparing compression curves from side drain tests to average uniaxial compression curve.

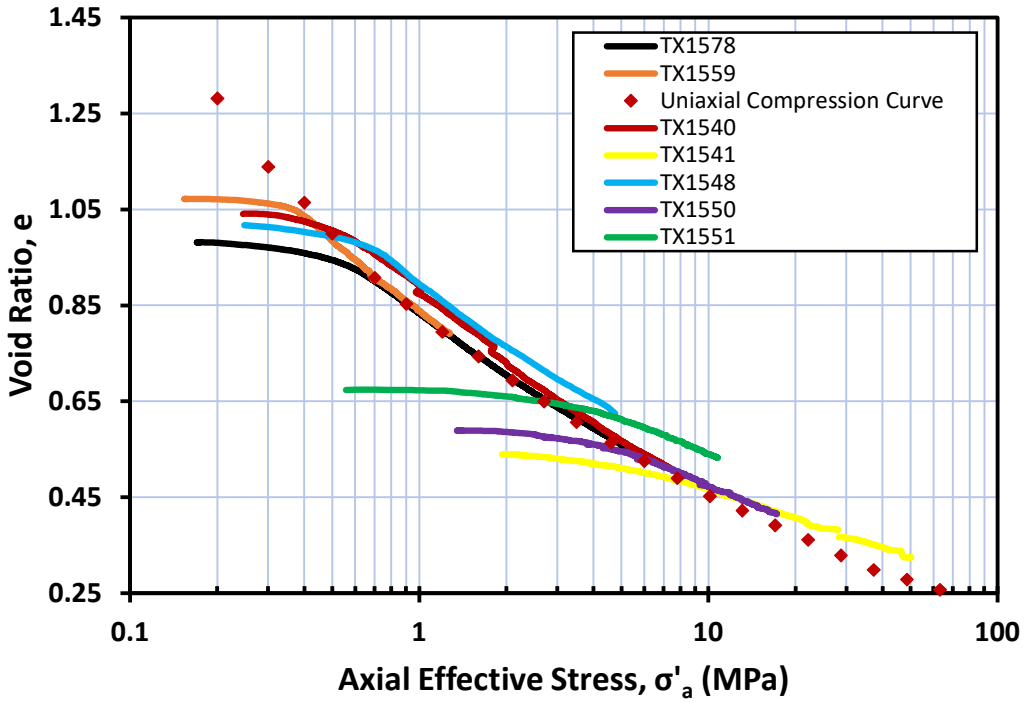

Figure 9-8 Void ratio versus axial effective stress comparing all tests to the average uniaxial compression curve for RGoM-EI.

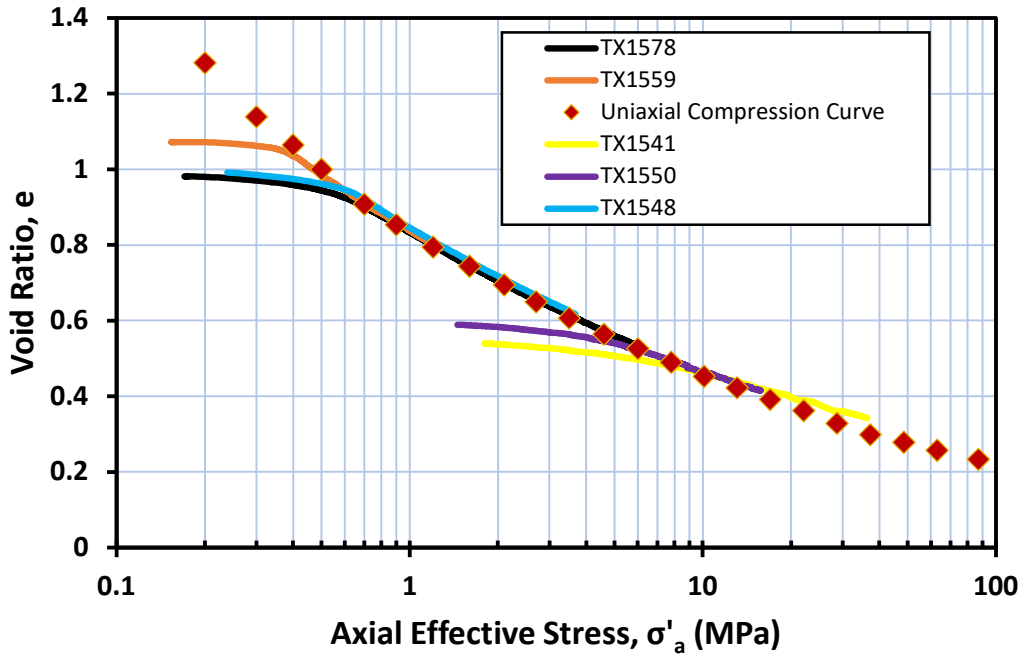

Figure 9-9 Void ratio versus axial effective stress comparing selected corrected data and side drain data to average uniaxial compression curve for RGoM-EI.

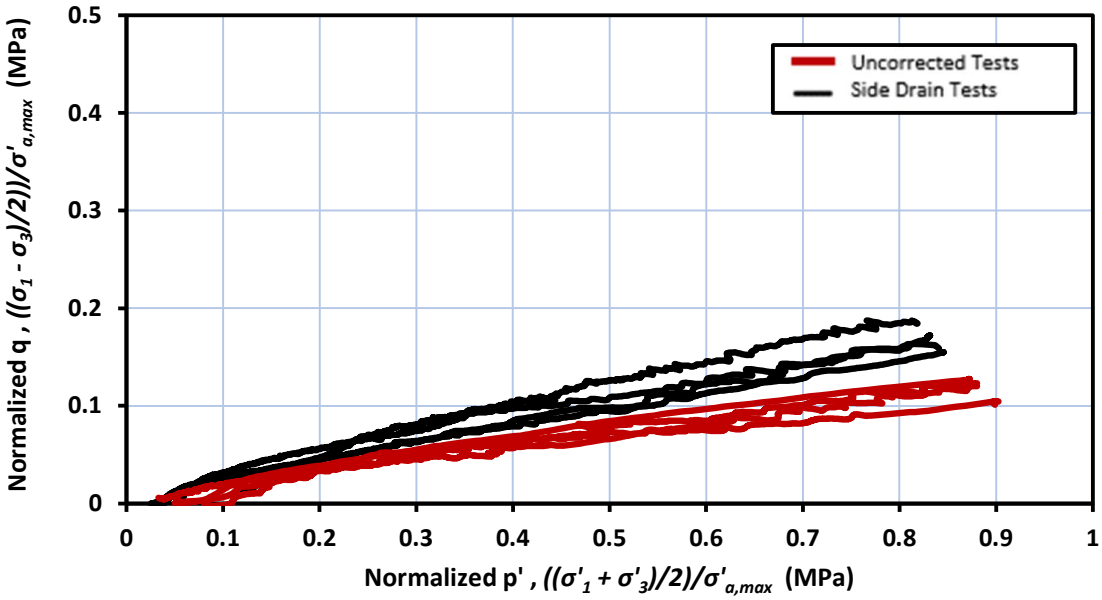

Figure 9-10 Normalized stress paths comparing tests on RGoM-EI with side drains and uncorrected tests with no side drains.

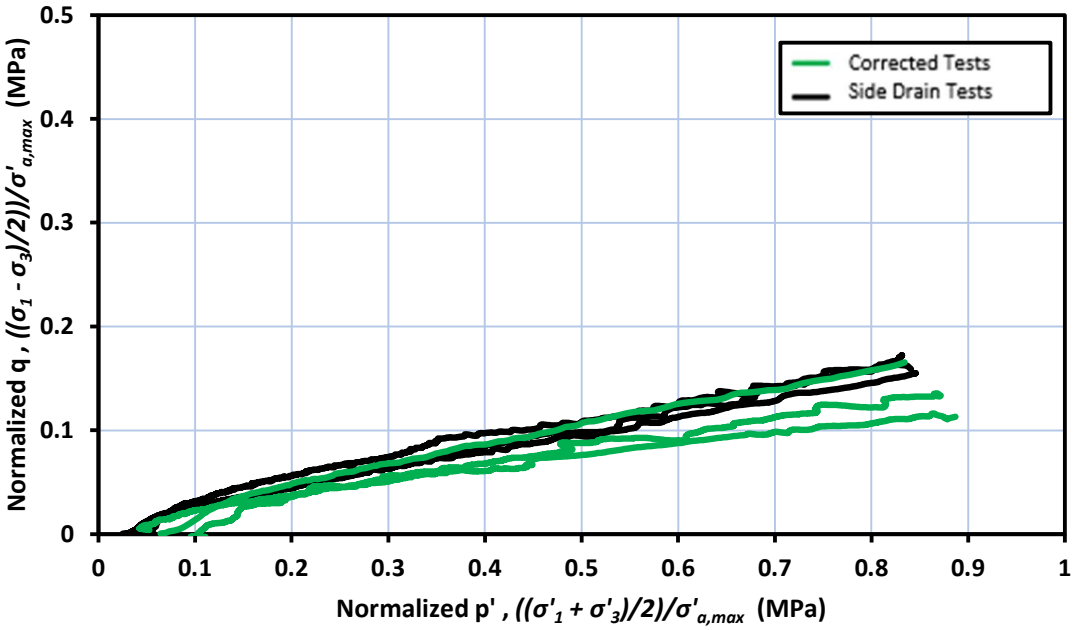

Figure 9-11 Normalized stress paths comparing tests on RGoM-EI with side drains and corrected tests with no side drains.

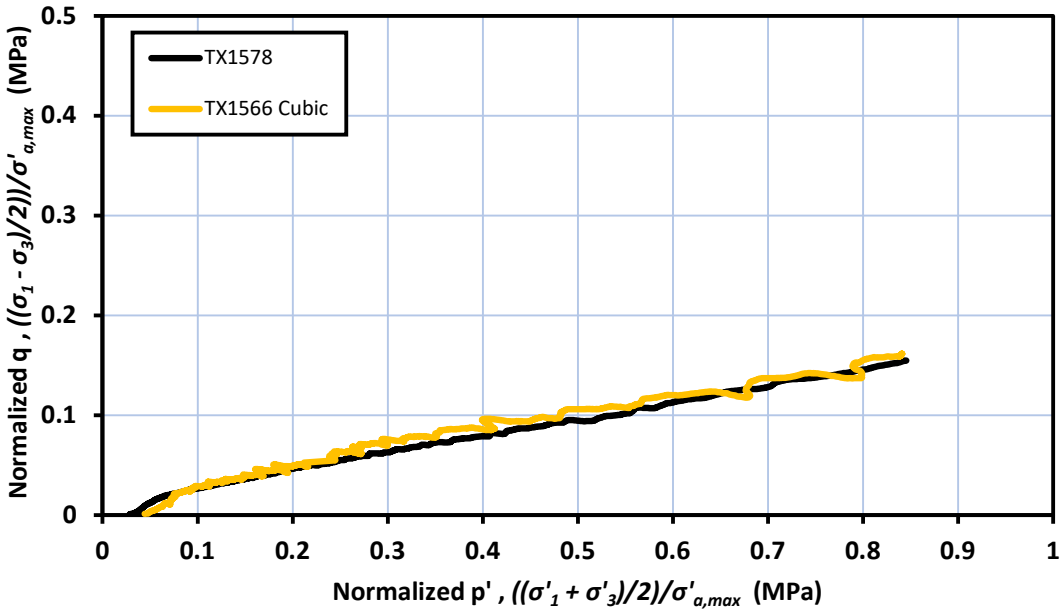

Figure 9-12 Comparison of test with side drains and cubic specimen TX1566 with low errors in effective stress.

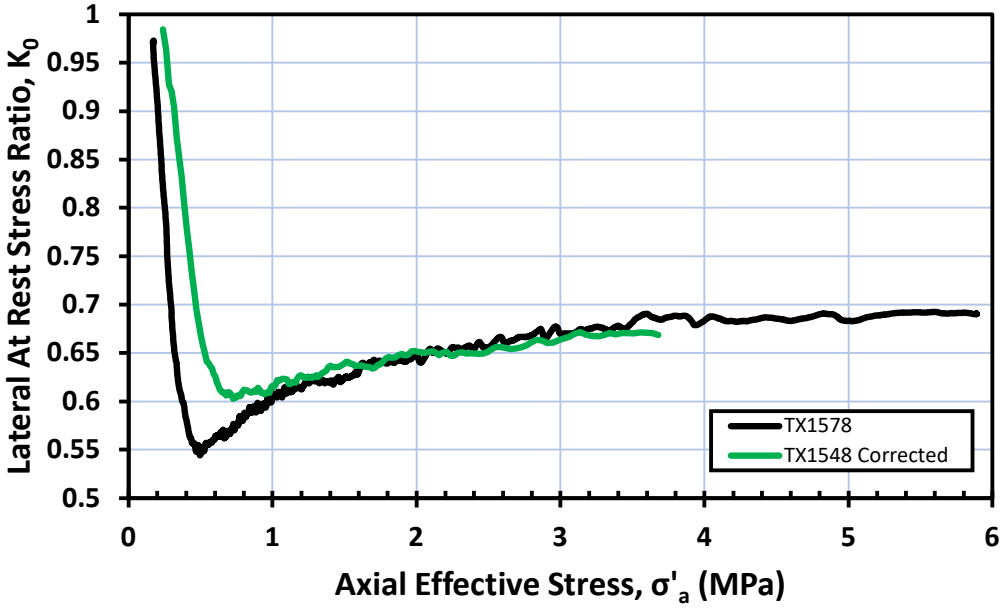

Figure 9-13 At rest lateral stress ratio versus axial effective stress comparing TX1578 with side drains to TX1548 corrected for excess pore pressure.

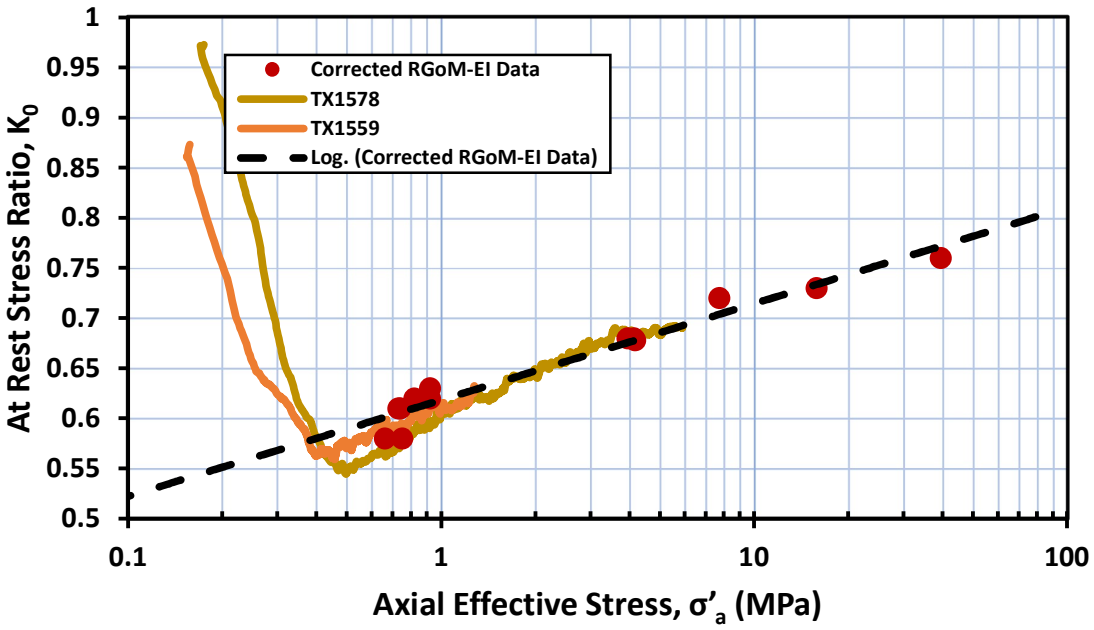

Figure 9-14 Comparison of TX1578 and TX1559 using side drains to data corrected for excess pore pressure.

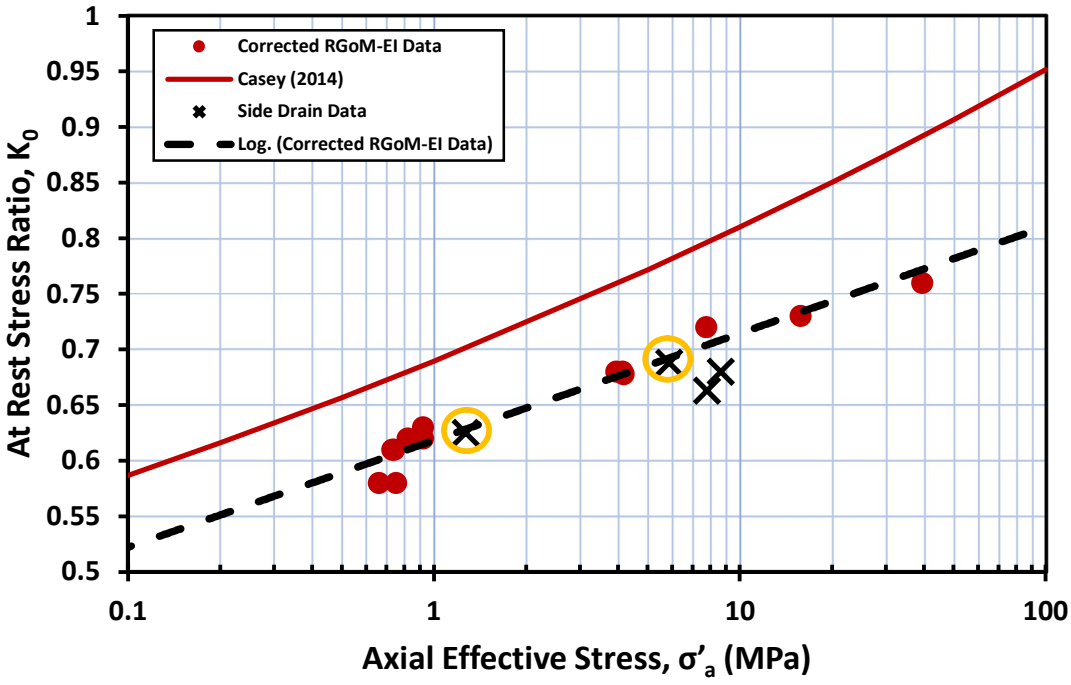

Figure 9-15 Comparison of all tests using side drains to data corrected for excess pore pressure.

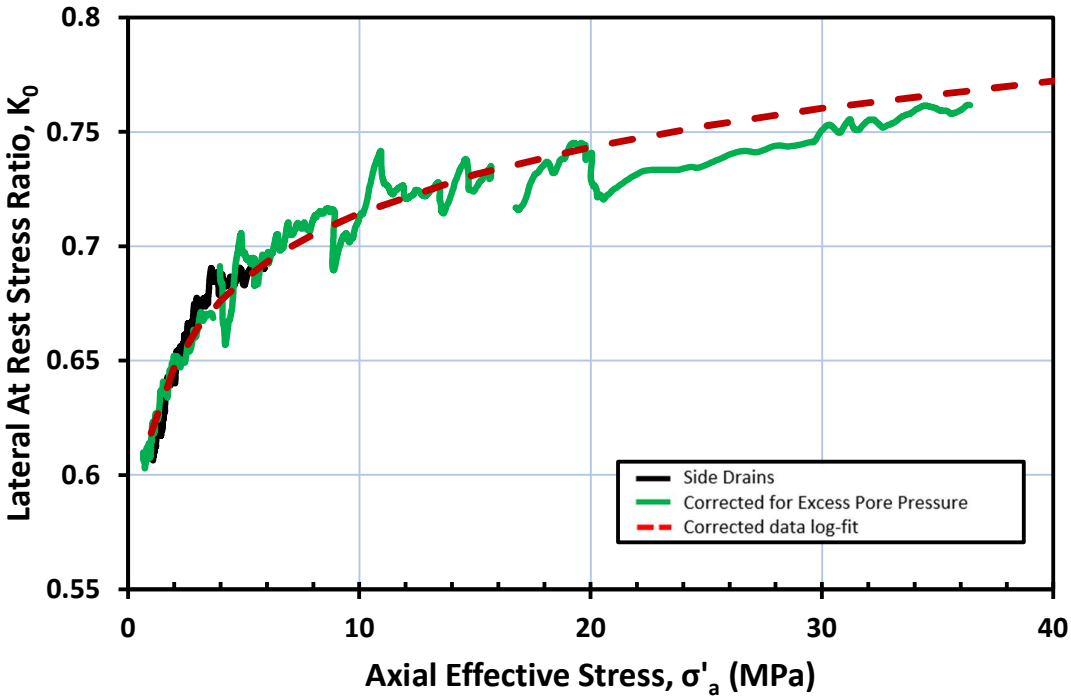

Figure 9-16 Comparison of TX1578 with side drains to selected corrected tests and $K_{0,NC}$ log-fit.

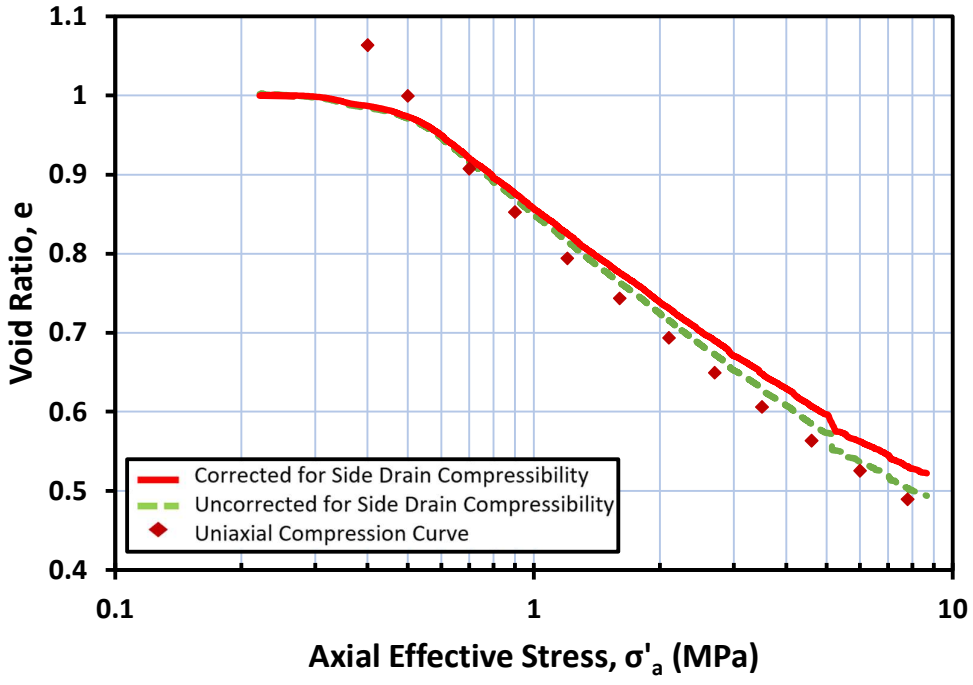

Figure 9-17 Comparison of the effects of side drain compressibility correction for TX1555.

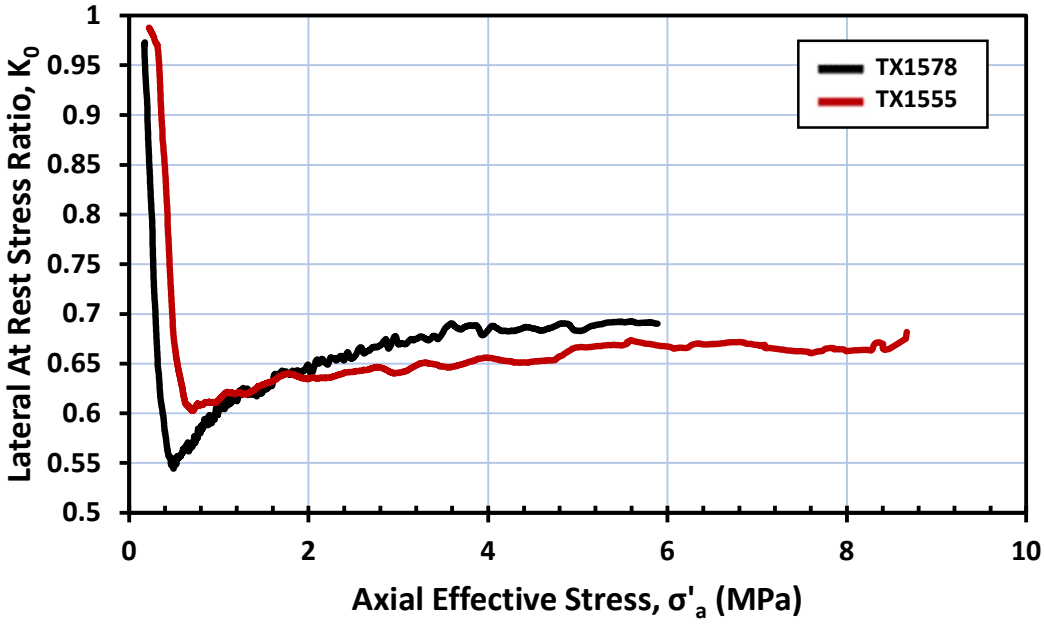

Figure 9-18 Comparison the effects of side drain compressibility on the at rest lateral stress ratio.

10 Conclusions and Recommendations

10.1 Conclusions

Two main errors in the K_0 triaxial testing protocol were discovered over the course of this research:

(1) the systematic radial contraction of specimens during triaxial K_0 consolidation due to the triaxial control programme not accounting for apparatus compressibility during axial strain calculations

(2) the generation of excess pore pressure within the specimen during K_0 consolidation of the low permeability clay RGoM-EI led to the calculated effective stresses being larger than those within the specimen.

Accounting for apparatus compressibility of the system within the triaxial control program during K_0 consolidation of RBBC has shown negligible effects on the measurement of $K_{0,NC}$. This is due to the large plastic axial deformation present during K_0 consolidation which dominate the K_0 behaviour of the material.

Geotextile side drains were found to be an effective method of reducing the excess pore pressure generation in RGoM-EI specimen during triaxial K_0 consolidation and allows for reliable measurements of axial and radial effective stress during consolidation. The use of side drains also allows an increase in allowable strain rates, as the generation of excess pore pressure is greatly reduced.

In this research, radial strain was maintained at a constant by keeping the change in axial strain equal to the change in volumetric strain. The volumetric strain of the specimen is the amount of pore fluid that is expelled from the specimen. However, the side drain material is a compressible material, and expels fluid as it compresses with increasing stress. Therefore, the

volumetric compressibility of the side drain material needs to be accounted for within the triaxial control programme in order to maintain uniaxial conditions. Not accounting for this will lead to lower measured K_0 values and will shift the compression behaviour of the material up in void ratio – log axial effective stress space. If the triaxial control program is using an internal radial strain measurement device to maintain uniaxial conditions, it is possible to neglect this side drain compressibility in the triaxial control program. It should be accounted for when reducing the test data after the test has been performed, in order to calculate reliable void ratios.

The analytical approach of quantifying excess pore pressure generation within a specimen using the Wissa Linear Theory was verified through comparison with experimental testing using side drainage. This method can be used to re-calculate effective stresses in past data sets and provide corrected compression and K_0 behaviour by computing the average effective stress in the specimen during experimental testing based on predicted pore pressure distributions.

Abaqus FEA was utilized to simulate past triaxial experimental tests and evaluate excess pore pressure generation during K_0 consolidation using its Modified Cam-Clay framework. These simulations were shown to agree with the analytical approach based on the Wissa Linear Theory, thereby substantiating the software's use for future research.

The K_0 behaviour of RGoM-EI, although still exhibiting stress dependency, was found to be different than that measured by previous researchers (Casey, 2014), (Hanley, 2017), with lower values of $K_{0,NC}$ over a stress range of 1 MPa to 40 MPa. This was due to excess pore pressure generation in the specimen leading to errors in the measurement of effective stresses. A new $K_{0,NC} - \sigma'_a$ relationship for RGoM-EI has been presented in this research.

10.2 Recommendations for Future Work

Based on the material presented in this research, the author suggests the following areas should be further investigated in future work:

- During this research, the author began the development of an internal radial strain measurement device in order to confirm that uniaxial conditions are being maintained during triaxial K_0 consolidation. The development of this device should be continued in future research.
- Further triaxial K_0 consolidation testing utilizing side drainage should be performed on RGoM-EI for the 0.1 to 1 MPa stress range to quantify the K_0 behaviour at these lower stress levels as the author cannot with confidence state that the new $K_{0,NC} - \sigma'_a$ relationship for RGoM-EI presented in this research applies to those lower stress levels. Furthermore, additional triaxial K_0 consolidation testing should be performed utilizing side drains in the 10 to 100 MPa stress range to further confirm what was shown in this research.
- This research focused on the K_0 consolidation portion of triaxial tests, however, did not look at the shear behaviour of fine-grained soils. Investigations into the undrained and drained shear behaviour of RGoM-EI should be performed in the future. These could quantify the effects of side drains on shear behaviour, provide strength corrections for the side drain strips, and explore the yield surface, and critical state friction angle of normally consolidated RGoM-EI in K_0 conditions. The author suspects that future research will find K_0 consolidated specimens sheared in the normally consolidated regime will exhibit lower undrained compressive strength and higher strength in undrained extension as during the hold stress stage of testing prior to undrained shearing, the specimen was allowed to drain excess pore pressure, leading to higher stress ratio values.

11 References

Abdulhadi, N. O. (2009). *An experimental investigation into the stress-dependent mechanical behavior of cohesive soil with application to wellbore instability* (thesis).

ASTM International. (2021). ASTM D7928-21e1 Standard Test Method for Particle-Size Distribution (Gradation) of Fine-Grained Soils Using the Sedimentation (Hydrometer) Analysis. *Annual Book of ASTM Standards*.

ASTM International. (2014). ASTM D854-14 Standard Test Methods for Specific Gravity of Soil Solids by Water Pycnometer. *Annual Book of ASTM Standards*.

ASTM International. (2017). "D4318-17e1 Standard Test Methods for Liquid Limit, Plastic Limit, and Plasticity Index of Soils. *Annual Book of ASTM Standards*.

ASTM International. (2020). ASTM D4767-11 Standard Test Method for Consolidated Undrained Triaxial Compression Test for Cohesive Soils. *Annual Book of ASTM Standards*.

ASTM International. (2020). D4186-20e1 Standard Test Method for One-Dimensional Consolidation Properties of Saturated Cohesive Soils Using Controlled-Strain Loading. *Annual Book of ASTM Standards*.

Bailey, W. A. (1961). *The effects of salt on the shear strength of Boston Blue Clay* (thesis).

Berman, D. R. (1993). *Characterization of the engineering properties of Boston Blue Clay at the MIT Campus* (thesis).

Betts, W. S. (2014). *Compressibility and Permeability of Gulf of Mexico Mudrocks, Resedimented and In-Situ.* (thesis).

Bishop, A. W. (1973). The influence of an undrained change in stress on the pore pressure in porous media of low compressibility. *Géotechnique*, *23*(3), 435–442. https://doi.org/10.1680/geot.1973.23.3.435

Bishop, A. W. (1976). The influence of system compressibility on the observed pore-pressure response to an undrained change in stress in Saturated Rock. *Géotechnique*, *26*(2), 371–375. https://doi.org/10.1680/geot.1976.26.2.371

Bishop, A. W. (1976). The influence of system compressibility on the observed pore-pressure response to an undrained change in stress in Saturated Rock. *Géotechnique*, *26*(2), 371–375. https://doi.org/10.1680/geot.1976.26.2.371

Bishop, A. W., & Gibson, R. E. (1963). The influence of the provisions for boundary drainage on strength and consolidation characteristics of soils measured in the triaxial apparatus. *Laboratory Shear Testing of Soils*. https://doi.org/10.1520/stp30020s

Bishop, A. W., & Henkel, D. J. (1962). *The measurement of soil properties in the triaxial test* (2nd ed.). Edward Arnold.

Bjerrum, L., & Andersen, K. (1972). In-situ measurement of lateral pressures in clay, in Proc. 5th European Conference SMFE, Madrid, Vol. 1, Spanish Society SMFE, Madrid, pp. 11–20.

Brooker, E. W., & Ireland, H. O. (1965). Earth pressures at rest related to stress history. *Canadian Geotechnical Journal*, *2*(1), 1–15. https://doi.org/10.1139/t65-001

Casey, B. (2011). *The significance of specimen end restraint in high pressure triaxial testing of cohesive soil* (thesis).

Casey, B. (2014). *The consolidation and strength behavior of mechanically compressed fine-grained sediments* (thesis).

Casey, B., & Germaine, J. T. (2014). An evaluation of three triaxial systems with results from 0.1 to 100 MPA. *Geotechnical Testing Journal*, *37*(6), 20130178. https://doi.org/10.1520/gtj20130178

Flemings, P. B. (2001). Consolidation state, permeability, and stress ratio as determined from uniaxial strain experiments on mudstone samples from the Eugene Island 330 area, offshore louisiana. (2001). *Pressure Regimes in Sedimentary Basins and Their Prediction*, 131–144. https://doi.org/10.1306/m76870c13

David Suits, L., Sheahan, T. C., Yune, C.-Y., & Chung, C.-K. (2005). Consolidation test at constant rate of strain for radial drainage. *Geotechnical Testing Journal*, *28*(1), 11922. https://doi.org/10.1520/gtj11922

Donath, A. (1981). Untersuchungen uber den Erddruck auf Stiitzwande. *Zeitschrift Fur Bauwesen*, *41*, 491–518.

Eagle, L. (2021). *Characterising the Gulf of Mexico Yield Surface at High Stress* (thesis).

Force, E. (1998). *Factors controlling pore pressure generation during k_0 consolidation of laboratory tests* (thesis).

Flemings, P. B. (2021). *A concise guide to geopressure: Origin, prediction, and applications*. Cambridge University Press.

Germaine, J. T., & Germaine, A. V. (2009). *Geotechnical Laboratory measurements for Engineers*. John Wiley.

Germaine, J. T. (2015). Trends in Mechanically Compressed Sediment Behavior with Stress and Plasticity. *2015 Charles C. Ladd Lecture*.

Gonzalez, J. (2000). *Experimental and Theoretical Investigation of Constant Rate of Strain Consolidation* (Thesis).

Hanley, A. J. (2017). *The Characterization of the Yield Surface for Fine-Grained Sediments* (thesis).

Heidari, M., Nikolinakou, M. A., & Flemings, P. B. (2020). Modified cam-clay model for large stress ranges and its predictions for geological and drilling processes. https://doi.org/10.1002/essoar.10501743.1

Horan, A. J. (2012). *The Mechanical Behavior of Normally Consolidated Soils As A Function Of Pore Fluid Salinity* (thesis).

Jaky, J. (1944). A nyugalmi nyomas tenyezoje (The coefficient of earth pressure at rest).

Kenney, T. C. (1964). Sea-level movements and the geologic histories of the post-glacial marine soils at Boston, Nicolet, Ottawa and Oslo. *Géotechnique*, *14*(3), 203–230. https://doi.org/10.1680/geot.1964.14.3.203

Knappett, J., Craig, R. F., & Craig, R. F. (2013). *Craig's Soil Mechanics*. CRC Press.

Knodel, P. C., Oswell, J. M., Graham, J., Lingnau, B. E., & King, M. W. (1991). Use of side drains in triaxial testing at moderate to high pressures. *Geotechnical Testing Journal*, *14*(3), 315. https://doi.org/10.1520/gtj10576j

Ladd, C. C., & Varallyay, J. (1965). (rep.). *The Influence of Stress System on the Behavior of Saturated Clays during Undrained Shear*. Soils Publication No. 177.

Ladd, C. C., Foot, R., Ishihara, K., Schlosser, F., & Poulos, H. G. (1977). 9th International Conference on Soil Mechanics and Foundation Engineering (Vol. 2). Erscheinungsort nicht ermittelbar; Verlag nicht ermittelbar.

Leroueil, S., Tavenas, F., La Rochelle, P., & Tremblay, M. (1988). Influence of filter paper and leakage on triaxial testing. *Advanced Triaxial Testing of Soil and Rock*. https://doi.org/10.1520/stp29078s

Losh, S., & Wood, J. (1995). Brine Chemistry, Blocks 330 and 316, Results of the Pathfinder drilling program into a major growth fault. *AAPG Bulletin*, *82*, 1694–1710.

Massarsch, K. R., & Broms, B. B. (1976). Lateral Earth pressure at rest in Soft Clay. *Journal of the Geotechnical Engineering Division*, *102*(10), 1041–1047. https://doi.org/10.1061/ajgeb6.0000329

McAneny, G. T. (2022). *Sensitivity of Shear and Longitudinal Wave Velocities to Compression and Shear Stress Paths in Cohesive Soils* (thesis).

Mesri, G., & Hayat, T. M. (1993). The coefficient of earth pressure at rest. *Canadian Geotechnical Journal*, *30*(4), 647–666. https://doi.org/10.1139/t93-056

Nordquist, T. J. (2015). *Permeability anisotropy of resedimented mudrocks* (thesis).

Phillips, I. M. (2009). Report on the Bulk and <2 Micron Clay Sized Fraction Mineralogy of Seven Samples by X-ray Powder Diffraction (XRPD): Craigiebuckler, Aberdeen, Scotland, Macaulay Scientific Consulting Ltd.

Phillips, I. M. (2011). Report on the Whole Rock and <2 Micron Clay Fraction Mineralogy of a Single Sample by X-Ray Powder Diffraction (XRPD): Craigiebuckler, Aberdeen, Scotland, Macaulay Scientific Consulting Ltd.

Potts, D., & Zdravkovic, L. (1999). Some Pitfalls when using Modified Cam Clay.

Roscoe, K. H., & Burland, J. B. (1968). *On the generalized stess-strain behaviour of 'wet' clay: Engineering plasticity. papers for a conference held in Cambridge March 1968*. University Press.

Santagata, M. C. (1999). *Factors affecting the initial stiffness and stiffness degradation of cohesive soils* (thesis).

Santagata, M. C., & Germaine, J. T. (2002). Sampling disturbance effects in normally consolidated clays. *Journal of Geotechnical and Geoenvironmental Engineering*, *128*(12), 997–1006. https://doi.org/10.1061/(asce)1090-0241(2002)128:12(997)

Schmertmann, J. H. (1955). The undisturbed consolidation behavior of clay. *Transactions of the American Society of Civil Engineers*, *120*(1), 1201–1227. https://doi.org/10.1061/taceat.0007231

Schofield, A. N., & Wroth, P. (1968). *Critical State Soil Mechanics*. McGraw-Hill.

Sheahan, T. C. (1991). *An Experimental Study of the Time-Dependent Undrained Shear Behaviour of Resedimented Clay Using Automated Stress-Path Triaxial Equipment* (thesis).

Skempton, A. W. (1954). The Pore-Pressure Coefficients A and B. *Géotechnique*, *4*(4), 143–147. https://doi.org/10.1680/geot.1954.4.4.143

Terzaghi, C. (1923). Discussion on Lateral Earth Pressure: The accurate experimental determination of the lateral earth pressure, together with a resume of previous experiments. *Transactions of the American Society of Civil Engineers*, *86*(1), 1525–1546. https://doi.org/10.1061/taceat.0003338

Tsuchida, T., & Kikuchi, Y. (1991). K0 consolidation of undisturbed clays by means of triaxial cell. *Soils and Foundations*, *31*(3), 127–137. https://doi.org/10.3208/sandf1972.31.3_127

Whitman, R., & Lambe, T. (1969). *Soils Mechanics*. J. Wiley.

Wissa, A. E., Christian, J. T., Davis, E. H., & Heiberg, S. (1971). Consolidation at constant rate of strain. *Journal of the Soil Mechanics and Foundations Division*, *97*(10), 1393–1413. https://doi.org/10.1061/jsfeaq.0001679

Appendix A FEA Methodology

A.1 **Introduction**

Abaqus FEA was utilized to run simulations of different tests under differing drainage conditions using its inbuilt MCC framework. This appendix will provide a step-by-step guid to how these simulations were performed. First, a description of each part will be provided, the steps utilized, then details on the boundary conditions used for each simulation, next the applied loads and finally the material input parameters.

A.2 **Part Description**

Three types of models were used during this research. The cubic specimen, TX1566, was simulated using a plane strain model. TX1548 was a standard cylindrical specimen, so was simulated using an axisymmetric model. The case utilizing side drains was modelled using a 3-dimensional model.

The options for this are shown in Figure A-1. Once the choice is made, the part can be sketched and extruded if 3-D. In the case of the 3-D model, two parts were sketched. These were then merged to remove the need for describing surface contact and partitioned to allow individual material descriptions for the soil and side drains.

After the parts are described, the user must go to the Assembly tab and create an instance for the model part.

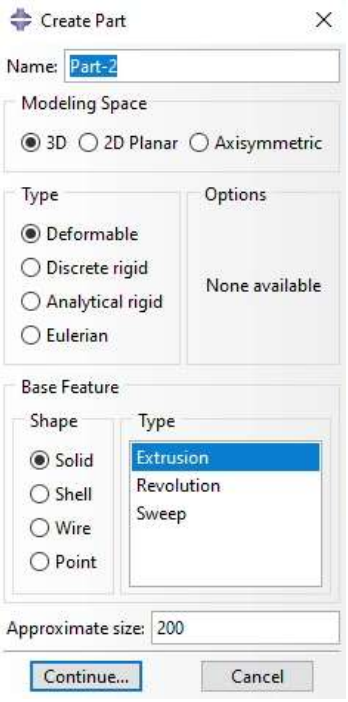

Figure 11-1 Create Part window.

A.3 **Steps**

Using the Step Manager tab, each step for the simulation can be created. Figure A-2 shows the steps used for each simulation. Non-linear geometry was turned on for each step. For the clay plasticity material parameter to be used, the user must define an initial geostatic step, to apply the in-situ or pressure-up stresses. The transient condition soils consolidation step (Figure A-3) time period is chosen to match the length of time for each test. This is done to achieve the required strain rate. Within the incrementation tab (Figure A-4), the maximum number of increments for the steps can be chosen, along with the maximum and minimum increment size. It is important to select a reasonable value for the maximum pore pressure for each increment. This is dependent on the strain rate applied, the material permeability and the consolidation stresses.

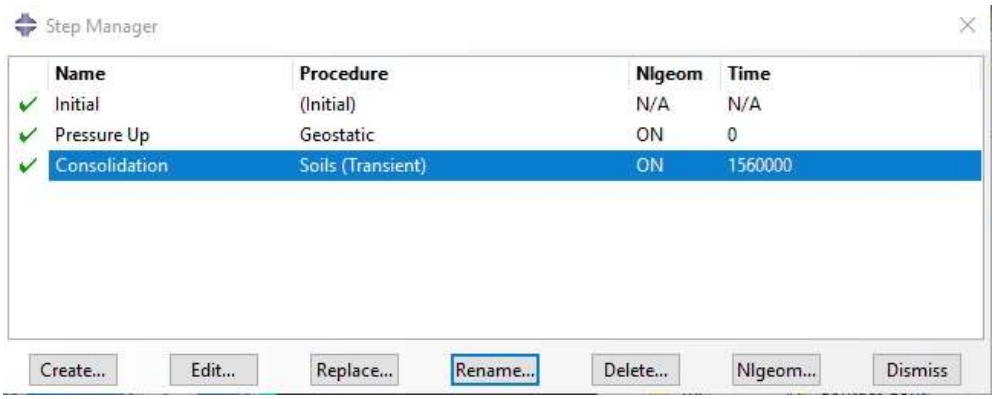

Figure 11-2 Step Manager Window

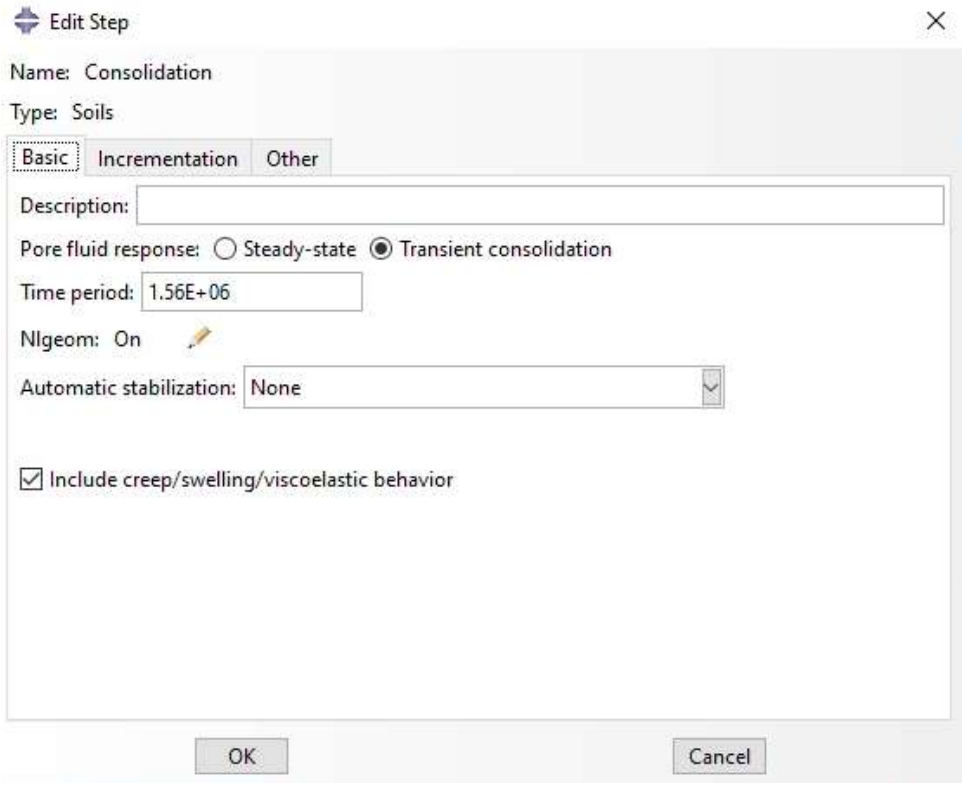

Figure 11-3 Edit Step Window Basic

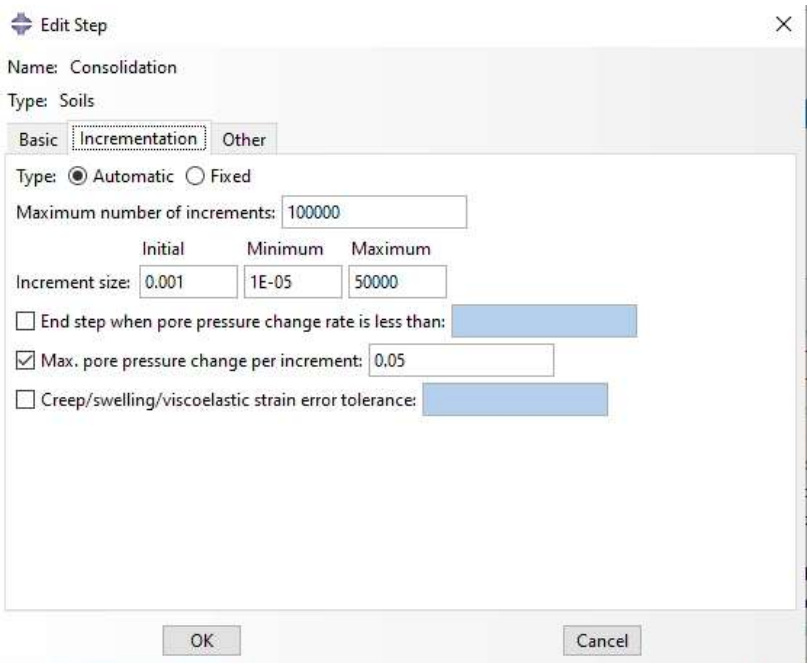

Figure 11-4 Edit Step Incrementation

A.4 **Boundary Conditions**

Figure A-5 shows the boundary conditions imposed for the plane strain model. For this model (Figure A-8), both the sides were fixed in the U1 direction. The bottom was fixed in both the U1 and U2 directions. The vertical drainage condition was imposed during this simulation, so the bottom and top surfaces were allowed to drain i.e., pore pressure was set to 0. During the consolidation step, a displacement was placed on the specimen in the U2 direction. This displacement matched the final displacement achieved in the experimental test being modelled. It's important to ensure that this displacement is ramped linearly over the course of the step to ensure constant rate of strain. The axisymmetric model (Figure A-6) had similar boundary conditions, however only one side needed to be fixed in the U1 direction. The other side lay along the axis of symmetry and had an X-Symmetry boundary condition. For the

simulation of the vertical drainage condition scenario, the pore pressure was set to 0 at the top and bottom surfaces. In the radial drainage scenario, the left edge was set to 0.

The boundary conditions for the 3-D deformable model (Figure A-7) were more complex than the previous two models. This was due to more complex geometry and the introduction of the side drains. One eighth of the specimen was modelled for efficiency, meaning one of the eight side drains used on a triaxial test specimen.

Figure A-9 shows the Boundary Condition manager for this simulation. Again, the bottom is fixed in all directions. The external perimeter, including the side drain, is fixed in the U1 and U2 directions, and free in the U3 direction. On each side of the "pie slice", a Z-Symmetry boundary condition is imposed. The pore pressure at the top and bottom boundaries was set to 0. Like the previous two models, an axial displacement was applied. In this case it was applied to produce a strain rate of 0.6 %/hr.

For all models, the initial state of the simulation must be set. Figure A-10 shows the Predefined Field Manager window, where the initial void ratio and geostatic stress were set. In the case of the 3-D simulation of the side drain test, this must be performed for both the geotextile side drain material and the soil.

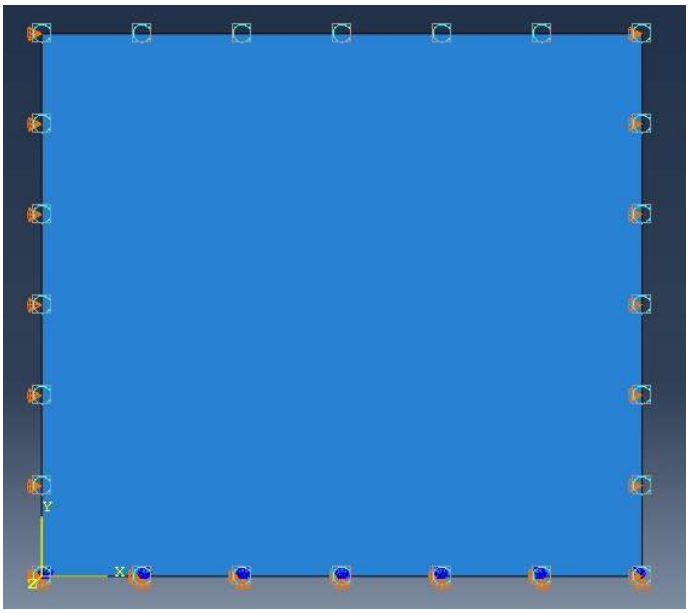

Figure 11-5 Plane strain boundary conditions.

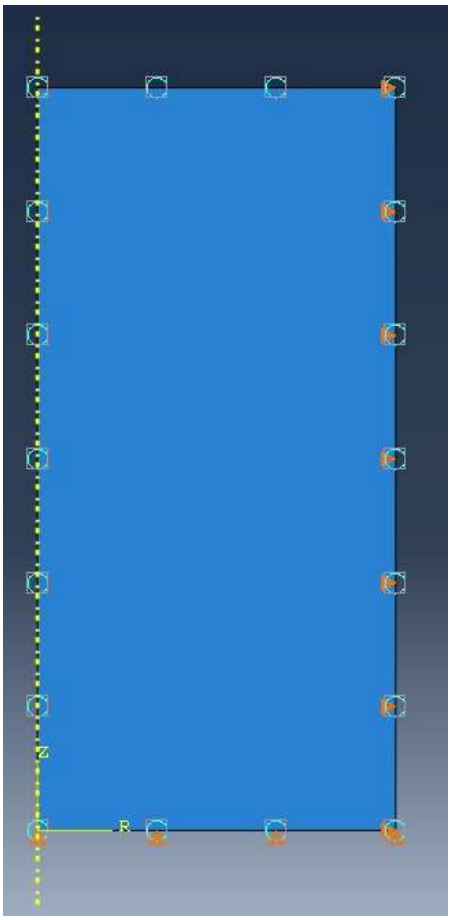

Figure 11-6 Axisymmetric boundary conditions

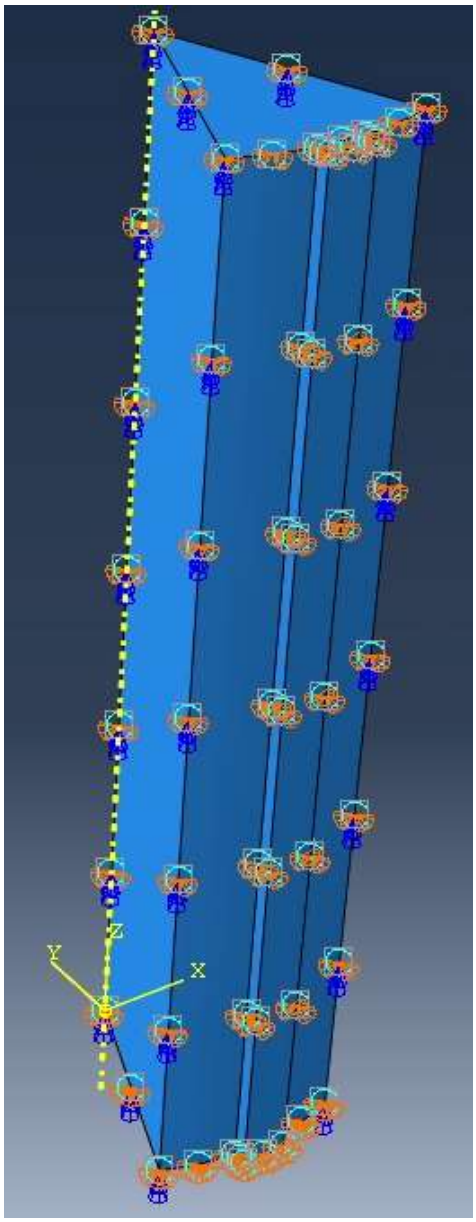

Figure 11-7 3-D deformable boundary conditions.

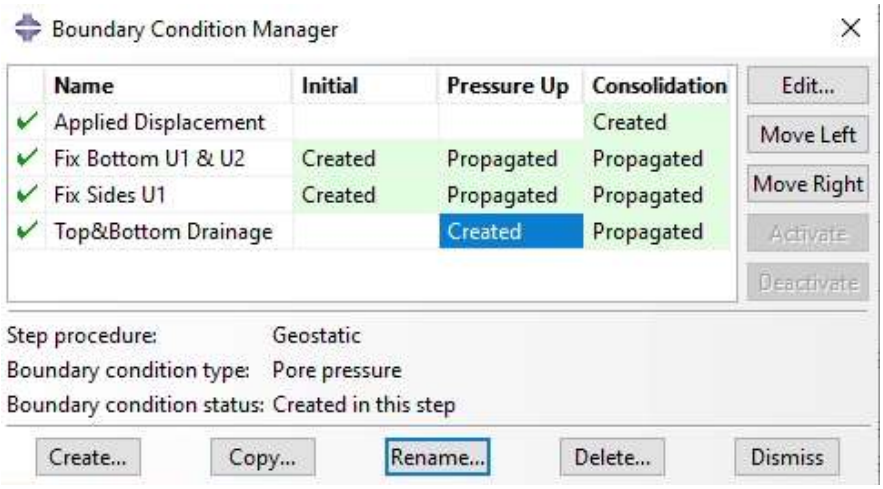

Figure 11-8 Boundary Condition Manager Window for plane strain and axisymmetric models.

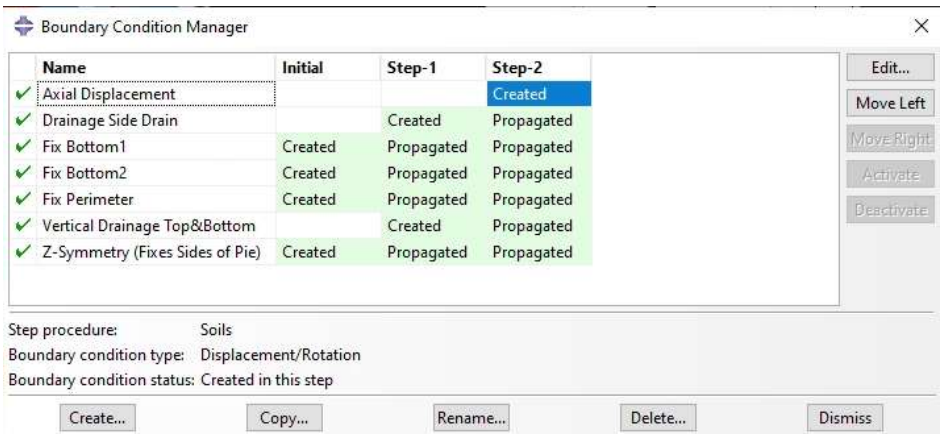

Figure 11-9 Boundary Condition Manager for 3-D deformable model.

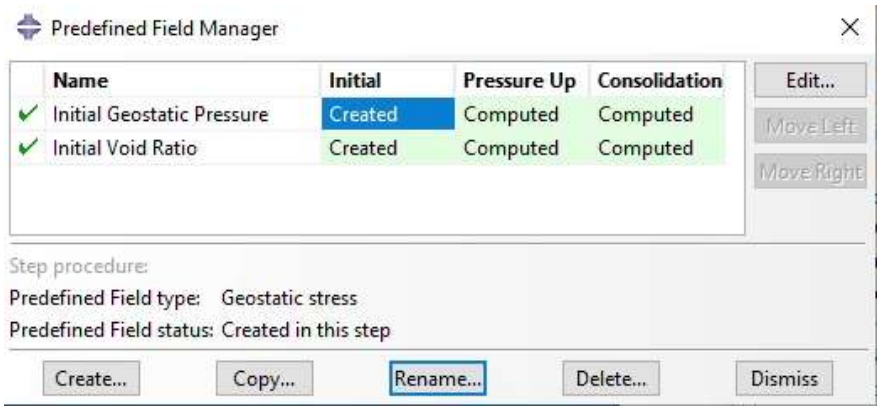

Figure 11-10 Predefined Field Manager.

A.5 **Material Properties**

When assigning material properties in the Properties tab, the user must first create individual sections for each material definition by selecting the portion of the part that a particular material definition is to be applied to, and then assigning it a section (Figure A-11).

The soil was then modelled as porous elastic, clay plastic (MCC framework), and a permeable medium. The porous elastic (Figure A-13) and permeability (Figure A-14) definitions were identical for all models used. Hydraulic conductivity versus void ratio was described for both the vertical and horizontal directions.

For the clay plasticity definition (Figure A-12), the log plastic bulk modulus, wet yield surface and flow stress ratio remained unchanged for all models, however the stress ratio and initial yield surface size was defined for each model based on experimental the experimental test being modelled. The 3-D deformable model used the same parameters for clay plasticity as the axisymmetric simulation of TX1548.

The geotextile material was defined as perfectly plastic and a porous permeable medium. Plasticity behaviour was inputted using the tabulated form, based on the experimental

compression tests performed on the geotextile material in the laboratory (Figure A-16). A hydraulic conductivity versus void ratio relationship (Figure 3-11) was inputted using data from both compression and hydraulic conductivity test data. The void ratio used was the volumetric reduction (m^3) of the material from the compression testing data.

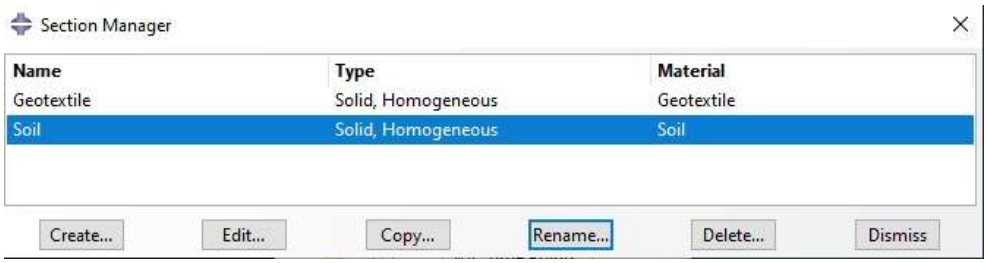

Figure 11-11 Section Manager window

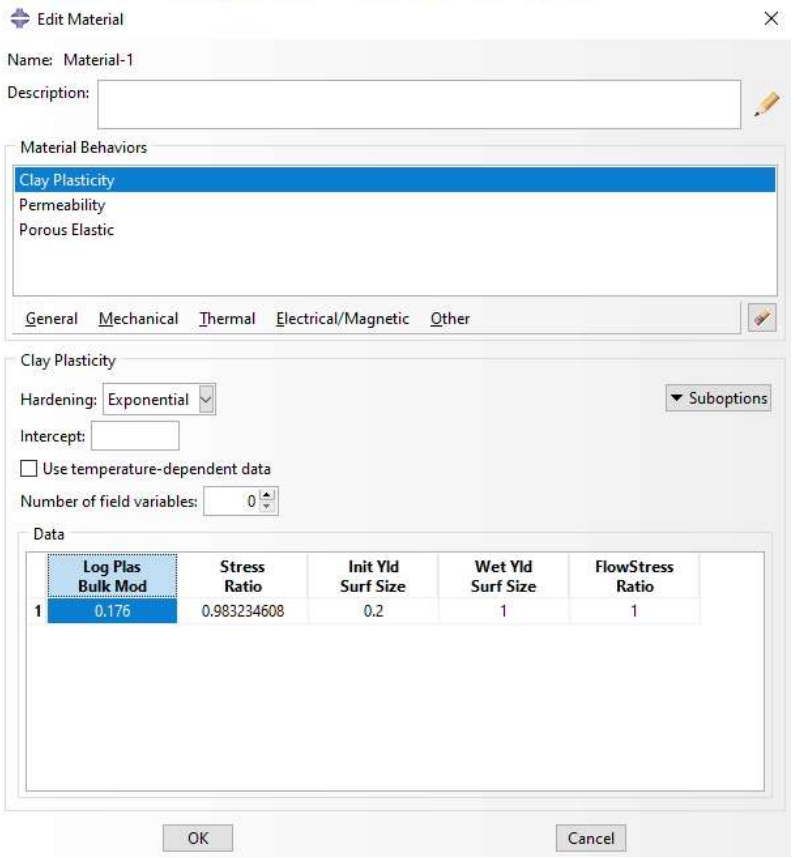

Figure 11-12 Soil (RGoM-EI) clay plasticity parameters.

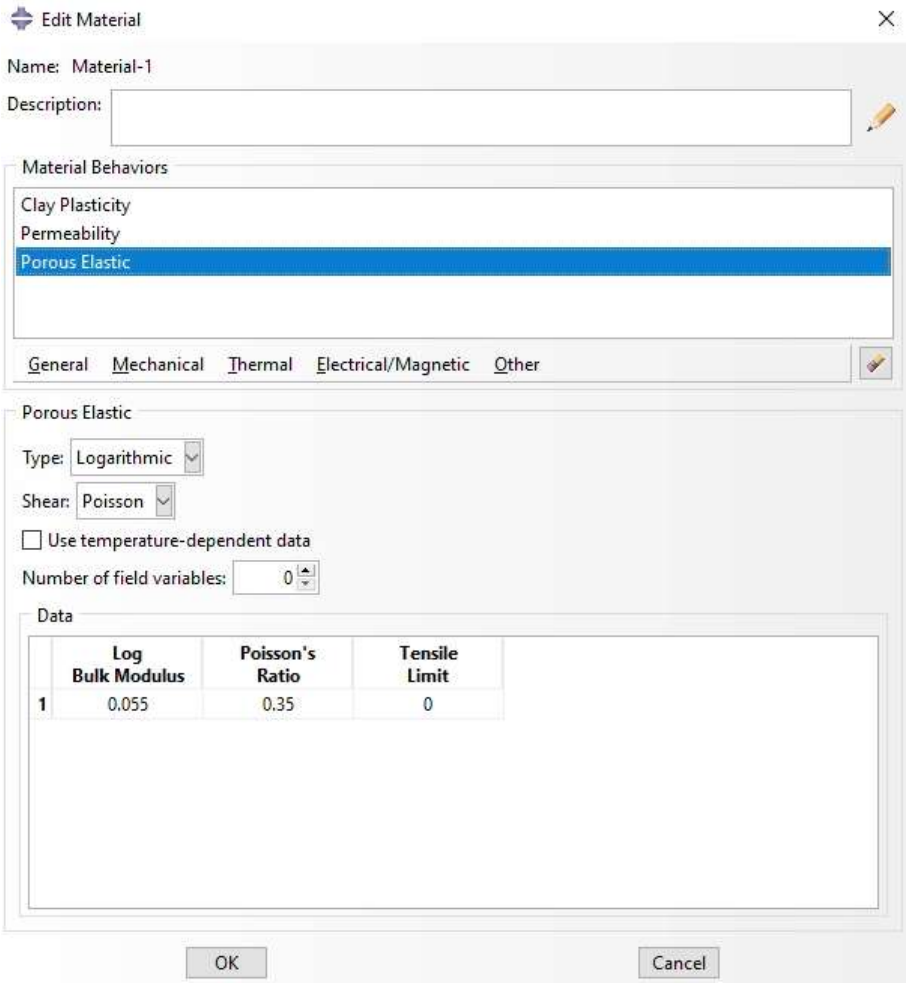

Figure 11-13 Soil (RGoM-EI) porous elastic material parameters.

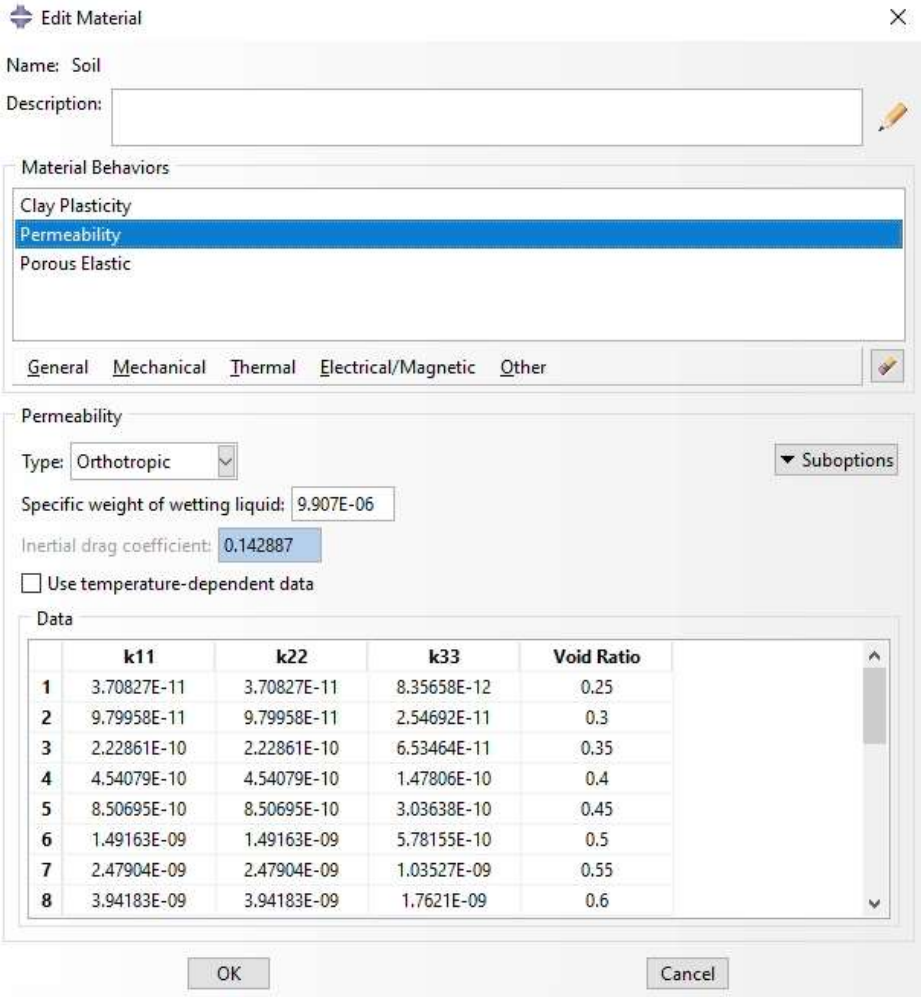

Figure 11-14 Soil (RGoM-EI) permeability material parameters.

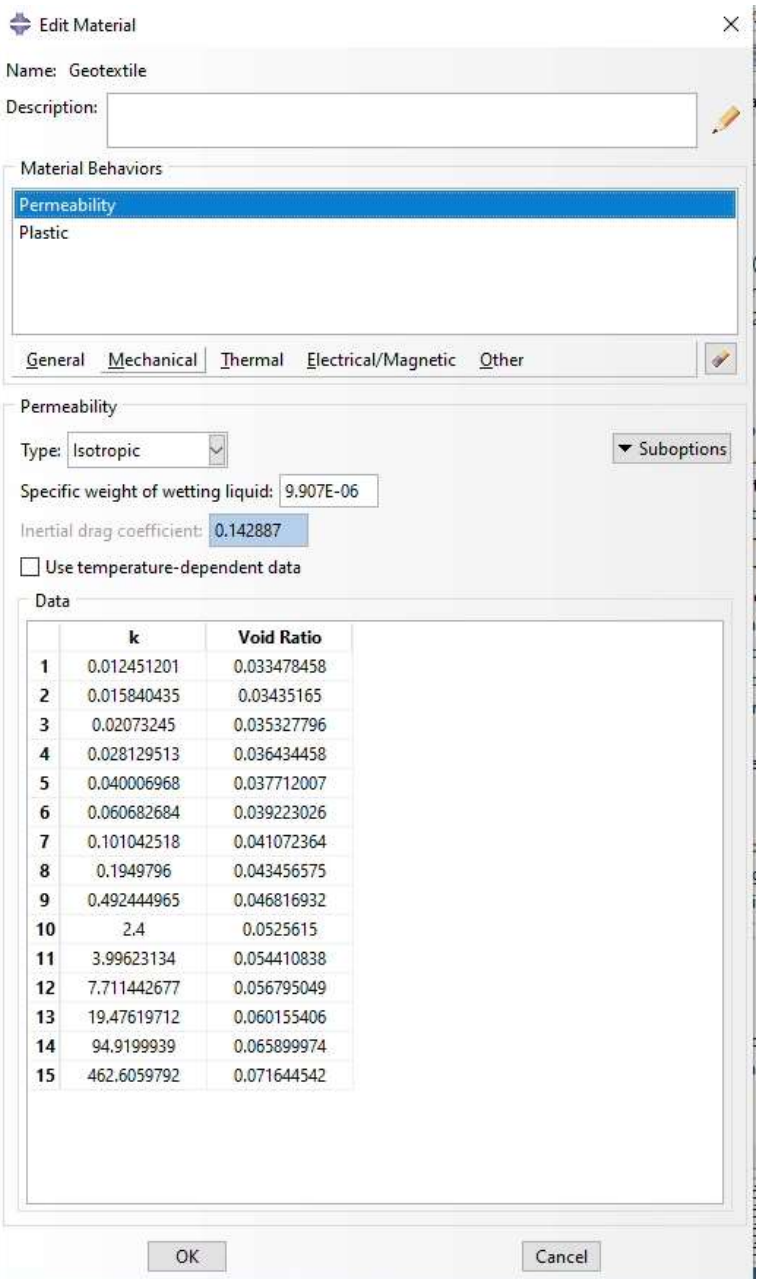

Figure 11-15 Geotextile side drain permeability material parameters.

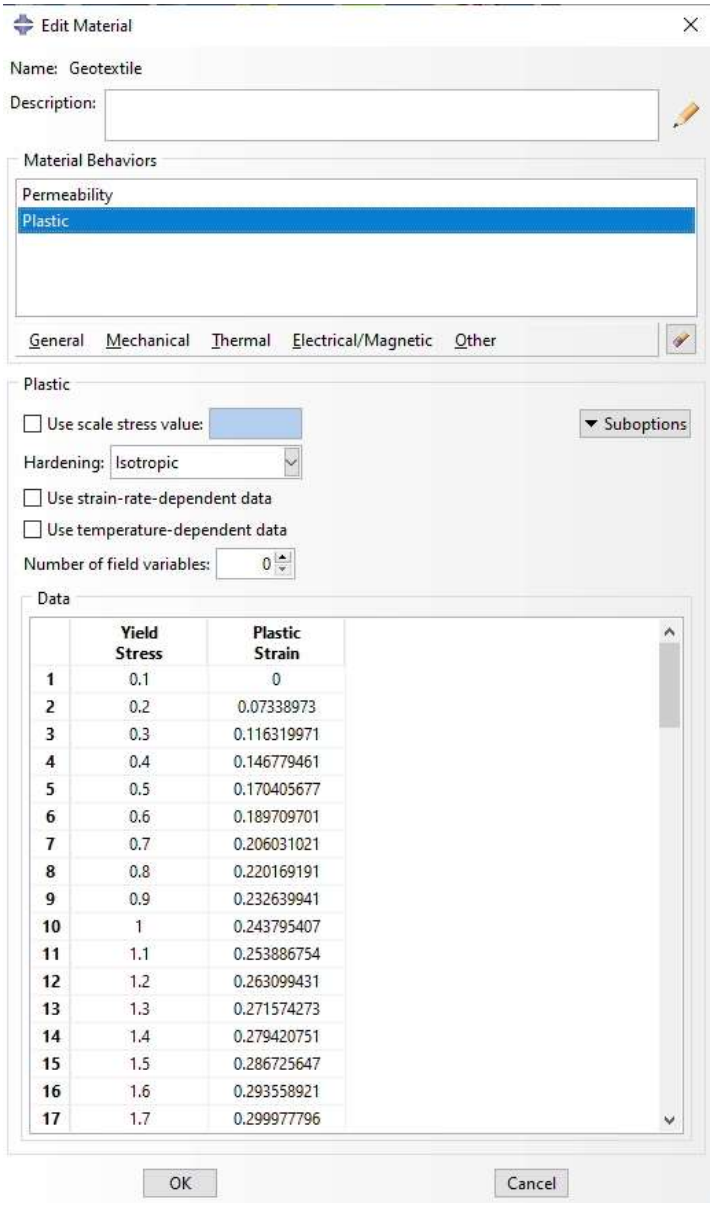

Figure 11-16 Geotextile side drain plasticity material definition.

A.6 **Meshing and Element Choice**

For an effective stress analysis in Abaqus FEA, Pore Fluid/Stress elements need to be selected (Figure A-17). These are hexagonal C3D20RP 20-node elements. Reduced integration was used for all simulations for efficiency. Figure A-18 shows the mesh generated for the 3-D deformable model.

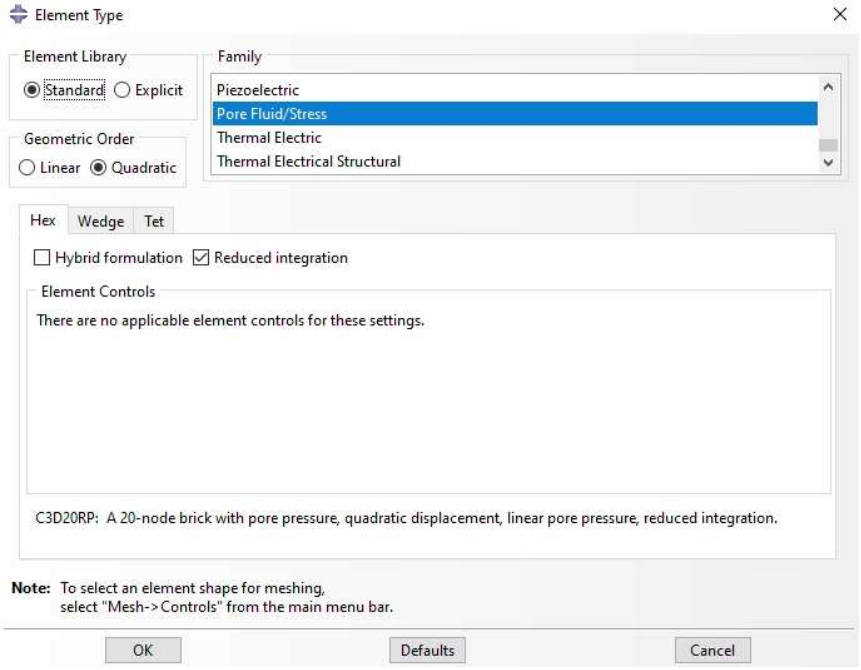

Figure 11-17 Element type selection for effective stress analyses using a transient soils step.

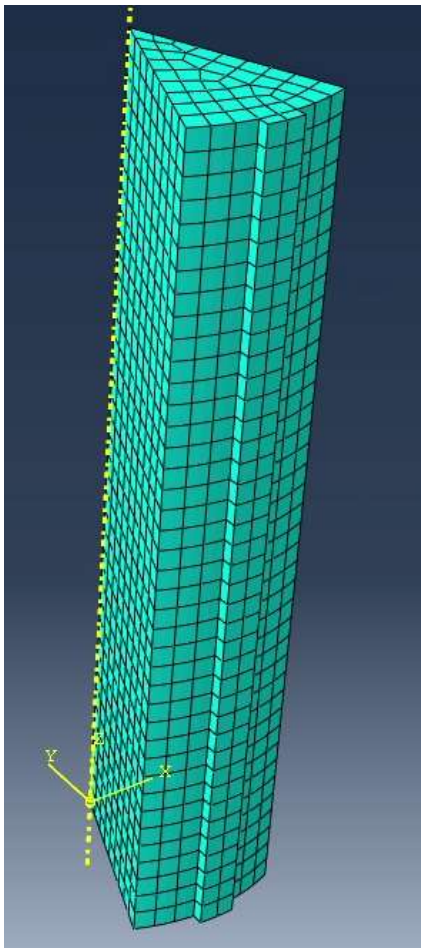

Figure 11-18 Mesh generated for 3-D deformable model.

A.7 **Data Processing**

A MATLAB script was used to reduce the data from each simulation and provide average values. A report of the relevant outputs was exported to a .csv file. From this .csv file the script could then average values. The script is shown in Figure A-19.

```
clear all
close all
clc

tic
data= readmatrix('VertDrains11111.csv'); %import the data

noOfSteps= max(data(:,1))+1;   % determine the number of steps
steps= cell(1,noOfSteps);
stepsAvg=cell(1,noOfSteps);

for i=1:noOfSteps
   stepFinder = data(:,1) == i-1;
   steps{i}= data(stepFinder,:);
   stepsAvg{i}=mean(steps{i});

end

stepsAvgTranspose=stepsAvg';
final=cell2mat(stepsAvgTranspose);


toc
```

Figure 11-19 MATLAB script used to reduce data.

Appendix B Test Data

Appendix B contains data plots for all tests uncorrected for excess pore pressure (Appendix B.1) and data plots for all tests using side drains (Appendix B.2). Compression curves (e versus σ'_a), K_0 - stress evolution (K_0 versus σ'_a), and MIT space stress path (q versus p'), are presented for each successful test run during this research.

B.1 **Tests Uncorrected for Excess Pore Pressure**

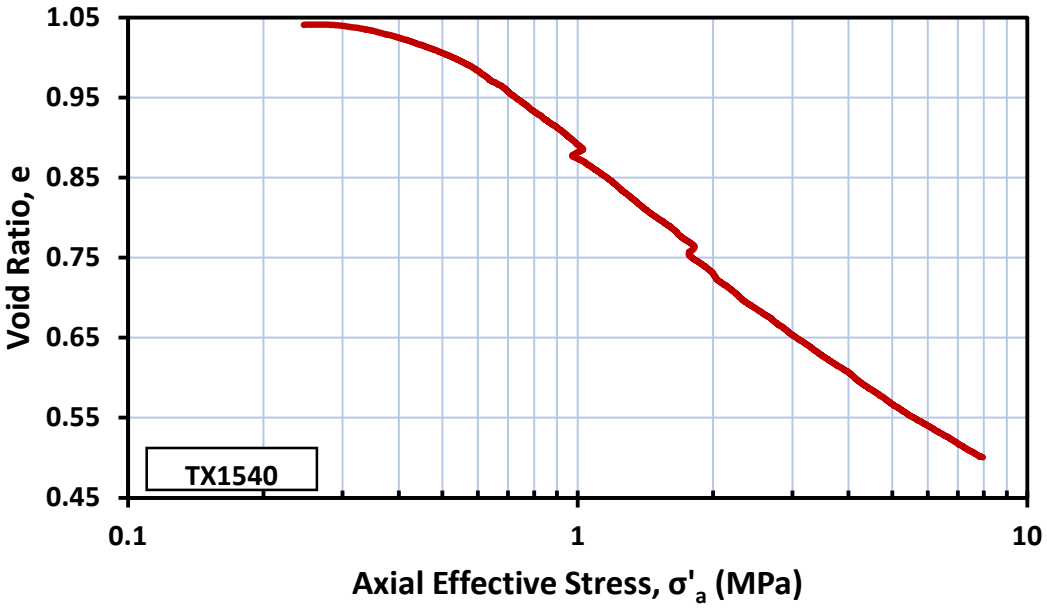

Figure 11-20 Uncorrected compression curve for TX1540.

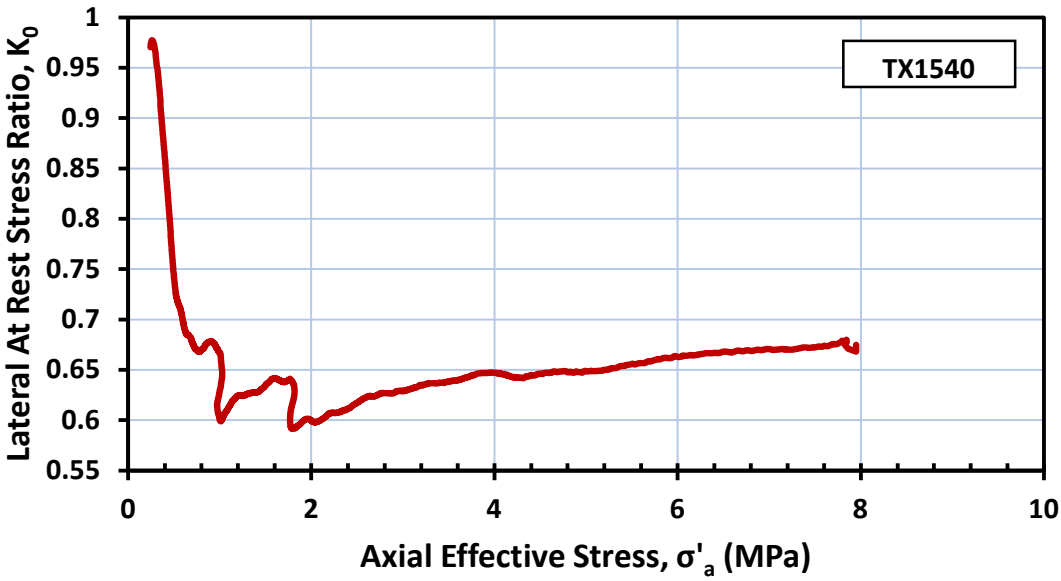

Figure 11-21 Uncorrected K_0 versus σ'_a for TX1540.

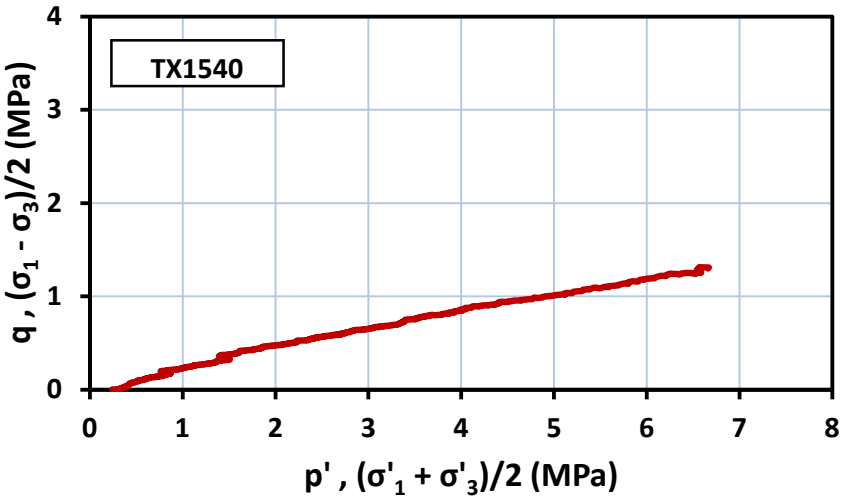

Figure 11-22 Uncorrected stress path in MIT stress-space for TX1540.

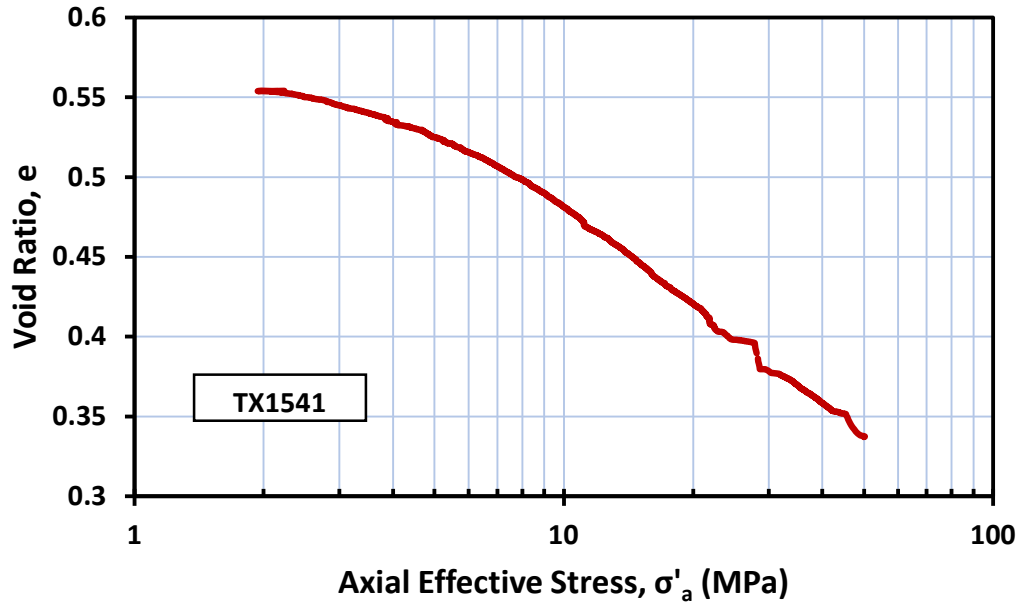

Figure 11-23 Uncorrected compression curve for TX1541.

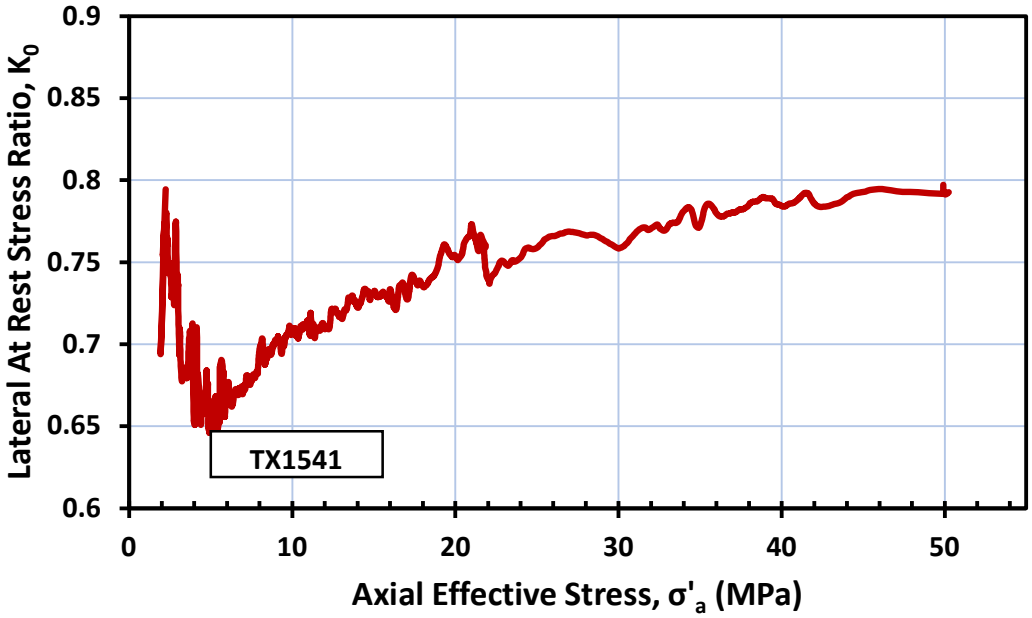

Figure 11-24 Uncorrected K_0 versus σ'_a for TX1541.

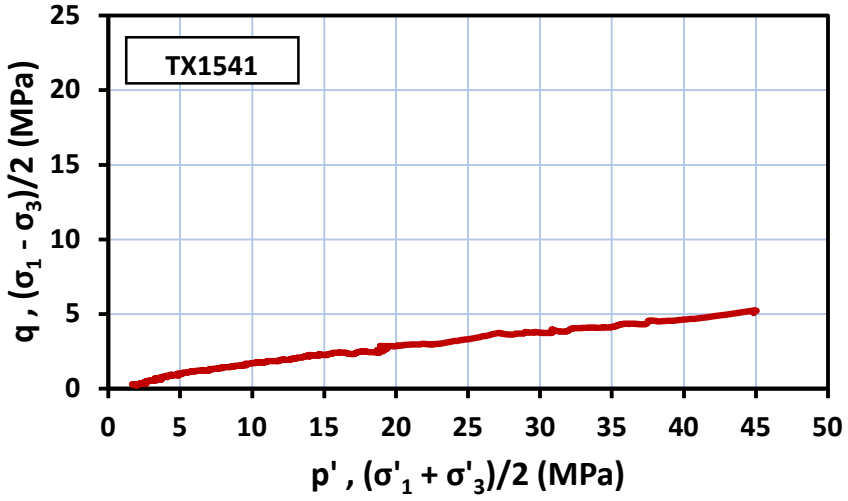

Figure 11-25 Uncorrected stress path in MIT stress-space for TX1541.

.

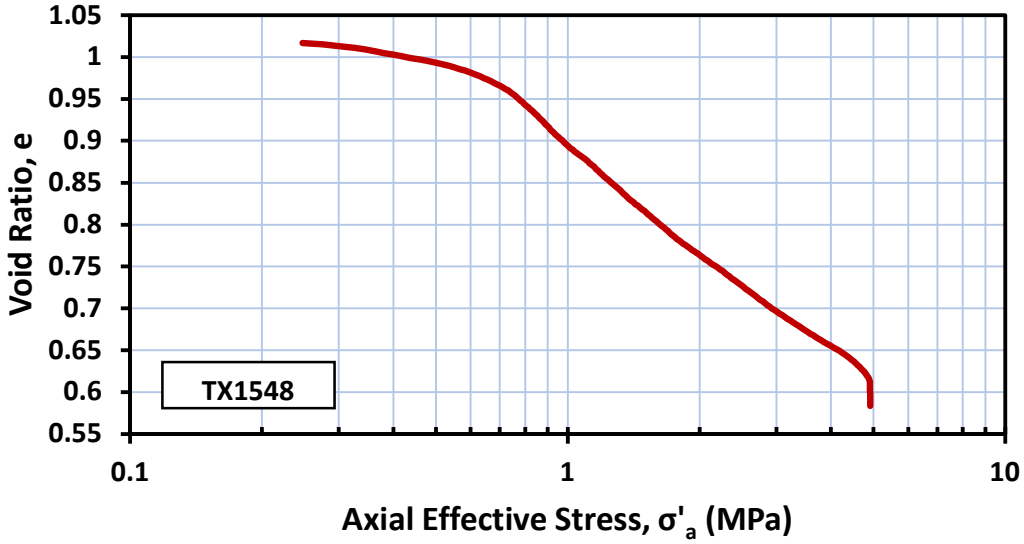

Figure 11-26 Uncorrected compression curve for TX1548.

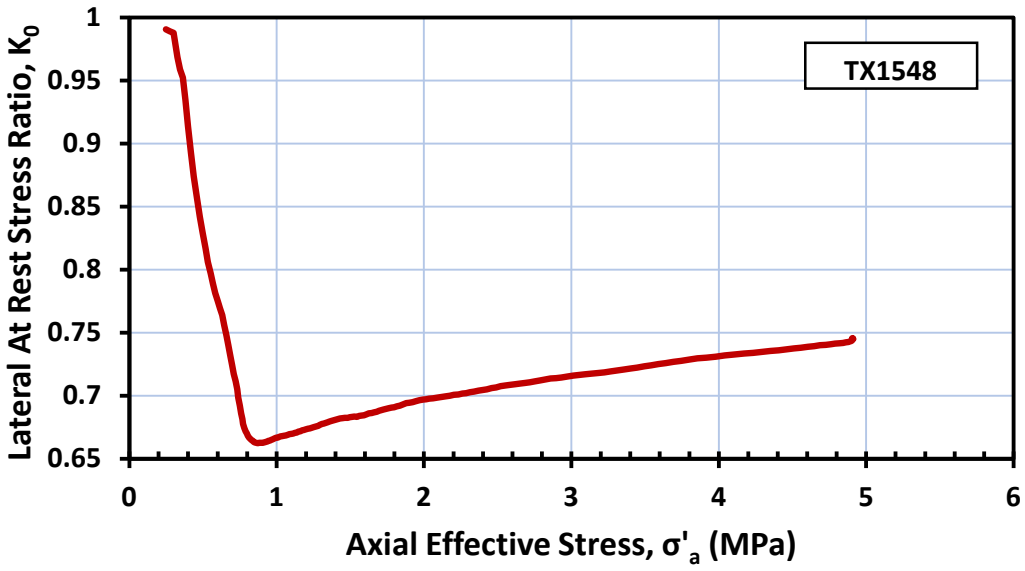

Figure 11-27 Uncorrected K_0 versus σ'_a for TX1548.

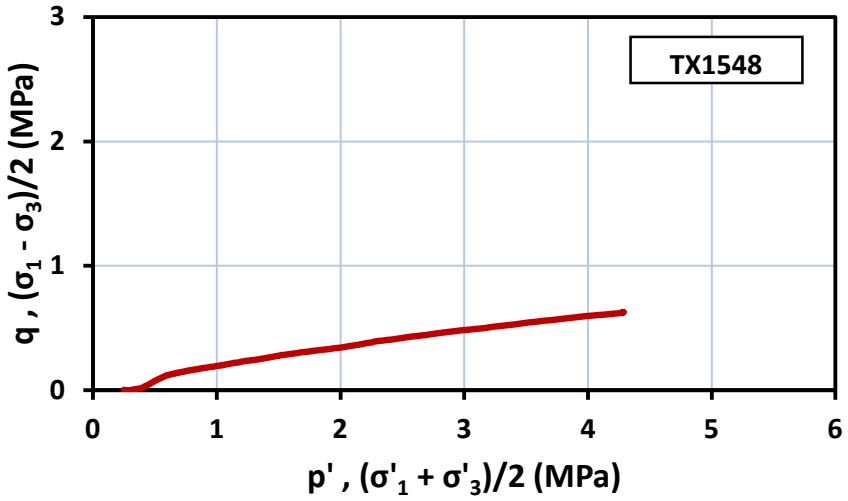

Figure 11-28 Uncorrected stress path in MIT stress-space for TX1548.

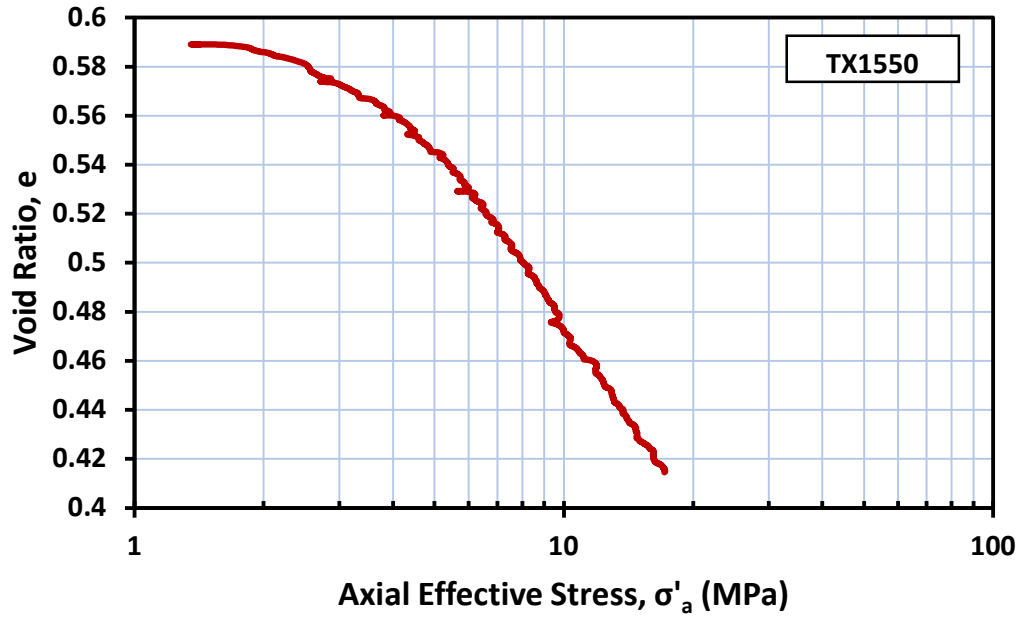

Figure 11-29 Uncorrected compression curve for TX1550.

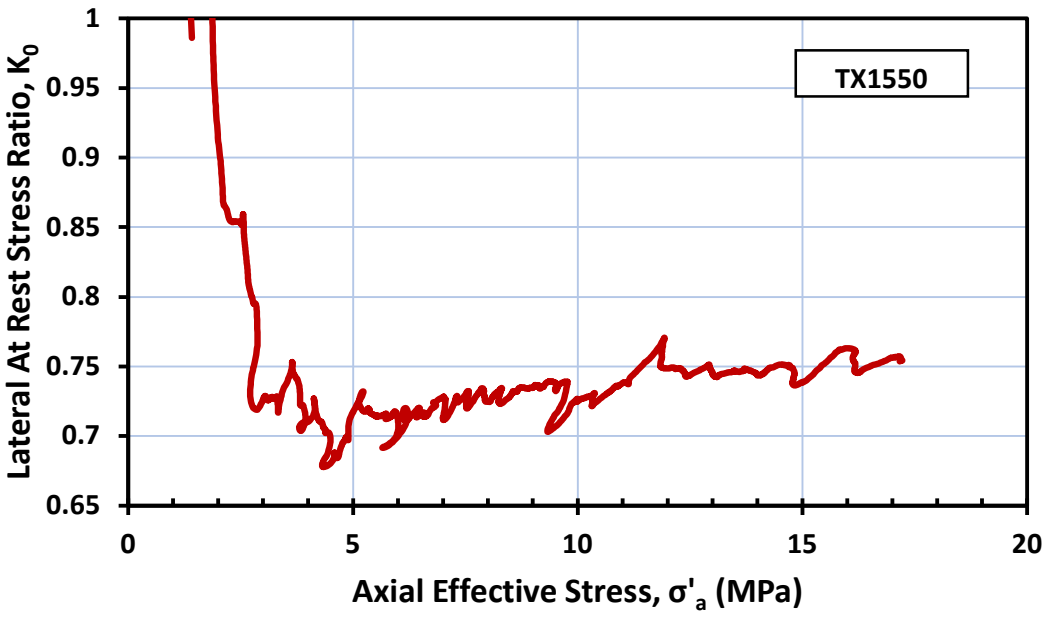

Figure 11-30 Uncorrected K_0 versus σ'_a for TX1550.

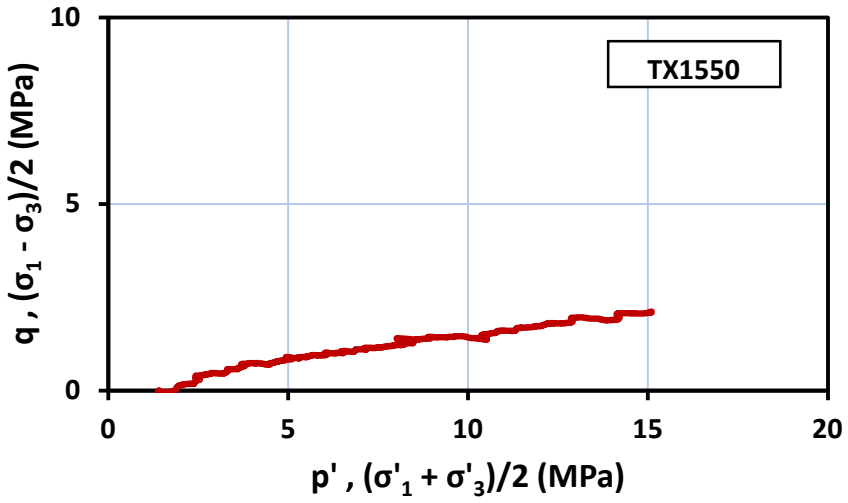

Figure 11-31 Uncorrected stress path in MIT stress-space for TX1550.

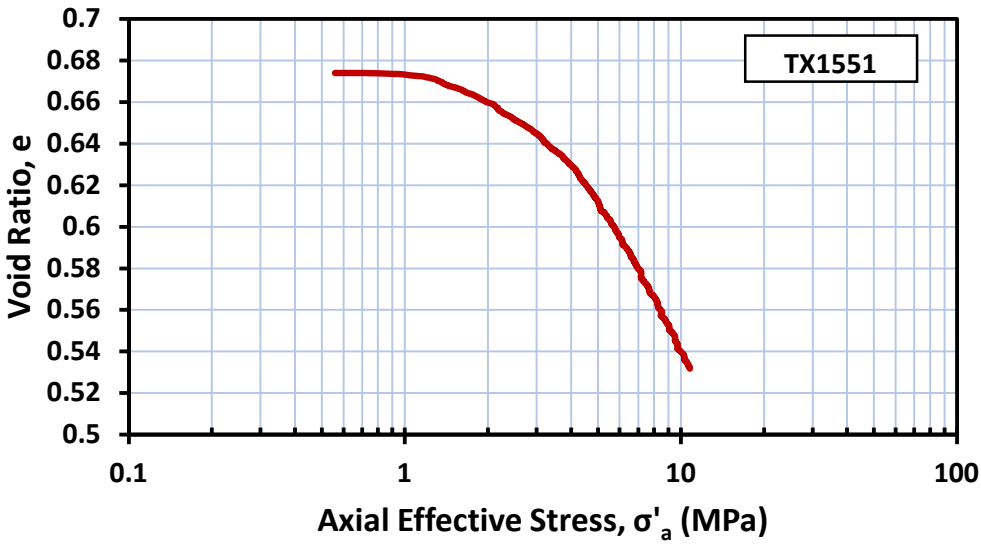

Figure 11-32 Uncorrected compression curve for TX1551.

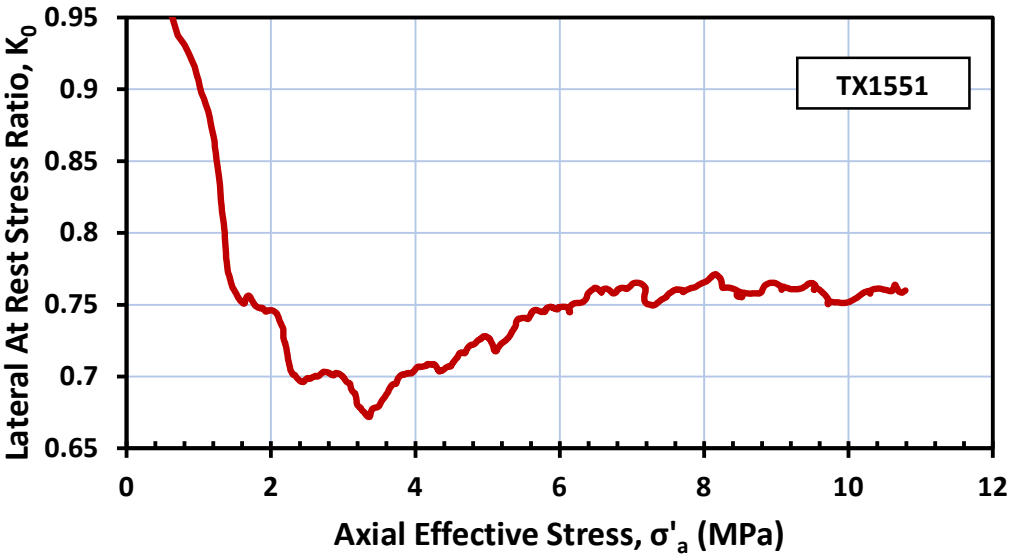

Figure 11-33 Uncorrected K_0 versus σ'_a for TX1551.

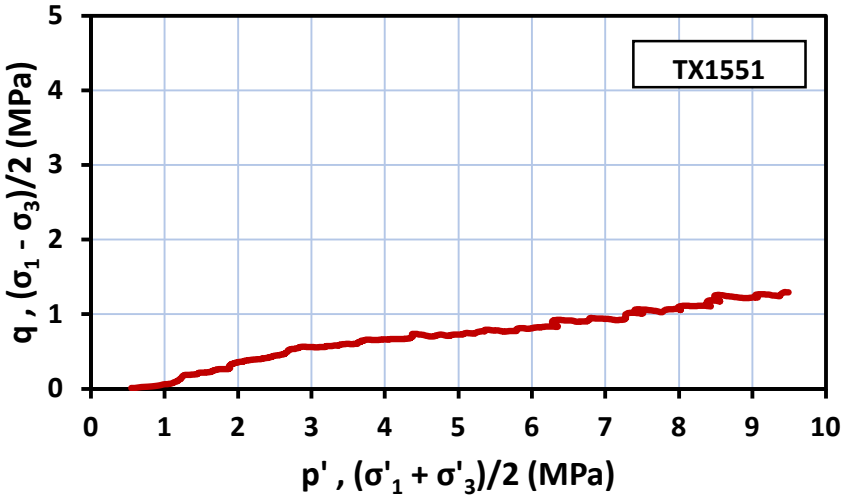

Figure 11-34 Uncorrected stress path in MIT stress-space for TX1551.

B.2 Tests Utilizing Side Drainage

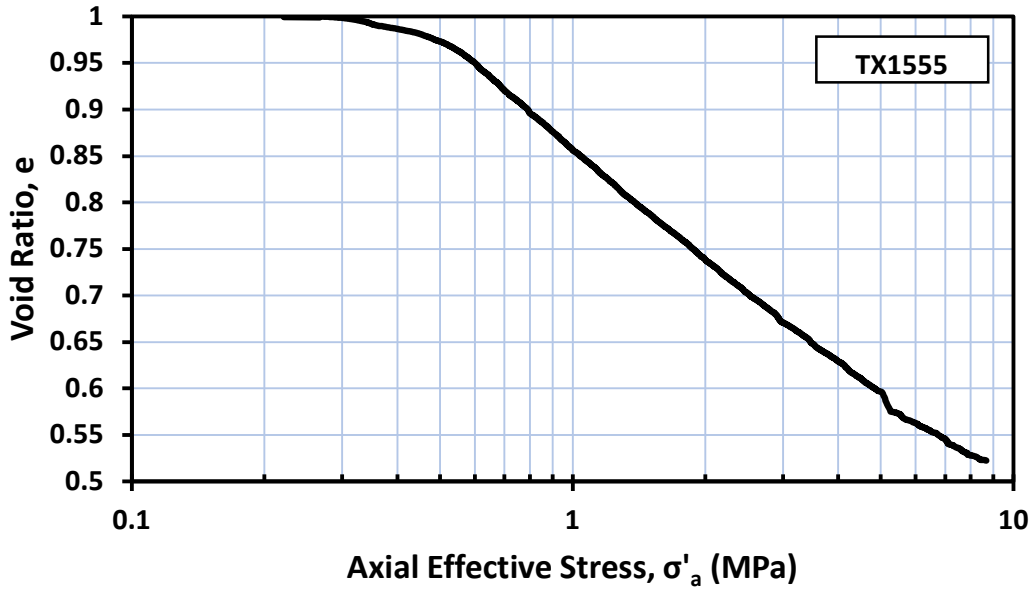

Figure 11-35 Compression curve for TX1555.

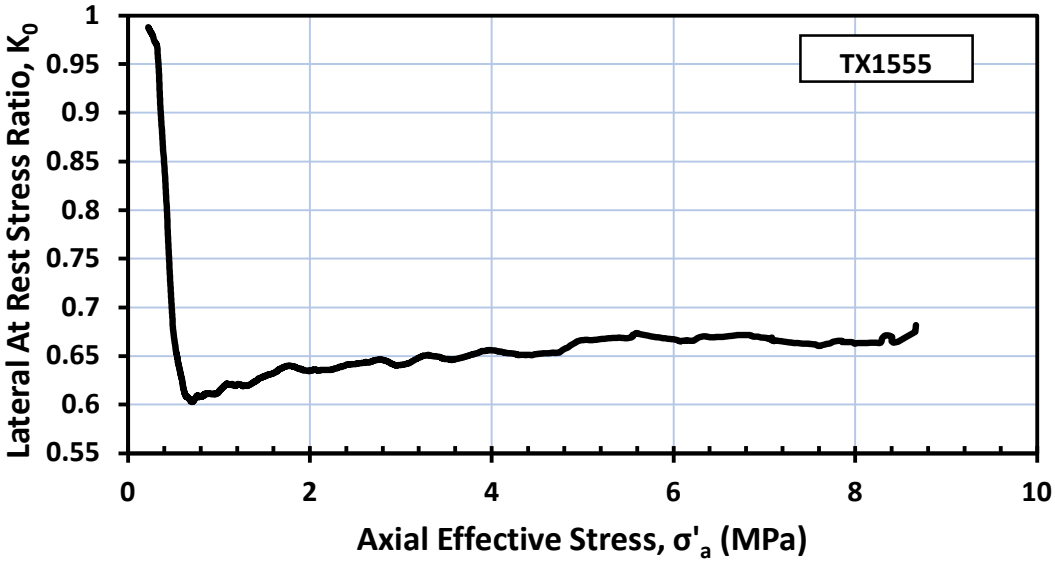

Figure 11-36 K_0 versus σ'_a for TX1555.

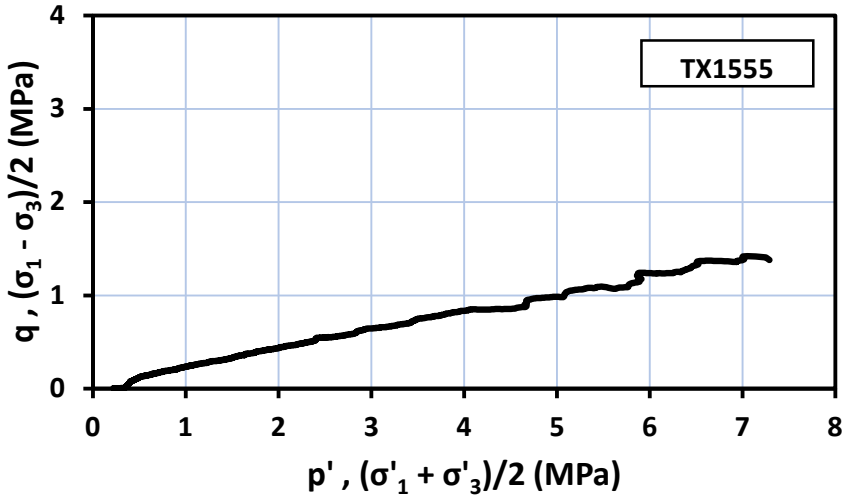

Figure 11-37 Stress path in MIT stress-space for TX1555.

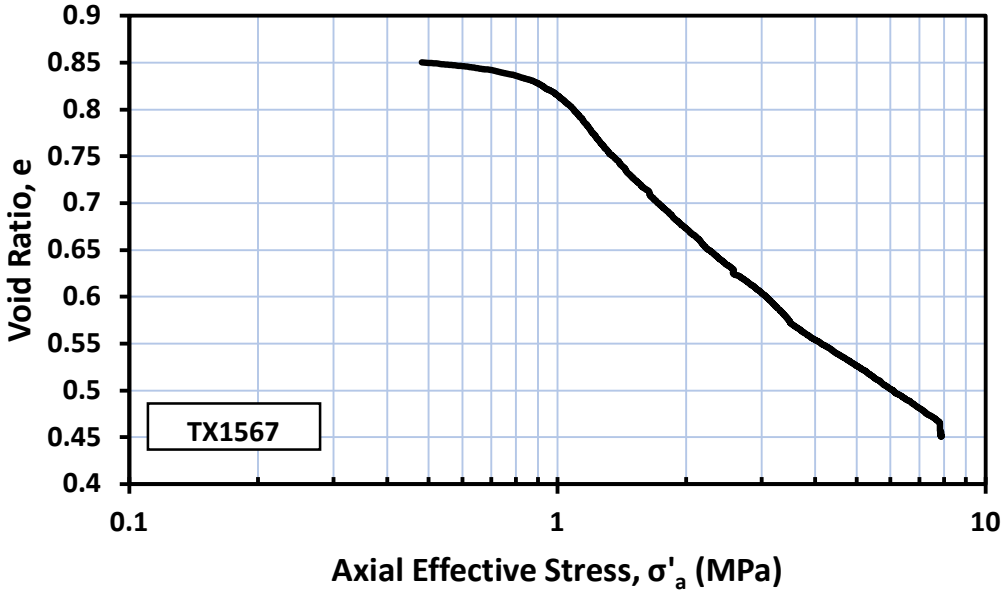

Figure 11-38 Compression curve for TX1567.

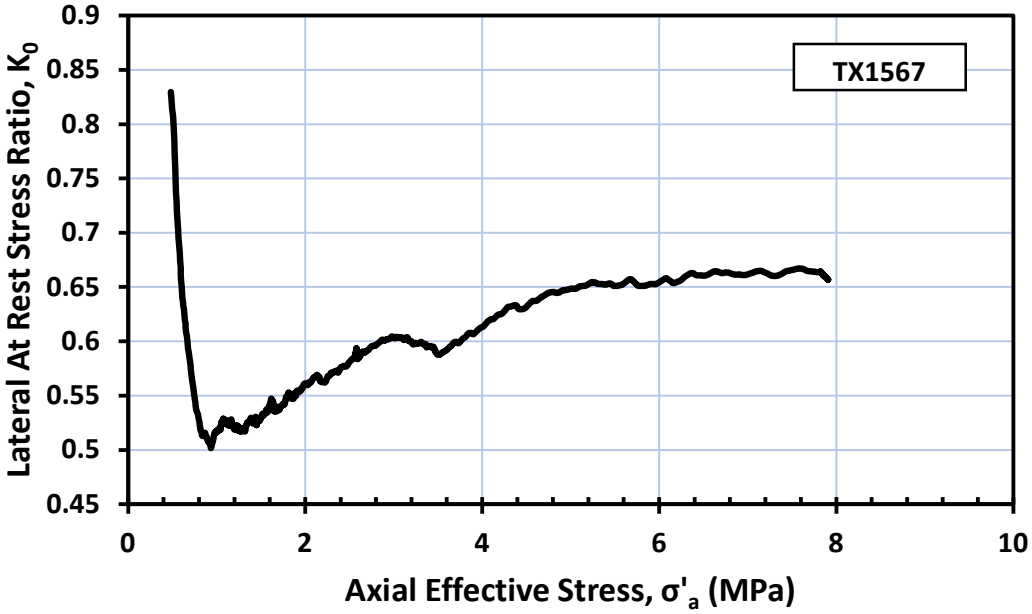

Figure 11-39 K_0 versus σ'_a for TX1567.

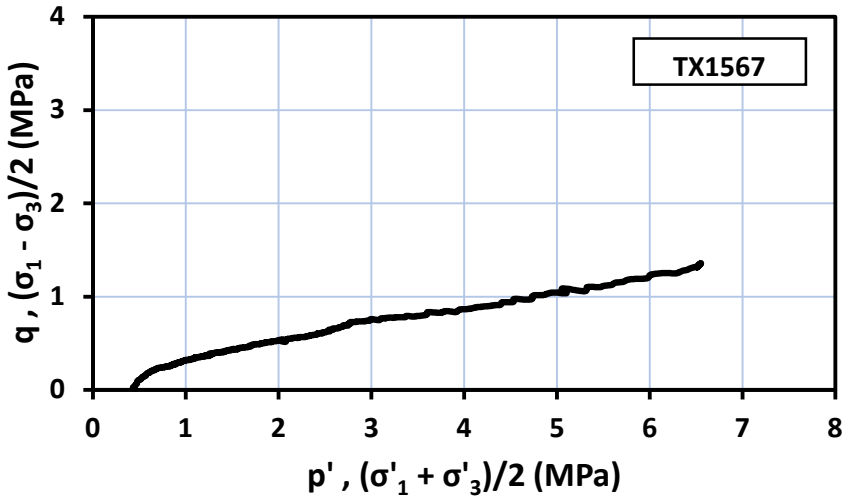

Figure 11-40 Stress path in MIT stress-space for TX1567.